SELECTIVELY ANISOTROPIC CONTINUOUS FIBRE CERAMIC COMPOSITES VIA SLURRY INJECTION

by

BENJAMIN ANDREW BAKER

A thesis submitted to the University of Birmingham for the degree of

DOCTOR OF PHILOSOPHY

School of Metallurgy and Materials
College of Engineering and Physical Sciences
University of Birmingham
October 2020

UNIVERSITY OF
BIRMINGHAM

University of Birmingham Research Archive

e-theses repository

This unpublished thesis/dissertation is copyright of the author and/or third parties. The intellectual property rights of the author or third parties in respect of this work are as defined by The Copyright Designs and Patents Act 1988 or as modified by any successor legislation.

Any use made of information contained in this thesis/dissertation must be in accordance with that legislation and must be properly acknowledged. Further distribution or reproduction in any format is prohibited without the permission of the copyright holder.

ABSTRACT

Continuous fibre ceramic composites for application in extreme environments is a burgeoning area in materials engineering. The production of sufficiently damage tolerant and reusable materials systems based on high fibre fraction and high dimensionality fibre substructures is widely considered to be a promising area for future refinements. One of these refinements is the ability to functionally grade materials in such a way as to impose a beneficial property gradient throughout a component's body. This thesis scrutinises a method for producing such anisotropic ceramic composites via injection of ceramic suspensions. The injection method is developed from previous work and literature to investigate the ability to place deposits selectively within a fibre architecture to build up a ceramic composition gradient. A series of such suspensions were formulated and tested to produce a property spectrum. A parametric study was then performed to consider the effects of the physical properties of the fluids – and how they couple with the processing variables on the timescale of the injection – on the shape and growth of the deposits in a particular fibre architecture. This information was then used to produce a set of statistical relations describing the production of deposits, and these were used to determine the viability in producing functionally graded structures within the preform type. The permeation mechanisms were investigated microstructurally, and the fracture behaviour of the composites with reference to ceramic interfaces within a contiguous fibre structure were addressed.

It was found that no conditions tested permitted large degrees of control in the deposit growth as defined in the study. Consequently, the ability to produce small-scale functional grading was considered to be minimal. Additionally, the mechanisms for spreading were found to be heavily impacted by the capillary forces in the narrow fibre pores, inferred from both experimental and numerical results. These channels were found to be

susceptible to flow channel constriction due to particulate clogging, thus adding complications to flow prediction. However, these conclusions are significantly based on the specific fabric substrate used. The details of the methods used are a useful transferable aspect of this study for the development of functionally graded materials by injection in other substrates. Specimens produced for this study demonstrated fracture patterns that did not necessarily propagate along the ceramic composition interface. This helps reinforce the base premise of this study; a composite produced from grading a continuous reinforcement substructure may retain a fracture pattern insensitive to the ceramic distribution, thus differentiating it from many laminate and coated materials. This conclusion may be applied to those materials that are of interest to this study; C_f/C composites modified by ceramic inclusions.

ACKNOWLEDGEMENTS

I would firstly like to acknowledge MBDA Systems and the School of Metallurgy and Materials for funding this project's research materials and my ability to perform it, respectively.

I have received much valuable support, advice and expertise from my advisor Professor Jon Binner. Equally, I have appreciated the efforts and inputs of my whole research group these past few years. In particular, I would like to thank James Wade and Vinothini Venkatachalam for their insight and experience.

I am grateful for the advice and input from Daniel Underhill and Christopher Garman at MBDA. I would also like to thank the members of the Materials Characterisation laboratory at MBDA Stevenage for all their help, both in non-destructive and mechanical testing. I would also like to thank Ji Zou for aid in electron microscopy.

Finally, I would like to thank my family for the invaluable support they have provided me with. I would not have reached this point without them.

CONTENTS

1 Introduction 1
2 Literature review 6
2.1.1 Materials for structural and thermostructural applications 6
2.1.2 Selectively heterogeneous material configurations 11
2.1.3 Production methods for CMCs 15
2.1.3.1 Precursor infiltration and pyrolysis 16
2.1.3.2 Reactive melt infiltration 17
2.1.3.3 Chemical vapour infiltration 17
2.1.3.4 Slurry infiltration 18
2.2 Controlling the physicochemical properties of ceramic suspensions 26
2.2.1 Basic properties of suspensions 26
2.2.2 Slurry composition and physicochemical effects 31
2.3 Porous media 39
2.3.1 An overview 39
2.3.2 Flow in composite architectures 49
2.3.3 Particulate or multiphase fluids 51
2.3.4 CFD approaches for multiphase porous media 53
2.4 Regularisation 56
3 Experimental 61
3.1 Ceramic suspensions 61
3.1.1 Selection and preparation 61
3.1.2 Surface tension measurement 63
3.1.3 Rheological analysis 63
3.1.4 Stability analysis 64
3.1.5 Fibre contact angle determination 64
3.1.6 Particle size determination 65
3.2 Fibre substrates 66
3.2.1 Raw materials and preform production 66
3.2.2 Pore analysis 67
3.2.3 Permeability analysis 70
3.3 Injection studies 72
3.3.1 Injection rig development 72
3.3.2 Calibration tests 73
3.3.3 Injection studies with fibre substrates 75

3.3.4 Injection studies statistical analysis 78
3.4 Tow impregnation analysis 83
3.4.1 Sample preparation 83
3.4.2 Washburn sorption 84
3.4.3 Clogging analysis 84
3.4.4 Microchannel flow experiments 85
3.5 Numerical modelling 86
3.5.1 Background and modelling procedure 86
3.5.2 Geometries and parameters 89
3.6 Composite production 93
3.7 Performance testing 94
3.7.1 Interfacial analysis 94
3.7.2 Flexural testing 95
3.7.3 Thermal testing 95
4 Results and discussion 96
4.1 Starting material characterisation and development 96
4.1.1 Injection fluid properties 96
4.1.2 Preform characterisation 106
4.2 Flow studies 121
4.2.1 Empirical injection studies 121
4.2.2 Numerical simulations of impregnation 163
4.2.3 Tow suction and capillary interactions 172
4.3 Composite performance and analysis 183
4.3.1 Microstructural analysis 183
4.3.2 Performance testing 188
4.3.3 Context of FGMs by injection 189
5 Conclusions and future work 192
List of references 198
Appendices 207
Appendix 1 207
Appendix 2 208

LIST OF FIGURES

Figure 1: Fracture toughness values found in the literature for 'fibre' UHTCMCs from: dispersed CNTs [33, 34], short-cut fibres [34-39], unidirectional [40-42], 2D [39, 40, 43-45], 2.5D [16] and 3D composites [46] 8

Figure 2: the characteristic relationship between the force and piston travel distance for (—) an unclogged needle, (---) a partially clogged needle and (•••) a fully clogged needle. 24

Figure 3: a graphical representation of DLVO theory for suspension interactions. The electrostatic potential (blue) and the dispersive potential combine to give the DLVO or 'total interaction' potential, an estimate of the total interaction between two charged bodies in a fluid medium.....28

Figure 4: The Stern model for the electric double layer of an arbitrarily charged surface. Effectively all surfaces are charged in solution. The spheres indicate positively and negatively charged ions. The dashed black line indicates the magnitude of the electrical potential. 29

Figure 5: Two schematics of 'porous media'. Left: a 2D space consisting of a number of grains with a variety of pore geometries and right: a cross section of a fibrous structure, consisting of bundles (dashed circle) of individual fibres packed into an array. Note that in both cases there are multiple scales of porosity. 40

Figure 6: Viscous dissipation related to pore size to neck-size ratio (adapted from Ozgumus et al. [192]) 47

Figure 7: The force vs submersion characteristic used in the determination of the contact angle for fibres. 65

Figure 8: The selection algorithm for the gap width between fibre tows. Here, p_i indicates the grey value of the peak immediately before the identified channel.....69

Figure 9: Schematic of the in-house permeation rig used for determination of the preforms used in this study. 71

Figure 10: A schematic of an injection deposit with a variety of defined parameters: l is the maximum extent of the deposit in the z direction, O_s is the offset of the top of the preform, α is the distance from the injection site to the top of the deposit and β is the distance from the injection site to the bottom of the deposit.....76

Figure 11: An example of one sample sectioned and used for image analysis 77

Figure 12: The regression procedure to generate the statistical models for the output variables for the injection studies. 78

Figure 13: A schematic to show the suction microchannels produced for the clogging analysis. 86

Figure 14: The geometry for the injection studies. It is a two dimensional representation of a cylindrical body. 90

Figure 15: The geometry used for the calculation of the through-thickness permeability of the preform consisting of layers of R and UD elements as in Figure 14. 91

Figure 16: The collated viscosity (at a shear rate of 120 s^{-1}) and surface tension of a number of the slurries shown in Table 4. The increasing entry number shows the chronological development of the obtained compositions. 97

Figure 17: Property matrix for the surface tensions and viscosities of the studied slurries. 98

Figure 18: Property matrix for contact angle and viscosities of the studied slurries. 98

Figure 19: The surface tension of the test slurries and their respective contact angles.. 99

Figure 20: The variation of the surface tension for a series of slurries with varying Tween80 concentration and nominally equal concentrations of other surfactant components and Al_2O_3. The entries are 21-32 in Table 4. 101

Figure 21: The variation of the viscosity (at a shear rate of 120 s^{-1}) for a series of slurries with varying Tween80 concentration and nominally equal concentrations of other surfactant components and Al_2O_3. The entries are 2, 22, 24, 26-32 in Table 4. 102

Figure 22: The variation of the surface tension for a series of slurries with varying PVP concentration and nominally equal concentrations of Tween80 and Al_2O_3. Dispex A4040 is varied for 7-9. The entries are 1-5, 7-9 and 17-20 in Table 4. 102

Figure 23: The variation of the viscosity at 120 s^{-1} for a series of slurries with varying PVP concentration and nominally equal concentrations of Tween80 and Al_2O_3. Dispex A4040 is varied for 7-9. The entries are 1-5, 7-9 and 17-20 in Table 4. 103

Figure 24: The depth of the turbid section of the slurry below a clear supernatant for a vial of slurry as a function of time. 104

Figure 25: The depth of turbid slurry beneath a clear supernatant for the stability analysis of the HfB_2 and ZrB_2 slurries used in composite production 106

Figure 26: SEM micrographs of (left) the 2.5D preform junction between the 90°, R and 0° layers, (centre) the I_{cf} preform, (right) the microstructure of the STUD layers. 107

Figure 27: Thresholded and binarised images of the unidirectional layers of the 2.5D preform at different magnifications. 100x and 50x show the general fibre packing structures in the tow. 10x and 5x give a greater indication of the packing of the tows together within the UD layers. 107

Figure 28: The radial distribution function for a 100x magnification image of the fibre tow, centred on the central pixel of the indicated fibre 109

Figure 29: The average 5-nearest neighbour separation distances of the image in Figure 28 (rounded to the nearest 0.5 μm). 110

Figure 30: The average 5-nearest neighbour separation distances of a 50x magnification image of a fibre tow (rounded to the nearest unit). 110

Figure 31: A surface plot of an inter-tow porosity region. The red line indicates the inferred channel width. 112

Figure 32: A histogram showing the distribution of intra-tow gaps for the unidirectional layer of the 2.5D preforms. 113

Figure 33: The mercury porosimetry analysis of the 2.5D preform, indicating the volume percentage contribution of each pore diameter 113

Figure 34: The Reynolds number of flow of the slurries developed for the optimisation studies through the characteristic dimensions indicated, and the flow at different flow speeds (m s^{-1}) 115

Figure 35: The flow speed (m s^{-1}) effect on the capillary number for the different test fluids investigated in this study. 115

Figure 36: The capillary pressure for unforced flow as a function of pore radius for the spectrum of slurries used in the injection studies. 117

Figure 37: The plots of pressure gradient across the sample vs the argon Darcian flow rate. Each fibre configuration was tested in transverse (T) and in plane (P) mode, with distinction made for the anisotropy for the STUD lay-ups (0 and 90° orientations, 0P, 90P). Horizontal error bars have been omitted for visual clarity, but an error of (50% of the difference between each point per test is standard). 118

Figure 38: A linear plot of STUD 90P and 0P to show the significant non-linearity. 120

Figure 39: An example of the force-displacement characteristic for a depression rate of 4.06 mm s^{-1} at 5 (black line), 20 (dark grey line) and 35 mm (light grey line) displacement. 122

Figure 40: The force required to begin the piston's movement (unfilled circles) and to keep the piston moving (filled circles) averaged across all total displacements (5, 20 and 35 mm). 122

Figure 41: the results of Figure 40 broken down into the constituent depression displacements. 123

Figure 42: An F-d characteristic in which a peak is seen coinciding with initial contact with the plunger, followed by a plateau corresponding to the steady sliding force of the piston in the syringe. An uneven region is observed at large displacements for most samples. 124

Figure 43: The force-depression rate relationship between for depressions of 35 mm of water from syringes with different gauge of needle. 125

Figure 44: The relationship between the stead flow force and the linear flow speed of the fluid from the needle. The viscosities of the different investigated slurries are indicated. 126

Figure 45: Multiple regression statistics for the effect of viscosity and flow speed on the initial and steady compression forces..... 127

Figure 46: General shapes produced by the injection of different slurries at different volumes and injection speeds. (a) an 'alternating brick stack' structure, with the largest dimensions being narrow channels along the principle UD axes and (b) spheroid/ellipsoidal structures..... 129

Figure 47: A flow chart detailing the regression procedure for the basic input variables. The output variable at the top is firstly regressed against all the predictor variables in the white box, and then subsequent rounds of L1 regression eliminate variables. Grey boxes indicate further rounds of L1. The final R_{adj}^2 value is of the final set of variables in the L1 regression, analysed as a separate multiple regression (i.e. no L1 penalty). 131

Figure 48: The synthesised input variable linear regression procedure and results..... 131

Figure 49: The mean error increase per variable inclusion, corresponding to variable importance, for H and W derived from the random forest analysis. 133

Figure 50: Adjusted R^2 for OLS (white bars), L1 regularisation (black bars) and L2 regularisation (dashed bars) and the penalisation magnitudes for L1 (filled diamonds) and L2 (empty diamonds) for H over the variable sets described in Table 21..... 136

Figure 51: Adjusted R^2 for OLS (white bars), L1 regularisation (black bars) and L2 regularisation (dashed bars) and the penalisation magnitudes for L1 (filled diamonds) and L2 (empty diamonds) for W over the variable sets described in Table 22..... 136

Figure 52: A depiction of the coefficient estimate variability in the regression procedure. The standardised range, maximum to minimum differences between determined coefficients divided by the standard deviations for each coefficient, are shown for H (white) and W (grey). 137

Figure 53: The differences between the OLS and L1 (red) and L2 (empty) residual values in the real/predicted output for (left) H(5) - a sparse data set and (right) H(9) – a dense data set. Note the differences in total scale..... 138

Figure 54: The standardised coefficients (left) with 95% confidence intervals and the model results superimposed with the true data points (right) for the L2 regularisation of variable set 9 for H. 141

Figure 55: The standardised residual plot for the L2 regularisation of H variable set 9, data points representing the number of standard deviations the predicted height lie from the observed height. 142

Figure 56: (left) The standardised residuals of entry 6 in Table 23 and (right) the superimposed model and real data points..... 143

Figure 57: The dependence (both value and error) of H on each constituent variable. In each case, the default values set for the variables is μ_{eff} = 0.01 Pa s, θ = 80°, V_s = 0.3 cm^3, v_f = 4 m s^{-1} and γ = 45 mN m^{-1}. The green shows the interpolation range of the variables investigated. 147

Figure 58: The dependence (both value and error) of W on each constituent variable. In each case, the default values set for the variables is μ_{eff} = 0.01 Pa s, θ=80°, V_s= 0.3 cm^3, v_f= 4 m s^{-1} and γ = 45 mN m^{-1}. The green shows the interpolation ranges of the variables investigated. 148

Figure 59: The standard error in the predicted dimension for H (top) and W (bottom) against predicted dimension. The black dots are the data points, and the red line is the value of error as a proportion of the total dimension. 149

Figure 60: The concentration gradient provided by injection of phases of either pure A, pure B or a ratio matching the expected linear profile (---) over the thickness, as the number of injections increases: (■) 2 injections, (◆) three injections, (●) four injections, (▲) five injections, (×) 6 injections. 150

Figure 61: The deposit height vs number of injections required to produce the example component described in Figure 60. 151

Figure 62: The effect of total thickness on the ratio of the overall error to the absolute height values. 152

Figure 63: The relationship between the desired qualities of the FG composite and the output parameters of the regression 153

Figure 64: An image of the intersection between the 0°, random and adjacent 90° UD layer at the lower portion of sample produced with the most viscous and least wetting slurry, at a low injection speed with a 21G needle. Here, white is the deposit, the circular, or high aspect ratio, grey zones are fibres in the 0 and 90° layers respectively, and the wide structureless grey patches are resin (i.e. pore space) 154

Figure 65: A higher magnification image on the 0° layer as seen in Figure 64 showing the details of the intratow porosity 155

Figure 66: the injection of the same slurry as in Figure 65, but at a far higher injection speed (~16x) and therefore expected capillary number regime. It can be seen that the filling of the UD layer is far more inconsistent. Inset: a zoomed out view of a UD region. 156

Figure 67: High-speed injection of a more wetting, lower viscosity slurry: (a) an extended view of the 0° layer, (b) the fringes of the impregnation, showing the slurry concentrated around the larger channels in the preform 157

Figure 68: The cross section of the injection study sample shown in Figure 67. The box indicates the extent of the flow in the UD layer demonstrating the largest extent of slurry flow. 158

Figure 69: The height, width and aspect ratio of the injection of Al_2O_3-2 into I_{cf}. 159

Figure 70: The spreading of slurry in the STUD preforms: (+) Major axis of slurry extent and (-) minor axis of slurry extent in plane as a function of depth. The dotted red line indicates the ratio of the major to minor axis permeability. (a) Injection of 0.1 cm^3 of Al_2O_3-2 and (b) injection of 0.2 cm^3 of Al_2O_3-2. 161

Figure 71: The deposit shape from test 3 in Table 13. 163

Figure 72: The ratio of the z to x extents of volume fraction>0.7 at 0.08 s for a 1:1, 3:1 and 100:1 viscous resistance in the UD-max:UD-min axes. Left: 0.001 kg s^{-1} flow rate and right: 0.0005 kg s^{-1}. 163

Figure 73: The ratio of the z to x extents of volume fraction>0.7 at 0.08 s for increasing transverse flow resistance in the UD layers, as in tests 7-9. 165

Figure 74: (right) The velocity distributions for test 16 (Table 13) at the location indicated by the arrow at 0.005 s in the simulation, (left) volume fraction plot. 166

Figure 75: The z-axis extent of the slurry volume fraction (border at volume fraction > 0.7) as the slurry type changes. 167

Figure 76: The deposit morphology from the injection into a preform whose permeability tensor components are those determined experimentally in this project. 167

Figure 77: (a) the permeability of the preform as it builds up layer by layer, (b) the comparison of the model 2.5 preform permeability to the empirically measured value. 168

Figure 78: The fibre fractions of PTFE tubing samples produced. The green triangles represent the homogeneously packed samples, and the red crosses the heterogeneous samples displaying fibre clumping and large regions of porosity. The x-axis holds no information. 172

Figure 79: An example of the mass gain and calculated flow speed for the 10 vol% sample. 174

Figure 80: The mass gain relative to as-prepared while wet at 300 s duration and after drying, in addition to the visual extent of the penetration. 174

Figure 81: The concentration (wt%) of water in the infiltrant liquid for different fibre volume fractions. 175

Figure 82: The dependence of nearest neighbour spacing on fibre volume fraction for an ideal square array of equal sized circles bounded by a circle 176

Figure 83: The change in deposit, pore and fibre volume fraction as the distance increases from the submerged end of the encapsulated tow 177

Figure 84: The ratio of deposit area to fibre area as the distance from the submerged tip increases. The inset micrographs show representative images of the tow. The black areas

show pore space, the white circles represent fibres (the red scale bar represents 80 μm) and the grey represents Al_2O_3 powder. 178

Figure 85: The results of the regression of W with the Washburn-sorption predicted values. 180

Figure 86: The penetration length of the microchannels shown in Figure 13 for full reservoirs of Al_2O_3-24. 182

Figure 87: BSE image of a position along the interface at the 0 mm surface. Three contrasts can be seen; bright grey (HfB_2), medium grey (ZrB_2) and dark grey (carbon: fibres, resin or PyC). 183

Figure 88: Concentration gradient for all the through-thickness scans at numerous depths and cross-section co-ordinates superimposed to show the variability of interface starting depth, thickness and gradient. 184

Figure 89: A schematic representation of the interface position for the sample investigated both at a 5 mm and 15 mm x co-ordinate position through the length of the sample. The central point represents the 50:50 concentration interface, and the upper and lower error bars represent the location of the 94% and 6% wt%(Hf)/[wt%(Hf)+wt%(Zr)] depths. The thick black line represents the nominal 50:50 level, the goal configuration. 185

Figure 90: The proportion of HfB_2 as a function of overall UHTC content in the samples. The solid line indicates the line of best fit and the dashed lines indicate the confidence interval within one standard deviation of the regression. 185

Figure 91: An example of an EDS dotmap at a transitional region at a depth of around 10 mm in the sample with (red) Zr and (blue) Hf indicated. 186

Figure 92: A BSE image of multiple phases and the presence of cracks in the C/UHTC matrix. Three contrasts can be seen: bright grey (HfB_2), medium grey (ZrB_2) and dark grey (carbon: fibres, resin or PyC). 187

Figure 93: The failure modes observed at high deflection for the 50:50 C_f/C-HfB_2-ZrB_2. Bars were 105 mm long. 189

Figure 94: A potential capillary suction stage to allow for single-layer capillary impregnation. 191

LIST OF TABLES

Table 1: Some relevant properties of candidate UHTCs and their oxides [23-30] 7

Table 2: The fundamental properties of ceramic suspensions as they apply to ceramic composite production 27

Table 3: The raw materials for the production of the suspensions for this study. 61

Table 4: The test fluid compositions for the slurry spectrum investigated in this study. 62

Table 5: A summary of the preform/fibre sheet properties used in this study. 66

Table 6: Preform sample dimensions for permeability determination, with their relevant flow geometries calculated 72

Table 7: The key probed parameters of the investigation 77

Table 8: The original set of input parameters for the injection studies 80

Table 9: Basic input - raw output (the different needle gauges were included in the regression as separate and mutually exclusive dummy variables). 82

Table 10: Synthesised input - raw output. 82

Table 11: Synthesised input - raw output, non-linear with interaction parameters. 83

Table 12: The default calculation parameters for the injection study simulations. 91

Table 13: The test parameters for the injection studies 92

Table 14: The testing regimen used for analysis of the unoptimised samples. 94

Table 15: The slurry compositions taken forward to the injection kinematics testing. . 100

Table 16: The slurry properties from the compositions in Table 1. 100

Table 17: Areal fractions of fibres thresholded from micrographs. 109

Table 18: the mean, standard deviations, medians and interquartile ranges for the distributions shown in Figure 29 and Figure 30. 111

Table 19: The calculated Darcian permeabilities from Equation 19 118

Table 20: The viscous permeability k_v and inertial resistance term k_1 calculated from the fit to Equation 20. The ratio of the Darcian permeability (Equation 19) and viscous permeability is shown for comparison. 119

Table 21: The variable sets for the regression analysis for H 135

Table 22: The variable sets for the regression analysis for W 135

Table 23: The regression statistics of a series of functions created from the dimensional analysis of the results of the initial linear regression shown in Figure 48. A constant of proportionality and dimensional correction is indicated as either α_i or β_i..... 140

Table 24: The final selected relations for H and W that displayed the highest statistical significance..... 144

Table 25: The regression equations for the I_{cf} injection..... 160

LIST OF ABBREVIATIONS

C_f	Carbon fibre
CFCC	Carbon fibre ceramic composite
CMC	Ceramic matrix composite
EDS	Energy dispersive spectroscopy
FGC	Functionally graded composite
FGM	Functionally graded material
I_{cf}	Isotropic carbon fibre preform
IFT/ST	Interfacial tension / surface tension
L1	L1 norm (i.e. Lasso) regularisation
L2	L2 norm (i.e. Ridge) regularisation
PVP	Polyvinylpyrrolidone
R	Randomly woven/stitched layer of the 2.5D preform
SEM	Scanning electron microscopy
SI	Slurry infiltration
SLE	Sharp leading edge
STUD	Split-tow unidirectional fibre
UD	Unidirectional layer of the 2.5D preform
UHTC	Ultra-high temperature ceramic
XCT	X-ray computed tomography

1 INTRODUCTION

The imaginations, ambitions and expectations of systems designers are advancing rapidly in this technological era. Materials, especially aerospace materials, are expected to be able to perform for longer, under higher loads, at higher temperatures and in increasingly aggressive chemical environments to fulfil these novel and innovative designs. For example, space re-entry vehicles need to have longer life-span heat shields to improve affordability. Zero-erosion rocket nozzles are vital for the development of reusable rocket systems or hypersonic engines. Sharp leading edges (SLEs) require long-term structural integrity for the feasibility of manoeuvrable and efficient hypersonic vehicles. The conditions expected for components in these applications are harsh. SLEs can be expected to reach surface temperatures from 2000°C to a possible ~4000°C [1], reusable re-entry shields may need to cycle from -200°C to 3000°C tens, preferably hundreds of times [2]. Whilst the role of the materials engineer is to provide the requisite tools for these applications, the toolbox may begin to run empty if adequate candidate materials are not found that can comfortably perform in these regimes. At present, the cutting edge (both figuratively and literally, in many cases) of high-performance aerospace materials are limited in their temperature ranges and reusability. Superalloys may be used to around 1200°C [3]. The throat materials of the highest performing solid and hybrid fuel rocket engines are the easily oxidisable graphite and carbon ceramic composites [4, 5]. Heat shields of Al_2O_3/SiO_2 used in systems such as the Space Shuttle and Buran are reusable, but only in operating regimes of around 1000-1200°C, at relatively low flight speeds. Whilst technological improvements like transpiration cooling [6] are being investigated as an avenue to enable carbon materials to perform as reusable heat shields there is still a dearth of potential materials capable of performing in extreme environments.

A promising new class of materials that have the potential to satisfy the demands of these challenging applications are the ultra-high temperature ceramic matrix composites (UHTCMCs) [7]; composites of carbon or silicon carbide fibres with ultra-high temperature ceramic (UHTC) compounds. UHTCs are a selection of group 4 and 5 borides, carbides and nitrides (or their higher order mixtures) that possess excellent thermal, oxidative, and mechanical properties [8-10]. However, like all ceramic materials, they suffer from inadequate toughness and thermal shock resistance that render them unfeasible for application as monoliths [11]. A potential solution for this is the incorporation of continuous fibres into ceramic components. Through such mechanisms as crack bridging [12], fibre debonding [13, 14] and crack deflection the resulting composite can mitigate these inherent drawbacks of single phase ceramics whilst also delivering reduced weight; this an indisputable benefit for aerospace applications. A major drawback for these materials is that the well-established ceramic forming techniques used to obtain low-porosity, defect free components are less relevant to the production of the composites. The consistent and high-quality production of these fibre/UHTC composites is currently a developing area; materials and methods suitable for easy commercialisation are not currently available. A number of methods exist for the introduction of ceramic material into a fibrous reinforcement. The best choice of method is, in many cases, entirely dependent upon the specific structure of the reinforcement, the specific ceramic material, and the intended use of the final component. It is warranted, therefore, to analyse the characteristic effects these methods and materials have upon the performance of final components in order to define what an 'optimum' material would even look like.

This project is concerned with one such method of producing UHTCMCs. Specifically, the introduction of ceramic material as a fluid suspension by injection into a pre-formed

('preform') carbon fibre structure [15-18] and the potential this has for the production of selectively anisotropic UHTCMCs in which the concentration gradient of the ceramic is variable with depth, via injection of suspensions of different constitution at different locations. This would allow for the production of functionally graded components in which the properties of interest could be thermomechanical, financial or oxidation protection. The ability to tailor these properties as a function of location in a component is critical for the ability to reduce material cost and improve material performance by optimising the mass and density distribution, thermal conductivity or protectiveness. This contrasts with multilayer materials in that the structural element - the fibre preform - is continuous throughout the whole body of the component and therefore does not introduce faults or weaknesses at lamination interfaces, a common flaw with such materials [19]. Optimising the specific performance of UHTCMC components is a critical step in demonstrating the commercial viability of these materials. However, this rests upon the ability to produce high quality *truly* selectively anisotropic materials, in which the scale of the concentration variation is achievable through the means of ceramic suspension injection. This, in some regards, reduces to a fluid flow process problem and this forms a significant focus of this work.

A fluid's properties are many and varied, and the interaction of a fluid and a porous substrate is contingent upon a number of variables. In a porous flow problem, parameters like viscosity, surface tension, wetting, porosity, tortuosity and injection pressure dominate the flow behaviour. For ceramic suspensions in carbon fibre preforms, the effect of these parameters both on the flow behaviour and controllability and on the final ceramic distribution and component structure and performance must be understood in order to ensure that this technology can be meaningfully applied to produce high quality components. This is the key area this research project seeks to advance. A number of

challenges do still exist, however. Stable suspensions of ceramic power particles, especially highly dense ceramics as UHTCs often are, are difficult to produce which introduces complexity into the reproducibility of the flow behaviours. The structure and interactions of porous media are poorly defined, and flow problems in porous substrates are difficult to address analytically [20]. The dual scale of preforms often used in this industry, with large scale intermingled with incredibly small-scale porosity (same order of magnitude as the suspended ceramic particulates), introduces new issues of clogging and flow retardation, which makes the study of multiphase flow phenomena particularly difficult.

To tackle this problem, the project sought to elucidate a few key areas of the injection process for ceramic matrix composites. What is the interaction of the ceramic suspension (henceforth 'slurry') viscosity, surface tension and wetting properties in the preform with the flow behaviour (namely the growth, extent and shape) of the ceramic powder deposits? What effect had the input pressure and flow velocity on the reproducibility of the deposits? Were these deposits 'packable' in the preform and could that be used to build up a functionally graded material successfully? More mechanically, what routes could be adopted to reduce the prevalence of ceramic particulate clogging in fibre preforms?

This thesis is laid out as follows. Firstly, a review of the literature relevant to the field of study and experimentation methodology is presented. Subsequently, the experimental materials and methods are described. Following this, the questions above are broadly divided into three sections for the results and discussion. In the first, the production and analysis of a set of test fluids with prescribed properties is detailed, and the potential effect of these on the flow studies is discussed. The second presents an investigation into the fundamental flow properties of these slurries in some relevant preform substrates.

This established the extent of the control possible in this system. This is achieved both practically and numerically. The final section relates to the production of an arbitrary material gradient to demonstrate the degree of success of this optimisation study. The results are discussed against the context of material requirements in this field, to what degree this method contributes to the ongoing improvement of UHTCMC components and conclusions are drawn and future work outlined.

2 LITERATURE REVIEW

Section 2 constitutes a review of the literature relevant to the understanding and discussion of the experimental work. Firstly, the requirements for and nature of UHTCMCs, laminates and functionally graded materials are laid out before a brief overview of some common fabrication methods. Slurry infiltration is then investigated to understand the important features for producing composites via this method and how to optimise the properties of the infiltrant liquids, before a detailed analysis of the dynamics of fluid flow through porous media at both large and small scale. Methods and results for modelling such flows are summarised and discussed. Finally, a specific element of statistical analysis is presented and discussed, as a reference for the discussion of the results later in this thesis.

2.1.1 Materials for structural and thermostructural applications

UHTCMCs, being potential materials for rocket nozzles or hypersonic control surfaces, need to possess the correct properties for high performance in these aggressive environments. UHTCs operate on re-radiative principles [19, 21] for controlling the thermal loads whilst in use, and bear the brunt of incredibly high pressures at stagnation points, locations where the curvature of the component reduces the flow field to zero, such as the tip of a leading edge. As such, the materials must possess high strengths and toughness, but also high thermal conductivity for use at these critical locations. Likewise, it is not solely the material properties that must be considered; due to the operational environment, almost immediate surface oxidation is an inevitability. Hence, the properties of the oxidation products of pure components must also be carefully optimised.

Commonly, UHTCs are materials whose melting points exceed 3000°C, or whose operation environment may exceed 1650°C for extended durations [9, 22]. Materials capable of fulfilling one or both of these criteria are the borides, carbides and nitrides of group 4 or 5 elements, and some are displayed in Table 1. SiC is shown for convenience, as it is an oft-included additive.

Table 1: Some relevant properties of candidate UHTCs and their oxides [23-30]

	Density / g cm^{-3}	**Melting point / °C**	**Oxide melting point / °C**	**Thermal conductivity / W m^{-1} K^{-1}**
HfB_2	10.5	3380	2800	105
ZrB_2	6.09	3246	2700	60
ZrC	6.73	3700	2700	21
HfC	12.2	3800	2800	13
TaC	14.5	3800	1870	180
TiB_2	4.52	2970	1855	90
SiC	3.21	1410	1713	220

Taking the materials whose oxide melting points are in excess of 2500°C, the borides and carbides of zirconium and hafnium become the most promising materials. Of these, the borides have higher thermal conductivity and, accordingly, are some of the most studied for aerospace applications. Additionally, they oxidise via a liquid intermediate at lower temperatures [25]; $B_2O_{3(l)}$ provides some oxidation protection as an impermeable liquid oxide below 1000°C and prevents the spalling that occurs more frequently in carbide systems due to the immediate formation of $CO_{(g)}$ and $CO_{2(g)}$ [31]. However, like all monolithic ceramics, their toughness and thermal shock resistance are sometimes inadequate for direct application in these sorts of environments. Hence, they are combined with fibre architectures to produce more damage resistant materials by exploitation of such mechanisms as crack deflection, fibre delamination and fibre bridging. For a discussion of the mechanical aspects of CMCs the reader is directed to works by Budiansky [13] or Koch [14]. The geometry of the fibre architecture is important; for dense materials highly dimensional (fibre content aligned in each of the

Cartesian directions) configurations provide superior damage tolerance and protection from fibre sheet delamination [32]. However, the production of low-porosity ceramic continuous fibre composites remains challenging. Equally, the notion that greater fibre dimensionality yields superior fracture toughness and damage tolerance for UHTCMCs is not, currently, represented in the literature. An attempted exhaustive search at the time of writing for K_{1c} values of a variety of fibre CMCs, Figure 1, does not show any particular trend other than the more widely studied 2D lay-up materials currently exhibit best the fracture toughness.

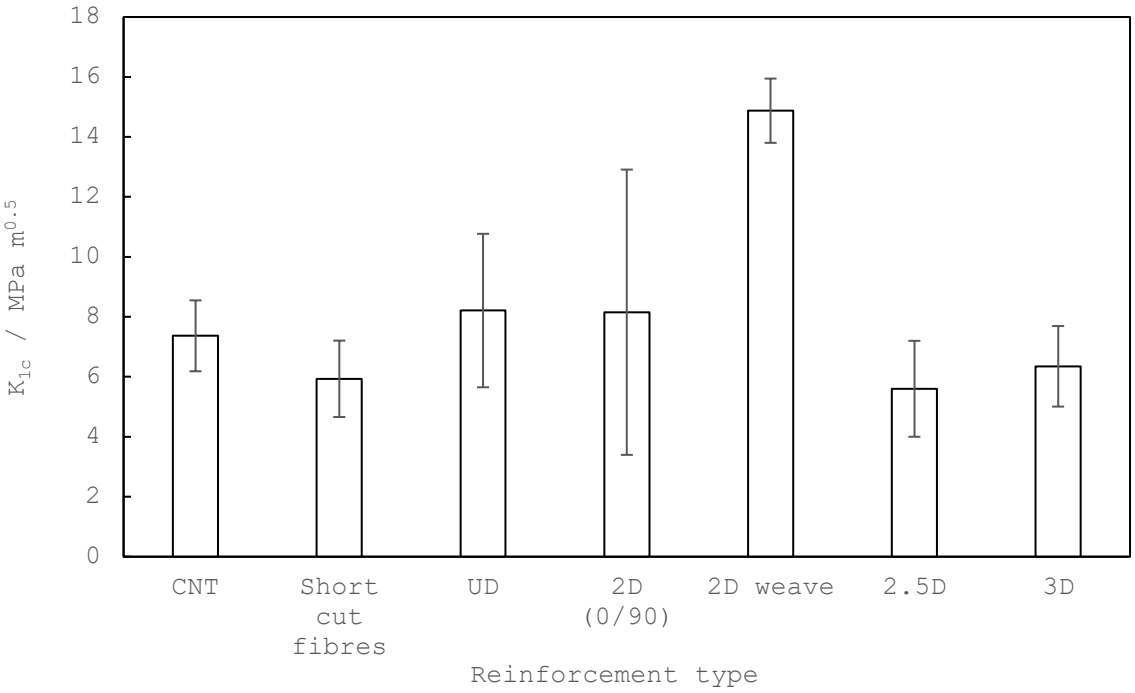


Figure 1: Fracture toughness values found in the literature for 'fibre' UHTCMCs from: dispersed CNTs [33, 34], short-cut fibres [34-39], unidirectional [40-42], 2D [39, 40, 43-45], 2.5D [16] and 3D composites [46]

This is, however, anecdotal and the myriad other factors (porosity, densification, etc.) are not consistent in any way throughout these studies. Equally, categorising materials this simply is also not trivial. No doubt more data will add to this picture as the area develops

further, and levels of confidence will be similar to that of the roll of fibre architecture in polymer composites [47].

Within the spectrum of thermostructural materials, UHTCMCs have shown promise. Vinci et al. [48] produced a unidirectional lay-up of C_f/HfC-SiC at both 40 and 55 vol% C_f. SiC is often incorporated in UHTC matrices to act as a sintering aid, to suppress grain growth during UHTC densification and to provide oxidation resistance in the <1650°C regime. Above this threshold, however, SiC is oxidised directly to $SiO_{(g)}$, opening numerous oxidation pathways through the component which can lead to catastrophic damage [49, 50]. Nevertheless, the C_f/HfC-SiC composites demonstrated high flexural strength at room temperature (340-380 MPa) which improved at 1800°C in inert atmospheres, accounted for by stress relaxation from sintering and by grain boundary sliding. At 2100°C, significant plasticity was seen and an ultimate strength of 534 MPa was measured. An issue observed was with producing dense samples at higher vol% C_f, as the presence of fibres was seen to hinder the initial slurry infiltration and also the densification of the samples.

Rubio et al. [51] produced HfB_2 powder modified C_f/C composites following the procedure presented in this thesis (see Section 4.3). The substrate was a 2.5D material consisting of alternating layers of 0/90° oriented weftless plies joined by a layer of Velcro-like stitching [17]. Flexural strengths were found to vary from 96-166 MPa, with most failure modes seen to result from interlaminar shear failure. The corresponding shear strength was measured and found to be 28.8 MPa, significantly weaker. The conclusion of this study was to suggest that, as most failures were found to originate in the unidirectional layers out of plane with the applied stress, that the in-plane 0° layers should be more numerous. This, perhaps, should have been stated in a more general way; the inherent anisotropy of directionally woven fibre substrates requires that the

application's likely stress field be taken into account for the design of composite materials. This has important ramifications for composite production procedure. For example, Inoue et al. [39] produced C_f/ZrB_2-ZrC-SiC composites using both short-cut fibres distributed homogeneously though the material and also a lay-up of plain-weave fibre layers. Whilst both materials were found to improve the fracture toughness of the corresponding monolithic ceramic, the spread of toughness endowed by the short-cut fibres was far larger, indicating the fluctuation in the fibre orientation at the point of fracture, and the corresponding effectiveness of the crack-bridging and deflection mechanisms. Another relevant feature was that the fibre lay-up was found far harder to densify and as a result had a far lower thermal conductivity and therefore oxidation resistance. This highlights the importance of low porosity in composites for ultra-high temperature applications.

A number of candidate UHTCs exist for incorporation into composites for thermostructural applications; the specific choice is highlighted by the regime expected in use. Silvestroni et al. [52] investigated the ablation resistance of monolithic ZrB_2-SiC-WC ceramics in both air and nitrogen and found that the formation of a protective oxide scale in the air environment was far superior than the bubbly, volcanic morphology formed in the residual O_2 containing nitrogen environment. This highlights that, dependent upon the projected atmospheric composition, some materials are far more tolerant than others. It has been theorised that the formation of an oxygen-impermeable, dimensionally stable surface glass is critical to the oxidation protection (and therefore structurally viability) of UHTCMCs [7, 53]. Yao et al. [54] demonstrated the efficacy of a ZrB_2-Si-SiC coating on a C_f/C substrate in protecting against material oxidation for 386 hours at 1500°C, due to the formation of a SiO_2-$ZrSiO_4$ glass phase through which oxygen did not diffuse successfully. However, when undergoing a series of thermal shocks, the coating was found to crack and cause mass loss up to 1.6%. Hence the development of a

chemically protective (low oxygen diffusivity through the lattice/glass) and thermostructurally protective (highly viscous, highly stable and highly wetting upon the oxidised substrate) exterior component layer is critical.

2.1.2 Selectively heterogeneous material configurations

Fine-tuning the properties of composites to optimise them for the expected environmental conditions is an important part of both ensuring viability for these materials systems and to improve their cost effectiveness. For UHTCMCs, there are three key parameters that overall components need to maximise: thermal conductance, oxidation resistance, and dimensional stability at high thermomechanical loads. This optimisation, in many cases, will not include the whole component; instead it can be desirable to have continuous spatial variations in constitution or configuration throughout the component. For example, an oxidation resistant skin may be deposited upon a highly thermally conductive substrate that, alone, would have minimal oxidation tolerance (though this must be managed carefully to avoid such incidents as the Columbia Space Shuttle disaster of 2003). Equally, a material can be envisaged whose stiffness varies throughout the thickness of a component such that a shock-absorbent exterior increases to a stiff and dimensionally stable inner surface for reliable adhesion to an underlying substrate. This world of environmental barrier coatings and functional grading is limited only by the knowledge of the application conditions and the imagination of the material designer.

There are not a large number of examples of functionally graded materials (FGMs) in the UHTCMC literature. Only one 'true' FGM is described by Silvestroni et al. [55]. This consisted of a three-region distribution of co-sintered ceramics involving a surface layer of ZrB_2-10$MoSi_2$, an underlayer of ZrB_2-8Si_3N_4, and then a gradient of $C_{short\text{-}cut}/ZrB_2$ from

20 to 50 vol% fibre content. Under mechanical and oxyacetylene torch ('OAT'- an ultra-high temperature testing scheme) ablation testing, no delamination was seen and the composite's fracture toughness was measured as 10.5 MPa $m^{0.5}$. The ceramic was graded this way to prevent the $MoSi_2$ sintering aid diffusing into the fibre region of the composite thereby reacting with the carbon fibres and causing a strong interface bond, and to provide a dense oxidation resistant surface. Delamination was not an issue as there were no discrete structural elements throughout the material, especially not coplanar to the interfaces. Also, as the concentration of the continuous matrix element, ZrB_2, was high throughout the thickness, the material did not possess some of the problematic aspects of many laminates or functionally graded (FG) coatings. Jayaseelan et al.[19] developed a multi-layered UHTC on the rationale of producing a material with an anti-oxidation layer, an oxygen impermeable layer and a final high-temperature structural material (MB_2/MC_xO_y/MB_2-SiC-La_2O_3/C_f-C-UHTC respectively, where M=Zr or Hf). Two varying stoichiometries of oxy-carbide were included in the second layer in an attempt to overcome the thermal expansion mismatch, however cracks formed and branched along the interfaces. Finite element analysis (FEA) modelling also suggested that the material combinations would produce thermally-induced delaminative stresses. FGMs are designed to avoid this by having a gradual change in thermal expansion through thickness [56-59]. Gayen [59] contrasted this with laminates, as they possess poor resistance to delamination and debonding due to residual stresses at the interfaces. In general, all 2D composites (composites that possess fibre reinforcement spanning only 1 plane of the component) can possess these delamination tendencies and residual stresses; indeed, this is the reason for the development of 2.5 and 3D composites. Hofmann [60] remarked that the differential shrinkage during processing of C_f/C-SiC is a common cause of interlaminar porosity, flaws or even delamination. Presby et al.[61] investigated ballistic damage with supersonic 1.6 mm diameter ball bearings (damage potentially expected in gas turbine

applications) of SiC_f/SiC 2D laminates and found, for both planar and U-shaped specimens, that delamination occurred very close to the back surface of the component. This suggested that the loss of the majority of the thickness of the composite component could be likely should airborne detritus strike a 2D CMC control surface, leading to catastrophic damage. In a separate study [62], Presby found that 2D composites of SiC_f/SiC were generally susceptible to shear failure due to their frequent interlaminar porosity, and that mode I failure (crack opening, shear stress perpendicular to plane of the crack) was far more prevalent than mode II (sliding crack opening in the direction of the crack). This suggests that friction is an important factor for composite delamination.

Another influential feature is thermal expansion and how that relates to the oxidation protection endowed by a surface layer. Li et al. [63] investigated the effect of the heating and cooling rates for samples of ZrB_2-SiC-WB intended for plasma sprayed coatings at 1500°C. Combinations of fast and slow rates greatly influenced the material structure. Fast cooling rates were found to induce the growth of large platelet B_2O_3 grains, which did not allow a dense, impermeable surface oxide structure to form. Likewise, high heating rates produced a large number of bubbles and surface cavities from the rapid volatilisation of B_2O_3 and SiO_2. This study showed the importance of oxidation mode for materials in environments with steep and sudden heat fluxes. Rapid volume change on these sudden heating gradients is also a problem for the stability of coatings. Coating strength was measured by Jiang et al. [64] for a TaB_2-SiC-Si coating for graphite which showed a binding strength of 21.79 MPa. Given that some stagnation pressures can be expected to reach 150 MPa [21], this is not particularly high. The authors commented on the stability of their coating at 1020 and 1550°C under static oxidation for 321 and 168 hours respectively, however it should be noted that these temperature regimes lie nominally under the service temperature of SiC_f/SiC or even ZrO_2 EBCs. During OAT

testing at a modest heat flux of 2.38 MW m^{-2}, the coating only survived for 2 minutes. This can be compared to Binner et al. [65], where materials withstood fluxes of 17 MW m^{-2} for over 5 minutes without catastrophic failure.

A number of studies have addressed the oxidation resistance of coatings under variously oxidising or ablative conditions. Liu et al. [66] observed that ZrC-SiC coatings performed better at moderate heat fluxes under laser oxidation but that the higher eutectic temperature of ZrC-TaC performed better at higher heat fluxes. Even in this regime, however, significant delamination was observed and the test did not consist of any scouring gas flow that would be expected in-service. Sun et al. [67] produced SiO_2 modified ZrB_2-SiC coatings for C_f/C via plasma spray in order to improve the densification of the material. The resulting OAT testing demonstrated that though the 30 vol% SiO_2 was the most densified, the 10 vol% SiO_2 produced the highest oxidation resistance. They justified this with a percolation-theory rooted argument about the lack of connectivity between the SiC regions, hence not opening up oxidation pathways after active SiC oxidation. However, it needs to borne in mind that the testing temperature was only 1800°C, hence it was not directly applicable to UHTC applications.

Selecting coating materials with matched coefficients of thermal expansion (CTE) is very important for the structural integrity. Dong et al. [68] showed a good CTE match to a C_f/SiC composite by use of a $Yb_{0.2}Y_{0.2}Lu_{0.2}Sc_{0.2}Gd_{0.2}Si_2O_7$ coating. No delamination or differential shrinkage was observed, something seen also by Anton et al. [69] with a HfO_2 doped Si top layer for SiC_f/SiC. In addition, this latter material exploited the molar volume increase on formation of $HfSiO_4$ to help close cracks and provide self-healing. Without this, 'mud cracks' can form on the surface SiO_2 layer due to CTE mismatch and propagate to the interface region and cause spalling, as innovatively measured by Arai [70] with pulse thermography. Using functionally graded coating materials (not graded into the

underlying substrate material, however) can help to overcome a number of these problems. Moro et al. [71] observed delamination in ZrO_2 and SiC EBCs for nickel and graphite combustion chambers respectively due to CTE mismatch. After changing to a gradient C_f/C-SiC EBC, however, and optimising the interfacial contact and thickness of the underlying substrate to provide some surface roughness anchoring, far better dimensional stability was observed. Rahnavard [72] compared the behaviours of graded vs laminate thermal barrier coatings (TBCs) to identify the best material configuration for gas turbines. Regular TBCs in this example were a steel substrate with an aluminium containing super-alloy bond coat with a ceramic top coat, $(Ce/Y/Zr)O_2$ in this case. The aluminium often diffuses out to form alumina between the bond and ceramic coating, which is structurally unstable due to the CTE mismatch. Comparing this to a graded intermediate layer of super-alloy/ceramic matrix composite, no Al_2O_3 formation was observed. However, the FGM material was also not stable, and the expansion mismatch caused eventual coat failure. It is likely that the composition could be adjusted to prevent this, however.

In summary, whilst there have been some successes in tuning multi-component anisotropic materials to some applications, there is by no means an established best-practice. Equally, those that exist often fall foul of heat gradients and oxidising atmospheres. In particular, only one [55] approach has demonstrated the performance needed in temperature regimes exceeding 2500°C. As such, exploration of functionally graded multi-dimensionally reinforced composites is an important next step.

2.1.3 Production methods for CMCs

Common methods used to lay a ceramic matrix within a reinforcing fibre substrate leave characteristic meso- and microstructures, and will hence heavily influence the properties

and performance of the resulting component. When dealing with fibre weaves or structured preforms, the production of a consistently dense matrix is a key fabrication challenge. Flaws, macro-pores and undesired chemical heterogeneities can cause components' properties to deviate widely from the expected values, or otherwise to be simply incapable of performing as desired. For this reason, fabrication techniques that have any potential for implementation in the real world must behave consistently. A necessary part of developing such robust procedures requires a great degree of understanding of the effect the parameters governing the procedures have on the quality of the final products.

A matrix material may be infiltrated directly into a reinforcement, or may be introduced as a precursor and produced in situ. There are a number of fabrication routes that exploit these mechanisms. Reviews by Binner et al. [7], Tang et al. [8] and Garshin et al. [73] provide a detailed discussion of the state of the art of UHTCMC processing; the following subsections summarise the salient differences between the most commonly adopted methods to place slurry infiltration techniques into context.

2.1.3.1 Precursor infiltration and pyrolysis

Precursor infiltration and pyrolysis (PIP) is the iterative introduction of a liquid chemical precursor into a reinforcement phase, followed by the high-temperature treatment of the chemical, which, as a result, decomposes in situ into a ceramic phase [74-77]. The nature of the precursors and resulting ceramic materials are many and varied throughout the literature, both with respect to physicochemical properties and final composition. This has the benefit of providing tolerant processing conditions (with respect to temperature, curability, pressure requirements, pyrolysis temperature) and promising variability in the final ceramic microstructure. However, PIP methods suffer from issues related to the

outgassing of volatile by-products and the shrinkage cracks from the pyrolysis stage [46, 78, 79]. The result is an inevitably porous matrix, which, for oxidation resistant materials, is a significant handicap. Additionally, the reactive chemicals used and their repeated heat treatments can result in fibre degradation, resulting in the loss of some structural integrity.

2.1.3.2 Reactive melt infiltration

Reactive melt infiltration (RMI) is the single-step introduction, under vacuum or applied pressure, of a molten metal/alloy into a porous pre-matrix deposited (through some means) in the reinforcement [80, 81]. The metal reacts with the pre-matrix in situ to produce the final ceramic matrix. This produces a reaction bonded matrix of low porosity, with low processing times relative to PIP or chemical vapour infiltration. However, the high temperature and reactivity of the liquid metal can damage the fibre network. Additionally, the flow in the porous pre-composite and the resulting stoichiometry need to be understood and stringently controlled to ensure complete reaction and to prevent formation of residual metal regions that are detrimental to the component properties, especially at ultra-high temperatures [82, 83].

2.1.3.3 Chemical vapour infiltration

Chemical vapour infiltration (CVI) is a gas-phase approach to matrix deposition. A gas is permeated into a porous reinforcement that has been heated through some means. The high temperature will induce the gas molecules to decompose, with a ceramic phase as a significant product of the reaction formed in situ [84]. This route is especially suited to thin fibre coatings, or the final densification of partially dense composites. However, this is a long-duration and high cost process [85], although work has been performed to

reduce the densification period for components by application of different heating profiles [86].

2.1.3.4 Slurry infiltration

Slurry infiltration (SI) is a method in which a fluid, produced by the suspension of a ceramic powder in a solution of dispersants, is introduced into a fibrous reinforcement via application or removal of pressure. The subsequent drying of the solvent yields a porous composite that can be impregnated iteratively with more slurry to improve the densification. The material may then be sintered, or densified through a combination of other methods. SI alone is an incredibly cheap process with low temperatures and short time scales, though sintering can result in fibre damage [87]. The physicochemical properties of the suspensions are highly tuneable by the constitution of the liquid, which is why it is of prime interest to this project. However, the limited possible solid loading of the slurry severely limits the total density of the final components. Equally, a common issue with slurry infiltration techniques is the fact that ceramic distributions are heterogeneous. Penetration of the ceramic particulates does not occur as completely in all locations in the preform. This can manifest as particulate clogging at the entrance to micro-porosity at the extremities of fibre bundles, or particulates can aggregate at or around the surface of the preform and prevent particle ingress into the main macro-pore channels in the substrate [88-98]. There are a number of parameters that control the tendencies of combinations of slurries and preforms to result in this behaviour. However, a full parametric meta-analysis of the significance of certain processing variables on the distribution and quality of slurry impregnated fibre preforms is difficult due to the wide range of relevant features and the sparsity with which many authors report these in their

methodologies. Adequately defining 'distribution' for different reinforcement structures or densities across studies is also difficult.

Throughout the literature, many parameters have been correlated with incomplete impregnation of preforms. These have included high dimensionality and density fibre preforms [88, 89, 91, 94, 95], use of high viscosity slurries [93-95, 97], high solid content slurries and slurries with large primary particle sizes [88-91, 94-96, 98], and volatile carrier liquids [88, 91, 94, 95] in reduced pressure processing. These latter vaporise, reducing the fluid fraction of the slurries resulting in higher viscosities over the duration of the process [99]. Sun et al. [90] describe a C_f/C-$ZrSiO_4$ composite produced through a vacuum assisted method using an aqueous zircon slurry. The reasonably large particles penetrated up to 3 mm into the surface of the preform, but little further. Jayaseelan [91] observed similar depths for ZrB_2-ethanol slurries, and it was speculated that the exterior pores were clogged with powder aggregates, leaving internal porosity inaccessible. The existence of these residual inner macro-pores have been suggested to be a result of the increased viscosity of the higher solids content slurries [97]. This, however, does not account for the grain-scale clogging/occlusion effects one may expect to expect in poorly stabilised suspensions. Different authors have made reports of good [100] and poor [89] infiltration of fibre tows. Wu [100] describes homogeneous and extensive penetration as a result of small particle sizes and a good wetting match between the slurry and fibres. This latter was not measured separately, however, and was based solely on speculation and the fact that the process is capillary pressure induced. Leslie et al. [101] attempted to establish the optimal conditions for slurry infiltration for a SiC_f/HfB_2 composite. They determined that for a low solids content, use of applied pressure provided superior particle loading than use of a vacuum assisted method. Additionally, the matrix density was higher when applying vibration to the procedure, a method that has been applied

elsewhere with success [15, 18, 102, 103]. Subsequent work showed that increased solid loading resulted in poorer extent of impregnation [104]. In particular, the smaller channels were left unimpregnated, which suggested either the higher viscosity was detrimental to the penetration of these pores or that there were higher order aggregates formed at higher concentration which clogged the entrances to these channels.

Classical slurry infiltration processes involve submersion of a preform in the slurry within a vacuum chamber. The reduced pressure above the liquid induces the high pressure air-filled pores in the preform to collapse and be displaced by the slurry. Alternatively, some processes constitute some form of applied pressure system that reduces in essence to using the preform as a filter, whereby the slurry is forced into and through the preform [91, 101, 105]. Less common approaches include slurry injection [15, 17, 18], pre-coating and weaving [106], the flexible injection process [105, 107], vibration (as mentioned) [103], electrophoretic deposition [108], or capillary action alone [98]. Vibration assistance is often claimed to produce more uniformly packed microstructures [101, 104] that improve the mechanical properties [102]. However, it is unknown to what degree this is true, as the series of papers of the Du research group [15, 16] shows mixed results from study to study on the benefits of the inclusion of vibration.

2.1.3.4.1 Injection impregnation

The filtration effect often observed in slurry impregnation is reasonably detrimental in many slurry/fibre systems of practical interest. Where applied pressure, vacuum assistance or application of vibration do not provide a sufficient drive to overcome the poor mobility of ceramic particles in a fibre substrate, researchers have found success in injecting slurries directly into the fibrous preforms [15, 17, 18]. Injection can be used to successfully introduce a ceramic slurry into the centre, or any other location, of a preform.

The size of the preform then becomes largely irrelevant to the degree of impregnation. In the aforementioned systems prone to clogging, injection can provide an effective solution to produce dense and homogeneous materials. Whilst materials produced in this manner share the general potential drawbacks of SI route materials, namely low ceramic content, a major route for exploitation is in the production of selectively heterogeneous materials. The ability to deposit distinct ceramic compounds in separate locations in a structured preform can be used to produce materials with a predictably anisotropic property distribution. This technology differs from laminate materials or coatings in that there is a continuous and through-thickness structural element to bolster the inter-phase adherence. Where coatings and laminates are prone to interfacial cracking under thermal or mechanical stresses, a heterogeneous component produced through injection of a preform would have a substantial resistance to this mode of failure. However, the flow through the preform and the extent of slurry ingress needs to be understood and exploited to produce high quality components consistently.

2.1.3.4.2 Injection

Injection is a well-established procedure in which a fluid is delivered, by extrusion, into some form of substrate. It is ubiquitous in the medical sciences or in food preparation, with injection of a range homogeneous fluids into veins, arteries or other fluid-filled tissues. In these applications, the most important parameters are the total forces and injection times for certain combinations of drug solutions and syringe designs, in order to ensure patient comfort and accuracy of delivery [109]. In application to heterogeneously dispersed CMCs, however, a different list of features take priority. To produce a selectively functionally graded material, the user has at their disposal the input force, duration, fluid rheology, surface tension and wettability, substrate structure and needle geometry. These

variables are, in many cases, interlinked. For example, the input force, needle geometry and fluid rheology will affect the flow rate of the fluid. The interactions and quantification of these factors need to be well understood in order to understand how a deposit's geometry can be laid selectively. Alternatively, the degree of selectivity possible will, for a given component size, influence the degree of prescriptive grading possible. A discussion of the relevant dynamics of fluid injection will be discussed to this end.

Fry [110] reviews some relevant factors for the difficulties in producing automatic injectors for high-viscosity drugs, listing plunger friction, viscous resistance and in-tissue resistance as particular impediments for injecting fluids. Also remarked on is the dependence on the radius of the needle for the flow rate as R^4, which is an expression of Hagen-Poiseuille's law, Equation 1 [111]. This describes the motion of a pressure-gradient driven fluid through a tube in the limit of suitable length and low Reynolds number.

$$\Delta P = \frac{8\mu L Q}{\pi R^4} \tag{1}$$

Here, ΔP is the pressure drop (Pa), μ is the dynamic viscosity (Pa s), L is the length of the tube (m), Q is the volumetric flow rate ($m^3\ s^{-1}$) and R is the radius of the tube (m). This shows that, for a fluid during injection, reduced flow rates for a given pressure gradient may be obtained by increasing the gauge of the needle (i.e. reduced radius). Equivalently, reduction of the aperture of the needle requires an increased applied pressure to produce the same flow rate, a result found by Edlich et al. [112] by the investigation of the flow dynamics of water through 25, 27 and 30 gauge needles (corresponding to ~0.311, 0.210, 0.159 mm inner diameter respectively) [113]. Stout et al. [114] built on this notion and pointed out that deviations from this law, in the sense of uneven diameters in the barrel of a syringe, will consequently affect the pressure-flow rate characteristics. Moreover, uneven surface coatings of the syringe will affect the sliding friction of the plunger. The

latter was calculated by Krayukhina et al. [115] by knowledge of the flow rate, force, fluid viscosity, and adaptation of the Hagen-Poiseuille equation to incorporate a term involving the plunger friction. Gadsden [116] reviewed the ability to monitor injection pressure in commercial injection devices for medical applications, and noted the importance of sliding friction in what was termed the 'static' injection phase. This occurs before initial plunger movement, where the total pressure in the system is resistant to the applied pressure. This involves the pressure of the plunger, hydrostatic pressure in the needle, the substrate resistance and the inertial resistance. When the applied pressure overcomes the system resistance, the plunger moves and fluid flows. This is the dynamic phase, where the pressure is no longer a constant and may become hard to measure. The pressures in the syringe, needle and tissue are different in this phase. Veilleux and Shepherd [117, 118] address some of the measurable and significant contributions to pressure during the static phase (though they refer to it more accurately as the transient regime). The initial pressurisation of the fluid was studied by the use of pressure transducers and strain gauges in custom built syringes at both the regular and large scale. The acoustic generation of pressure waves in the fluid from the compression of the liquid (both with and without initial air gaps) can deform the body of the syringe, cause vaporous cavitation and generate pressure waves of up to 4 MPa. They also remark on the homogeneity of chemical treatment of the syringe interior as a significant contributor to sliding friction.

The substrate resistance is discussed as a key parameter which may retard the flow rate for given pressures. Yu et al. [119] investigated the femtolitre injection of water into oils of various viscosity and find that, for a given pressure, an eight-fold drop in viscosity resulted in a deposit of over twice the volume. Krayukhina [115] also investigated the effect of substrate, injecting fluids both into air and porcine muscle flesh, finding

increased forces of up to 30% required to ensure flow. In addition to this, they discussed the importance of needle diameter. As Edlich found, narrower needles were found to require increased forces to produce the same volumetric flow rate but, moreover, tapered needles produced far lower flow rates than would be expected from either the maximum or minimum gauge of the tapering. This was discussed in the context of the flow field provided by the taper, in conjunction with the shear-thinning fluids being injected. The higher shear rate induced a far lower viscosity in the liquid, and resulted in a larger effective diameter of the needle as back-calculated from their expression for shear rate, $\dot{\gamma_{w,N}}$, based upon Equation 2 for extrusion of a Newtonian fluid from a cylindrical tube of radius R and volumetric flow rate Q [120].

$$\dot{\gamma_{w,N}} = \frac{4Q}{\pi R^3} \tag{2}$$

These papers, however, discuss flow of a homogeneous liquid without solid particulates suspended, which have been studied by fewer authors. De Bardi et al. [121] considered the flow through a needle clogged with flocculated antibody solution and described a characteristic force/injection volume characteristic summarised in Figure 2.

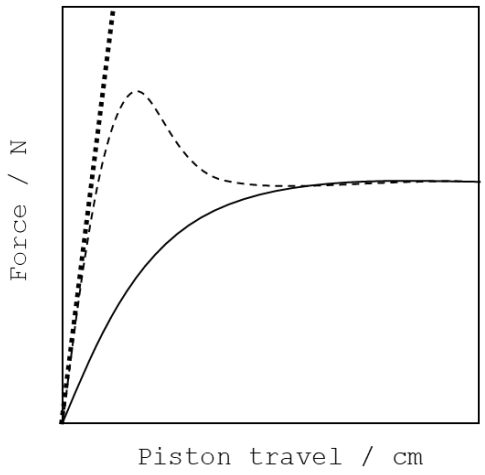


Figure 2: the characteristic relationship between the force and piston travel distance for (—) an unclogged needle, (---) a partially clogged needle and (⋯) a fully clogged needle.

Here, a partial clog is a movable, semi-permeable structure at some critical location in the syringe or needle that can be moved or broken with applied pressure. Xing et al. [122] studied such structures numerically and determined that aggregates of nano-scale can develop in protein solutions at regions of high velocity gradient and curvature in the flow-fields. This included both the needle entrance and needle itself. They, however, used an uncoupled single-phase approach to their modelling which did not detail sharp surface interactions and likely underestimated the issue of particulate aggregation and its knock-on effects on flow fields and pathway constriction. Long et al. [123] remarked on the need to accurately model the flow channel geometry to gain representative final results, and highlighted that without this there can be very little application for the output flow properties. Segré et al. [124] discussed both the tendency for particles to deposit on surfaces in flow channels, and observed and theoretically justified an effect seen for particles of migration outwards in a flow channel to form a region of higher concentration at approximately the 2/3 position from the central axis due to inertial and angular momentum effects. Though this effect was only derived for low concentrations with relatively large scale spherical particles, it demonstrated the added complexities of granular flows.

Finally, operator error must be noted. The control of a flow is dependent not only on the physical parameters (where measurable) of the syringe and liquid combinations, but on the input pressures. Claudio et al. [125] demonstrated the importance of mechanisation for any truly controllable injection process. By challenging 30 self-described expert anaesthetists to inject fluid at a constant flow rate with identical syringes and needles, the applied pressure was measured to determine the influence of human perception. To achieve what they considered ‘constant flow’ at the prescribed rate, a huge range of input pressures were observed. 10% applied a pressure of >200 kPa, 50% a pressure of >170

kPa and 70% a pressure of >140 kPa. Not only this, but a twenty-fold increase in the spread of pressure was observed when changing the needle and syringe to an identical specification from a different manufacturer. This was regarded by the authors as a perception-based effect, though this negates the potential of different inner coating in the syringe and hence a change in sliding friction.

This section has shown that to produce a selective deposit, the conditions of the injection procedure must be rigidly controlled. However, it is clear that the fluid properties play a significant role in the generation of a stable injection procedure, and will influence the interaction with the injection substrate.

2.2 Controlling the physicochemical properties of ceramic suspensions

2.2.1 Basic properties of suspensions

There are many properties of suspensions that affect their suitability both in injection and in composite production; a number of these have been described in previous sections. The ability to take a process and design a suspension of suitable physicochemical properties is important, both for process design and reliable component production. Hence, a discussion of the link between composition and properties of a ceramic suspension is vital. The macroscopic properties of interest are the viscosity (at various shear rates and timescales), the temporal stability, the surface tension and the wettability of the suspension on the impregnation substrate. For clarity, a brief and simplified overview of these as they pertain to granular fluids and the mechanisms dominating them is included in Section 2.2.1. A fuller discussion of the details of these fundamental properties may be found in the associated linked publications in Table 2. Section 2.2.2 is dedicated to the effects of suspension composition on these fundamental properties.

Table 2: The fundamental properties of ceramic suspensions as they apply to ceramic composite production

Property	Basic overview	References
Viscosity	The deformation resistance of a fluid, caused by the momentum dissipation from shearing between layers of fluid. High viscosities are encountered in suspensions with significant interactions between particles, and are often dependent on timescale and shear rate.	[126]
Surface tension	The imbalance of surface intermolecular forces that results in a net internally directed force (and hence a pressure) on a fluid element at a surface. This surface tension results in the minimisation of surface area, the driving force for which increases with increased surface tension. Molecules that align at the surface and reduce the surface imbalance (surfactants and amphiphiles) reduce the surface tension.	[127]
Substrate wettability	The tendency for a fluid to spread over a surface spontaneously. This occurs in situations where the energetic penalty for the maximisation of a fluid surface is compensated for by the reduction in the total energy penalty associated with the unsatisfied bonding potential of the substrate surface. In situations where this is not compensated for wholly, there are degrees of wetting which can be indicated by the three-phase contact angle between liquid, solid and gas in the case of a droplet on the surface. Large contact angles indicate poor wetting, and angles smaller than 90° indicate that spreading yields a net reduction in free energy.	[128]
Stability	The ability for solid particles to stay both i) separate and dispersed and ii) in suspension. The former is dominated by particle-particle interactions. Attraction of particles is inherent due to dispersive forces and can be induced further by the incorporation of bridging species or depletants in solution (usually some form of polymer). Repulsive forces can be produced by an increase in the charge of the particle surface or by the inclusion of surface agents providing steric stabilisation towards aggregation. The settling rate for particles in suspension is governed by the relative phase density between solid and liquid, the gravitation forces and the effective radius of the particles. At low particle size (i.e. colloids) the thermally accessible energy is sufficient for Brownian motion to keep the suspension homogeneity high indefinitely.	[129]

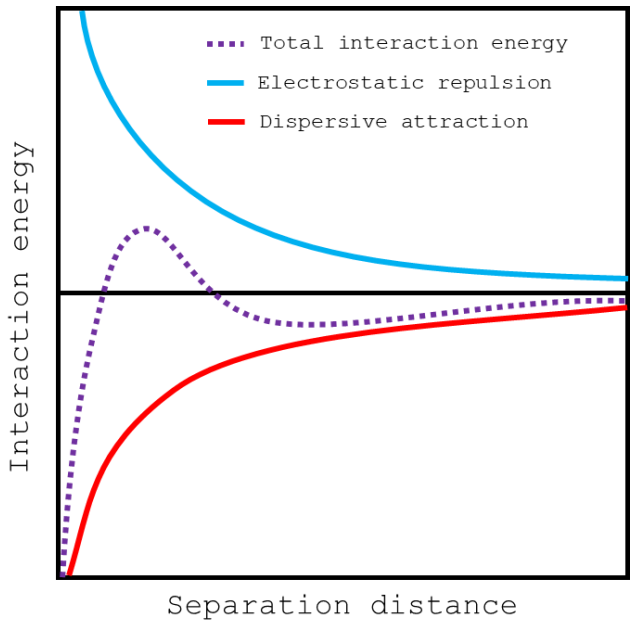


Figure 3: a graphical representation of DLVO theory for suspension interactions. The electrostatic potential (blue) and the dispersive potential combine to give the DLVO or 'total interaction' potential, an estimate of the total interaction between two charged bodies in a fluid medium.

Figure 3 shows the repulsive electrostatic and attractive dispersive interactions between two bodies in a fluid as a function of their separation, as described by Derjaguin-Landau-Verwey-Overbeek theory (DLVO) [130]. The sum of these interactions yields the total interaction energy. When positive, this indicates that the bodies repel one another and that there is a thermodynamic driving force against aggregation and flocculation. This, in turn, reduces the likelihood for poorly stabilised and highly viscous suspensions as a result of particle interaction. When negative, it shows that the attractive interactions dominate the system, and flocs will form, resulting in poor dispersion. As described in Table 2, there are different mechanisms of suspension control that additives can exert. Electrostatic control will change the shape and magnitude of the electrostatic potential as a function of distance, thereby changing the locations of the maxima and minima in the overall interaction potential. An overview of this is discussed in Figure 4. Steric control imposes a restriction on the distance of approach for particles by adsorption of high

radius species like polymers. This, in effect, shifts the separation distance in Figure 3 to a higher 'effective' minimum, and can push this to coincide with the maxima in the total interaction energies. This means that particles will not get close enough to one another for the attractive interactions to dominate the electrostatic repulsions. Electrosteric control can occur when the additives responsible for steric inhibition are charged.

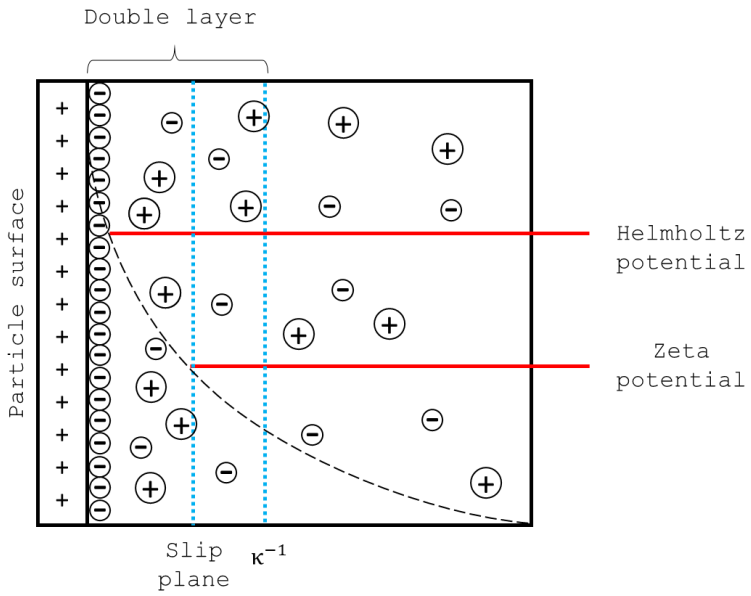


Figure 4: The Stern model for the electric double layer of an arbitrarily charged surface. Effectively all surfaces are charged in solution. The spheres indicate positively and negatively charged ions. The dashed black line indicates the magnitude of the electrical potential.

Figure 4 shows the electrical potential as a function of distance from a positively charged surface in solution, as described by the Stern model [131]. There are a number of structures involved in this model. The Helmholtz layer refers to the first layer of adsorbed counterions on the surface of the particle. The electric potential falls from a finite value at the surface as a function of the distance. The distance shown as κ^{-1} is known as the Debye length and this distance is referred to as the 'double layer thickness'. The Debye length is the decay constant of the electrical potential and is influenced by dielectric constant and ionic strength of the fluid medium [132]. At higher values of ionic strength for most solutions, the Debye length is smaller, the electrical potential decays faster and the

electrostatic repulsion is therefore reduced. The slip plane refers to the distance from the surface where the ionic solvation shell becomes mobile. Here, viscous dissipation can influence movement of the charges and the fluid can flow. The charge at this layer is known as the zeta (ζ) potential [133]. This is the only directly measureable value of 'surface charge' of a particle in a fluid. It is always lower than the particle surface charge and the electric potential at the Helmholtz layer. Depending upon the concentration of the ions in solution, the ζ-potential can be zero. This yields a net zero electrostatic repulsion at distances beyond the slip plane from the surface.

There are many specific chemical interactions at the molecular scale that can manifest themselves in the physical properties of a bulk material. This project concerns itself with bulk physical properties of a suspension, even when the specific chemical composition is different. Whether or not this is a valid assumption is a question in a wide range of areas. In an extensive series of work, Fuoss and Kraus [134, 135] with other authors analysed the effects of solvent identity, ion and counter ion pairs and other variables on the conductance of electrolytic solutions, the most sensitive parameter with regards to physicochemical balances. As observed in their work on the solvent structures and observed by Van der Hoeven [136], treating solvents by their bulk parameters like viscosity and dielectric constant and comparing between them is valid when no radically different species are formed by chemical reaction or chelation by the solvent. This assumption is maintained in this work for consideration of suspensions with different solvents.

2.2.2 Slurry composition and physicochemical effects

The viscosity of a suspension, as described in Table 2, is a complicated function of particle shape and size distribution, fluid medium viscosity, particle-particle interaction, particle-fluid interaction, and the coupling of each of these with gravity. A huge number of parameters are active in this interplay, and the relationship between viscosity, stability, electric charge and the particle slip plane is often investigated in the literature. Leo et al. [137] investigated the rheology, zeta potential, stability and green density of slip-cast ZrB_2 bodies whilst varying the nature of the dispersant used and polarity of the fluid medium. It was found that processing of material in non-aqueous media yielded denser, more homogeneous green bodies due to the greater ease of producing suspensions with greater repulsive total interaction energy between particles and a more well-dispersed suspension. This high dispersion reduced the modal aggregate size and viscosity, and ensured good packing density after slip casting. The greater repulsion was permitted in non-aqueous media as water, a highly polar fluid, screens a substantial quantity of the electrostatic interaction at long ranges. A later publication from the same author also suggests that the dispersive attraction is reduced in non-aqueous media due to the difference in solid-fluid Hamaker constant, hence allowing electrostatic forces to dominate [138]. Producing such well-dispersed suspensions is incredibly important both for high density but also material texturing; a review from Franks [139] highlights that the grain structure of sintered ceramics with high anisotropic aspect ratio starting powders is far easier to manipulate when the level of dispersion is high. Various strategies can be adopted to control dispersion; dispersants can be used or particle surfaces chemically modified to include organic chains to induce either steric or electrostatic stabilisation. Tanurdjaja [140] investigated the efficacy of these methods by modifying the surface of Al_2O_3 (highly polar) with n-(octyl, decyl or hexadecyl) alcohols and

comparing the stability of the resulting particles to the use of commercial dispersants, in dodecane. The physisorption mechanism of the commercial dispersant was found to be superior to the modified powder surfaces. Of the modified powders, the longer alkyl chains provided the highest degree of stabilisation as determined through rheological analysis. This difference was believed to be due to the incredibly large hydrodynamic radius of the polymeric dispersant, providing higher steric repulsion than the chemisorbed carbon chains. Whilst the use of non-aqueous solvents has been shown to yield lower viscosities and higher fluid stabilities, selection of the correct solvent for the respective process is important. Tallon et al. [141] noted the significant difficulties induced by using a high-volatility non-polar solvent (cyclohexane) in reduced atmosphere processes.

Whilst these authors select the best conditions for stability as a function of dispersant and pH (thereby controlling the surface charge), the picture is more complex than implied by simply considering these parameters as they are not independent with respect to stability. Goski et al. [142] mapped the stability (minimised viscosity) of alumina-kyanite suspensions with varying pH and electrophoretic mobility and discovered that the highest surface charge yielded the most stable suspension. This pH (and therefore degree of ionisation) did not coincide with other similar composition minerals, showing the dependence of surface chemistry on the properties. This, however, is not the only relevant parameter. Brahma et al. [143] studied a similar spectrum of Al_2O_3 suspensions both with and without sodium dodecyl sulfate (SDS) dispersant. In considering not only the surface charge but also the degree of electrostatic screening by variation of the ionic strength, they showed that aggregation could be induced at an otherwise incredibly stable pH when SDS was added. This demonstrated the sensitivity both of the surface charge but also the degree of ionisation of the additives, as the protonated dodecyl sulfonic acid caused

bridging flocculation and instability. There are greater complications with pH control however, Wang et al. [144] showed that high acidity could result in the hydrolysis of surface groups in alumina suspensions and surface adsorption of $Al(OH)_3$ groups, complicating the stability curve as a function of pH. Equally, exceeding a concentration of dispersant in solution can be detrimental to the overall stability, as noted by Singh for Al_2O_3 suspensions [145]. Excess of dispersants can cause depletion flocculation, where the entropic pressure of a coiled polymer in solution effectively forces the solid particles together. This is especially prevalent in the case of polyelectrolytes, which Singh notes already compress the electrical double layer and screen the electrostatic interactions.

Contact angles and surface tensions for single-phase fluids are dependent on the presence and distribution of amphiphiles in the fluid and the structure and chemical homogeneity of the substrate. For multiple phase fluids, there are three types of interface for amphiphiles to organise themselves preferentially at: the fluid-particle interface, the fluid-gas interface and the fluid-substrate interface. Attempting to design the physical properties of these liquids is, as a result, complex. Examples of contact angles of ceramic suspensions are not prevalent in the literature, as it is an oft-overlooked parameter. Trunec et al. [146] considered the contact angle of Al_2O_3 slurries for slip casting onto plasma treated/untreated surfaces, in combination with different dispersants. They showed that the plasma treatment increased the surface polarity and increased water wettability, and that use of dispersants in the organic-based slurry increased the wettability on the untreated surfaces. However, there was no synergy in these strategies; the dispersant-doped slurries were not more wetting on the plasma treated surfaces. This highlights the importance of good polarity matching of the substrate and fluid. Where dispersive forces and polar attractive forces match most closely in the fluid and solid surface energies, the contact angle is smallest (wetting is most favourable). However,

Trunec did not probe this systematically, as neither of the surface energy components were determined nor the dynamic contact angles measured. This latter introduces a significant margin of systematic error into the results.

Chen et al. [147] described the production of hollow B_4C microbeads via slurry coating of poly(α-methyl styrene) (PAMS) with an aqueous dispersion of ~30 vol% micron-scale B_4C, preceding PAMS burnout. Increased solids content of the slurry was found to yield a more uniform shell with fewer holes and lower roughness. This was hypothesised as being due to the manipulation of the surface tension of the slurry. The proposed mechanism was that the low solid content regions of the heterogeneously dispersed slurry possessed lower surface tension, and that when higher surface energy regions dry, the low solids content fluid migrates on top of these regions to minimise total surface energy, hence resulting in holes in the coating. For higher solids content slurry, there are fewer low-concentration regions and hence a more uniform coating is produced. A study by Brian [148] is referenced for this mechanism. However, Chen does not demonstrate that their fluids were heterogeneously dispersed, nor do they consider that drying is likely to be inhomogeneous for slurries due to the energetic preference for dispersed particles to remain suspended. At low solids content, this effect will be disproportionately observed due to the greater average distances between particles, hence greater observation of clumping, roughness and holes. More worryingly, the referenced study by Brian does not invoke the mechanism suggested by Chen. Brian specifically recounts that micron-sized particles (from 10^0 to 10^2 μm) in slurries were not observed to have any noticeable effect on the surface tension of the base fluids (water or isoparaffin). They remarked that surface tension is an entropic effect in the case of additives with molecular interactions, and that solid inclusions would need to have length scales similar to the fluid units to influence the surface tension, or otherwise change the fluid composition via

dissolution or competitive surfactant adsorption from solution. This effect was clearly demonstrated by Liu et al. [149], comparing the surface tension of water and a novel malachite dispersant with and without malachite powder. The surface tension vs time was found to increase initially upon addition of powder as the ligand reorganised from the liquid-gas interface, followed by a decrease as the now-coated particles aligned at the surface to act as amphiphiles. The lower surface tension may be attributed to greater polarisation in the dispersant, due to adsorption at the solid surface.

The effect of a polystyrene (PS) microbead suspension's concentration on surface tension and dynamic contact angles were investigated by Waghmare [150]. Commercial microbead fluids were taken and diluted with deionised water and their surface tensions and contact angles on glass were measured. Both the surface tension and equilibrium contact angles were found to decrease at increasing concentration. However, the underlying justification ran counter to Brian's interpretation of micron particle suspension interactions. Waghmare also did not discuss the effect of either the presence or potential concentration of dispersants in the system. As PS is non-polar, it is likely a dispersant would need to be present to stabilise a micro dispersion, and as the commercial fluid was diluted, the exact equilibrium between water and surface adsorbed dispersant may change, thus effecting the surface tension. The same may be said of leached plasticisers from the PS particles. They discuss the contact angle and contact angle hysteresis (difference between the advancing and receding contact angles caused by changing wetting conditions, i.e. time dependent change in composition or configuration of the surface or fluid element on top of it) as being a result of the structural disjoining pressure. This is the pressure that is associated with the dispersive interaction between a fluid and a surface, and may increase with increasing solid particle packing at an interface. This mechanism was highlighted by Wasan [151] for the spreading of

'nanofluids' on solids by the microscopic analysis of latex particles at a glass-bubble interface in a suspension. The latex particles (roughly micron sized) were found to organise into a 2D colloid crystal and the edge of the bubble-fluid region at the glass interface, and was confirmed to provide a more 'adhesive' interface through numerical analysis. In this way, it was theorised that the structural disjoining pressure improves wettability. This has also been studied experimentally. Vafaei et al. [152] showed that the presence, size and concentration of nano-particles of thioglycolic acid modified bismuth telluride all influenced the wettability on SiO_2 or Si surfaces. Nanoparticle concentration was found to increase the contact angle up to a peak, and was discussed in terms of interaction of the charged carboxylate group on the nanoparticles with polar surface groups. The smaller size nanoparticles (2.5 nm) were found to have the most pronounced effect when compared to larger sizes, but this may have been a red herring in that the mass concentration of the particles was kept the same irrespective of nanoparticle size, hence the number of nanoparticles would have been greater by almost two orders of magnitude. The particles in this study were far smaller (and hence closer to the functional group scale conventional wetting interactions are influenced by). Sefiane et al. [153] showed a similar rising and falling contact angle trend with Al nanoparticles in ethanol, though their experimental errors were too significant to confirm this. They did, however, show that the contact line speed of the nanofluid droplet on the substrate increased with increasing nanoparticle concentration. They confirmed this for both advancing and receding angles, and described the effect as a lubricating effect likely associated with the structural disjoining pressure.

Nanofluid suspensions and their interfacial tensions and contact angles are especially relevant in enhanced oil recovery technology [154-157]. The use of these fluids is in displacing oil from a porous mineral substrate, stabilising the oil in water (o-w) emulsion

and transporting the emulsion droplets out of the substrate. Hence, by manipulation of the suspension constituents, reducing the oil-water interfacial tension (IFT) and minimising the suspension-substrate contact angle relative to the oil-substrate contact angle are the twin goals. Zhou et al. [154] compared the performance of oil displacement fluid with the addition of polymer nanoparticles with a zwitterionic steric stabilising surfactant. The surfactant alone reduced the o-w IFT by 95%, which was reduced further to 99.5% on the addition of 0.08 wt% of nanoparticle. The same effect was observed in the contact angle. However, whilst structural disjoining pressure was discussed in the latter case, no mechanism was proposed for the IFT reduction. It is useful to contrast this with a similar study by Yekeen et al. [155], who observed a similar synergy. They described two potential mechanisms: surfactant coated nanoparticles increase the effective concentration of surfactant at the o-w interface (due to the relative packing shapes), or that the CuO nanoparticles and cetyl trimethylammonium bromide (CTAB) dispersant co-adsorbed at the interface to produce a gel-like network that significantly reduced the IFT. The first of the mechanisms does not stand up to scrutiny, however, as the packing efficiency of the surfactant-coated nanoparticles can only be lower compared to conventional interfacial alignment of amphiphiles. Either way, the composition was found to improve oil-removal efficiency in a pore-scale model. Rostami et al. [156] argue that wettability modification of nanoparticle suspensions is largely due to particle deposition on the surface (hence chemical change of the surface). However, no surface analysis was performed to confirm this. An additional suggested mechanism for IFT modification is the effect of capillary forces at the interface due to differential wettability of the particles. One phase will be more wetting on the particle at the interface, hence will warp around the surface. This increase in fluid-fluid interface will be energetically unfavourable and could cause particle aggregation (to minimise interface area) and instability of the suspensions [157].

The stability of suspensions is often inferred or manipulated by powder wetting. Both Li [158] and Xing [159] judged the stabilisation efficacy of additives based on the contact angle of the slurry solvent on a powder compact. However, this is fraught with experimental complications. The surface contouring and roughness dominates the contact angle and powder compacts provide heterogeneous surfaces at the scale of the contact line. The measurements by Li quote contact angles to two decimal places, which is unprecedented precision for goniometric measurements with no description of surface geometry. Xing also refrains from discussion of measurement error. Both authors neglect to consider that the contact angle, taken as a thermodynamic value, could, in this case, be a red herring; greater stability in the slurry will result in a better packed, lower roughness substrate and hence lower hysteresis contact angle. This formed no part of their analysis, however. Liang [160] studied the stability of electrorheological suspensions by adding bi-phase liquid, one component of which preferentially wet the solid inclusions. Aggregation was then induced by the meso-scale structures formed between the powder and wetting component, producing a flocculated gel at low shear rate. Similarly, Cheng [161] studied the aggregation of needle-like cefotaxime sodium crystals by determining the solvent adhesion energy on the crystals. By balancing the strength of interaction and volume ratio of immiscible wetting and poorly wetting solvents, they found they could induce either aggregation, or the production of a loose paste or gel.

These studies demonstrate the importance of considering the multiplicity of chemical effects additives and particles can have on slurry properties in general, and that complicated mixtures can have a number of interactions that must be understood to produce fluids of the correct properties. It is important, therefore, to discuss also some of the key additives used in this study to understand their behaviour.

Dispex A4040 is a commonly used dispersant for a range of ceramic oxide suspensions. An ammonium polyacrylate, it has been applied to $BaTiO_3$ [162, 163] at around 0.1 to 0.5 wt%, for example. It was found to be most effective at pH>6, with the polyelectrolyte being fully ionised at pH 8. Dispex works through an electrostatic mechanism, adsorbing flat on the powder surfaces, and has been observed to cause depletion flocculation at excessive concentration. It was used at pH<6 by Yang et al. [164], but this was to induce aggregation of $Ca(OH)_2$ particles, hence is consistent with the above analysis. Tween80 is a non-ionic foaming agent (hence active at the liquid-gas interface) frequently used in cosmetics, drug delivery, food and agriculture [165]. It is a PEG ester of sorbitan monooleate [166] used variously as an emulsifier [167] for o-w suspensions. It has been found to be active in the range of 2 wt% to 10 wt% [166, 168], though these are incredibly large values classically for surfactants (often efficacious in the ppm range). Polyvinylpyrrolidone (PVP) is a neutral polymer, historically used as a hydrophilic surfactant [169-171] and adhesive [172]. It has been found to interact with charged surfactants by inducing pre-critical micelle concentration aggregation by stabilising both the charged portions and oleophillic portions of the CTAB molecules, preventing much of the entropic penalty associated with the presence of amphiphile dissolution. It can be seen that these studies set a precedent for interaction between the additives used, and that a rigorous optimisation procedure may be needed for this work.

2.3 Porous media

2.3.1 An overview

The injection of a fluid can be controlled with respect to dosage, as has been established in Section 2.1.3.4.2, by careful selection of the fluid properties and the pressure and duration regime of the injection. However, the subsequent flow will depend on the

coupling of these variables with the structure and geometry of the substrate. In addition to understanding these latter two features, the flow through such types of materials (porous fibre substrates) needs to be understood at both a qualitative and quantitative level. As production of anisotropic composites through a slurry infiltration route is, in essence, the study of the control of liquid infiltration, this problem reduces to a porous flow problem, the analysis of which is central to a large number of fields in science and engineering. This section will discuss the nature and classification of porous media, the types of flow relevant to this problem, the effects of scale on flow kinematics, flow of granular liquids in small-scale pores and the approaches to modelling multiphase flow problems in porous media. This will permit adequate analysis of the results of the injection behaviour, and the ability to generalise to other substrates of interest.

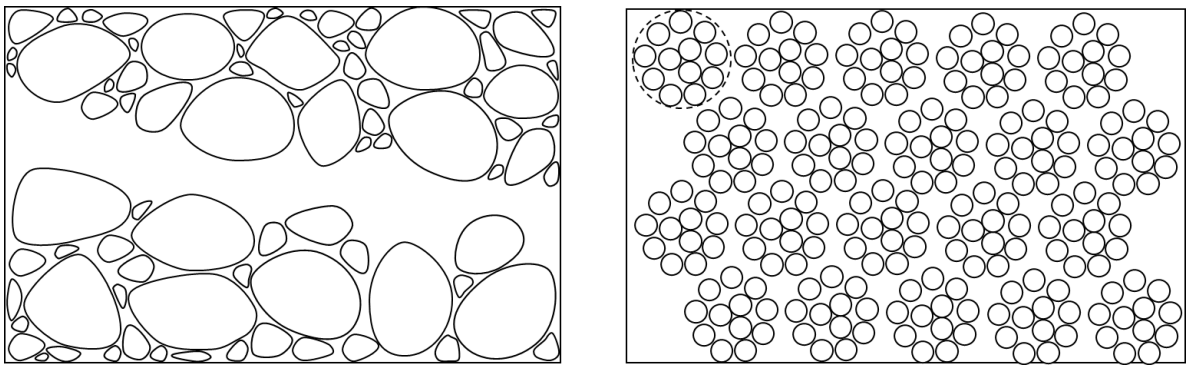


Figure 5: Two schematics of 'porous media'. Left: a 2D space consisting of a number of grains with a variety of pore geometries and right: a cross section of a fibrous structure, consisting of bundles (dashed circle) of individual fibres packed into an array. Note that in both cases there are multiple scales of porosity.

A porous medium is any substrate in which there are channels or pores. For problems concerning porous flow, at least one of these pores need to constitute a continuous path from the ‘entrance’ to the ‘exit’ in some way [173]. The number of the pores, their geometry and their relative connectivity will define how a fluid will move through the medium and how the applied forces will dictate the flow front speed and shape. Substrate dependent, pores can have a huge range of sizes, from the nanometre scale [174] up to

several centimetres across, in samples often 10s of millimetres in scale [175]. Combining this with the hugely variable spatial distribution and the complexity associated with analytical definition of boundary conditions for fluid mechanics problems in non-idealised geometries, mathematical analysis of flow patterns becomes challenging [176]. Analytically, defining the flow space becomes practically impossible and solving for multiphase flow properties through the conventional methods in fluid dynamics such as the Navier-Stokes equations is not possible numerically; generating flow geometries that accurately reflect the microstructural features at a macroscopic flow scale becomes too computationally intensive [177].

As such, convention in fields like chemical engineering, oil-well engineering and hydrology is to take a more 'ensemble' approach. Firstly, as Bear [20] and Allen [176] discuss, it is normal to treat porous media as a continuum and, in multiphase flows, overlapping continua. In so doing, volume fraction weightings can be assigned to each material. However, as Allen remarks, it is usual that constitutive equations for flow properties (pressure, speed, velocity distribution, etc.) are phenomenological, and do not tie the flow behaviour to inherent and transferable variables. The author also reinforces the challenge associated with the solubility of these multiphase flow problems, emphasising the need to use numerical methods. For this reason, there is a tradition of attempting to characterise a material's resistance to flow as a material property, as contrasted to an inherent link to material structure. Henry Darcy [178, 179], through an extensive set of experiments, characterised the flow resistance of liquid with viscosity μ through columns of sand with respect to the pressure gradient (∇P) and flow speed (q), in which a material variable K, or the permeability, acts as the constant of proportionality (Equation 3)

$$q = \frac{-K}{\mu}\nabla P \tag{3}$$

This has been demonstrated empirically, for unidirectional, creeping flow at low Reynolds number, but also been derived analytically by Whitaker [180] via volume averaging of Stokes flow for arbitrarily structured media. A framework for the calculation of K from geometric information was presented, but equally it was remarked that it was a "formidable computational problem', and as such for practical purposes, measurement of material permeability is both more useful and convenient. This equation can be extended into three dimensions as discussed by Sozer et al. [181]:

$$\overline{\boldsymbol{U}} = \begin{pmatrix} \overline{u} \\ \overline{v} \\ \overline{w} \end{pmatrix} = -\frac{1}{\mu}\begin{pmatrix} K_{xx} & K_{xy} & K_{xz} \\ K_{yx} & K_{yy} & K_{yz} \\ K_{zx} & K_{zy} & K_{zz} \end{pmatrix}\begin{pmatrix} \partial P/\partial x \\ \partial P/\partial y \\ \partial P/\partial z \end{pmatrix} \tag{4}$$

The experimental issue then becomes accurate measurement of the permeability tensor by ensuring precise flow measurements and that the flow regime is truly Darcian. At high pressure gradients or in high speed flows, often there are deviations from this law. Many authors have applied higher-order terms to account for this. Forchheimer's law [182] and the Hazen-Dupuit-Darcy [183] law (Equations 5 and 6) add a quadratic term with respect to the flow rate to model higher-order interactions. The viscous permeability, the contribution expected from Darcian-like behaviour, here is k_v.

$$-\frac{dp}{dx} = \alpha u + \beta \rho u^2 \tag{5}$$

$$-\frac{dp}{dx} = \frac{\mu}{k_v}u + C_d \rho u^2 \tag{6}$$

$$\boldsymbol{\nabla P} = \frac{-\mu}{k_v}\boldsymbol{u} + \mu' \boldsymbol{\nabla}^2 \boldsymbol{u} \tag{7}$$

Ruth [182] discusses the origin of this term, not as the onset of turbulence at high flow speed as suggested by some authors, but due to the microscopic inertial interactions in the liquid. This is corroborated by Cheng et al. [184], who observed that turbulence almost never arose in subsurface flow problems. Moreover, Medraj et al. [183] related the deviance coefficient C_d in Equation 6 to the complexity (and, the reader infers, the tortuosity) of the structure; this suggests that the deviation from the unidirectional flow assumed in Darcy's law is also significant in producing this effect.

The Darcy-Brinkman equation, Equation 7, is used to model flows in porous media consisting of elements that are themselves porous [185]. For this reason it is a potentially promising approach for flow analysis in fibrous media (as indicated on the right in Figure 5), where fibre bundles can absorb fluid with different characteristic pore dimensions (and hence pressure distributions). The correction factor in this case is the Laplacian (∇^2) of the velocity field, which represents viscous stresses when multiplied by an effective viscosity μ' and represents a momentum sink for fluid ingress in the porous regions. However, a study by Nichele [186] showed that the inclusion of this correction was unnecessary for generating accurate flow behaviour for a numerical modelling of oil flow in rock, and was only noticeable at incredibly high mesh densities.

Whilst the establishment of a permeability value was to enable quantitative analysis to be made without relation to substrate structure, the connection between permeability and geometry is incredibly important from a systems design point of view. This is the basis of the Carmen-Kozeny approach [187], Equation 8.

$$K = \frac{D_f^2}{16k_k} \frac{(1 - V_f)^3}{V_f^2} \tag{8}$$

Devised originally for beds of spherical particles of diameter D_f, the Carmen-Kozeny equation, Equation 8, explicitly extricates the porosity (1-V_f) of the medium from the permeability. The result is the definition of the Kozeny constant k_k which is a parameter reflecting the geometric properties of a material. In this way, the analysis of the structural effects can be obtained as distinct from purely the porosity content. This will be addressed in detail later. A final important model for porous flow is the Lucas-Washburn equation [188], Equation 9, and the modified Washburn equation, Equation 10:

$$l^2 = \left(\frac{\gamma \cos\theta}{2\,\mu}\right) rt \tag{9}$$

$$m^2 = \left(\frac{C\,\rho^2\,\gamma \cos\theta}{\mu}\right) t \tag{10}$$

Equation 9 relates the capillary-action induced penetration length l in a horizontal capillary of radius r to the time t that is required, given a liquid's surface tension and viscosity (γ and μ) and the advancing contact angle between the fluid and the capillary θ. This is designed for a cylindrical capillary and serves as an incredibly simple model for 'porous media'. However, it can be extended to more generalised media with substantial success [128] by the relation of the mass change over time as in Equation 10. In the case of cylindrical capillaries, the factor C is the equivalence factor between Equations 9 and 10, namely the factor relating the mass and the length change for the cylinder ($r^5\pi^2/2$). However, in more general porous media, the relation between the mass^2 and other variables is generally good and C becomes an empirically determined variable relating to the structure and packing of the porous substrate. The method is mostly used in determination of liquid-solid contact angles, and this will be discussed as an experimental methodology in a later section. In principle, however, the rise is controlled by the properties of the liquid and the wall interaction. The fastest rising liquids are those with

high surface tensions, low contact angles and low viscosities. The effect of the C factor for arbitrary porous media, however, is important. One of the core stages of the derivation of Equation 9 is to assume constant Laplace pressure, hence constant curvature of the interface which requires constant cross-section. Chassagne [189] used the Lattice-Boltzmann method to study the capillary rise in diverging and converging cross-section axisymmetric pores. They found that, unlike the assumption in Equation 10 that a nonwetting fluid ($cos\ \theta = 0$) cannot be absorbed, geometry dependent, an 'effective contact angle' could be imposed by tilted capillary walls. In this regime, the 'real' angle of contact between the wall and the interface needed to sum to less than 90°, including the wall off-set, for successful sorbtion. In this way, the geometry of the capillaries can manipulate the wettability. This, however, would have been accounted for as a non-linearity in C in the application of Equation 9. Dullien et al. [190] completed a similar analysis analytically, considering the case of pores with step-changes in their diameter. He found, by categorising pores by two parameters: neck diameter and bulge diameter (with the assumption that neck length ≪ bulge length) that the resistance to capillary rise was dictated by the restrictiveness of neck diameter, and that the driving force was related to the width of the bulge. This is understandable, both in terms discussed by Chassagne as the effect of a geometrically imposed 'effective contact angle', but also in that the necks will simply act as flow impediments and will create an inhibiting back-pressure in the system.

It is natural to compare the C factor in the Washburn equation with the Kozeny constant k_k in Equation 8, as both are factors implicitly related to the pore geometry. Galet et al. [191] attempted to relate the gas permeability of powder beds and their capillary sorption behaviour.

$$C = \frac{V_p^4}{(1 - V_p)} \frac{D_p A^2}{3k_k} \tag{11}$$

In Equation 11, A is the cross sectional area of the bed. This was determined theoretically and compared to experimental values, and the contact angle measured for the powder beds varied in the expect manner with an increase in bed porosity. The aim of this study was to establish a method to pack powder samples more reproducibly. However, whilst the authors discuss the effect of packing differences, no constitutive relations were presented between more specific geometric quantities.

That the Kozeny constant is a reflection of the geometry of a porous medium is accepted; how it takes the value it does, however, is difficult to determine a priori. Ozgumus et al. [192] numerically probed the relationship between the Kozeny constant and both the aspect ratio and pore size to neck size ratio for model, rod-based porous media. They found that the permeability of the medium was not simply a function of porosity for a given structural type, as suggested by Equation 8, and derived an equation that accounted for the pore-size to neck-size ratio for this medium also. Whilst the specific relation is not relevant outside of this context, it demonstrates the dependence of the Kozeny constant on a specific structural feature, namely the pore diameter differences. They found that the type of flow was very different in the narrower necked pores; there was significant generation of secondary flows due to viscous dissipation, Figure 6, hence suggesting a mechanism for this change.

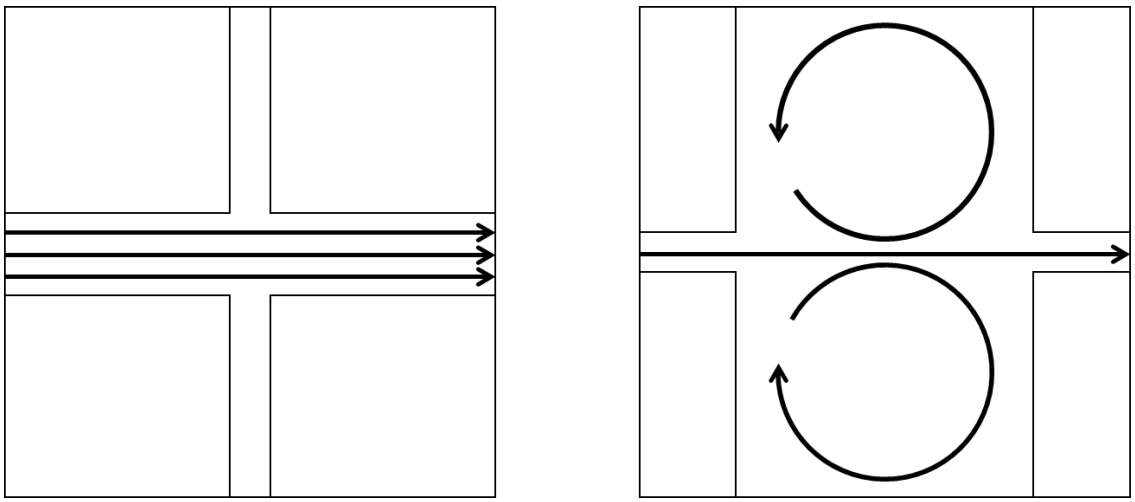


Figure 6: Viscous dissipation related to pore size to neck-size ratio (adapted from Ozgumus et al. [192])

Yazdchi [193] performed a similar investigation to understand the influence of orientation of fibrous media on the determined value of permeability. The author comments that, for modelling purposes, the assumption of a bundle of cylindrical pores does not function well for flow in transverse fibre arrangements. The study finds that the Kozeny constant is, in the first instance, a product of the tortuosity of the medium (i.e., l/l_0 where l is the characteristic length of a pore and l_0 is the total thickness of the medium in the flow direction) and some shape factor φ, which varies for the shape of the porous medium and particularly the orientation of the particles/fibres. Though this does not seem to extract much specific geometric information, the tortuosity is a very specific parameter whose value is easy to determine from numerical simulations, as highlighted by Sobieski et al. [194]. They remark that analysis of tortuosity from a geometric approach through pore modelling is far superior to determination of the hydraulic tortuosity ($\langle v \rangle / v_0$) from velocity field calculations, as the latter often computes the values from dead-end pores, which have no effect on the hydraulic conductivity of a medium.

Bringing the permeabilities of different idealised media together into a single medium more representative of a real, commercially relevant, substrate is the goal of many works;

that is to try, as Sobieski suggests, to be able to effectively represent complex geometries with simpler permeation models for computational efficiency. Liu and Hwang [195] attempted permeability averaging for simple geometric models to represent more complex fibre weaves of real fabrics used in composite manufacture. They performed flow simulation for single unit cells of different structures, and then brought these together and calculated the overall permeability for composite structures. It was found that, in some cases, permeability averaging (simply by weighted arithmetic averaging or inverse averaging, depending on whether the regions were in series or parallel with respect to flow direction) was successful, but in other cases gave large differences from the measured permeability. These latter cases were correlated with scenarios in which the perturbed streamlines from the fibre curvatures crossed the cell-zones from one structure type to another. More widely, this shows the huge sensitivity of the permeability to the specifics of the microstructure of the medium. As Nguyen et al. [187] point out, the geometric aspects of a fibre substrate can change over an infiltration process. They measured the pressure gradient for wetting and non-wetting liquids in preform permeation and found that the Kozeny constant was changed over the timescale of the process, which decreased the permeability. In this case, the fluid was absorbed by the natural fibres used and modified channel widths, but this could equally be induced in other environments by fibre clumping and shifting due to poor wettability. In any case, it made the infiltration process harder to predict, and therefore optimise for superior final properties in the material.

A final comment on the nature of 'permeability' as a concept is that in usual formulations (Darcy, Kozeny, etc) it is defined as a single-phase flow property for a saturated flow. In other words, the pressure to flow speed ratio for a first impregnation is different for that

of a continuous flow set up, due to the effect of capillarity [196]. The importance of this in being able to model and measure the impregnation in composites will be addressed.

2.3.2 Flow in composite architectures

As discussed by Sozer [181] and highlighted in Equation 4, modelling and analysis of flows for composite materials is usually done by assigning a permeability tensor to certain regions of the design space. Measurement of this permeability is performed by the pressure drop and flow rate characteristics through fibrous materials, including in different directions for anisotropic media. As Gebart [197] observes, the measurement of parameters by different authors often results in very distinct values of permeability. An extensive review by Naik [198] makes the same observation and suggests that the lack of universal procedure or equipment, as well as practical complications in measuring these values, is responsible for the disparate findings of different authors. Naik makes a number of observations on the deviation observed by many authors from Darcy's law; the most common model used. These centre on the use of unsaturated values of permeability determined for fabric reinforcements and the use of often non-Newtonian fluids, as the bulk of the literature is in the area of polymer composite moulding, of which shear-thinning resins are principle ingredients. For the first of these, unsaturated permeability and the effect of capillarity in fluid flow, there is much discussion. Kuentzer et al. [199] probed the effect of saturation numerically and experimentally. Modelling the fibre tows as a lower permeability region in the preform compared to the intertow spaces resulted in zones that wicked away resin from the fluid front. This was observed experimentally, with a 'partially saturated zone' developing where the resin had yet to permeate the tows fully. The work showed, primarily, the danger in premature termination of the infiltration, when tows were not yet fully filled by the resin and, more importantly, where inconsistent

filling of tows existed across the specimen thickness. Baché [177] made a similar distinction, but incorporated wetting parameters into a model for the two-region impregnation. The fluid viscosity was found to be the most crucial parameter to improve the time-to-saturation, followed by the surface tension and contact angle (though these were irrelevant outside the tow regions due to the means of integration in the model), with density being inconsequential. It was found that, for the input pressure regime in question, capillary pressure was the dominant force with regards to saturation. The differences in timescale associated with the different spatial scales being saturated were investigated in detail by Binetruy et al. [200]. They attempted to refine the infiltration speed such that tows were impregnated at the same speed as the macroscopic flow front, as opposed to being tangentially infiltrated by the fluid in the inter-tow space. Their work, however, did not consider the effect of the system's contact angle, nor the effect that pre-wetting has on the resin permeating the narrow channels of the pores. In fact, the effect of pre-wetting both on contact angle and on contact line friction has been found to be incredibly large [201], and as such needed to be considered by the authors.

Many authors assert that the capillarity is only an impactful feature in certain pressure regimes. Both Vernet [196] and Senoguz [202] suggest that capillarity is not relevant for higher pressure regimes such as that found in transfer or injection moulding of polymer matrix composites. However, Senoguz indicates that it is important at lower injection pressures or for processes such as prepregging. However even for low pressure injection (75 kPa), they observed that capillary pressures of 23 kPa had been reached in their resin system. The differences in impregnation were observed numerically at 10 kPa when considering the impregnation with or without the effects of surface tension.

Li et al. [203] directly measured the effects of capillary pressure on the permeability of fibre tows by varying the resin impregnation pressure (either with applied pressure or in

negative pressure). They found first that, when taking capillary pressure into account, the value for permeability was always higher. However, a number of important details are notable. Firstly, applying a vacuum actually produced a negative capillary pressure. This was compared to the contact angle under reduced pressure that equally showed a tendency to increase to less wetting values. It was conjectured that this was due to the liquid-gas interfacial energy changing due to the reduced vapour pressure. However, a decrease in the Kozeny constant was also measured in this case, suggesting that structural rearrangement in the tow could cause this feature. Secondly, the capillary pressures became more positive at higher applied pressures, which belies the expectation of Senoguz [202] that they should become diminishingly relevant at higher processing pressures. However, the relative effects of applied pressure on macro-pore filling and micro-pore filling were not discussed, which may ameliorate this apparent difference.

2.3.3 Particulate or multiphase fluids

Discussion has been limited to this point to the flow of resins and other single-phase liquids, as these are the commercially relevant applications in which multiphase flow is usually investigated. However, the flow of particle-laden fluids in narrow channels is incredibly important to a number of chemical engineering applications, as indeed to the slurry processing of porous fibre preforms. These flows will be discussed as a point of comparison.

Studying the formation of flow blockages of microtubes 100 μm across by suspensions of 0.5-5 vol% of 10 μm particles, Sharp et al. [204] showed that at even this low concentration of stabilised spherical particles, flow constricting arches could form as a result of a stochastic frictional process on otherwise smooth microchannels. This highlights a trend seen throughout microfluidics; flow maintenance is often challenging.

Goldsztein [205] considered the blockages at bottlenecks when multiple millimetre-sized particles attempted to enter at once. The retarding wall interactions lower the particle speed relative to the liquid speed and when a number of particles tried to enter the narrow region at once, the resulting clog narrows the effective entrance area which will increase the flow speed further (for constant applied force), in turn increasing the number of particle collisions, exacerbating the blockage. Mustin and Stoeber [206] investigated the effect of particle size distribution of polystyrene particles on the clogging of a system with 10, 20 and 30 μm wide channels. With a spectrum of neutrally buoyant particles with distributions centring from 0.5 μm to 1.5 μm, the authors found that two main mechanisms influenced flow blockages. The shortest timescale mechanism was size exclusion of particles too large for the channels themselves. Over a longer period, however, gradual flow channel constriction was observed by the deposition of smaller particles on the walls of the channel, and subsequently on each other. This happened in spite of repulsive surface treatments. The authors concluded that the blockage timescale could be indicative of the mechanism as a diagnostic tool. It can inferred that, should a wide distribution of particles exist, particle packing and deposition on the walls would have been made more facile.

The study of microchannel fouling in this way has been the focus of a number of numerical studies. Trofa et al. [207] favourably compared real microchannel fouling by a KBr solid by-product to a computational fluid dynamics-discrete element method (CFD-DEM) simulation of soft-sphere particles. This coupled the fluid motions in the channel with the adhesion energies and distance dependant interactions, as found in real suspensions, to analyse the tendency for particles to foul the channels. They found that the observed behaviour could be matched completely to the modelling. In similar pieces, Shahzad [208, 209] showed that clogging could be induced by an increase in the adhesion parameter in

the system. Whilst the hydrodynamic interactions were not fully involved as in the case of Trofa, this is a clear demonstration of the need for good particle stability to reduce the clogging tendency of a microfluidic system, to which the microstructured fibre preforms used in this work are similar.

2.3.4 CFD approaches for multiphase porous media

Modelling of multiphase flow, or determination of various relevant constants, has been performed in a number of ways in the literature. These generally reflect the principle asserted by Sobieski [194]; either the explicit geometry of the substrate is ignored, an attempt is made to replicate it exactly, or some geometry is chosen that, when various material parameters are applied to it, provides an adequate model of the salient aspects of the fluid-solid interaction. Macro scale modelling of micro-structured materials is computationally intensive; Senoguz [202] observed that classic CFD modelling of the Navier-Stokes equations can really only accurately be done in small domains. The common uses of modelling generally take the form of: analysis of the classic flow and continuity equations in a structural fibre element to solve for the Darcy permeability via the velocity and pressure fields, extension to a wider scale medium consisting of porous elements with their determined permeability, and final macroscopic flow modelling [210]. Some dual scale modelling ("mesoscale") has also been attempted [177].

Microstructural modelling of fibre substrates was first attempted by Gebart [197] following the procedure above. The work drew important differences between different packing regimes of unidirectional fibres, cubic or hexagonal, and analysed the effect of collinear or transverse flow on the determined permeability. This analysis was important because it was discovered that the Carmen-Kozeny equation, for transverse flow, did not

allow the permeability to tend to 0 at packing densities that would result in the total closure of flow paths. Hence, a better relation between fibre packing and permeability was required. Two methods are mainly applied here: either the solution of the Navier-Stokes equations [195, 211, 212] or by the Lattice-Boltzmann method [213-216]. The latter is an approach that describes the time, location and velocity distribution of control volumes of fluid as a Maxwell-Boltzmann distribution, and solves changes in these iteratively and on a nearest neighbour basis. It is mathematically equivalent to the Navier-Stokes approach, but lacks the ubiquity in commercial codes [215]. These approaches can accurately predict the permeabilities of isotropic fibre media, and the determined permeability can be extended to the macroscale for comparison with experiments [211]. Both Sozer [181] and Gebart [197] warn that this is only useful where 'racetracking', where flow takes high-permeability paths not through the fibre architecture, does not prominently feature in the experimental results. Where it does, it can be modelled as flow paths of significantly higher permeability.

The Lattice-Boltzmann method has also been employed in mesoscale studies. Nabovati [214] considered a larger unit cell, consisting of porous tows and varying both the structure of the weave (spatial distribution of the tows) and the tow porosity (affecting the permeability of the tow). It was found that, even at high values of tow porosity and low values of weave porosity, that most of the flow was concentrated in the intertow space. If the weave porosity was high, no tow parameter (radius or porosity) meaningfully influenced the flow. These, however, were still single phase models and thus the effect of initial wetting was not investigated.

Macroscopic studies have involved the assignation of regions of certain porosity to a larger structure. This can take the form of adding 1D elements at nodes in a 3D geometry as in the case of Kuentzer [199] to manipulate the flow characteristics in the infiltration

direction of a preform. Kuentzer matched the 'tow permeability' iteratively to the experimentally observed features in order to back-calculate the permeability. However, this method did not take into account a number of physical properties (contact angle, capillary pressure, geometry), hence the evaluation of the permeability parameters is only useful in the precise formulation in which the authors integrated the variables. A caveat by Yazgan-Birgi [217] is that the most effective modelling method for a specific problem should only be thought of as valid in that specific instance, due to the particularities of the many input variables. A similar approach as Kuentzer was taken by Louis et al. [218] for the effect of fabric shearing on the impregnation kinematics, they however derived the applied permeability values experimentally and applied them to the modelling of a single phase medium. A good correlation was determined, but constitutive relation of the actual fibre structure to the infiltration was not possible. In most macroscopic studies, this is the expected trade-off between large scale flow simulation and microscale flow mechanism discovery. This can be somewhat attenuated by the approach of Baché [177], who used a 2-region model to produce cylinders representing tows in a substrate, with two different values of porosity. To reduce the computational expense further, the author used the Darcy-Brinkman equation to remove the need for coupling [185]. Whilst promising for flow front progression, this would be a waste of time in attempting to model an explicitly granular flow, as solid-liquid coupling is of vital importance.

The methods for characterising, analysing and modelling porous media discussed in Section 2 will be influential for the successful analysis of the fibre preforms investigated in this work.

2.4 Regularisation

Regression is a statistical tool used to generate a mathematical relationship between output (response) and input (predictor) variables. In its simplest manifestation, it is a method of drawing a line of best fit through a graph of data points on a pair of axes. The equation of this line can then be used to predict the expected response for further measurements. The data used to produce the line of best fit is known as the 'training' data, whereas future measurements are the 'testing' data. In simple regression between a single scalar variable input and a scalar output, the method to produce such a line of best fit is called Ordinary Least Squares (OLS) [219] which is an algorithm. In effect, a line is drawn through the data set and the gradient and y-axis intercept of the line is adjusted so that the sum of the squared residuals (SSRs) between the observed data points' response variable and the estimated response variable from the trend line is minimised. This procedure means that the total variance of all the points from the trend line is minimised. When there is one predictor variable X and one response variable Y, this space exists on a pair of axes and the 'model' constitutes an equation of the form:

$$Y = bX + c$$

which is the equation of a straight line. If there are two predictor variables and one response variable, this then exists in a 3D space. The best fit output from the SSRs then constitutes a surface, with an equation of:

$$Y = b_1X_1 + b_2X_2 + c$$

As the number of predictor variables increases, the dimension of the descriptive equation increases and will change from 2D planes to 3+ dimensional hypersurfaces that can no longer be meaningfully visualised. However, the core aspect of the regression remains the same. The b_j parameters are adjusted so that the SSR in the response axis are minimised

between the data set and the model. The output from this constitutes the regression equation. The R^2 value indicates the goodness of fit. It is calculated by determining the value of:

$$R^2 = 1 - \frac{SSR}{SSM}$$

where SSM is the sum of the square distance from the mean. This value is equal to the sum of the differences squared between each data point's response variable and the mean of the response variables of the data set. To define any n^{th}-dimensional surface, n+1 data points are required. For instance, 2 points are required to define a unique line. 3 points are required to define a unique plane. 101 points are required to define a 100-dimensional hypersurface. Hence, for data sets with large numbers of potential predictor variables, large numbers of data points are needed. Equally, when large data sets with large numbers of predictor variables are used, OLS regression has a tendency to 'over-fit' the solution to the data. That is, the employed training data is used to produce a linear model that has very low variance, but when new data is added the variance is high and, consequently, the predictions are poor relative to the indicated quality of fit established by the regression procedure (i.e. R^2 value) [220]. In effect, the noise in the data is built into the predictive capability of the model, which results in a model that cannot accurately predict future results. Such a model will reproduce the training data with a very small degree of variance, but testing data will not be accurately mapped. A method of accounting for this tendency in the least squares algorithm is to introduce a function that desensitises the final model to the influence of some of the variables. This constitutes a process known as regularisation.

Regularisation is a machine learning method of multivariable analysis for large data sets, where the number of potential predictor variables is large, or even exceeds the number

of observations (i.e. N < p) [221]. To avoid the overfitting effect, a term is included into the function on which the minimisation acts. Not only does the algorithm minimise the SSR, but an additional penalisation term too:

$$SSR + \lambda_i \sum_{j=1}^{p} |b_j|^i$$

Again, b_j represents the terms in the regression equations shown above, and i=1 or 2 depending on the type of penalisation term. This extra term involved in the minimisation essentially adds a pressure to bias the minimisation against high values of coefficients b_j. OLS tunes the b_j parameters in order to minimise the SSR. The difference in this method is that there is now an interplay between the SSR and the penalisation term, the strength of which is tuned by the λ_i parameter. At high values of λ_i the contribution of the second term is very high, so the b_j parameters are reduced to minimise the whole function's value. The effect of this on the output regression equation is that the model has smaller variable coefficients, and therefore has become less sensitive to each input. Likewise, as λ_i tends to 0 the result tends to the normal OLS result [222]. The effect of i is to change how the penalisation term is calculated. When i=1 the penalisation is determined by the sum of the magnitudes of the coefficients. This is called L1 regularisation, and is commonly known as Lasso regression. When i=2, the penalisation is determined by the sum of the squares of the coefficients. This is called L2 regularisation, or Ridge regression. Both L1 and L2 regularisation reduces overfitting in the model, by adding a small degree of initial bias. A full discussion of the mechanics and underlying principles of performing regularisation may be found in a review by Bickel and Li [220] or a directive textbook by Hastie [223]. The main difference between L1 and L2 regularisation is that L1 regularisation can result in selection of b_j parameters as 0, hence removing parameters from the model. This is due to the explicit form of the minimisation term. This can inform

the physical relationship between the predictor and response variables and help categorise redundant and useful predictors from cases when p is large.

Clearly, an influential aspect of the process is the selection of λ_i. This is usually achieved through a procedure known as k-fold cross-validation. In this process, a random sample of N/k entries of the training data is employed with a user-defined choice of λ_i. The function is minimised and the mean squared error (MSE) valued recorded, and performed on all the random samples. The value of λ_i is then progressively changed and the minimisation performed iteratively. The value of λ_i that obtains the lowest MSE across the data sets is selected. The use of random samples of the training data allows the general trends to be extracted from the data set, while a large amount of the noise is ignored. Hence, a more general and less sensitive model is produced.

Vidaurre et al. [224] show that Lasso regression is superior when the number of predictor variables is large compared to the data set size, and Ridge regression is most suitable for a dense data set, when the number of efficacious predictor variables make up a large percent of the variables in the regression (i.e. $b_j > 0$ for most j). In other words, L1 is best for variable selection (as it can remove variables) and L2 is best for MSE reduction of a dense data set. It was also shown that λ_2 is often larger than λ_1; the most suitable penalisation weighting for selection is smaller than for prediction. Efron et al. [222] showed that, for a small dataset of 442 samples with 10 predictors, the values and minimisation behaviour was similar for both algorithms. However, it was remarked by Zhao [225] and Benfenati [226] that care should be taken in the variable selection properties of Lasso in the case of highly covariant redundant and effective predictor variables, as some useful parameters can be excluded and some conceptually unrelated parameters can be misleadingly incorporated. Hence, the realm of applicability must be

considered for results of these analyses. However, these analysis methods are both standard and incredibly robust in many fields of study.

3 EXPERIMENTAL

3.1 Ceramic suspensions

3.1.1 Selection and preparation

Suspensions with a range of properties were prepared from constituents as listed in Table 3.

Table 3: The raw materials for the production of the suspensions for this study.

Material	Density / g cm^{-3}	Particle size (d_{50}) / µm	Source
Ultra-fine calcined Al_2O_3	3.95	1.0	Logitech (OCON-016)
ZrB_2	6.08	1.0	H.C. Starck (grade B)
HfB_2	10.5	3.0	Treibacher (P-74-VC)
H_2O	1.00		In-house
PVP, 360 kDa	1.2		Sigma-Aldrich
Tween 80	1.075		Sigma-Aldrich
Dispex A4040	1.3		BASF
Isopropyl alcohol	0.786		Honeywell
PEG 400 Da	1.13		Sigma Aldrich
Diacetin	1.12		Sigma Aldrich
Phenolic resin	1.225		Hexion
Acetone	0.79		Fisher Scientific

Slurries were fabricated by wet ball milling of the ingredients together in a single step for 24 hours with Al_2O_3 media in a polyurethane lined bottle. The investigated compositions are detailed separately in Table 4. Compositions were selected from literature results and sequential property measurements to produce the required property spectrum.

Hafnium diboride and zirconium diboride slurries were prepared at constant volume fraction of solids, 72 and 60 wt% solids respectively, with an equal volume of phenolic

resin and acetone, the former constituting 24 wt% of the ZrB_2 slurry and 17 wt% of the HfB_2 slurry.

Table 4: The test fluid compositions for the slurry spectrum investigated in this study.

##	Formulation details / wt%							
	Al2O3	Water	Iso-propyl alcohol	PEG	Dispex A4040	Tween80	Diacetin	PVP
1	49.66	49.95	0	0	0.39	0	0	0
2	49.62	49.59	0	0	0.39	0	0	0.39
3	49.54	49.22	0	0	0.41	0	0	0.83
4	49.52	49.00	0	0	0.42	0	0	1.06
5	49.49	48.86	0	0	0.42	0	0	1.23
6	49.62	49.92	0	0	0	0	0	0.47
7	49.29	49.83	0	0	0.16	0	0	0.72
8	49.50	49.70	0	0	0.31	0	0	0.49
9	49.05	49.62	0	0	0.78	0	0	0.55
10	49.48	48.86	0	0	1.21	0	0	0.45
11	49.63	49.29	0	0	0.39	0.30	0	0.39
12	49.60	48.93	0	0	0.39	0.67	0	0.40
13	49.54	48.26	0	0	0.38	1.41	0	0.40
14	44.46	0	54.24	0	0	0	1.30	0
15	44.09	0	51.45	3.15	0	0	1.32	0
16	43.61	0	48.87	6.22	0	0	1.29	0
17	49.48	48.58	0	0	0.41	0	0	1.53
18	49.37	47.84	0	0	0.42	0	0	2.37
19	49.45	47.11	0	0	0.40	0	0	3.04
20	49.41	46.42	0	0	0.41	0	0	3.76
21	49.70	49.45	0	0	0.41	0.063	0	0.38
22	49.61	49.39	0	0	0.47	0.142	0	0.39
23	49.67	49.35	0	0	0.40	0.189	0	0.39
24	49.55	49.33	0	0	0.41	0.263	0	0.45
25	49.47	49.69	0	0	0.40	0	0	0.44
26	49.50	49.62	0	0	0.41	0.0127	0	0.45
27	49.44	49.66	0	0	0.40	0.0253	0	0.47
28	49.44	49.67	0	0	0.40	0.0378	0	0.45
29	49.52	49.57	0	0	0.41	0.0505	0	0.45
30	49.57	49.65	0	0	0.39	0.0030	0	0.39
31	49.46	49.71	0	0	0.39	0.0063	0	0.44
32	49.51	49.65	0	0	0.42	0.0093	0	0.42
33	43.85	0	40.57	13.84	0	0	1.74	0
34	44.10	0	37.88	16.25	0	0	1.77	0
35	41.66	0	30.41	26.28	0	0	1.65	0
36	36.27	0	0.00	62.13	0	0	1.60	0
37	36.88	0	5.23	56.13	0	0	1.76	0
38	37.71	0	10.72	49.86	0	0	1.71	0

3.1.2 Surface tension measurement

Surface tensions were calculated at 22°C using the axisymmetric pendant drop technique with a Theta Optical Tensiometer (Biolin Scientific, Gothenburg, Sweden). A droplet of fluid was expelled from a needle (needles used were either 21G steel or 16G PTFE cannulae) and an image analysis software (OneAttension, Biolin Scientific) fit a Young-Laplace curve to the profile of the droplet. This calculates the balance of gravitational and surface tension forces and therefore determines the surface tension of the fluid.

3.1.3 Rheological analysis

The shear-rate dependent shear stresses of the listed test fluids were obtained at 22°C with a parallel plate geometry (40 mm ∅, 500 μm gap) in the shear rate range 0-900 s^{-1} using a Discovery HR-1 rheometer (TA Instruments, New Castle Detroit, USA). The shear sweeps were performed 5 times per test fluid at both increasing and decreasing shear rate. Where appropriate, the shear-rate dependant stresses were modelled with an appropriate model. Unless otherwise specified, the model chosen was the three-component Herschel-Buckley model, Equations 12 and 13. Here, τ and τ_0 are the shear stress and yield stress (Pa) respectively, k is the consistency index (a constant of proportionality, units Pa s^n), $\dot{\gamma}_w$ is the shear rate (s^{-1}) determined by the Rabinowitsch-Moony method (see section 3.3.4) and n is the flow index (determining the extent of non-Newtonian behaviour).

$$\tau = \tau_0 + k\dot{\gamma_w}^n \tag{12}$$

$$\mu_{eff}(\dot{\gamma_w}) = \frac{\tau_0}{\dot{\gamma_w}} + k\dot{\gamma_w}^{n-1} \tag{13}$$

For compositional screening, the viscosity at 120 s^{-1} was taken as a comparator.

3.1.4 Stability analysis

The stability of as-prepared suspensions were determined qualitatively by analysis of the settling rate. Slurries were prepared as detailed above and were dosed into glass vials. These were monitored over 48 hours and the length of the transparent fluid column and the length of the observed sediment bed measured. The settling rate was then calculated.

3.1.5 Fibre contact angle determination

The contact angle of the fibres in the study with the test fluids were determined at 22°C with multiple fibre tensiometry using a K100 force tensiometer (Krüss GmbH, Hamburg, Germany). Uncoated fibres, extracted from the 2.5D preform, (~20 mm length, 20 < n < 40) were aligned on an adhesive strip at equal spacing, parallel to one another and perpendicular to the strip spaced over a distance of around 30 mm. These were attached to the balance of the K100 with a proprietary clip. A vessel of test fluid was positioned on a movable stage below the fibres, and raised up slowly (6 mm min^{-1}) for surface detection. Surface detection occurred at a balance reading of ± 0.0050 g, whereupon further submersion of 1-2 mm ensued, depending on the length of fibres. At this point, the advancing and receding contact angles were measured over a 4 mm distance with a 2 mm min^{-1} submersion speed. The curves were extrapolated back to 0 mm submersion to negate the buoyancy force of the fibres.

$$\theta = arccos\left(\frac{F}{L\,\sigma}\right) \tag{14}$$

Equation 14 was used to calculate the contact angle. F is the force at 0 submersion, σ is the surface tension of the fluid, and L is the wetted length of the sample. In this case, it is $n\,\pi\,d$, where n is the number of fibres in the sample, and d is the average fibre diameter

(calculated from micrograph analysis). The advancing contact angle was obtained from the initial submersion and the receding angle from the extraction of the fibres from the fluid. An example of the raw trace for determination of the contact is shown in Figure 7. Where the argument of the *arccos* exceeded 1, the imaginary contact angle formalism was not used; the argument was merely recorded. This coincided with the receding angles, hence was less relevant in unsaturated flow problems such as the impregnation studies here.

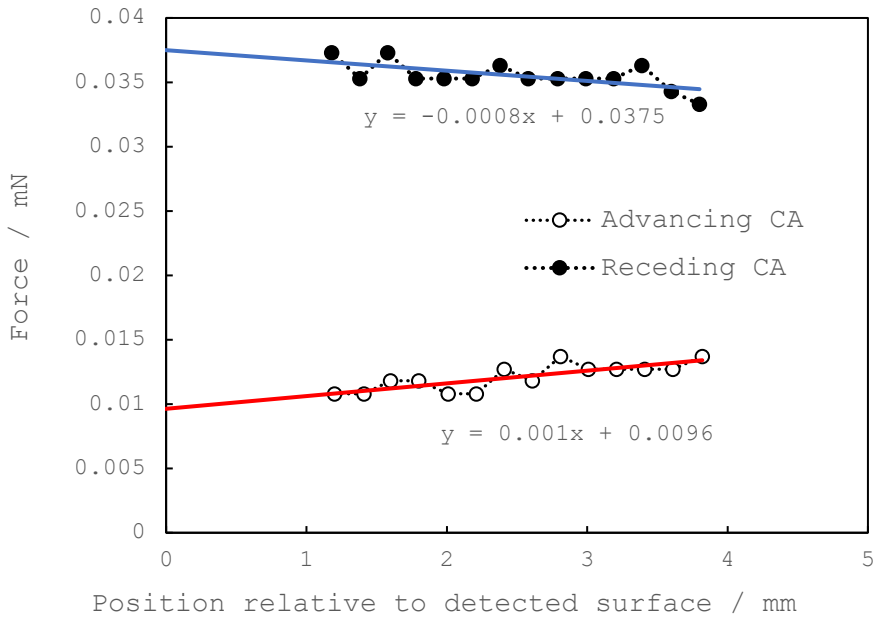


Figure 7: The force vs submersion characteristic used in the determination of the contact angle for fibres.

3.1.6 Particle size determination

Particle sizes in the as-prepared slurry were measured with a High Performance Particle Sizer (Malvern Instruments Ltd, UK) using a 613 nm laser. A cuvette of liquid was added to the measurement cell and the measurement was performed. The volume average particle size and standard deviation was determined from three samples.

Primary particle sizes were measured using a HELOS laser diffractometer (Sympatec, Claustal-Zellerfeld, Germany) using trisodium phosphate dispersant in water. An average of five measurements were used, all observed distributions were monomodal.

3.2 Fibre substrates

3.2.1 Raw materials and preform production

Table 5: A summary of the preform/fibre sheet properties used in this study.

	Isotropic (I_{cf})	**1D (STUD)**	**2.5D**
Structure	Randomly oriented in x-y, laminate	Split tow unidirectional sheets	R/0/R/90 repeating
Source	FuelCellStore	Cristex Composite Materials	Surface Transforms
Fibre diameter / µm	11.1 ± 2.3	6.9 ± 0.4	8.4 ± 0.5
Fibre precursor	PAN	Pitch	PAN
Fibre density / g cm^{-3}	1.53	1.76	1.46
Fibre fraction / vol%	4	8 mm 33-ply lay up; 57	23
Bulk density g cm^{-3}	0.065	0.94	0.33

The 2.5D preform structure consisted of unidirectional (UD) fibre layers oriented perpendicularly to one another, bonded together with a layers of random stitching formed by the needling technique that bonds the adjacent UD layers together. The isotropic (I_{cf}) preform was a pressed felt consisting of short cut carbon fibres, whilst the STUD plies each consisted of two sheets of randomly packed fibre layers aligned in the same direction, lightly adhered to one another with a phenolic resin. The fibre mass consisted of 92% the mass of the whole ply. Fibres were stuck to their neighbours in their sheet, and the sheets lightly stuck to the layer beneath.

The 2.5D and I_{cf} preforms were supplied as 18 and 12 mm thick panels and were used as procured. The split tow unidirectional (STUD) sheets were supplied as a single layer on a spool. Preforms were produced by aligning layers 0°/0° on top of one another and rolling in duct tape while compressed to produce a preform with little interlaminar porosity. A laminate of 8 mm thickness was used for the injection studies. The compressed STUD fibre layers were found to tend to a preform volume fraction of 0.57 at increasing ply number. Bulk densities were determined geometrically.

3.2.2 Pore analysis

Porosity was analysed by Archimedes' method using vacuum infusion for the preforms, with water as the fluid. Fibre diameters were measured through scanning electron microscopy (SEM) of polished section of mounted preforms (Phillips XL-30 FEG ESEM, Thermo Fisher Scientific, Waltham MA, USA).

The pore size distribution was determined by both porosimetry and microstructural analysis. The porosimetry was performed using an AutoPore IV Mercury Porosimeter (Micrometrics, Drive Norcross, USA) between 3.4 kPa and 210 MPa. Nanoscale X-ray computer tomography (CT) was performed using a Pheonix Nanotom (General Electric, Boston, MA USA) at a range of voltages to 180 kV at 20 W.

Pore size and structure were analysed with optical (Axioscope, Zeiss, Oberkocken, Germany) and electron microstructural analysis (Jeol 6060, Tokyo, Japan). A fibre preform sample was mounted in transparent resin and polished to 1 μm grit. The sample was then imaged with a Zeiss Axioscope and the images, at different magnification, analysed in ImageJ (National Institute of Health, Wisconsin USA) with the in-built profile plotting, thresholding, and particle analysis functions in addition to the ND_ plugin [227]

(for nearest neighbour algorithm calculations) and the Radial Distribution plugin [228] (for pairwise distribution functions).

The fibre volume fractions in all images were investigated by image thresholding and particle counting through the ImageJ programme. All fibre areas were thresholded to black contrast and all other areas to white after grey-scale binarisation, the area of black pixels in a scaled image were counted and the volume fraction inferred from the areal fraction. This is, of course, a 2 dimensional representation of a 3D structure and hence was considered during the resulting interpretation.

The fibre packing was assessed via three methods. Firstly, the radial distribution function was calculated from a central part of a fibre in the centre of a micrograph. The exact location was assessed by eye. The distance between peaks were used to infer long-range order and nearest neighbour spacing. It was calculated by normalising the grey value intensity in progressively larger concentric rings around a centrally defined pixel by the circumference length. Secondly, the ND_ (standing for 'nearest distance') plugin was used to calculate the average distance between the centroids of the five nearest neighbours of every particle identified from the thresholding procedure. Additionally, the nearest neighbour distances were recorded and the average distance of the pore from each fibre to its nearest five neighbours. This latter value was inferred as a measure of average pore radius and a histogram was plotted for this as a 'pore size distribution'. This was performed for a number of magnification scales.

To assess channel width between fibre tows in the UD layer, a 2D surface plot was made of binarised images, as described above. The average grey value for the i^{th} x-coordinate strip in the y-direction was calculated by Equation 15:

$$\overline{GV} = 255\left(\frac{n_{255}}{n_{255} + n_0}\right) \tag{15}$$

where n_{255} is the number of 255 grey value pixels and n_0 is the number of 0 grey value pixels. It is, thus, the proportion of in-fibre pixels in the strip of pixels at the (x_i,y) line. For qualitatively selected regions, the peak separations in this plot were then inferred to be the channel widths. This was done as indicated by the schematic in Figure 8.

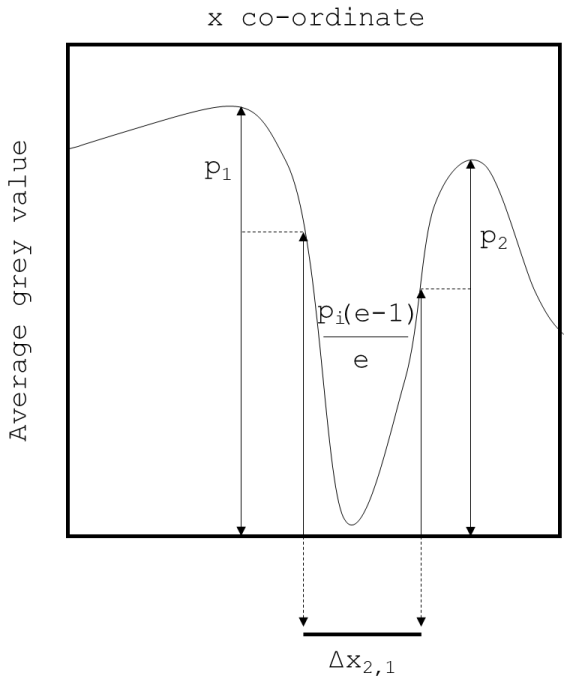


Figure 8: The selection algorithm for the gap width between fibre tows. Here, p_i indicates the grey value of the peak immediately before the identified channel.

The selection of the 'width' of the channel was, to some extent, non-definite due to the continuous nature of the boundary. For consistency, values that dropped to below 20 for a few fibre widths (15 μm) were classified as channels, and the wall was classified as the thickness at which about 63% of the grey value of the highest adjacent parent peak was reached. Only channels that were visually straight in the image were selected for this assessment, which may have introduced an element of bias in the results. Any tortuous channels were analysed in separate images.

The Reynolds numbers, Equation 16, were calculated using the slurry properties presented elsewhere in conjunction with the scale of pore sizes derived in this study. The capillary number, Equation 17, was calculated via flow speeds calculated from the tow flow studies (measured observations) or from first principles using Equation 18 and the procedure detailed in Appendix 1. This latter represents the radial growth of a sphere for which dV/dt (Q) is constant. This is an order-of magnitude estimate to gauge the range of potential flow rates.

$$Re = \frac{\rho u L}{\mu} \tag{16}$$

$$Ca = \frac{\mu V}{\gamma} \tag{17}$$

$$\frac{dr}{dt} = \left(\frac{Q\,\pi}{36\,t^2}\right)^{1/3} \tag{18}$$

Micro- and nano-XCT were also attempted but did not yield adequate phase differentiation at the required scale between air and carbon fibre to yield useful reconstruction of the pore space.

3.2.3 Permeability analysis

Preform permeability was measured using a bespoke gas permeation rig. This flow cell was based on that used in ASTM D6539 [229], and is shown in Figure 9. A 10 sL min^{-1} argon flow meter was used to control the flow of argon. A differential pressure gauge (Kane 3500-1, Kane, UK) was used to determine the pressure drop across the flow cell. The honeycomb helped develop a laminar flow through the preform, and the series of O-rings and annuli helped support the sample, define the flow area and retain laminar flow. Samples were prepared by cutting the preform into the requisite shapes, or sandwiching

fibre plies into the correct configuration and securing with laboratory Parafilm™. These are shown in Table 6. Cylindrical samples (for the through-thickness analysis) were sandwiched between the annuli of 35.6 mm inner diameter, whereas the cuboid samples were held within or beneath the rectangular holder with specific cross sections and thicknesses each. Tape was then used to ensure that large race-tracking channels were covered and inaccessible. The gas flow rate was set on the variable area flow meter (calibrated for argon), and held until the pressure difference remained stable at a stable flow rate. This value was then recorded and the flow rate increased incrementally. This procedure was repeated three times for each sample.

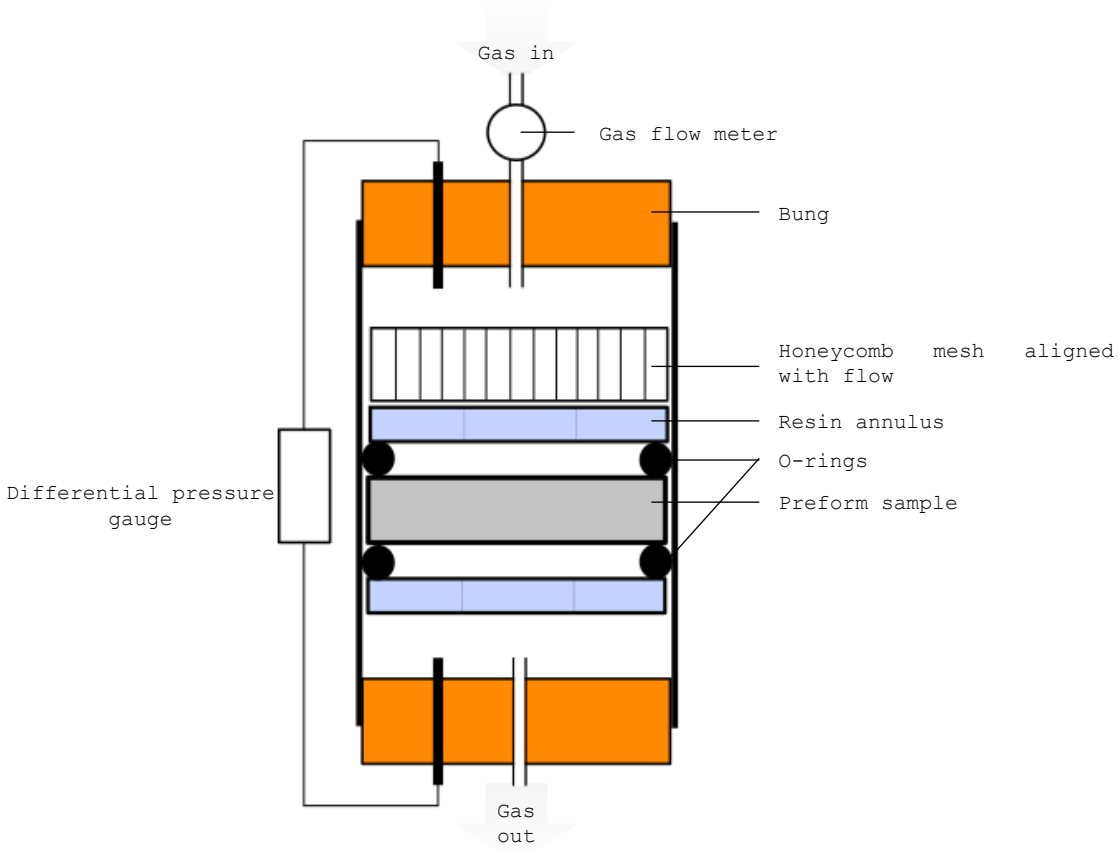


Figure 9: Schematic of the in-house permeation rig used for determination of the preforms used in this study.

The pressure gradient over the sample thickness was plotted as a function of Darcian flow rate V (volume flux/flow area) and the linear region used to calculate the Darcy

permeability K of the sample as per Equation 19. The viscosity of $Ar_{(g)}$ at 20°C was taken as 2.23 x 10^{-5} Pa s [230]. Non-linearity may be an indication of non-Darcian flow, either due to turbulence or non-unidirectionality of the flow field. The Hazen-Dupuit law, Equation 20 [231] was also used in the calculation of the permeability terms k_v (the viscous permeability, m^2) and k_1 (the inertial resistance, m) for comparing fitting for these non-linear regions. Standard errors were determined by the regression errors from the least-squares analysis for each plot.

$$\frac{\Delta P}{L} = \frac{\mu}{K} V \tag{19}$$

$$\frac{\Delta P}{L} = \frac{\mu}{k_v} V + \frac{\rho}{k_1} V^2 \tag{20}$$

Table 6: Preform sample dimensions for permeability determination, with their relevant flow geometries calculated.

Sample		Dimensions / mm	A_{flow} / cm^2	L / cm
2.5D	*Transverse*	51 ⌀, *d* = 18	9.95	1.8
	In-plane	30 x 18 x 22.8	5.4	2.28
I_{Cf}	*Transverse*	51 ⌀, *d* = 15	9.95	1.5
	In-plane	15 x 30 x 19	4.5	1.9
STUD	*Transverse*	51 ⌀, *d* = 3	9.95	0.3
	In-plane: 0°	10 x 40 x 16	4.0	1.6
	In-plane: 90°	10 x 31 x 23	3.1	2.3

3.3 Injection studies

3.3.1 Injection rig development

The injection rig was produced in-house. It consisted of an aluminium baseplate on four legs (150 mm) with a hole in the centre. A syringe sat in this hole, with the finger supports of the syringe allowing the syringe to be suspended by the plate. The plunger was then depressed by the work head of an Instron universal testing machine (model 5522, 100 N load cell, Norwood MA, USA), while the syringe remained stationary, with the tip of the

needle embedded at a specified depth into the sample. The work head was zeroed at around 0.3 mm from the top of the plunger to ensure that no pre-strain was generated before the tests began.

The syringes used were 1 ml Luer lock, inner diameter (*ID*) 4.57 mm for the scale, narrowing to 1.91 mm at the tip of the syringe. The plunger had a diameter of 10.2 mm. As a result, crosshead speeds $\dot{d}$ (cm s^{-1}) could be transformed into volumetric flow rates by:

$$Crosshead\ speed = \dot{d} = \frac{d}{\Delta t}$$

$$Q = \frac{\Delta V}{\Delta t} = \frac{d\ A}{\Delta t} = \dot{d} \cdot \pi \left(\frac{ID}{2}\right)^2$$

where d represents depression length and Δt represents duration. For the syringes used, this transformed as $Q = 0.164\ \dot{d}\ cm^3\ s^{-1}$.

Data acquisition was adjusted such that 1000 data points were acquired for each experiment by use of the equation below, to assure adequate resolution.

$$n(points) = \frac{d}{\dot{d}}\left(\frac{\partial n}{\partial t}\right)$$

The linear flow speed of fluids from the needles were calculated by Equation 21:

$$v_f = \frac{Q}{A_{needle}} \tag{21}$$

3.3.2 Calibration tests

Initially, the syringes were filled with air with the plunger in the fully out position. The force required to push the syringe without fluid was then measured.

Crosshead speeds of 0.51, 1.02, 2.03, 4.06, 6.09 and 8 mm s^{-1} were selected to provide flow rates of 0.00836, 0.0167, 0.0333, 0.0666, 0.100 and 0.131 cm^3 s^{-1}, the last representing the maximum flow rate producible by the crosshead for this syringe bore. Total displacements of 5, 20 and 35 mm were investigated to determine the initial sliding resistance and the steady sliding friction. The compression tests were performed and the data processed by quantitative analysis of the initial force peak and the subsequent steady state situation (when the graphs conformed to such an archetype). Other shapes yielded other data points recorded which will be commented upon separately and qualitatively. The discharge was investigated for 16G needles (length 35 mm, nominal inner diameter 1.194 mm).

Water (distilled, viscosity 0.89 mPa s, density 1.00 g cm^{-3}) and mineral oil (kinematic viscosity 67 mm^2 s^{-1}, calculated dynamic viscosity of 57.6 mPa s) were then extruded through the needle and syringe combinations. The graphs were analysed for the effect of the viscosity/density on the required injection pressure at the investigated flow rates/volumes, and also the qualitative differences with respect to discharging fluid or gas from the piston when equipped with either no needle or 16, 21, 25, 30G blunt needles (translated as: 1.194, 0.514, 0.260 and 0.159 mm internal diameter respectively). The intial force required for the piston to begin moving, or for the 'steady state' force required on the piston to retain flow were then plotted as a function of depression rate. When injecting any fluid, it was important that any air bubbles in the syringe were removed before the compression began.

Slurry samples of each material were injected into air (i.e. no preform sample) to determine the force-injection progress behaviour and to attempt to calculate the shear rate of the injection through Hagen-Poiseuille's law. 16, 21, 25 and 30 gauge needles were again used as above.

3.3.3 Injection studies with fibre substrates

Specimens of preform were injected with the above procedure to a depth of half the maximum thickness with different volumes of slurry and subsequently dried. The preform specimens used were 20 mm diameter cylinders of 18 mm (2.5D), 12 mm (I_{cf}) or 8 mm depth (STUD). The force/displacement characteristics ('F-d trace') were recorded by the Instron Bluehill 3 software. After drying, the samples were sectioned across the injection hole in a direction parallel to the bottom UD layer of the preform for the 2.5D specimens such that the maximum and minimum flow axes were observable within the preform. Some of these were set in resin and prepared for microstructural analysis. They were also imaged at 7.5x magnification without mounting, and the cross-sections analysed using ImageJ to determine the extent of slurry spread in each layer. It should be noted that the minimum and maximum flow axes (corresponding to the out and in plane UD layers respectively) only indicated flow in the sectioning plane. The distance of the midpoint of each layer (UD or R) from the top surface was used as the reference depth for each layer. A scalar quantity of 'extent of slurry spread' was used for the in-layer spreading, as the sample deposit distribution was suitably discrete to warrant this procedure (i.e. obvious differences in spreading between adjacent layers) and the flow in each layer was symmetric around the central axis of the preform. The pixel/distance ratio was calculated via comparison to a known length scale at the same magnification and focal length. For the I_{cf} preforms, sectioning occurred at an arbitrary angle, whilst for the STUD sample the layers were dissassembled and the slurry extent inspected in each plane.

Subsequently, these measurements were used to correlate against a variety of input variables, and involved in calculation for aspect ratio and needle centredness. The latter can be defined as α/β from the description of the parameters in Figure 10.

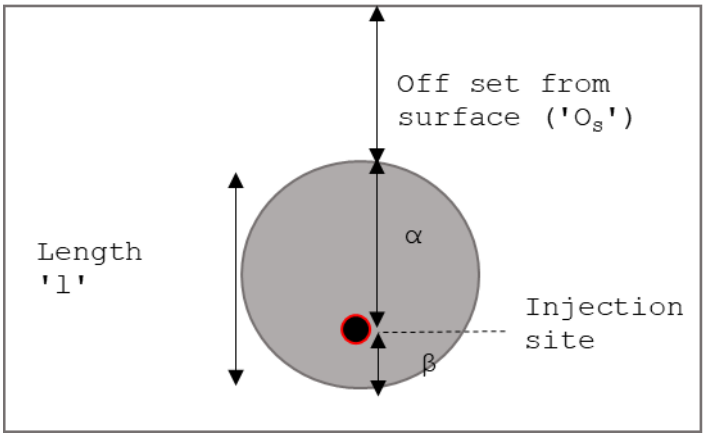


Figure 10: A schematic of an injection deposit with a variety of defined parameters: l is the maximum extent of the deposit in the z direction, O_s is the offset of the top of the preform, α is the distance from the injection site to the top of the deposit and β is the distance from the injection site to the bottom of the deposit.

Here, l and O_s were measured from the image analysis, and the location of the injection site ($O_s+\alpha$) was known from the needle depth (8 mm). An example of an image used for analysis is shown in Figure 11. Measured values were: the width of slurry in each layer, the maximum spread, the maximum height of the deposit, the aspect ratio, the needle centredness, and the forces associated with the injection.

Table 7: The key probed parameters of the investigation

Slurries	Substrates	Injection flow rates	Volumes	Needle gauge
20: 0.5% Dispex, 5% PVP	2.5D preform (2.5D)	8 mm s^{-1} (0.131 cm^3 s^{-1})	0.1 cm^3	16
19: 0.5% Dispex, 4% PVP	Split tow uni-directional lay-up (STUD)	2.03 mm s^{-1} (0.033 cm^3 s^{-1})	0.2 cm^3	21
2: 0.5% Dispex, 0.5% PVP	Carbon felt (I_{cf})	0.51 mm s^{-1} (0.008 cm^3 s^{-1})	0.5 cm^3	25
29: 0.5% Dispex, 0.5% PVP, 0.08% Tween80		0.051 mm s^{-1} (0.0008 cm^3 s^{-1})	Low speed injection: 0.025, 0.05, 0.3, 0.4 cm^3	30
24: 0.5% Dispex, 0.5% PVP, 0.4% Tween80		0.0051 mm s^{-1} (0.00008 cm^3 s^{-1})		
27: 0.5% Dispex, 0.5% PVP, 0.04% Tween80				

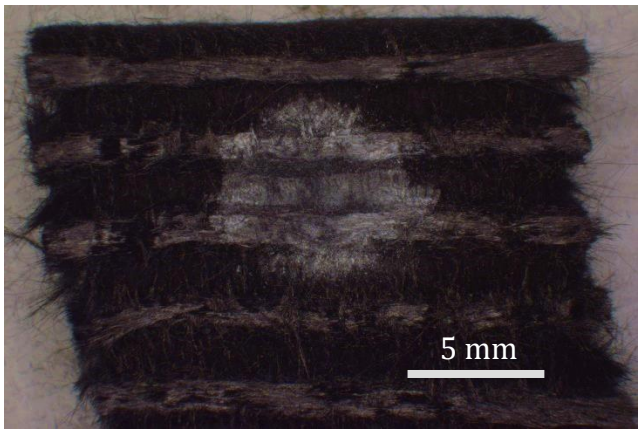


Figure 11: An example of one sample sectioned and used for image analysis

All slurries indicated in Table 7 were injected at 0.1, 0.2 and 0.5 cm^3 volumes at 8, 2.03 and 0.51 mm s^{-1} speed into the 2.5D preform, with the 21G needles. Slurry 2 was used for investigation of the lower injection speeds, volume ranges and different needle gauges. A summary of the input parameters in this study are shown in Table 7. The slurry properties

are detailed in Table 16. The volume and flow rates were chosen to provide wide coverage of potentially useful processing variables.

3.3.4 Injection studies statistical analysis

The analysis selected for the results of the injection study was multivariate regression, via ordinary least squares, Lasso (L1) and Ridge (L2) regression. 10-fold cross validation was performed with the data set in the determination of the optimal value of λ, which was swept through 100 values between 0 and 1. The multivariate analysis was performed in XLSTAT (Addinsoft, Paris, France) with algorithms sourced from glmnet, an R database [232]. The coefficients were all standardised as part of the procedure. The analysis procedure followed is laid out in Figure 12.

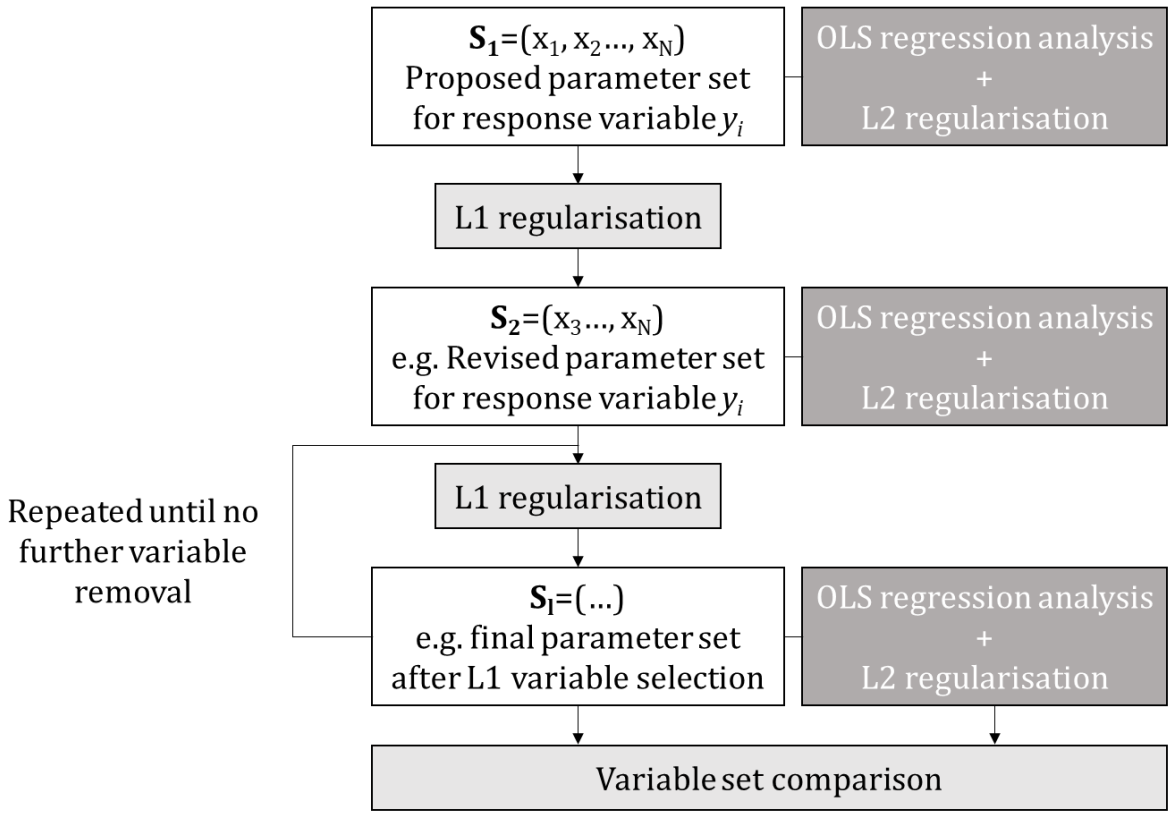


Figure 12: The regression procedure to generate the statistical models for the output variables for the injection studies.

The procedure first defined a trial predictor variable set for a given output variable. L1 regularisation was performed iteratively on this data set, with any variables set to 0 coefficient removed from the analysis. The OLS regression and L2 regularisation was performed on each variable set at every stage for the purposes of tracking the correlation coefficients and L2 penalisation magnitude. This continued until the L1 regularisation no longer removed any variables from the analysis. The parameter spaces produced (coefficients b_j and $\lambda_{1/2}$) were then compared to previous parameter spaces. At this point, the output(Predicted) vs output(real) was plotted to gauge the success of the regression procedure.

The correlation coefficient analysed was the R^2_{adj} value which was determined by Equation 22:

$$R^2_{adj} = 1 - \left((1 - R^2) \cdot \left(\frac{n-1}{n-p-1} \right) \right) \tag{22}$$

R^2 is the regular value for determining goodness of fit (sum of square of residuals normalised by sum of squares from the mean), n is the number of data points and p is the number of predictor variables. The use of this variable was to prevent the automatic and misleading inflation of R^2 as the predictor variable number increases (i.e. reduces the bias inherent in the R^2 value). The models selected were compared based on the penalisation strength λ_i, the R_{adj}^2 and the output(predicted) vs output(real) from the OLS regression procedure to determine the most effective and least biased models.

The standard errors on the coefficient estimates produced by the regularisation procedure were determined using Equation 23. The standardised coefficients were estimated through a scaling procedure, as described by Vittinghof et al. [233].

$$s_{b_k} = \frac{s_y}{s_{X_k}} \sqrt{\frac{1 - R_{YH}^2}{(1 - R_{X_k G_k}^2)(N - p - 1)}} \quad (23)$$

where s_w refers to the standard error of element w, R_{YH}^2 refers to the R^2 value of variable Y against the predictor variable set H ($X_1, \ldots, X_N$) $R_{X_k G_k}^2$ refers to the R^2 value of variable X_k regressed against the set H excluding X_k. The errors of coefficient estimates are derived from the sampling error of the independent variables.

The set of trial predictor variables and the output variables depended on the stage of the analysis. There were a number of input variables for the injection studies and these are shown in Table 8.

Table 8: The original set of input parameters for the injection studies

Material parameters	**Process parameters**
Density (deposit, slurry)	Needle gauge
Surface tension	Plunger displacement speed
Viscosity (determined)	Plunger displacement distance
Contact angle	

These inputs are, to some degree, interlinked. Hence, analysis was first performed on the as-selected parameters to consider the strength of the correlation with more underlying physical features. Subsequently, variables produced by the synthesis of some of these variables were analysed as potential predictor variables. Particularly, needle gauge and plunger speed permitted the flow speed to be calculated by Equation 21. Effective viscosity μ_{eff} was determined from the true shear rate $\dot{\gamma_w}$ from the Rabinowitsch-Mooney equation, combined with Equation 2 to determine the apparent shear rate $\dot{\gamma_{w,N}}$ based on the procedure from reference [234], and knowledge of the Herschel Buckley parameters of the slurries used, Equation 13, to give Equation 24:

$$\mu_{eff}(Q,R) = \frac{\tau_0}{\dot{\gamma_w}} + k(\dot{\gamma_w})^{n-1} \tag{24}$$

$$\dot{\gamma_w} = \dot{\gamma_{w,N}}\left[\frac{3n'+1}{4n'}\right] = \frac{4Q}{\pi R^3}\left[\frac{3n'+1}{4n'}\right]$$

$$n' = \frac{d(\ln \tau)}{d(\ln \dot{\gamma_{w,N}})}$$

The value of *n'* was determined as the gradient of a log-log plot of raw shear stress τ vs raw apparent shear rate. The Rabinowitsch-Mooney equation is used to calculate the deviation in the shear rate quoted by the rheometer as a result of the non-Newtonian nature of the flow in these slurries.

Additionally, the knowledge of the slurry composition allowed the plunger displacement and mass of the deposit to yield the deposit volume (residue) and injected volume (slurry). As these parameters were related to one another, it was important that the variables involved in calculation were not used in the same regression as one another without due consideration to the resulting covariances, as this could have introduced interaction terms not accounted for by the structure of the regression. In particular, slurry identity (S#, a dummy variable) could not be regressed with the actual values of the parameters; the flow speed could not be regressed with the relevant inputs (needle gauge, plunger speed), nor could the effective viscosity be regressed with any parameter used to calculate the shear rate used in the analysis of the viscosity from the Herschel Buckley model without first ensuring that the covariance was not excessive. In some cases, these may not be true interactions, and the large magnitudes of covariance would have increased the standard errors on variable estimates.

Stage one involved the regression of the raw parameters shown in Table 9. Stage two involved the regression of the underlying physical properties of the injection as shown in Table 10. Stage three involved interaction parameters of the underlying physical

properties selected on the basis of proposed physical interactions or due to observed signs and covariance in stages one and two. The specific variable sets for stage three are defined in Table 11 and the combinations detailed in Table 21 and Table 22.

The output variables included the maximum extents in the vertical (H) and horizontal (W) directions, the aspect ratio of deposit in the section as cut (AR=W/H), the maximum value of horizontal extent by layer type (Max R and Max UD), the values of force measured during the experiment (peak, PF, median force, MF and the difference thereof, dF), and the ratio of the Max UD and Max R values, UR.

Table 9: Basic input - raw output (the different needle gauges were included in the regression as separate and mutually exclusive dummy variables).

Input	**Output**
Nominal viscosity (120 s^{-1})- μ_n	Final height- H
Surface tension- γ	Max width- W
Contact angle- θ	Aspect ratio - AR (W/H)
Needle gauge (16, 21, 25, 30G)	Max R extent- mR
Velocity (piston)- v_p	Max UD extent- mU
Displacement (piston)- d_p	Peak force- PF
Residual mass- m_r	Median force- MF
	Max UD / Max R- UR
	Peak – median force- dF

Table 10: Synthesised input - raw output.

Input	**Output**
Effective viscosity- μ_{eff}	Final height- H
Surface tension- γ	Max width- W
Cosine(contact angle)- $\cos\theta$	Aspect ratio - AR
Flow speed- v_f	Max R extent- mR
Slurry volume-V_s	Max UD extent- mU
	Peak force- PF
	Median force- MF
	Max UD / Max R- UR
	Peak – median force- dF

Table 11: Synthesised input - raw output, non-linear with interaction parameters.

Input	Output
Effective viscosity- μ_{eff}	Final height- H
Surface tension- γ	Max width- W
Contact angle- θ	
Flow speed- v_f	
Slurry volume-V_s	
Interaction terms: $\sqrt[3]{V_s}$, $\frac{\sqrt[3]{V_s}}{v_f}$, $\mu_{eff}\sqrt[3]{V_s}$ and $\mu_{eff}^{-1}\sqrt[3]{V_s}$, $\frac{v_f}{\gamma}$, $\frac{\sqrt[3]{V_s}}{\gamma}$, $v_f cos\theta$	

3.3.4.1 Random forest analysis

Random forest analysis (RFA) was also used to qualify variable importance. RFA is a machine learning technique in which random samples of a data set with multiple potential predictor variables are used to produce a range of regression trees. The latter is a classification technique that thresholds certain outputs as a product of the range of input variables in different nodes of a flow chart. RFA constructs a regression tree with a subset of the data, and then defines an error criterion with how well this tree categorises the rest of the data and correlates that with the range of variables that are categorised accurately by the tree. A high error associated with certain variables across a range of randomly generated trees indicates the significance of that variable as a valid predictor for the given output.

3.4 Tow impregnation analysis

3.4.1 Sample preparation

Encapsulated fibre tows of different fibre volume fraction were produced by calculating the required fibre mass based on the nominal inner diameter of the PTFE tubes used as containers. Fibres of the correct length were manually extracted from the 2.5D preform

UD layers. Subsequently, one end of the tubing was split into four 'petals' that were peeled back. This allowed the fibres to be funnelled into the tube easily. After this, they were pushed to the end of the tube and the excess were trimmed. The tubes were then tapped to homogenise the fibres as much as possible, and weighed. This gave the value of mass to calculate the fibre packing. Samples of 60 mm length were produced, with nominal desired volume fractions of 5, 10, 20 and 30 vol%. This last value represented the limit of the handling procedure with regards to maximum density of samples. Issues with this method centred on the packing of some fibres tows; they did not fill the cross section of the tube homogeneously, but a single incredibly large void sometimes existed due to the lack of flexibility of the tube and the 'clumping' of the fibres in the tube. On these occasions the 'vol%' of these samples were not really known. The results of these samples were discounted for this reason, and only those which, visually and macroscopically, seemed regularly packed were used in analysis.

3.4.2 Washburn sorption

The Kruss K100 tensiometer was set to a 0.005 g surface detection limit and a 6 mm s^{-1} surface detection speed for the sample of Al_2O_3-24 slurry, the most wetting tested. Fast data acquisition occurred in the first 2 seconds of measurement. For the variable volume fraction series, the contact time was set to 300 seconds. For the variable time series, a set of ~30 vol% samples were selected and dipped into the slurry for 20, 60 or 800 seconds.

3.4.3 Clogging analysis

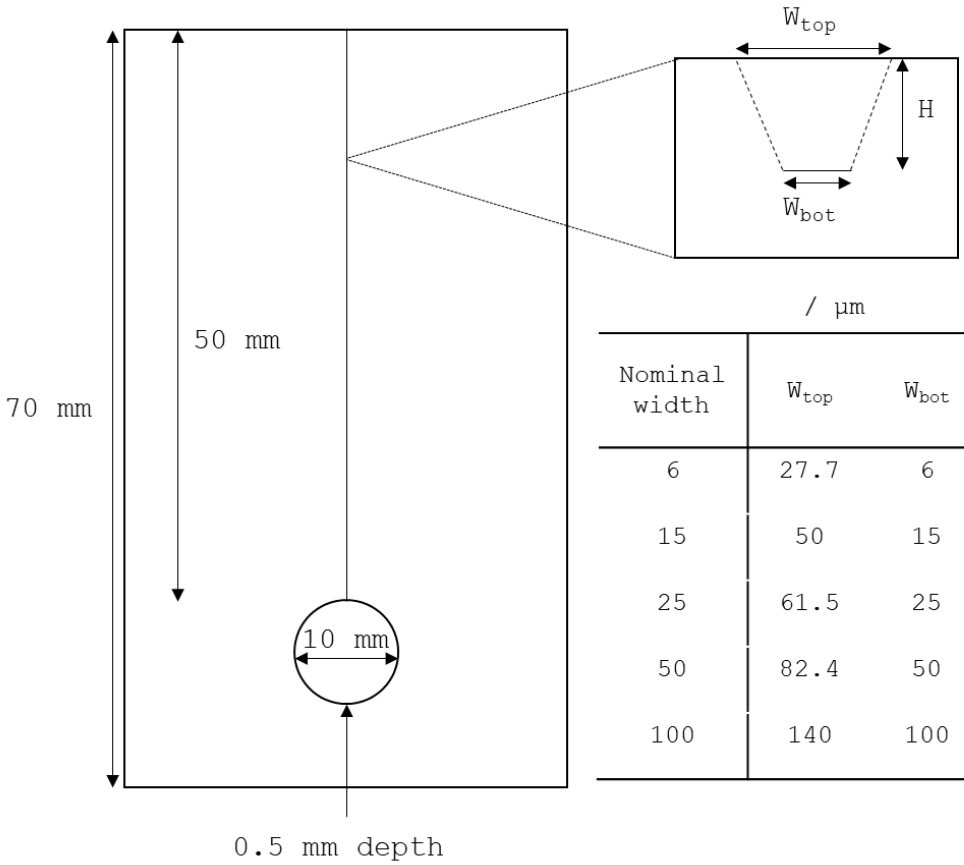
A 32 vol% fibre sample, post sorption, was set in epoxy resin and sectioned at different distances from the submerged end. These cross sections were then examined optically and the fibre, pore and powder volume fractions determined from image analysis with

ImageJ. Two large mosaics of 9 images of the tow at 50x magnification were used in the image analysis of representative areas in the middle region of the tow were selected.

3.4.4 Microchannel flow experiments

Acrylic microchannels were machined by LaserMicroMachining (St Asaph, Wales) to the specification shown in Figure 13**.** The microchannels were nominally assigned desired widths of 6, 15, 25, 50 and 100 μm. However, due to the power distribution across the laser spot, the spot size and the channel widths desired, there was a degree of concavity to the channel walls. The magnitude of this changed as the width increased. This information is shown in the table in Figure 13.

Drops of slurry 24 were added to the reservoir until the droplet formed a convex meniscus in the depression. Samples were left to dry and were investigated using optical microscopy to determine penetration length.



/ µm

Nominal width	W_{top}	W_{bot}	H
6	27.7	6	
15	50	15	
25	61.5	25	20
50	82.4	50	
100	140	100	

Figure 13: A schematic to show the suction microchannels produced for the clogging analysis.

3.5 Numerical modelling

A number of simulations to mirror the injection studies were performed to elucidate the injection mechanism and to develop a potentially effective predictive tool.

3.5.1 Background and modelling procedure

The modelling was performed using the commercial CFD package Fluent, and the mesh created in the Ansys 18.2 software. The details of the computation, discretisation and solution methodologies, can be found in the Fluent user guide [235]. The relevant aspects of the calculation set-up are described below. It should be noted that due to time constraints, a thorough mesh and time-step independence study was not completed and some discretisation parameters were not fully explored.

3.5.1.1 Multiphase injection study simulation

The chosen formulation for the calculation was a transient step-wise multiphase simulation. The mesh was a combination of structured (tubular, preform elements) and unstructured (needle elements and central core) regions and consisted of 525,000 elements. A volume of fluid (VoF) approach was adopted with implicit volume fraction formulation and a sharp interface model. VoF is a method of free surface tracking [236] in which a scalar field α is added to the momentum and continuity equations representing the volume fraction of different phases present in the simulation space. A value of $\alpha=0$ represents a cell filled with phase 1, $\alpha=1$ a cell filled with phase 2, and $0<\alpha<1$ a cell at the interface. In this way, the interface regions can be inferred. The VoF method, being an Eulerian method (and thus considering control volumes of particles and their diffusion) [237], performs convective averaging which can smooth out interface values which can reduce interface resolution [238]. The methods by which the interface is inferred can vary, and are based on implicit (solves for α in the current time step) or explicit (solves for α using a finite differencing scheme based on the previous time step). To combat the loss of interface resolution, sharpening schemes are utilised that determine the flux across cell faces time step-to-time step, to determine how phases are being transferred and to reconstruct the sharp boundary. This requires explicit volume fraction formulations [239], and is often used for determining time-accurate interface shapes and locations [240]. An implicit volume fraction formulation was used for this work, hence a diffuse interface was obtained. This was thought to be adequate, as the flow regime had geometric diffusiveness from the nature of the porous medium. To indicate the extent of the phase extent, an isosurface of slurry volume fraction of 0.7 was used as a pseudo-free surface in post-processing. The porous media formulation was used for the preform

zones. This adds a source/sink term into the momentum equation that modifies the velocity according to the input resistances [241]. This adds both inertial and viscous resistances to flow, and has no effect on the physical structure of the space. The resistances applied are discussed in section 3.5.2. Coupled with the low mesh density and use of a static mesh, it was thought that sharp interface reconstruction would not be physically meaningful and the spread of the volume fraction over space more indicative of the effect of the different permeability tensors, as discussed in Figure 14. Viscosity was determined by the standard k-ε model [242]. The standard model was used instead of the RNG or realisable k-ε models, as the improved treatment of eddy physics and swirls were thought to be unnecessary; the turbulent viscosity generation was set to 0 for the porous regions of the fluid zones, as Reynolds number analysis suggested turbulence would not be likely. Also, the length scale of these structures compared to the porosity size is also unknown. A coupled scheme was adopted for the velocity and pressure determination. This scheme was selected as it is more suitable for coarse meshes such as the one used when compared to segregated algorithms [243]. Pressure was discretised with the 'PRESTO!' regime due to its suitability for VoF [244] and the momentum, turbulent kinetic energy and dissipation were formulated with a second order upwind approach [245]. This was to account for the low mesh density. 35 iterations per time step were found to stabilise the calculation adequately. All parameters were initialised to 0, including volume fraction of slurry.

3.5.1.2 Single phase preform permeability determination

The mesh was unstructured and consisted of 95,000 elements. The calculation was steady-state. Viscosity was determined by a k-epsilon regime with standard wall functions. A coupled scheme was adopted for the velocity and pressure determination.

Pressure was discretised in a second order system, and momentum, turbulent kinetic energy and dissipation were formulated with a second order upwind approach. 75 to 200 iterations were found to be needed to stabilise the outlet mass flow rate as the thickness increased from 1 UD layer and 1R layer (1UD1R) to 11 of each layer stacked alternately (11UD11R).

3.5.2 Geometries and parameters

The geometry investigated for the injection studies is shown in Figure 14 whilst that investigated for the permeability determination of the preform is shown in Figure 15. In each, the layer R corresponds to the random woven layer in the 2.5D preform. It has an input permeability distribution as shown in Figure 14. The K vector denotes the viscous resistance (the inverse of permeability due to viscous forces) and the J vector denotes the inertial resistance as in the Forchheimer equation, Equation 5. The software inputs are inverse compared to 'permeability' and hence this section will use these resistance terms. The mass flow rate, porous flow resistance terms, time step number and duration were varied as per the requirements of the tests. The 'default' terms for these values are listed in Table 12.

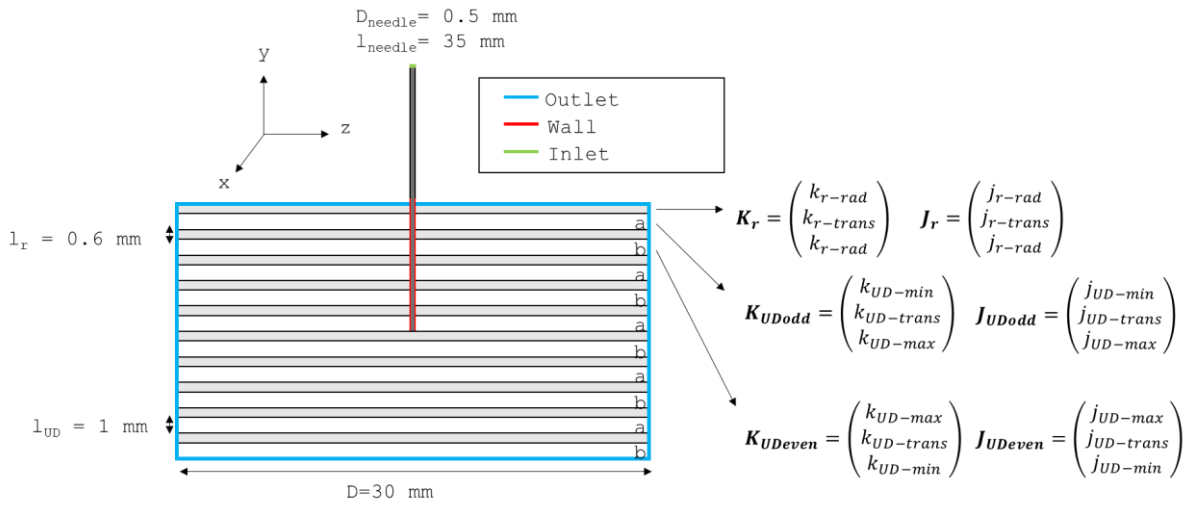


Figure 14: The geometry for the injection studies. It is a two dimensional representation of a cylindrical body.

The simulation space shown in Figure 14 consists of an inlet representing a needle, feeding into the centre of a 'preform' consisting of cylindrical elements of alternating 0.6 and 1 mm thickness. The 0.6 mm thick elements represent the R layers and the 1 mm thick layers represent the UD layers. The permeability tensors used in the study are indicated. There are two types of UD layer in this simulation, corresponding to those in the 2.5D preform with the major and minor permeability axes aligned perpendicularly with one another. This can be inferred from the permeability tensors shown.

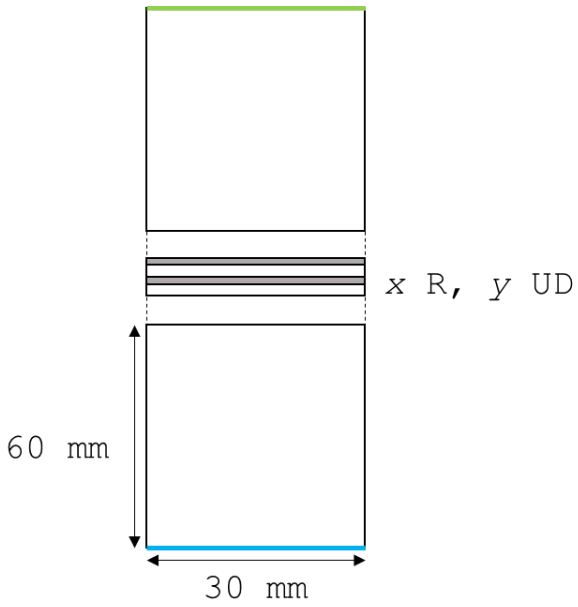


Figure 15: The geometry used for the calculation of the through-thickness permeability of the preform consisting of layers of R and UD elements as in Figure 14.

Figure 15 shows the geometry used for the through-thickness permeability simulations. In this model, there were two non-porous sections above and below the preform of 60 mm length. This was to allow the flow profile to develop fully before and after flow through the porous section.

Table 12: The default calculation parameters for the injection study simulations.

Layer (i)	k_i (viscous) / 10^5 m^{-2}	j_i (inertial) / m^{-1}
r_rad	1.00	316
r_trans	150	3870
UD_min	2.00	447
UD_max	2.00	775
UD_trans	300	5480
MFR	0.001 kg s^{-1}	

For the injection simulations, the time step number was kept at 5000, and the time step duration was varied with MFR so that the total extruded volume was retained at 0.05 cm^3 for all tests. The 'default' values listed in Table 12 were used as the references for the test descriptions in Table 13. The j term for any particular test was calculated by:

$$j_i = \sqrt{k_i}$$

Table 13: The test parameters for the injection studies

Test	Parameter deviations from default
1	N/A
2	3 UD_max
3	100 UD_max
4	0.5 MFR
5	0.5 MFR, 3 UD_max
6	0.5 MFR, 100 UD_max
7	100 UD_max, UD_trans = 5 x 10^7
8	100 UD_max, UD_trans = 8 x 10^6
9	100 UD_max, UD_trans = 1 x 10^6
10	100 UD_max, UD_trans = 1 x 10^6, 3 r_rad
11	100 UD_max, UD_trans = 1 x 10^6, 10 r_rad
12	100 UD_max, UD_trans = 1 x 10^6, 50 r_rad
13	100 UD_max, UD_trans = 1 x 10^6, 100 r_rad
14	100 UD_max, UD_trans = 1 x 10^6, 300 r_rad
15	100 UD_max, UD_trans = 1 x 10^6, 3000 r_rad
16	100 UD_max, 10 MFR
17	100 UD_max (Al_2O_3-2)
18	100 UD_max (Al_2O_3-19)
19	100 UD_max (Al_2O_3-24)

Tests 1-16 were carried out with the viscosity, surface tension and density of Al_2O_3-20 from Table 16. Tests 17-19 were identical to test 3 but performed with the parameters from slurries 2, 19 and 24 respectively. Following this, the whole permeability set was modified to be consistent with values obtained from the experimental analysis of the preform constituents (I_{cf} permeability used for the R layers and STUD permeability used for the UD layers). These properties are shown in Table 19. The slurry properties used were that of Al_2O_3-20. For the permeability determination of the preform, the permeability of the layers were assigned again from Table 19. Air was used as the fluid at a range of flow rates of 1 to 10 $dm^3\ min^{-1}$. No significant differences were found in the final calculated permeability values, hence 10 $dm^3\ min^{-1}$ was used for the full set of geometries. The velocity and pressure fields were determined across the test section and substituted into Darcy's law, Equation 3, and the permeability determined. The permeability was also

calculated from harmonic averaging for series combinations of porous media using a well-established method [246], using Equation 25, and compared to the computational results.

$$K_{average} = \frac{L}{\sum_{i=1}^{N} \frac{l_i}{K_i}} \quad (25)$$

Here, L corresponds to the total thickness, l_i to the thickness of layer i, K_i to the permeability of layer i and N to the total number of layers. The layer number was increased from 1R, 1UD to 11R, 11UD (the whole preform).

3.6 Composite production

C_f/C-HfB_2-ZrB_2 composite samples were produced through an unoptimised route. The samples were intended to be 50:50 volume mixes of HfB_2 and ZrB_2 ceramics, along the central plane of the preform and so they were fabricated by injection of 0.5 cm^3 HfB_2/PR/acetone (72 wt% solids) slurry into the preforms' top surface (R layer) while upside down, with the needle ¾ way through the sample. This was repeated in a 5x5 mm grid across the whole sample and was followed by drying and curing (80, 125°C respectively). Then, the rest of the space was injected until moist with ZrB_2/PR/acetone (62 wt% solids) and dried and cured again. Finally, the samples were pyrolysed in an atmosphere of flowing $Ar_{(g)}$ at 850°C for 3h, with a heating/cooling rate of 1.5°C min^{-1}. The samples were then weighed and measured, and the volume fractions calculated to determine the efficiency and consistency of the method at this stage.

This route was developed from previous works [17, 51], with the transition from 1 cm^3 per grid point injected through the whole preform, to 0.5 cm^3 of different slurries in two halves of the preform, centred at the first and third quarter points.

Samples were produced for the testing regime shown in Table 14 in order to gauge the properties and fracture modes of this layered material as a baseline.

Table 14: The testing regimen used for analysis of the unoptimised samples.

Type of test	Relevant standard procedure	Sample dimensions / mm	Number of samples
Flexural	ASTM C1341	105 x 18 x 18	8
Interfacial analysis	N/A	30 x 20 x 20	1
Thermal analysis	N/A	30 ⌀, 18	5

3.7 Performance testing

3.7.1 Interfacial analysis

Samples were mounted in resin and cut into a number of cross-sections spaced throughout the length of the sample. After preparation for SEM analysis by polishing with diamond suspension to 1 μm grit, the surfaces were measured to yield the distance from the end of the sample. The cross sections were then analysed. Firstly, backscattered electron (Jeol 6060, Jeol, Tokyo, Japan) images were taken of the material interface in the sample. These were analysed qualitatively to demonstrate the shape of the interface within the material. Secondly, energy dispersive spectroscopy (EDS) measurements (Inca, Oxford Instruments, Oxford UK) were made through the thickness for each slice, analysing the powder composition at certain heights to obtain an average ceramic concentration through thickness. The relative signal strength of Hf and Zr was used to determine the concentrations of each material.

The interface location was determined by calculating the depth of the 50% mark based on linear progression of concentration across the interface region. The upper and lower thresholds used were 94 and 6% respectively.

3.7.2 Flexural testing

Samples (105 x 18 x 18 mm) were tested according to ASTM C1341 [247]. A 200 kN load cell was used in conjunction with an Instron 5500R universal testing machine (Instron, Norwood MA, USA). Samples were tested in the flexural mode, using a 3-point configuration. The crosshead speed was 0.26 mm s^{-1}. Flexural strength was determined after the procedure in the aforementioned ASTM. The load rod diameter was 25 mm, and the support rod diameters were 20 mm. The samples were loaded until initial yield in four cases and until significant fracture in four cases.

3.7.3 Thermal testing

A 30 mm depth composite specimen was placed on a laboratory hotplate, the power supply to which was controlled with a thermocouple and a temperature differencing power supply program. The tip of the thermocouple was placed on the hotplate surface and nested in Al foil to ensure as accurate as possible a gauge for surface temperature. Setting the surface temperature to 100°C yielded a temperature average of 130±10°C. No finer control was possible. The sample was placed onto the surface of the plate when the plate temperature had been stable for around 2 minutes in this temperature range. A thermocouple tip was placed on the surface, and an Al foil cap was placed over the top surface of the sample. The logging then began. The heater was switched off when the sample temperature reached a plateau. The cooling was then observed until the temperature of the sample surface was <50°C.

Single phase ZrB_2, HfB_2 samples and a two-phase HfB_2/ZrB_2 sample were investigated by this method. The heating/cooling cycle was observed twice for each single phase sample, and twice for both the upwards and downwards orientation of the two-phase sample.

4 RESULTS AND DISCUSSION

4.1 Starting material characterisation and development

4.1.1 Injection fluid properties

4.1.1.1 Alumina injection study slurries

4.1.1.1.1 Slurry preparation

Table 4 shows the suspensions prepared for the slurry spectrum. The aim of this part of the study was to produce a series of fluids of constant viscosity and variable contact angle/surface tension, and one of constant contact angle/surface tension and variable viscosity. This was to provide an orthogonal data set when it came to the injection studies, so that data analysis could properly separate the input variables. The viscosity and surface tension were used to screen compositions for contact angle analysis; hence there was not a full set of test data for every composition. The procedure, firstly, yielded production of a large set of slurries which were then selected for further compositional adjustment due to their viscosity or surface tension values. Finally, the contact angles of the final set of slurries were measured to confirm that the property spectrum had been properly established.

One main assumption underlying this work is that the physical manifestations of specific chemical differences that may exist between slurries are the relevant interaction parameters at this scale of process. In other words, that the regime is fully described by the macroscopic parameters of viscosity, surface tension and contact angle. There is significant literature support for this assumption. One area that may belie this is the particle size, but this will be investigated in Section 4.2.

4.1.1.1.2 Properties

Figure 16 shows the determined range of viscosities and surface tensions obtained for the test fluids in Table 4. The entries for which both viscosity and surface tension were

obtained are plotted as a property matrix in Figure 17. A number of these slurries were excluded from further testing on the basis of the similarity of their properties to other slurries. For instance, entries 3-9 possessed incredibly similar surface tension and viscosities to one another. These were produced by variation of PVP and Dispex A4040 concentration by around 0.5 wt% in total. This clearly was insufficient to produce the desired property variation.

Slurries were selected from the two perpendicular axes seen on the lower right hand side of Figure 17 for contact angle analysis, Figure 18.

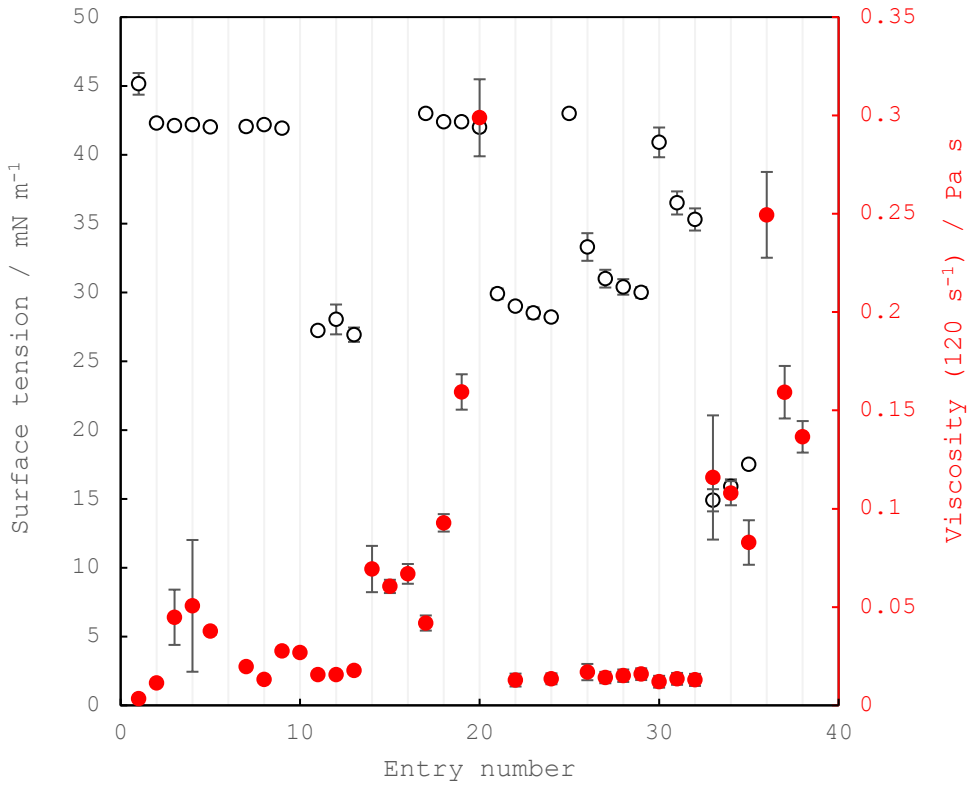


Figure 16: The collated viscosity (at a shear rate of 120 s^{-1}) and surface tension of a number of the slurries shown in Table 4. The increasing entry number shows the chronological development of the obtained compositions.

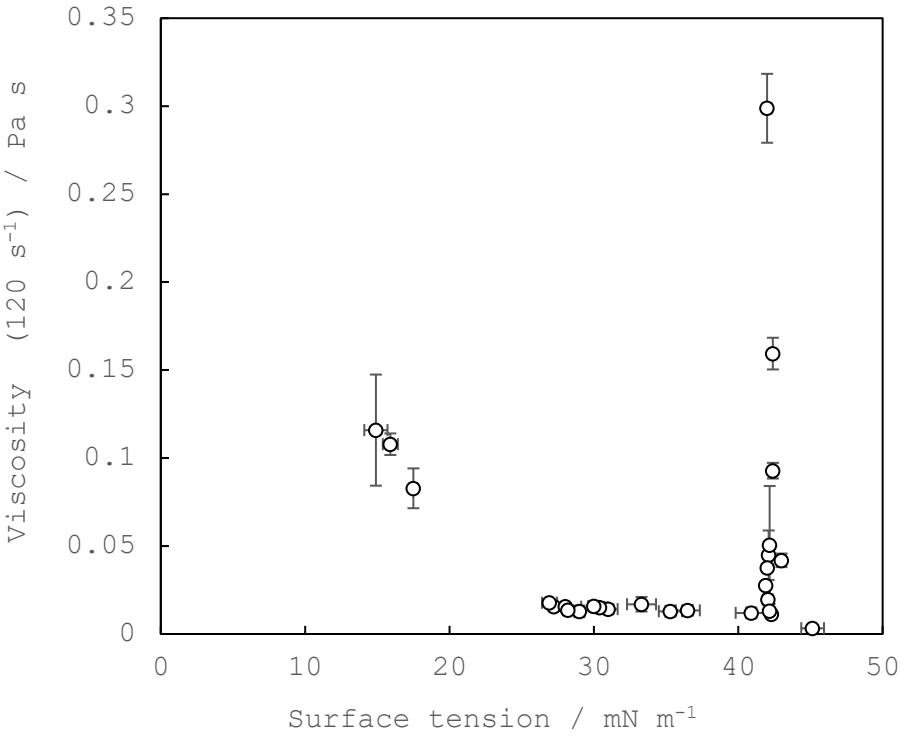


Figure 17: Property matrix for the surface tensions and viscosities of the studied slurries.

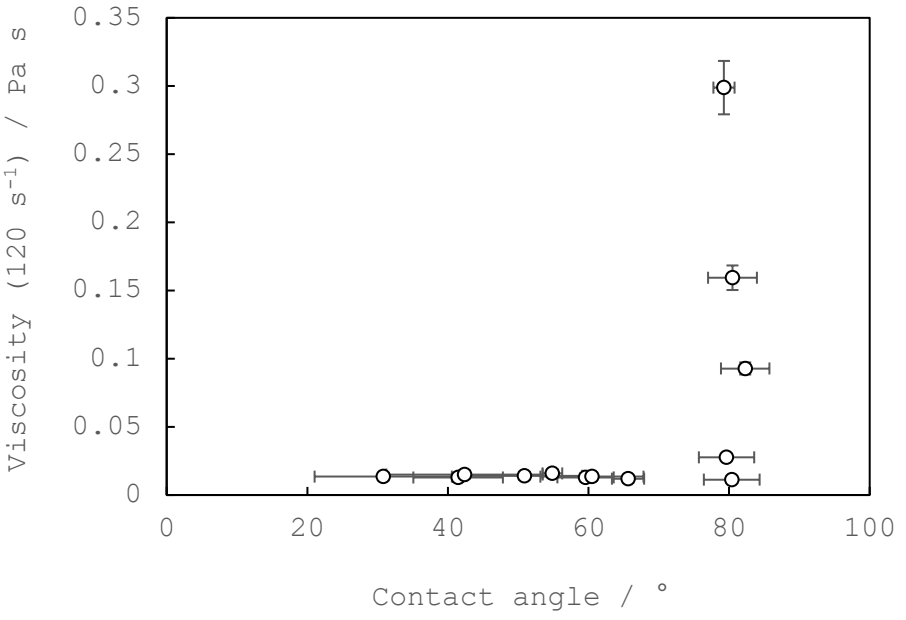


Figure 18: Property matrix for contact angle and viscosities of the studied slurries.

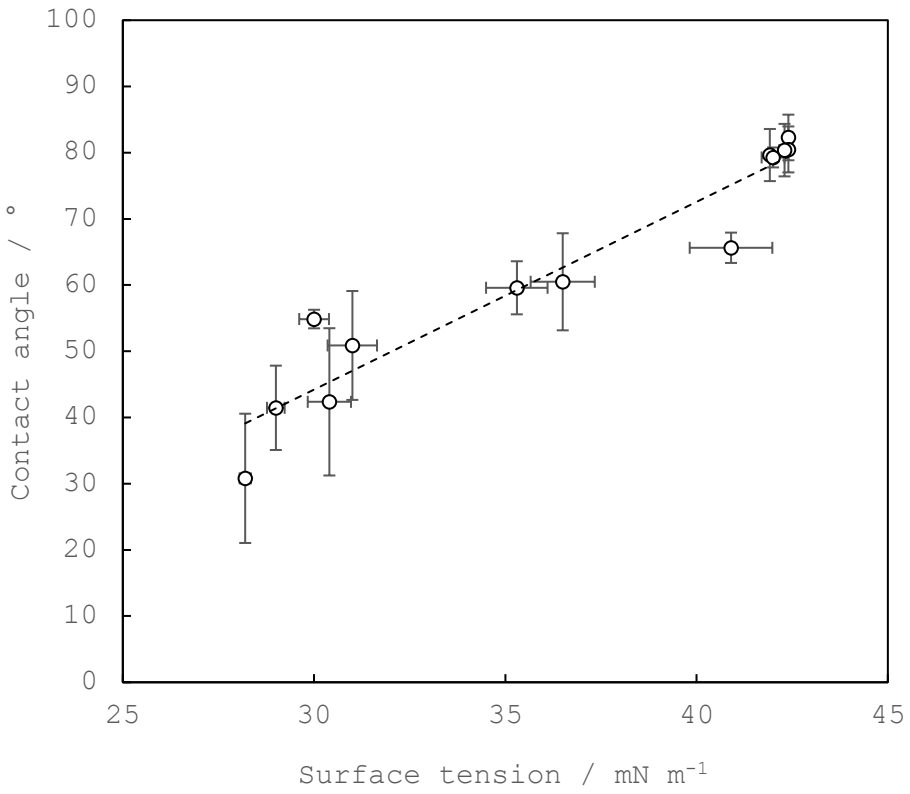


Figure 19: The surface tension of the test slurries and their respective contact angles.

The perpendicular trend of viscosity and contact angle observed in Figure 18 was the desired output of this fluid production section in order to be able to study the effects of orthogonal changes in either property in the injection studies. The selected compositions for taking forward on the basis of the obtained properties are listed in Table 15 and Table 16. One observed trend is that the contact angle and surface tension are linearly correlated in the range investigated. As the concentration of Tween80 is increased, the surface tension (the liquid vapour surface energy, γ_{lv}) decreases.

$$cos\ \theta = \frac{\gamma_{sv} - \gamma_{sl}}{\gamma_{lv}} \tag{26}$$

As the expectation from Young's Equation, Equation 26, is that $cos\ \theta$ will decrease, should the numerator remain constant, the contact angle will subsequently increase. This was found experimentally, hence it is suggested that Tween80 acts mainly at the liquid-vapour interface, and that the contact angle manipulation is based on the reduced surface tension.

This is consistent with its use as a foaming agent in other industries. High surface tension and contact angle will increase the tendency for high fluid shape lifetime, as both entrainment of air and capillary flow will be supressed. Hence, this is a desirable property for this side of the property spectrum used in this study. These are, also, the values the viscous slurries possess, which will endow the fluids with mechanical resistance to deformation.

However, as Figure 19 shows, the contact angle and surface tension are linearly correlated. While this is both expected and acceptable as a physical phenomenon as described above, the multiple regression will have difficulty separating the contributions from either of these variables. This occurs in cases where variables have a high covariance. This may manifest as one variable being assigned far more significance than the other.

Table 15: The slurry compositions taken forward to the injection kinematics testing.

Slurry number	Composition / wt%				
	Al_2O_3	H_2O	Dispex A4040	PVP	Tween80
2	49.62	49.59	0.39	0.39	0
19	49.45	47.11	0.40	3.04	0
20	49.41	46.42	0.41	3.76	0
24	49.55	49.33	0.41	0.45	0.263
27	49.44	49.66	0.40	0.47	0.0253
29	49.52	49.57	0.41	0.45	0.0505

Table 16: The slurry properties from the compositions in Table 1.

Slurry number	Rheometry				γ_{lv}/ mN m^{-1}	θ_a / °
	τ_0 / Pa	k / Pa s^n	n	$\mu_{120/s}$ / Pa s		
2	0.40	0.0081	1.008	0.0113	42.2 ± 0.1	80 ± 4
19	2.3	0.11	1.032	0.159	42.4 ± 0.1	80 ± 3
20	2.8	0.27	1.003	0.299	42.0 ± 0.3	79 ± 1
24	0.76	0.0029	1.198	0.0135	28.2 ± 0.1	31 ± 9
27	0.63	0.010	1.000	0.0141	31.0 ± 0.6	51 ± 8
29	0.72	0.012	0.9660	0.0159	30.0 ± 0.4	54 ± 1

The trends of composition vs surface tension and viscosity are not simple due to the multi-component nature of these compositions. There are three heteroatomic organic additives of differing functionality, the interactions of which will depend largely on the ratio and magnitudes of their concentration in solution. The chemistries of these additives have been discussed in detail in a previous section.

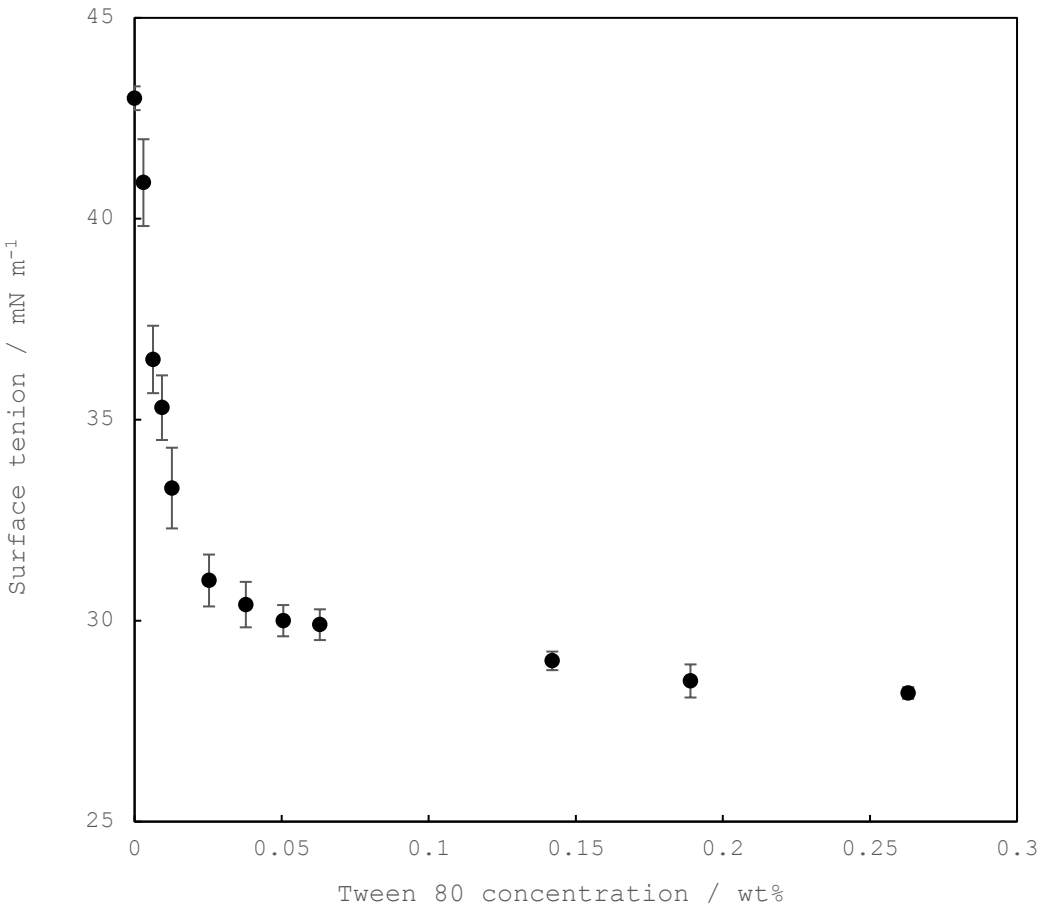


Figure 20: The variation of the surface tension for a series of slurries with varying Tween80 concentration and nominally equal concentrations of other surfactant components and Al_2O_3. The entries are 21-32 in Table 4.

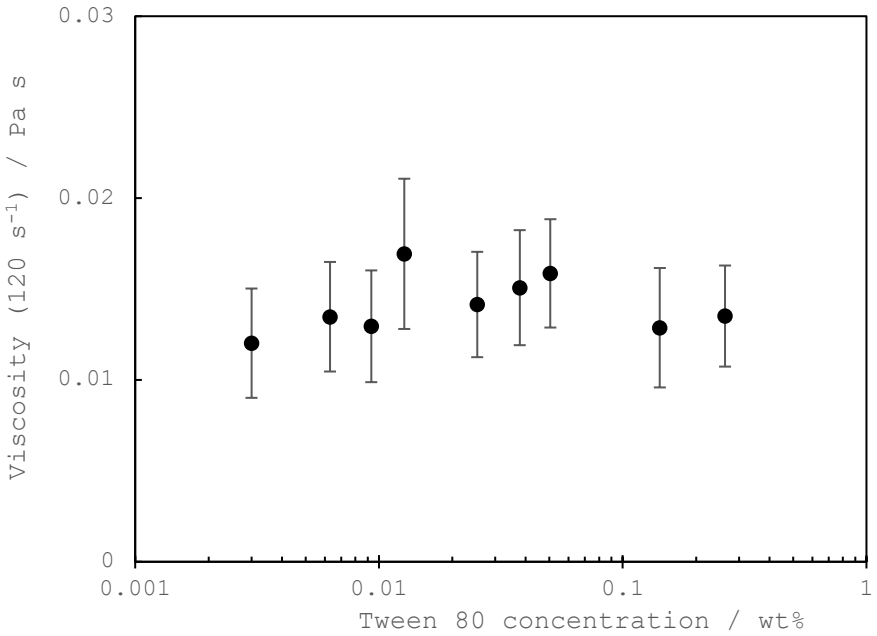


Figure 21: The variation of the viscosity (at a shear rate of 120 s^{-1}) for a series of slurries with varying Tween80 concentration and nominally equal concentrations of other surfactant components and Al_2O_3. The entries are 2, 22, 24, 26-32 in Table 4.

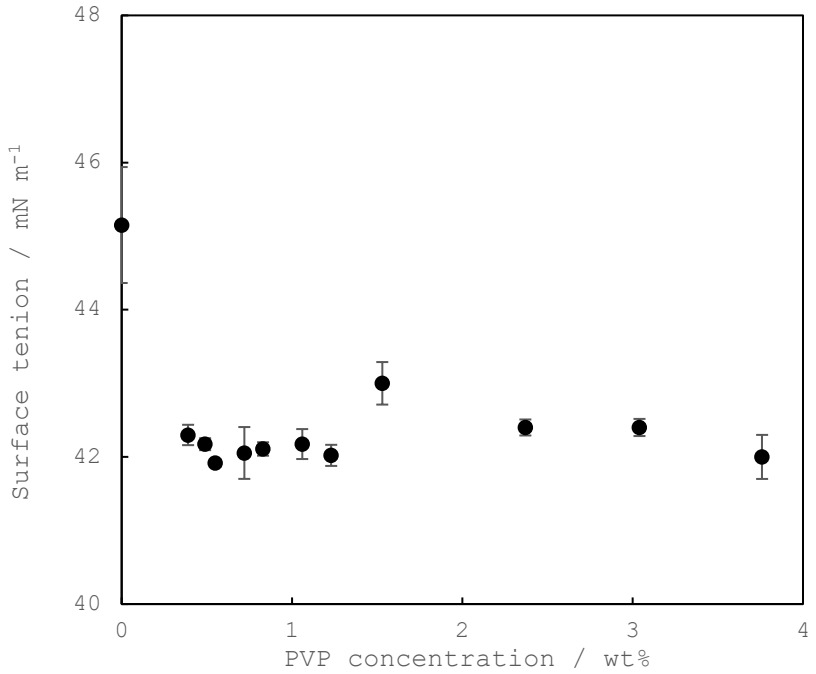


Figure 22: The variation of the surface tension for a series of slurries with varying PVP concentration and nominally equal concentrations of Tween80 and Al_2O_3. Dispex A4040 is varied for 7-9. The entries are 1-5, 7-9 and 17-20 in Table 4.

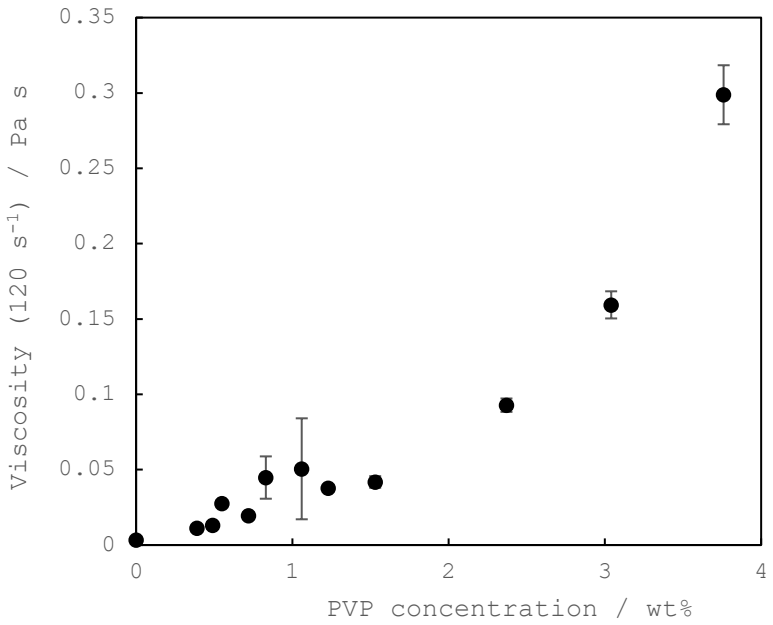


Figure 23: The variation of the viscosity at 120 s^{-1} for a series of slurries with varying PVP concentration and nominally equal concentrations of Tween80 and Al_2O_3. Dispex A4040 is varied for 7-9. The entries are 1-5, 7-9 and 17-20 in Table 4.

The largest variation of surface tension can be seen with Tween80, with an exponential decrease in surface tension to a minimum of around 28 mN m^{-1} at 0.25 wt%. This will coincide with maximum coverage at the liquid-vapour interface. As there is no significant variation of viscosity (at 120 s^{-1}) over this range it can be assumed that there is little structural change in the fluid bulk, hence that the Tween80-Al_2O_3 interaction is minimal, at least at the concentrations of other components. However, the Herschel-Buckley yield stress is found to increase slightly, which suggests that some interaction exists between the Tween80 and other fluid components at low stress. Excluding the first increment in Figure 22, increase of PVP concentration is found to produce little change in the surface tension. The first increment, though lower in magnitude, can be compared to the entirety of the increase in Figure 20, which is over a narrower concentration scale. This suggests that there is competition for liquid-vapour interface alignment between the two additives. Increase in the concentration beyond 1 wt% shows a significant increase in viscosity, Figure 23, and particularly in yield stress.

Considering the range of fluid properties chosen for inclusion in the injection studies, Table 16, there is a span in both rheological and wettability properties. This provides a solid basis for the injection studies in Section 4.2 to proceed. 'Completing the square' found in Figure 18 would have provided a totally non-correlated set of inputs, thus preventing the situation that the high viscosity slurries are all marginally-wetting. As it stands, there is a correlation between contact angle and viscosity that showed in the regression statistics, specifically in the covariance matrices. However, as they do vary independently there is no issue with being able to separate the effect of each variable on the spreading outputs. The covariances are, in this respect, misleading. While separate series of constant highly wetting slurries with variable viscosity, and variably wetting slurries at high viscosity would have provided greater mechanistic information for the injection studies, the lack thereof does not compromise the orthogonality of the inputs.

4.1.1.1.3 Stability analysis

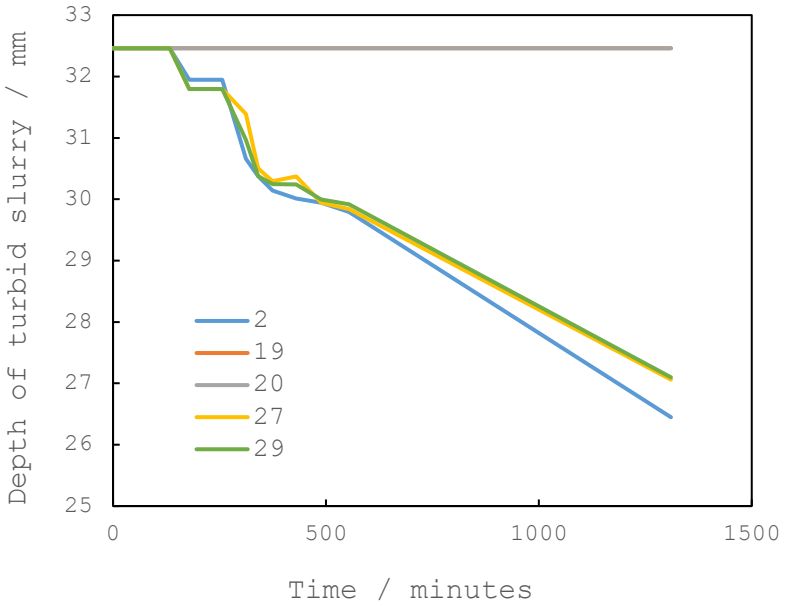


Figure 24: The depth of the turbid section of the slurry below a clear supernatant for a vial of slurry as a function of time.

The analysis of the selected slurries' stability shows that all are stable for a significant period of time, in which there is no noticeable settling or production of a clear supernatant, up to around 2 hours. Following this, some slurries show largely linear sedimentation behaviour in which the supernatant increases at a rate of around 0.005 mm min^{-1}. This shows that there is, therefore, little concern that there will be density and property gradients as a result of the stability over the course of the injection process. Filtration effects are a separate issue and are addressed in Section 4.2. The relatively good state of suspension is a positive indication for industrial utility. Additionally, particle size measurements of these do not indicate the growth of any hard aggregates. The more viscous pair of slurries shown in Figure 24 did not show any sedimentation over the time period investigated.

4.1.1.2 UHTC slurries

UHTC slurries were produced in the same fashion as the alumina slurries. The viscosity was found to be 0.19 Pa s at 120 s^{-1}, with a Herschel Buckley description of τ_0=5.4±0.6 Pa, k=0.53±0.1, n=0.85±0.02.

They were highly shear-thinning with a substantial yield stress. The large pre-exponential factor and small flow index shows that the viscosity is quite variable over the various shear rates during injection.

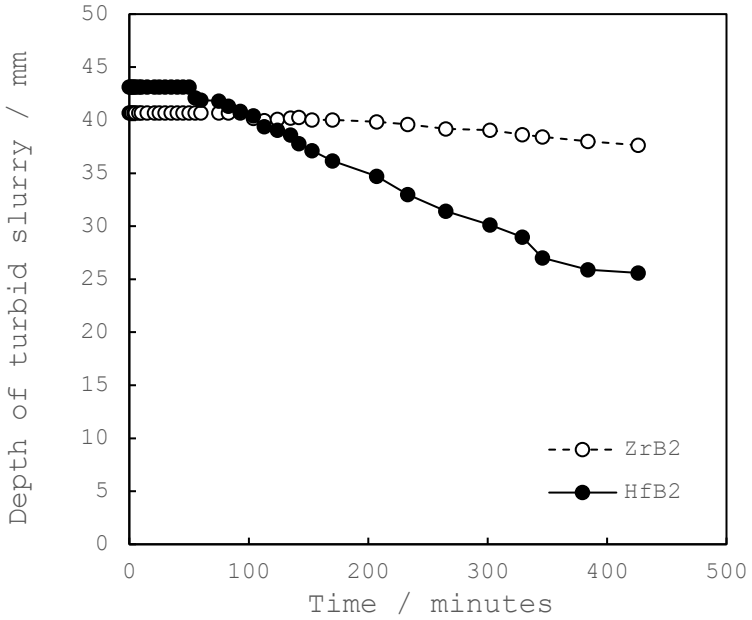


Figure 25: The depth of turbid slurry beneath a clear supernatant for the stability analysis of the HfB_2 and ZrB_2 slurries used in composite production

Considering the stability of the slurries, Figure 25, it can be seen that even given their high viscosity, similar to that of slurries Al_2O_3-19 and 20, they are not stable for a long time. This is due to the substantially larger particle sizes and density of the UHTC slurries compared to the Al_2O_3 case. As both a larger particle size fluid, with greater Bingham-like behaviour, this may complicate the filtration dynamics in the preform when compared to the Al_2O_3 suspensions. The stability of the ZrB_2 is higher than that of the HfB_2 slurry, which is consistent with the difference in density (6.08, versus 10.5 g cm^{-3} respectively).

4.1.2 Preform characterisation

The fibre diameters, densities and fibre volume fractions of the preforms are presented in Table 5.

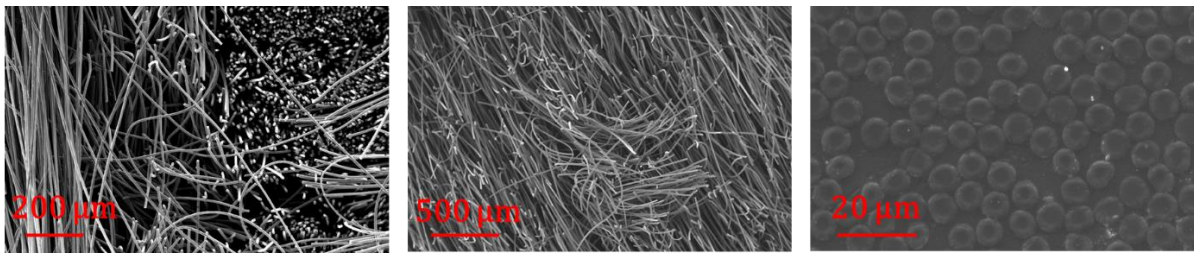


Figure 26: SEM micrographs of (left) the 2.5D preform junction between the 90°, R and 0° layers, (centre) the I_{cf} preform, (right) the microstructure of the STUD layers.

Figure 26 shows the general structures of the preforms/fibre materials used in this study. The general structure of the 2.5D preform is a layered structure with unidirectional and random woven layers interpenetrating to build up the whole structure. The I_{cf} preform is largely isotropic in 2 dimensions, with layers of this web building up the thickness. The STUD fibre layers are structured simply as randomly packed unidirectional layers. An example of the packing is shown on the right of Figure 26.

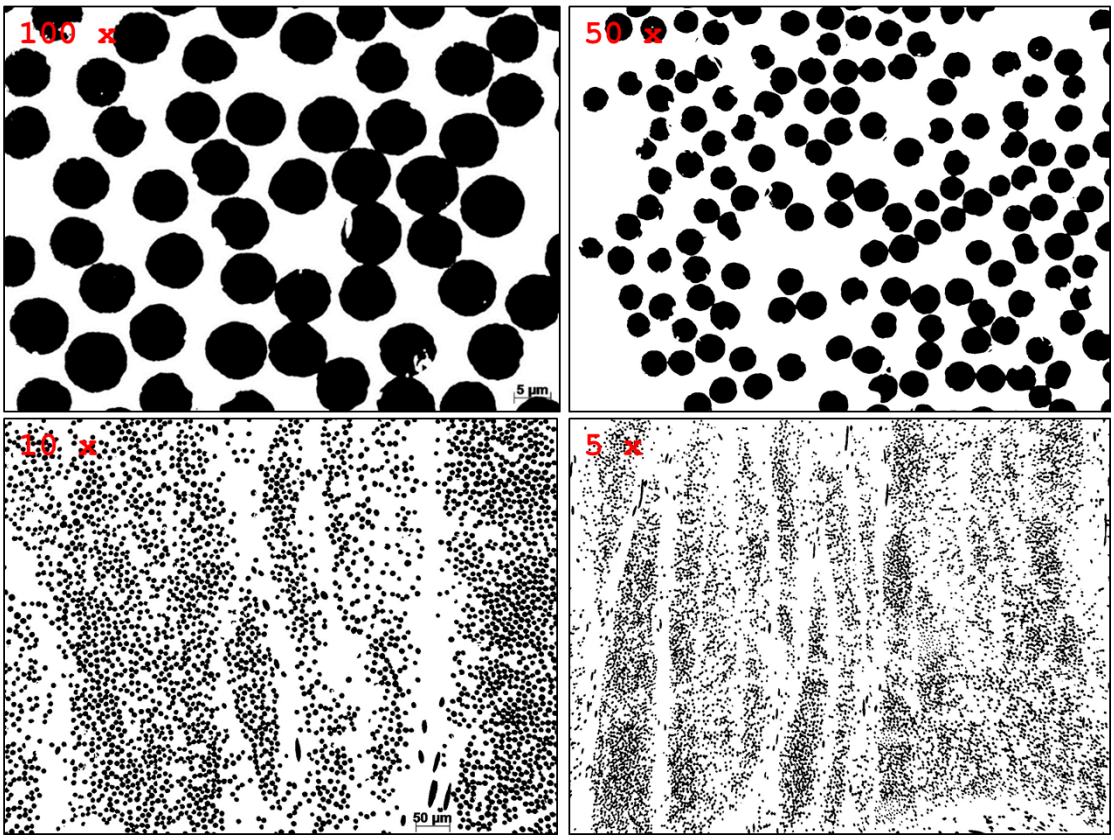


Figure 27: Thresholded and binarised images of the unidirectional layers of the 2.5D preform at different magnifications. 100x and 50x show the general fibre packing structures in the tow. 10x and 5x give a greater indication of the packing of the tows together within the UD layers.

4.1.2.1 Fibre diameter

From particle counting scripts on Figure 27 (100x), a value of 7.2 ± 0.9 μm was calculated for the fibre diameter for the 2.5D preform. This is consistent with the SEM analysis and the SEM value was used to calculation of porosity, fibre density and other related parameters due to the superior detail images having more accurate edge definition for measurement.

4.1.2.2 Volumetric fibre density

Fibre volume fraction is clearly variable at different scales of the fabric. Table 17 details the calculated areal fractions at different values of magnification and in different areas. It can be seen that the maximum packing is observed in the centre of tows at high magnification, over 50%. However, more holistic pictures capturing the nature of the pore scale of the whole layer, such as 10x magnification, indicate a milder value of 27%. Given that the whole preform fibre fraction is 23 vol%, the fibre volume fraction of the R layer can be calculated if the R layer thickness can be determined. From image analysis, the average value of the R layer thickness is 535 ± 45 μm. Using a value of 18 mm thickness for the whole preform and the fact that there are 11 layers of both UD and R fabric in most of the preforms, the rule of mixtures results in a value of 15 ± 2 vol% for the R layer fibre fraction.

Table 17: Areal fractions of fibres thresholded from micrographs.

Magnification	Areal fibre density / %
100x	Centre of tow: 53.4
50x	Centre of tow: 34 ± 2 Near edge of tow: 20 ± 4
10x	Whole image: 27 ± 2 Centre of tow: 33 ± 11

4.1.2.3 Fibre packing geometries

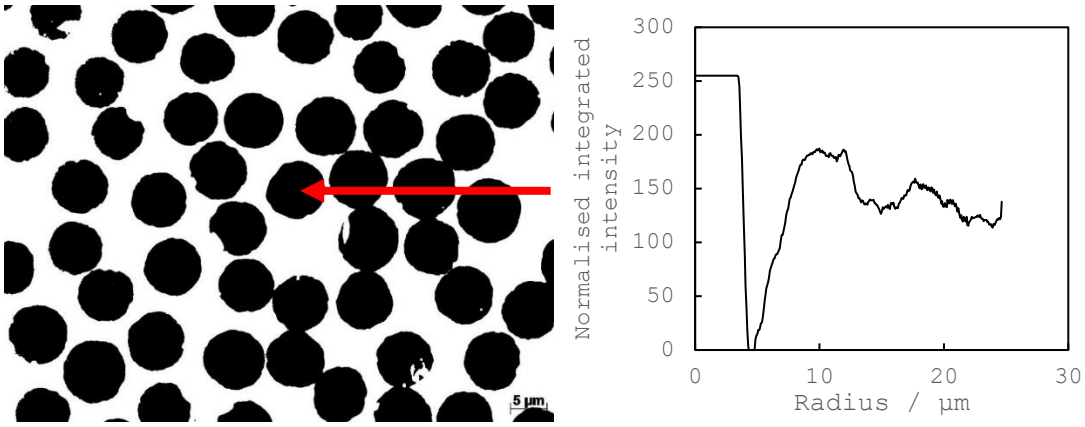


Figure 28: The radial distribution function for a 100x magnification image of the fibre tow, centred on the central pixel of the indicated fibre

Figure 28 shows the radial distribution function for the central pixel of the indicated fibre. The peaks of the graph show the normalised intensity around the central pixel, which in turn provide an indication of the packing. The average value of 255 persists from 0 to 3.47 µm coinciding with the radius of the initial fibre. The drop to 0 indicates the lack of contiguous neighbours. The adjacent local maxima at 10.2 µm has a shoulder at 6.1 µm showing the lack of regular spacing around the central fibre. The width of the peak, around 3.7 µm, indicates a large concentration of fibres across the radius range. The adjacent trough centred at 14.9 µm indicates that there is a lower concentration of fibre pixels in this range. The width of the trough being ~5 µm, which is not consistent with the fibre width, shows there is substantial overlap and non-alignment of the fibre shells, i.e.

that there is no dense packed network and also little structural regularity within the fibre packing. This is an intuitive result from the visualisation, but the radial distribution function is effective at demonstrating it. As a result, it is required to have a more specific statistical investigation of the pore size distribution.

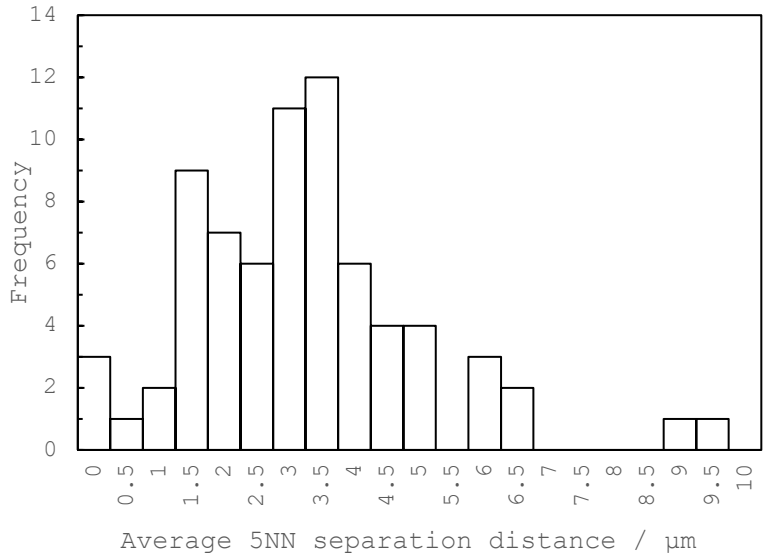


Figure 29: The average 5-nearest neighbour separation distances of the image in Figure 28 (rounded to the nearest 0.5 µm).

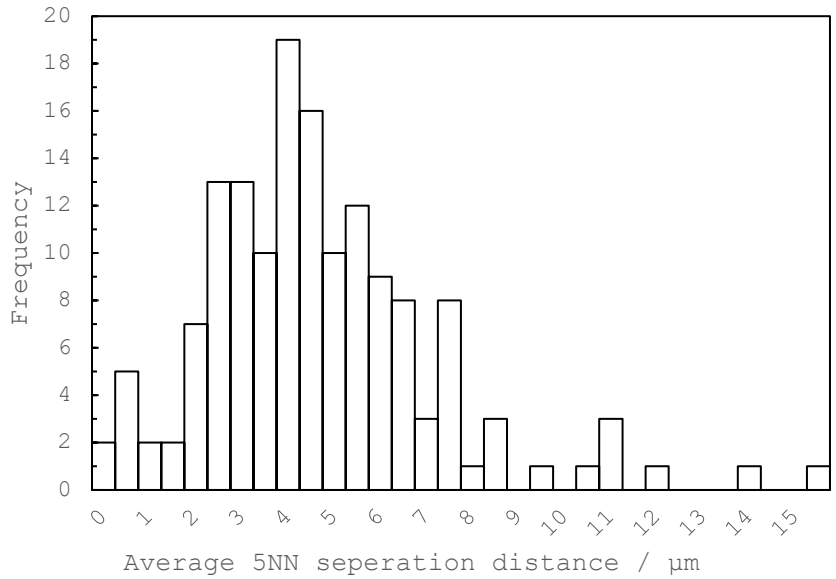


Figure 30: The average 5-nearest neighbour separation distances of a 50x magnification image of a fibre tow (rounded to the nearest unit).

Figure 29 and Figure 30 shows the distribution of averages for the separation distances of every fibre from its five nearest neighbours. These values are interpreted as 'average pore sizes' in the sense of assuming axisymmetric pores through the substrate. Both histograms show peaks at 3-4 μm and are approximately shaped like Boltzmann distributions. Table 18 shows the average descriptive values for these distributions.

Table 18: the mean, standard deviations, medians and interquartile ranges for the distributions shown in Figure 29 and Figure 30.

Magnification	**Mean and standard deviation / μm**	**Median and IQR / μm**
50 x	4.43 ± 2.57	4.06, 2.80
100 x	2.92 ± 1.84	2.77, 1.10

Figure 31 and Figure 32 show the analysis of the intra-tow pore widths for the 2.5D unidirectional layers, and the distribution of pore sizes, respectively. The pore size distribution in Figure 32 is described by a mean and standard deviation of 60.8 ± 24.7 μm and a median and interquartile range of 60.3 and 33.6 μm.

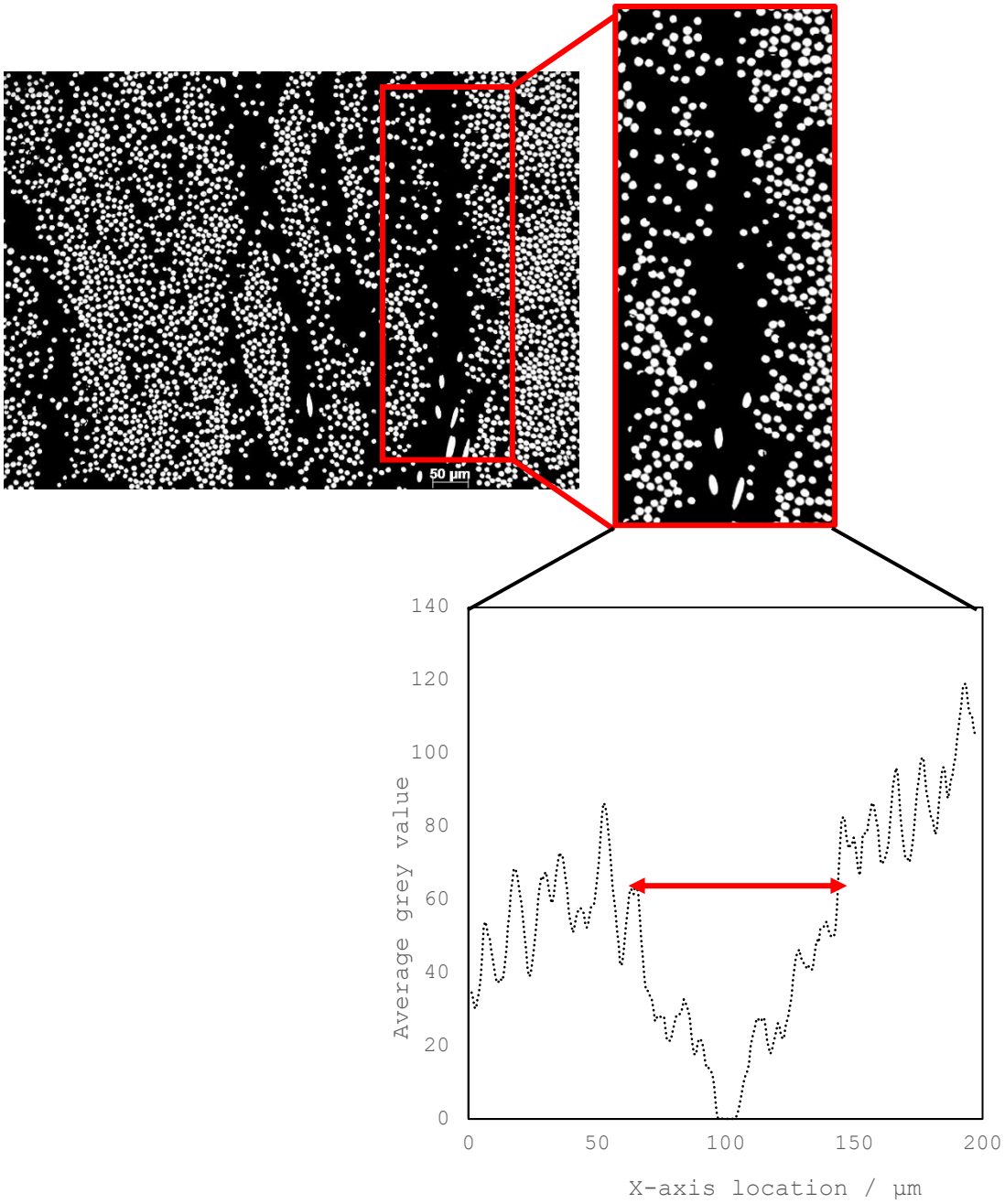


Figure 31: A surface plot of an inter-tow porosity region. The red line indicates the inferred channel width.

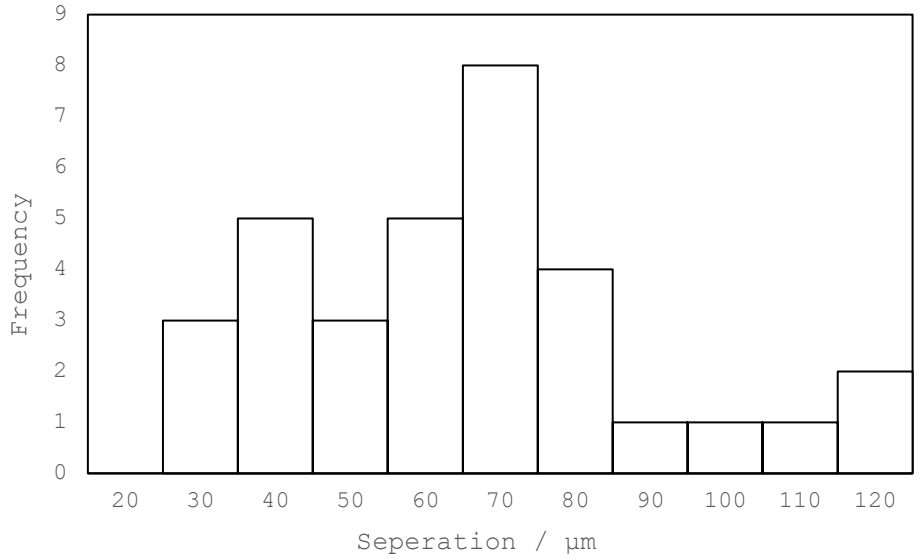


Figure 32: A histogram showing the distribution of intra-tow gaps for the unidirectional layer of the 2.5D preforms.

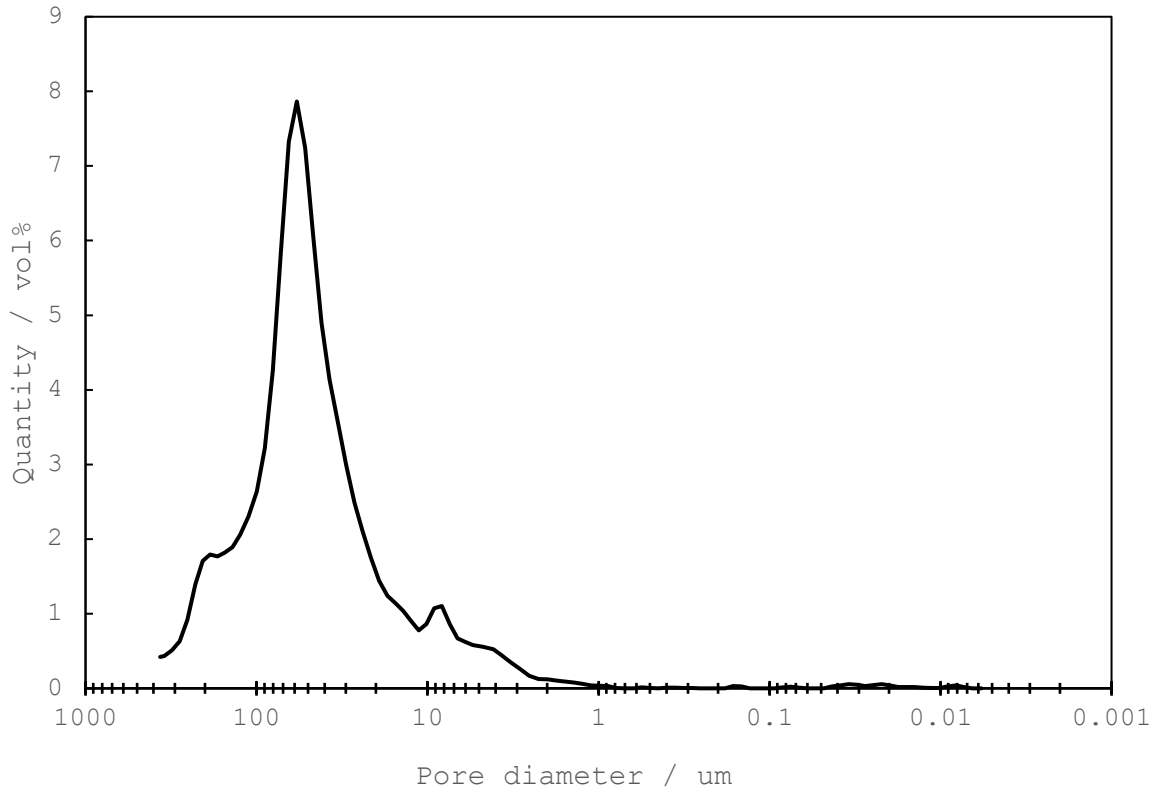


Figure 33: The mercury porosimetry analysis of the 2.5D preform, indicating the volume percentage contribution of each pore diameter

Clearly, there was a substantial degree of variation in pore geometry and width. Comparing the porosimetry results with the peaks in Figure 30 and Figure 32, the peaks

at both 5 μm and around 60 μm can be seen to coincide. As the peak at 60 μm is the tallest and broadest peak in the Hg porosimetry results, it can be seen that the flow through the intra-tow regions in the UD layers is important for the impregnation dynamics. It is also possible that the value coincides with pore sizes in the R layer, given the domination of this peak. There is a significant shoulder at around 200 μm, which will also coincide with the 15 vol% R layer. This space will represent a 'path of least resistance' with respect to pressure driven flows, compared to forced flows through fibre tows themselves, as pressure is related to the fourth power of the radius by the Hagen-Poiseuille equation.

The expected capillary pressures or pressures from assuming Hagen-Poiseuille flow through the pores (idealised as cylindrical pores) can give estimates for the flow through the preform by the slurries. Equally, analysis of the Reynolds number can gauge the effects of turbulence in this system. Using the pore size distributions seen above, the flow speeds predicted from Equation 18 analysis shown in Appendix 1 and the results of the injection studies and tow sorption studies (Section 4.2), these values can be plotted as in Figure 34 and Figure 35.

By use of dimensionless numbers, the flow states expected in different pore sizes and at different flow rates can be determined for reference and in application to modelling.

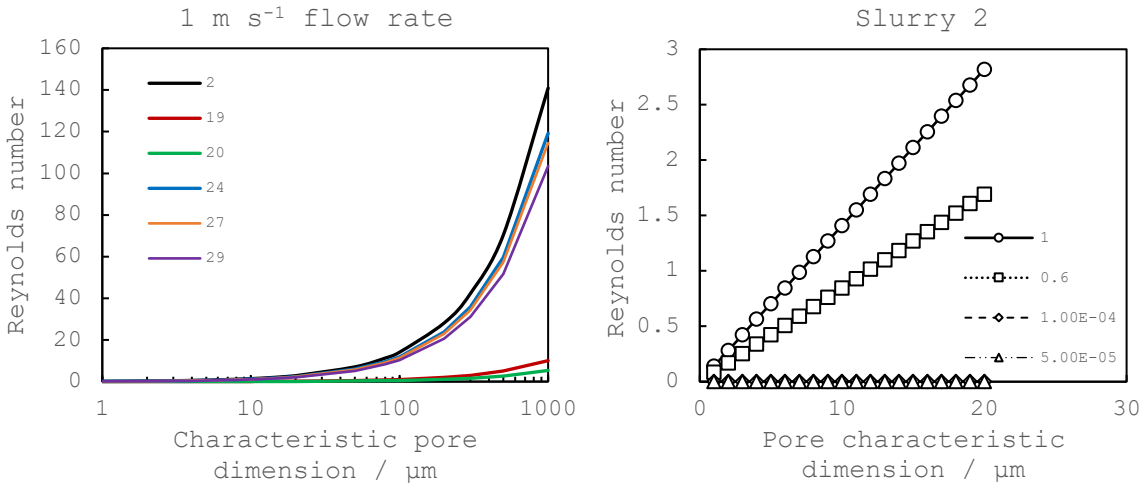


Figure 34: The Reynolds number of flow of the slurries developed for the optimisation studies through the characteristic dimensions indicated, and the flow at different flow speeds (m s^{-1})

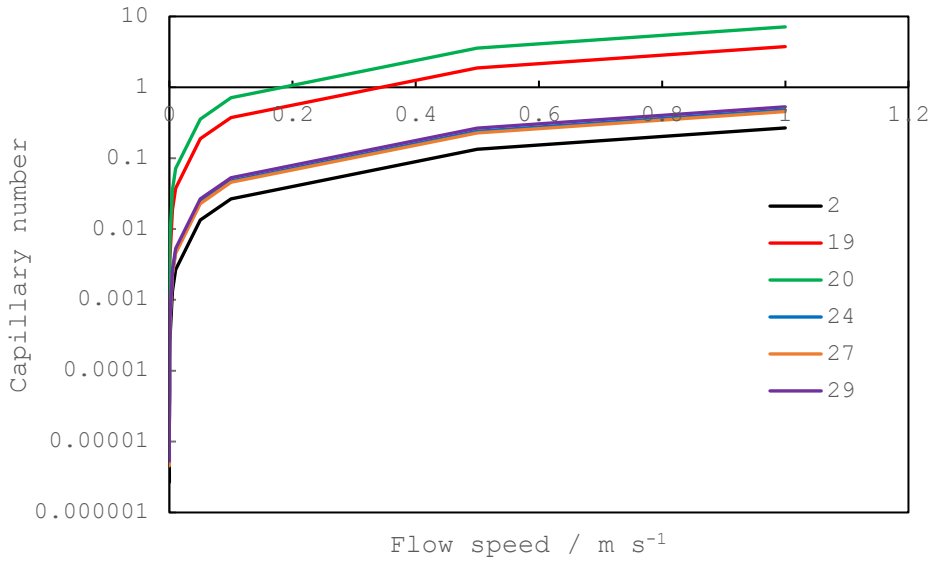


Figure 35: The flow speed (m s^{-1}) effect on the capillary number for the different test fluids investigated in this study.

Large values of Reynolds number correlate with the transition from laminar to turbulent flow, and the values represents the ratio of inertial to viscous forces in a flow. Low Reynolds number consists of viscosity-dominated flow, where consistent fluid motion and smooth streamlines are present. Inertial forces dominate at high Reynolds number and produce vortices and flow instability. The transition value from laminar to turbulent flow

for fully developed flow in a pipe is before 2900 but usually after 2300 [248]. Figure 34 shows that, for the conditions determined for the cases in this study, that the observed Reynolds numbers are lower than this value. In addition, the more viscous slurries have a substantially lower Reynolds number still and are less expected to produce turbulent flow.

The capillary number is the ratio of viscous to surface tension forces, and is usually applied for the behaviour of liquid-gas interfaces and menisci. In this case, it can indicate how relevant surface tension-related forces are for the flow dynamics at the flow speeds encountered. Viscosity dominated flow occurs at Ca values of around 1, whereas capillary dominated flow is indicated by capillary numbers of around 10^{-5} [249]. As can be seen from Figure 35, the slurries will, depending on the flow rate, exhibit the full range of values depending on the flow speed. This is turn will be dominated by the pore geometry and driving pressure. Small pores with slow driving forces will be dominated by the capillary action. The more viscous slurries 19 and 20 consistently have capillary numbers an order of magnitude higher than the lower viscosity fluids, which are more similar to one another. For capillary dominated flow, the associated driving pressure may be approximated via [250]:

$$p_c = \frac{2\gamma cos\theta}{r}$$

where p_c is the capillary pressure in a cylindrical pore of radius r; γ and θ are respectively the surface tension and contact angle of the infiltrant.

These capillary pressures are indicated in Figure 36. This indicates that the flow through pores of radius equal to the intra-tow spacing, 50-60 μm, the expected capillary pressures are around 300 kPa. This is higher than that measured by Li et al. [203], though the fluid properties are not the same.

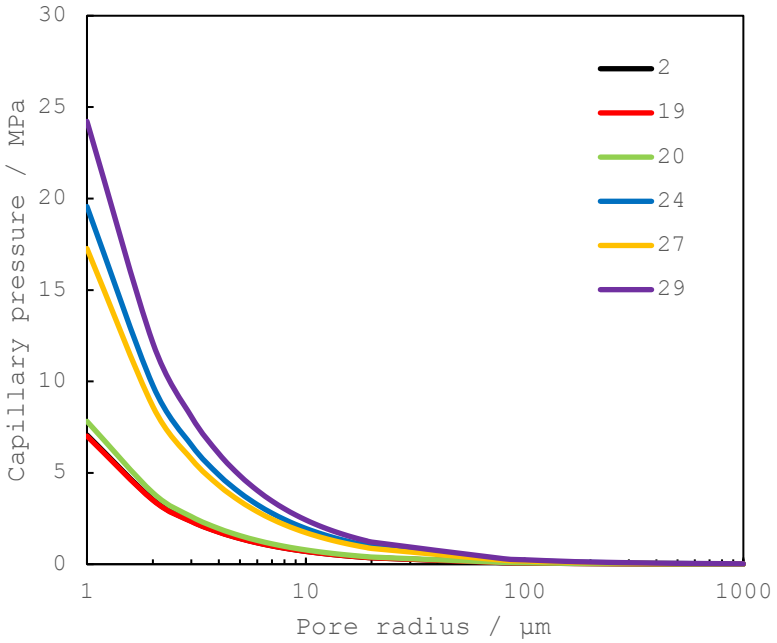


Figure 36: The capillary pressure for unforced flow as a function of pore radius for the spectrum of slurries used in the injection studies.

The analysis of the 2.5D preform has shown that there is scope for both capillary and pressure dominated flows due to the multiple length scales and pressure relations of the different flow regimes: viscous or sorption. The change in impregnation morphology and extent will be expected to relate to the flow through these pathways. The lower input pressure flows of wetting, low viscosity fluid may be expected to percolate through smaller radius pores more easily than through larger porosity. The counter is true for poorly wetting, high viscosity fluids. Equally, the penetration of particulate fluids through these narrow spaces will adapt the flow preferences, due to particle deposition and flow channel constriction. This will be studied empirically in Section 4.2.

4.1.2.4 Permeability analysis

Table 19: The calculated Darcian permeabilities from Equation 19

Sample		K /10^{-11} m^2
2.5D	*Transverse*	9.88 ± 0.04
	In-plane	103 ± 3
Icf	*Transverse*	49.3 ± 0.6
	In-plane	134.0 ± 0.7
STUD	*Transverse*	0.92 ± 0.01
	In-plane: 0°	19.6 ± 1.5
	In-plane: 90°	153 ± 2

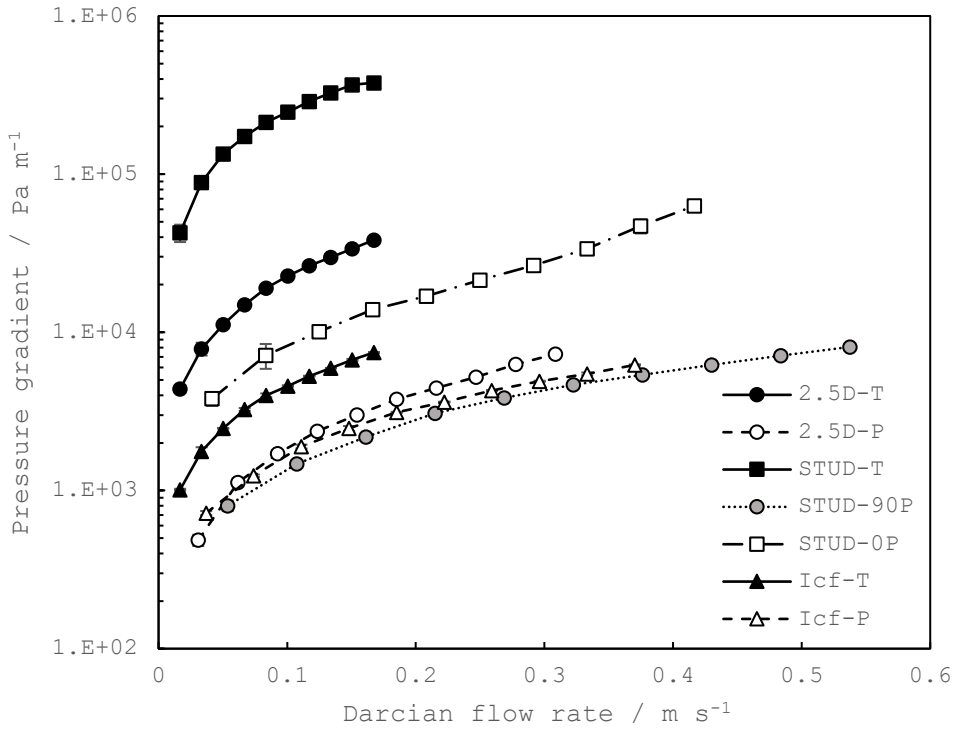


Figure 37: The plots of pressure gradient across the sample vs the argon Darcian flow rate. Each fibre configuration was tested in transverse (T) and in plane (P) mode, with distinction made for the anisotropy for the STUD lay-ups (0 and 90° orientations, 0P, 90P). Horizontal error bars have been omitted for visual clarity, but an error of (50% of the difference between each point per test is standard).

Using a linear fit for the pressure gradient vs Darcian flow rate in Figure 37 to Darcy's law (Equation 19) yields the permeabilities in Table 19. There are, however, some serious deviations from linearity shown in this analysis. Hence, the Hazen-Dupuit equation,

Equation 20, was used for each data set to determine the viscous and inertial contributions to flow resistance. The results are shown Table 20, with the ratio between the Darcy permeability and viscous permeability indicated. The upper limit of the Reynolds number expected in micron-scale pore systems is around 1000, however in larger gaps (e.g. 0.5 mm as may be expected in the R layer), an Re of ~6000 results from the flow rates used. Hence, an investigation of higher order terms is warranted.

Table 20: The viscous permeability k_v and inertial resistance term k_1 calculated from the fit to Equation 20. The ratio of the Darcian permeability (Equation 19) and viscous permeability is shown for comparison.

Sample		k_v / 10^{-11} m^2	k_1 / 10^{-5} m	K/k_v
2.5D	*Transverse*	9.9 ± 0.2	15 ± 45	0.99
	In-plane	142 ± 5	6.5 ± 0.6	0.72
I_{cf}	*Transverse*	49.3 ± 0.6	-3.9 ± 0.9	1.12
	In-plane	134.0 ± 0.7	400 ± 1000	1.00
STUD	*Transverse*	0.80 ± 0.02	-0.05± 0.01	1.15
	In-plane: 0°	100 ± 78	0.57 ± 0.10	0.20
	In-plane: 90°	166 ± 3	57 ± 10	0.92

The deviation from linearity of STUD-0P is compared to STUD-90P in Figure 38. This is the case most obviously non-linear. The second order fit for 2.5D-T is generally poor, and K/k_v is essentially 1. This is also the case for I_{cf}-P. Statistically significant negative values for the k_1 were found. This is mentioned as a potential case from experimentation in the Fluent theory guide [241] but no underlying physical phenomena are listed as explanations. Mohais [251] and Takhanov [252] suggest that such deviations from the fitting may be due to fractures in the walls of porous substrates and may thereby indicate racetrack channels, but this isn't a well-addressed area of literature.

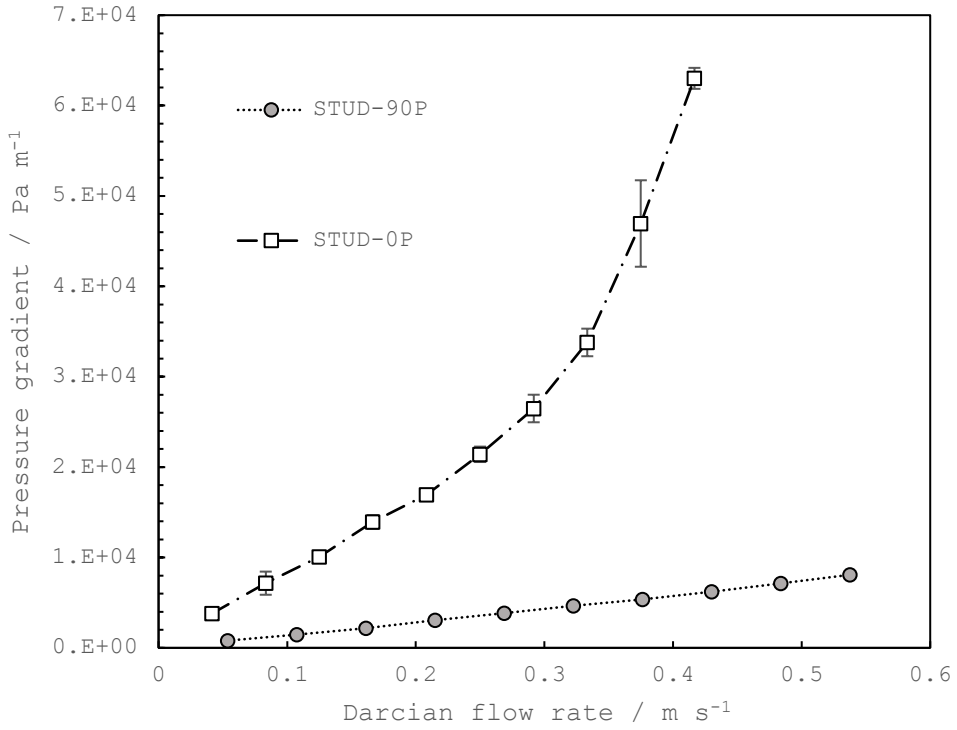


Figure 38: A linear plot of STUD 90P and 0P to show the significant non-linearity.

The permeabilities indicate that the transverse flow through the STUD preform encounters the greatest resistance. It is likely, due to the resin-bonded nature of the fibres and layers, that the flow channels are sealed in many locations and that, therefore, the flow through the thickness is tortuous. The transverse flow through the 2.5D preform also follows this trend. This is understandable, as the UD layers are reasonably tightly packed structures when compared to the I_{cf} layers.

Without exception, the in-plane permeabilities are found to be higher than the transverse permeabilities. This is understandable, as there are linear flow channels in all of the preforms in the radial planes. This will even be the case in the STUD-90P, as there will be gaps between the fibre layers. This suggests that viscous-based flow through preforms should be biased in the radial vs transverse direction. Interestingly, the viscous permeability and the k_1 along the fibre direction was found to be lower than across the fibres for the STUD preforms. This is unlike the results found by Gebart [197] and many

other authors, and may indicate that there was significant gaps between these layers, as the inertial aspect of the permeability was low; something expected in higher Reynolds number flows, which here would indicate large pore sizes.

Excluding the across-fibre direction of the STUD, flow through the I_{cf} preform had the lowest resistance from the linear fit. Transverse flow had a lower permeability than the STUD-(90/0)P. As a laminate of short-cut fibre layers, there is very low volume fraction (4%) of fibres aligned in this plane, and no structures running perpendicular to the flow direction. Hence, flow through this layer is found to be facile when compared to the other architectures.

The comparison between the linear and quadratic fit permeability results shows that, in most cases the linear fit produces similar results with lower standard errors. The only significant deviations are 2.5D-P, STUD-0P and STUD-90P. These layers, as described, have statistically significant values of k_1 which suggests that the deviations from linearity could be due to anisotropy in the layer gaps (either in the STUD layer gaps or the 2.5D R layer) and the subsequent generation of turbulence. In general, the K and k_v values are similar, and where they are not it is indicated by the data and comparative Re number analysis that turbulence may be generated in poorly laminated test pieces. Primarily, the STUD-90P and 0P values should be used with some caution.

4.2 Flow studies

4.2.1 Empirical injection studies

4.2.1.1 Injection of air from the syringe

An example of the depression of the empty syringe is shown in Figure 39, for a depression speed of 4.06 mm s^{-1}. The peak force is defined as the initial force to begin piston movement, and the average steady force is the median force. The depression forces

associated with empty piston depression are shown in Figure 40. It can be seen that the required force decays quite substantially as the depression rate increases for the steady state force, while the peak force tends to increase linearly at higher depression rates.

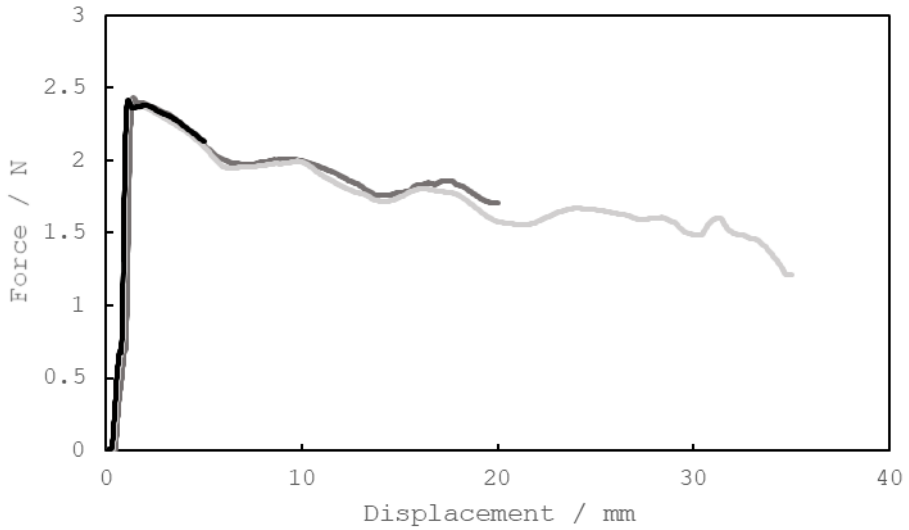


Figure 39: An example of the force-displacement characteristic for a depression rate of 4.06 mm s^{-1} at 5 (black line), 20 (dark grey line) and 35 mm (light grey line) displacement.

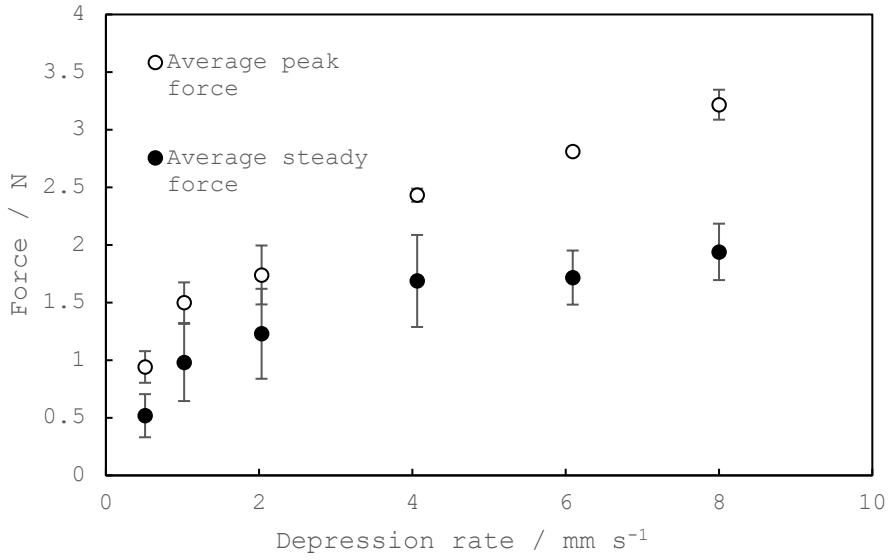


Figure 40: The force required to begin the piston's movement (unfilled circles) and to keep the piston moving (filled circles) averaged across all total displacements (5, 20 and 35 mm).

These are more clearly pictured in Figure 39, and this figure archetype constitutes the majority of the calibration F-d characteristics.

Breaking Figure 40 down into the constituent depression distances results in Figure 41.

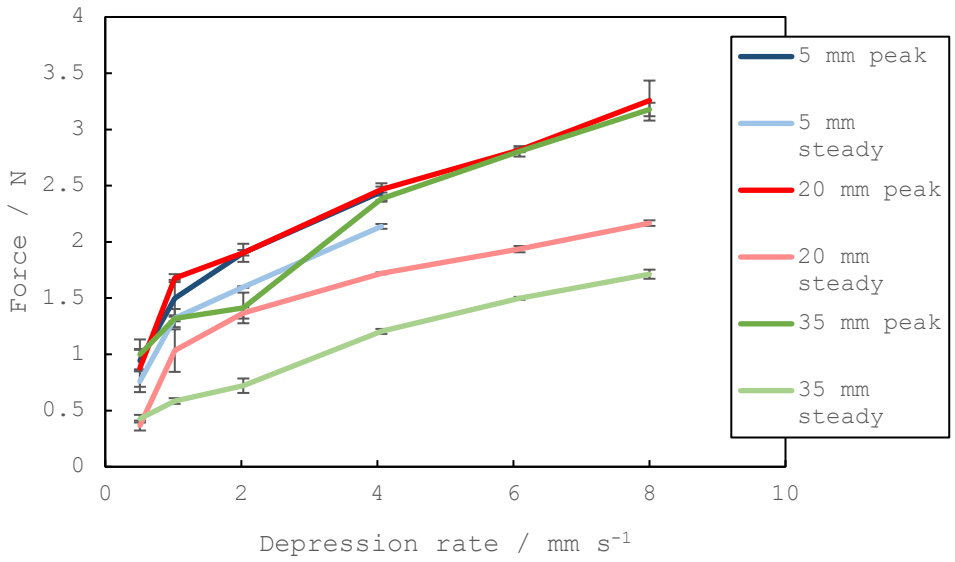


Figure 41: the results of Figure 40 broken down into the constituent depression displacements.

The peak forces are high, but do not depend greatly on the depression displacement. This stands to reason, as the force will be a function of surface contact and rate of movement, and will be a location-defined property. The steady forces, however, decrease as a function of the distance, which suggests that the sliding friction is obtained at a limit of distance.

This analysis shows that the shape of the F-d characteristic is reasonably variable. This stands to reason. There will variability in how the plunger sits in the syringe, how the syringe sits in the mount (there is little movement but at this level of sensitivity any movement of the crosshead that translates to rotation or rocking in the mount will be recorded). Equally, the exact curve shape insofar as it relates to the viscosity, the viscous dissipation, the inertial change of the fluid state and so on is unknown. All that was hoped to be gained was some understanding, at this stage, of the system's response to compression. The curves and behaviour will be used to analyse any interesting behaviour seen during the injection of material into the preforms themselves.

There is some inconsistency in the force measurement in the syringes. Figure 42 shows the F-d characteristic for a 6.09 mm s^{-1} syringe depression rate.

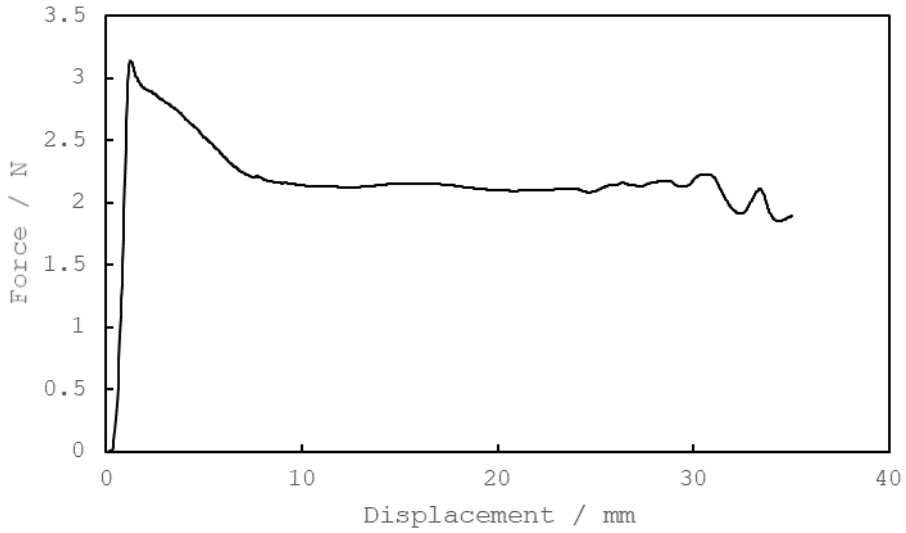


Figure 42: An F-d characteristic in which a peak is seen coinciding with initial contact with the plunger, followed by a plateau corresponding to the steady sliding force of the piston in the syringe. An uneven region is observed at large displacements for most samples.

It is unknown what the bumpy unstable region after 30 mm in Figure 42 relates to. These are only prevalent in the medium-fast displacement rates of 4.06 and 6.09 mm s^{-1}. This suggests it could be related to some form of angular instability due to the alignment of the syringe in the supportive baseplate. As the piston pushes lower into the syringe, any misalignment in the holder is likely to cause rotation or movement of the syringe relative to the baseplate. Slower rates may increase the feature so that it does not manifest as bumps but as distinct ending positions for the graph. This demonstrates the variability associated with the syringe in the force-displacement trace.

4.2.1.2 Fluid injection into air

Injecting water from the syringe through increasingly narrow needles was found to have a significant effect on the force required, Figure 43. As the needle gauge increased (and radius thereby decreased), the force for both initial and steady movement increased. The

jump from 25G to 30G was significant, and the steady motion force for 30G exceeded the peak force of 25G at almost all depression rates above 1.02 mm s^{-1}.

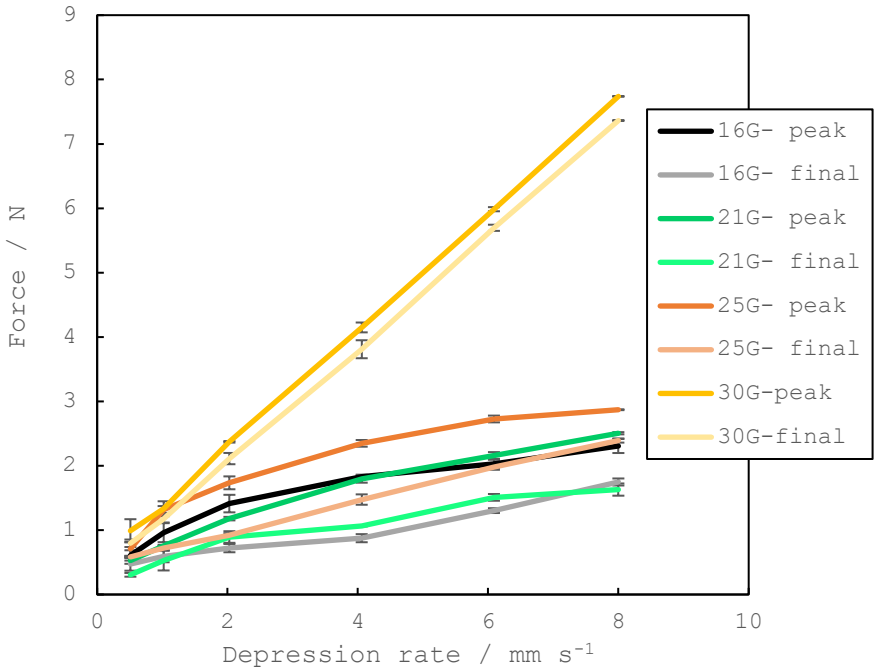


Figure 43: The force-depression rate relationship between for depressions of 35 mm of water from syringes with different gauge of needle.

Determining the linear flow speed from, Equation 21, and comparing the flow of slurries at different injection conditions, the influence of the slurry viscosity can be seen, Figure 44.

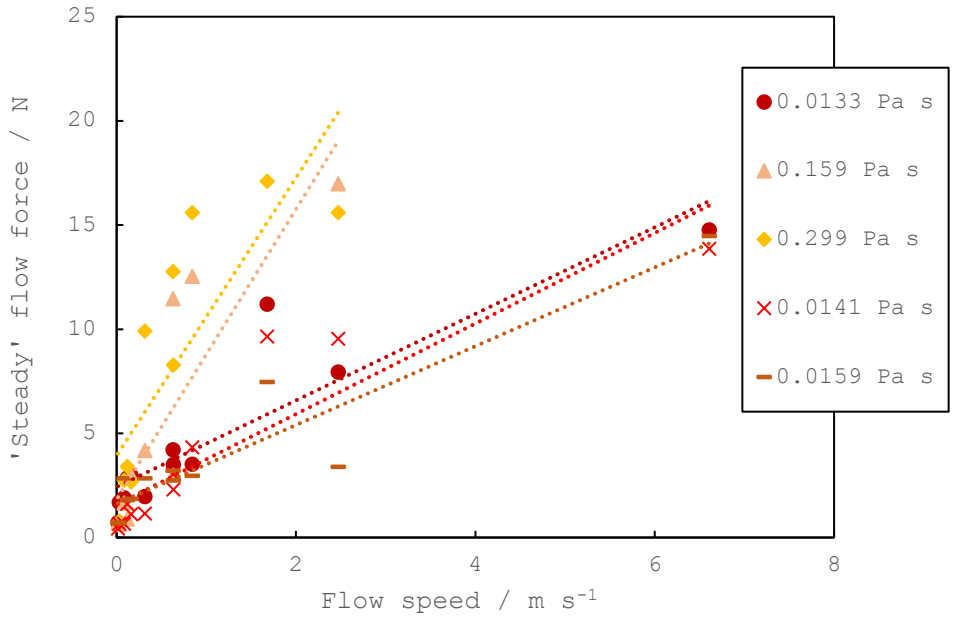


Figure 44: The relationship between the stead flow force and the linear flow speed of the fluid from the needle. The viscosities of the different investigated slurries are indicated.

Figure 44 indicates that the steady flow force required increased with increasing linear flow speed for the slurries, and that the larger the viscosity of the slurry, the greater the force required for a given flow rate. This matches the prediction of the Hagen-Poiseuille equation. Taking the linear flow speed on exit from the needle tip and viscosity of the various slurries, a multiple regression was performed to determine the effect of each on the initial and steady forces respectively. The results of this are shown in Figure 45.

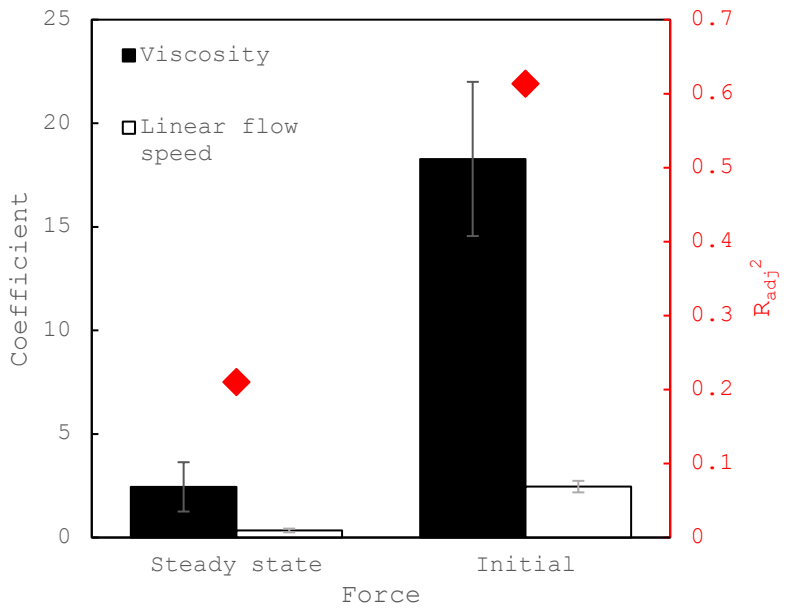


Figure 45: Multiple regression statistics for the effect of viscosity and flow speed on the initial and steady compression forces.

The results of this regression show that the viscosity is influential in both the initial and steady state forces, and the effect of the linear flow speed is mostly concentrated in the initial force. However, the values of adjusted R^2 for both of these variables are low (0.2 in the case of steady flow), which indicates a large degree of variability is not accounted for by these variables. It is likely that this variation is due to the nature of the specific surface treatments and states of the interior of the syringes and the orientation of the syringes. Surface quality has been associated with plunger sliding friction, and significant particle adsorption could occur in this system. This would add a not negligible element of structural disjoining pressure, which would need to be overcome both to induce plunger movement and also to continue moving. Uneven amounts of particle coating would add a stochastic element to the F-d trace.

The results of the calibration analysis suggest that there is a significant degree of error in the measurement of the force in the needle. This is mainly due to two sources: the uncertain interior surface of the needles used and the possible alignment issues of the

needle in the holder. In either case, the variability is unaccounted for and therefore calculations of shear-rate or sliding friction will not be made for this data. Equally, it is unlikely that the F-d traces will yield useful kinematic information concerning the flow resistance during the progression of the injection.

4.2.1.3 Substrate injection studies

4.2.1.4 2.5D preform

The injection of slurries resulted in two different general morphologies. A simple graphical representation of the effects of all the variables is not possible, as there are many and they are interconnected. However, Figure 46 shows the two structures observed most frequently. (a) shows what is termed the 'alternating brick stack' structure, with high aspect ratio flows along the principle directions defined by the UD layers, so named as it bears a resemblance to long blocks stacked in a 0/90° orientation to one another. There is minimal apparent slurry occupancy in the R layers. This flow is often (though neither exclusively nor exhaustively) seen for highly wetting, low viscosity and low injection speed conditions. (b) shows a more regular ellipsoid, with higher R layer occupancy and a more gradual shape change as the depth changes, with greater cylindrical symmetry. This, again, is loosely correlated with high viscosity, poorly wetting slurries and high injection speeds. However, the shape and extensions require more systematic analysis against the whole input parameter set. This is performed via multiple linear regression, using OLS, L1 norm and L2 norm regression techniques.

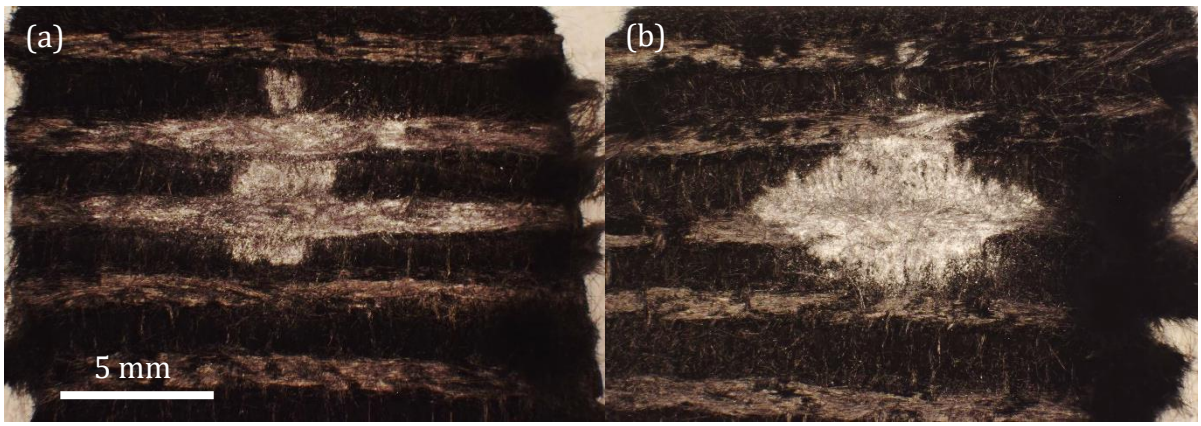


Figure 46: General shapes produced by the injection of different slurries at different volumes and injection speeds. (a) an 'alternating brick stack' structure, with the largest dimensions being narrow channels along the principle UD axes and (b) spheroid/ellipsoidal structures.

The following sections detail the multivariable statistical analysis results for the output variables measured from the injection morphologies and the input variables indicated in Table 8.

4.2.1.4.1 Linear analysis

The L1 norm regression procedure resulted in the input-output distribution shown in Figure 47. The top layer shows the separate output variables that were regressed individually with the input variable set in the white box. Dropping down, the grey boxes show the variables that were found to be useful predictor variables in L1 regression. Subsequent L1 rounds yield further grey boxes and the flow chart branches end with the R_{adj}^2 value determined by normal OLS. From this procedure, only three outputs correlated well with the inputs ($R_{adj}^2 > 0.6$), and even given this, the correlations are not particularly strong. These are H – deposit height, W – deposit width and mU – the maximum UD layer deposit width, which is a subset of W in most cases. The predictor variables explain 60, 65 and 61% of the variance, respectively, in the output. H is not found to be influenced by viscosity or contact angle, meanwhile W is found to be uninfluenced by the surface

tension. It is, however, explained by the contact angle and so does involve some surface phenomena. H being uninfluenced by viscosity is interesting, as viscosity is a key parameter in porous flow problems. It is possible that the magnitude of the difference of the viscosity was insufficient to accommodate for the through-flow resistance at the investigated pressure range. Analysing the low R^2 value outputs is potentially misleading. However, the differences between the median and peak compression forces are found to correlate with 25 and 30G needles exclusively. Given that these two dummy variables are sufficient to produce an R^2 of 0.43 suggests that they are strongly correlated with the high variation seen in forces, and that whatever mechanism causes the spikes in injection force are strongly exacerbated by the physical bottleneck these narrower needles represent.

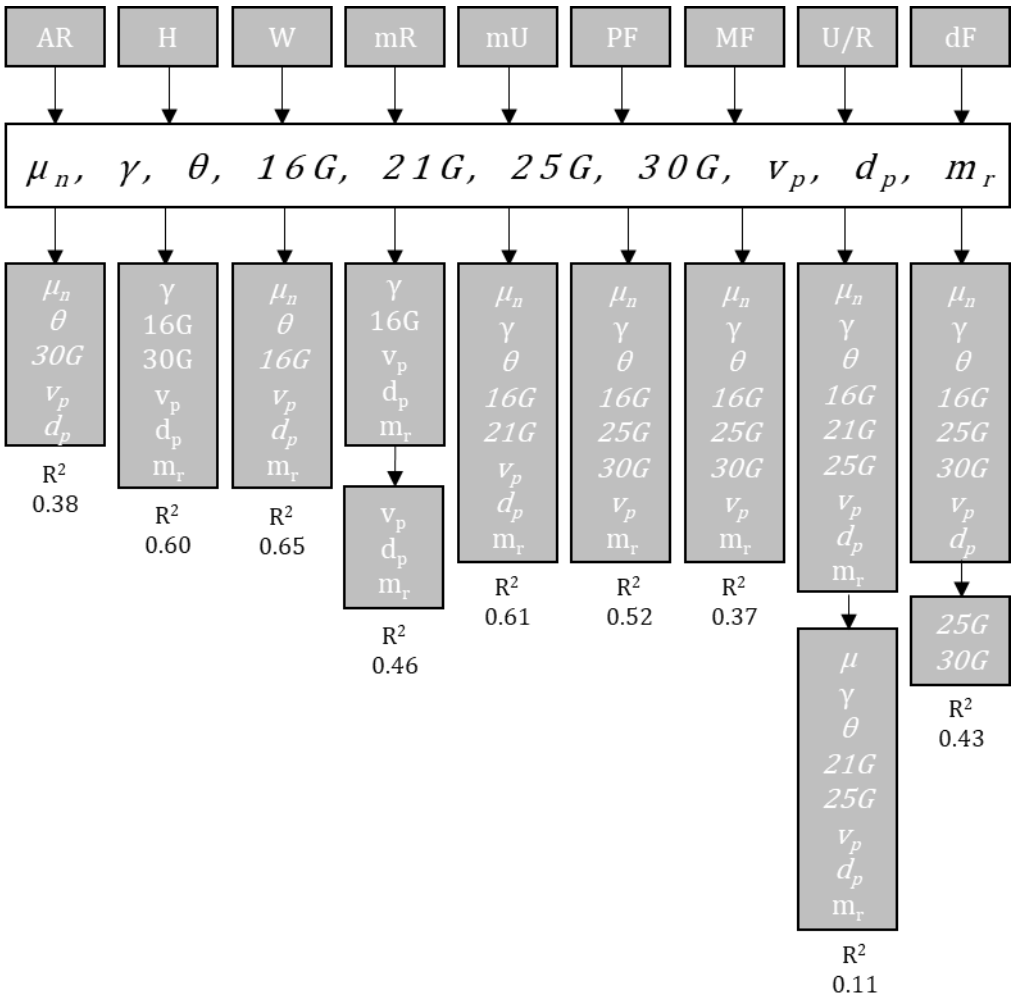


Figure 47: A flow chart detailing the regression procedure for the basic input variables. The output variable at the top is firstly regressed against all the predictor variables in the white box, and then subsequent rounds of L1 regression eliminate variables. Grey boxes indicate further rounds of L1. The final R_{adj}^2 value is of the final set of variables in the L1 regression, analysed as a separate multiple regression (i.e. no L1 penalty).

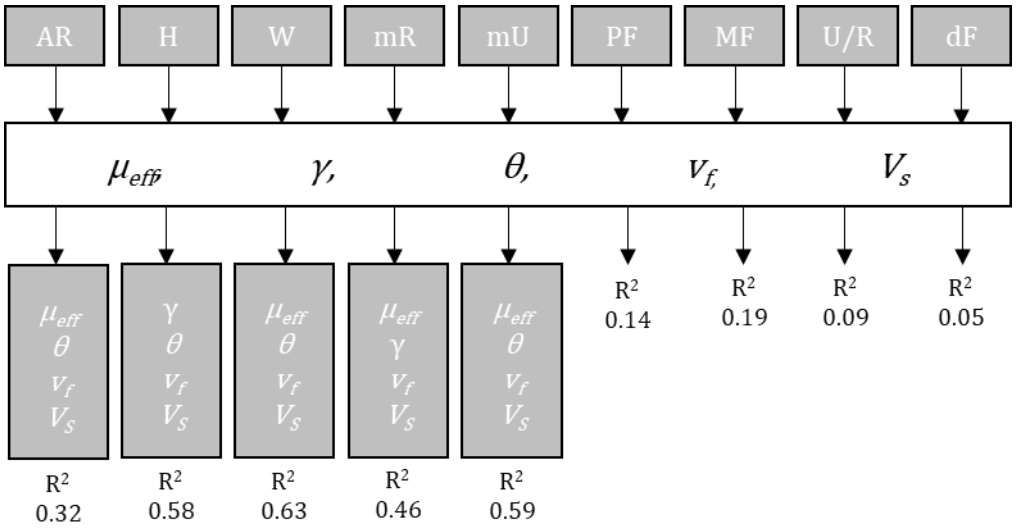


Figure 48: The synthesised input variable linear regression procedure and results.

Figure 48 shows the linear regression of the synthesised variables. The correlations against these variables are worse than in the basic input case. However, this is attenuated by the fact that they are better representatives of the properties relevant to the fundamental aspects of the flow. It is likely, therefore, that the nonlinear constructs and interaction terms will be more meaningful when using the synthesised variables. The key differences between the H and W factors are retained from the move between the basic to synthesised representations of the properties. Equally, there are a number of dummy variables containing categorical information, namely the needle gauges. Incorporation of these into a single quantitative variable with the flow speed v_f reduces the model complexity and possibly reduces the tendency for an over-fit to the noise produced by limiting the degrees of freedom. Indeed, the covariance between the higher needle gauges and the flow speed will be quite high, which is why both the quantitative combined variable and the categorical dummy variables are not both included.

For a qualitative analysis of the impactful properties, random forest analysis was performed on the data set with respect to H and W. The mean increase error of the variables on H and W over the course of the random forest analysis is shown in Figure 49. This shows that, comparatively, W is more sensitive to the material and process variables than H, especially considering viscosity and flow speed. Both are incredibly sensitive to volume, which is understandable and inconsequential as volume is a prerequisite to height and width. The lack of influence of viscosity as a singular variable on H is mirrored in the normal regression shown in Figure 47 and Figure 48. However, it demonstrates that H is more influenced by the contact angle than W. This suggests that the up-down spreading is dominated by the wettability, at least when compared to W. This makes sense, as transverse flow relies on good transmission through narrower flow channels,

and exclusively across fibre-directions as no fibres were aligned in the through thickness direction in any great proportion.

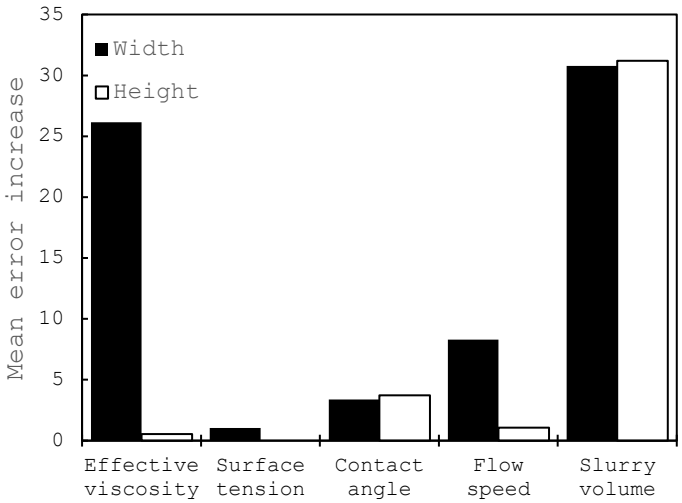


Figure 49: The mean error increase per variable inclusion, corresponding to variable importance, for H and W derived from the random forest analysis.

4.2.1.4.2 Non-linear analysis

Subsequently, interaction terms were sequentially included from Table 11 to the parameters that successfully passed the linear regression procedure indicated in Figure 48. The regression against transformed variables and variables with interaction constitutes the non-linear analysis. This was done in phases, with parameters added and investigated sequentially. The nomenclature for these terms may be found in Table 11. The phases are indicated in Table 21 and Table 22 respectively for H and W; the results of the regressions are shown in Figure 50 and Figure 51. The objective of these variable sets was to find the best combination of variables to maximise R_{adj}^2 and minimise the regression penalty λ. The interaction terms were selected based on the signs of the individual parameter coefficients as obtained in the linear regression analysis from Figure 48, and on proposed interactions from a physical point of view. The volume may be expected to interact with the velocity as a representation of the increasing force needed

to displace greater quantities of fluid inside the substrate. Volume may also be expected to be influenced by surface tension, as in the Young-Laplace equation where the curvature and internal pressure relates a droplet's volume and surface tension. The volume is included in this model as the third root of the volume to reflect that the measures H and W are singular with respect to length. The product of the flow speed and the cosine of the contact angle is an element associated to contact line friction, as discussed by Brunel [128]. To reiterate, however, the objective was to produce a predictive model, not an explanatory model. The change of the variable sets through Table 21 and Table 22 reflects, in some cases, the removal of parameters from the previous set through L1 regularisation. For H, this occurs in the change from variable sets 1 to 2, 3 to 4, 5 to 6 and 7 to 8. For W, this occurs in 1 to 3, 5 to 6, 7 to 8 and 9 to 10. The other transitions occur when new parameters were introduced to previous variable sets to test for new interactions as described above. The variable selection procedure was, in some ways, arbitrary. Interactions between surface tension and contact angle were excluded due to their high collinearity. For the same reason, viscosity and fluid speed were not combined into interaction parameters. Otherwise, most interactions were investigated. Higher order interactions (tertiary, quaternary interaction terms, et cetera) were also not included; these variables would have high collinearity with the base variables and one another due to the denseness of the data set. This would make variable selection difficult for both the OLS and the regularisation, and there would be significant degree of multicollinearity that would increase the coefficient estimates' standard error as clearly seen from Equation 23.

Table 21: The variable sets for the regression analysis for H

Variable set number	Variables
1	μ_{eff}, γ, cos θ, v_f, $V_s^{1/3}$, $V_s^{1/3}$ v_f^{-1}, μ_{eff} $V_s^{1/3}$, μ_{eff}^{-1} $V_s^{1/3}$, v_f cos θ
2	μ_{eff}, cos θ, $V_s^{1/3}$, $V_s^{1/3}$ v_f^{-1}, μ_{eff}^{-1} $V_s^{1/3}$
3	μ_{eff}, γ, cos θ, v_f, $V_s^{1/3}$
4	γ, cos θ, $V_s^{1/3}$
5	μ_{eff}, γ, cos θ, v_f, $V_s^{1/3}$, $V_s^{1/3}$ v_f^{-1}, μ_{eff} $V_s^{1/3}$, v_f cos θ
6	μ_{eff}, cos θ, $V_s^{1/3}$, $V_s^{1/3}$ v_f^{-1}
7	μ_{eff}, γ, cos θ, v_f, $V_s^{1/3}$, $V_s^{1/3}$ v_f^{-1}, μ_{eff}^{-1} $V_s^{1/3}$, v_f cos θ
8	μ_{eff}, cos θ, $V_s^{1/3}$, $V_s^{1/3}$ v_f^{-1}, μ_{eff}^{-1} $V_s^{1/3}$
9	μ_{eff}, cos θ, $V_s^{1/3}$, $V_s^{1/3}$ v_f^{-1}, $v_f\gamma^{-1}$, $V_s^{1/3}\gamma^{-1}$

Table 22: The variable sets for the regression analysis for W

Variable set number	Variables
1	μ_{eff}, γ, cos θ, v_f, $V_s^{1/3}$, $V_s^{1/3}$ v_f^{-1}, μ_{eff} $V_s^{1/3}$, μ_{eff}^{-1} $V_s^{1/3}$, v_f cos θ
2	μ_{eff}, cos θ, v_f, $V_s^{1/3}$, $V_s^{1/3}$ v_f^{-1}, μ_{eff} $V_s^{1/3}$, μ_{eff}^{-1} $V_s^{1/3}$
3	μ_{eff}, v_f, $V_s^{1/3}$, $V_s^{1/3}$ v_f^{-1}, μ_{eff}^{-1} $V_s^{1/3}$
4	μ_{eff}, γ, cos θ, v_f, $V_s^{1/3}$
5	μ_{eff}, γ, cos θ, v_f, $V_s^{1/3}$, $V_s^{1/3}$ v_f^{-1}, μ_{eff} $V_s^{1/3}$, v_f cos θ
6	μ_{eff}, cos θ, v_f, $V_s^{1/3}$, $V_s^{1/3}$ v_f^{-1}, μ_{eff} $V_s^{1/3}$
7	μ_{eff}, γ, cos θ, v_f, $V_s^{1/3}$, $V_s^{1/3}$ v_f^{-1}, μ_{eff}^{-1} $V_s^{1/3}$, v_f cos θ
8	μ_{eff}, cos θ, $V_s^{1/3}$, $V_s^{1/3}$ v_f^{-1}, μ_{eff}^{-1} $V_s^{1/3}$
9	μ_{eff}, cos θ, $V_s^{1/3}$, $V_s^{1/3}$ v_f^{-1}, μ_{eff}^{-1} $V_s^{1/3}$, $v_f\gamma^{-1}$, $V_s^{1/3}\gamma^{-1}$
10	μ_{eff}, $V_s^{1/3}$, $V_s^{1/3}$ v_f^{-1}, μ_{eff}^{-1} $V_s^{1/3}$, $V_s^{1/3}\gamma^{-1}$

In these figures, a large regression penalty shows that sensitivity of the output to the input is low, and that the cross validation minimises the fitting equation better without reference to the input variables. Likewise, the R_{adj}^2 shows the predictive power of the models with coefficient estimates made based on OLS, L1 or L2 regularisation containing the variables indicated.

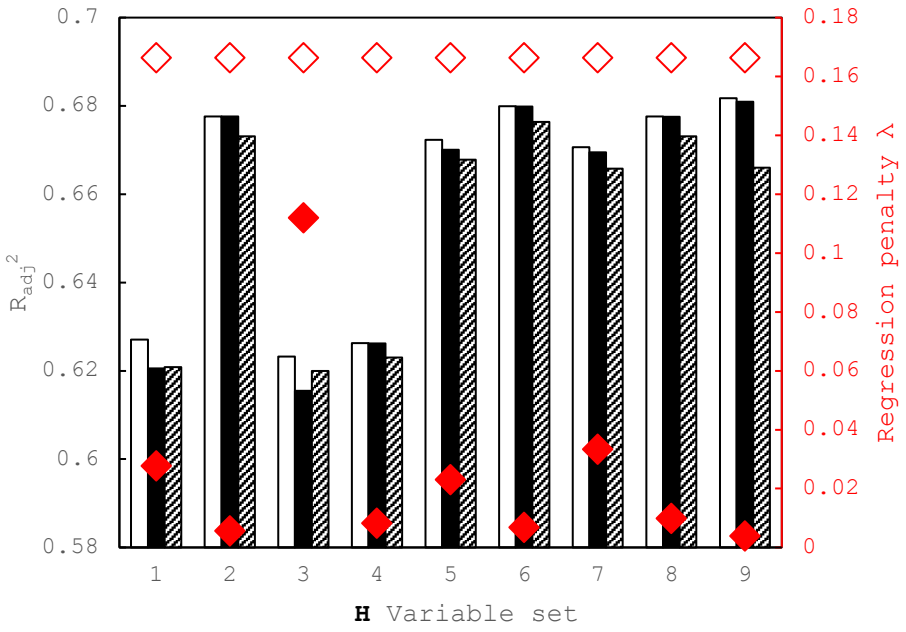


Figure 50: Adjusted R^2 for OLS (white bars), L1 regularisation (black bars) and L2 regularisation (dashed bars) and the penalisation magnitudes for L1 (filled diamonds) and L2 (empty diamonds) for H over the variable sets described in Table 21.

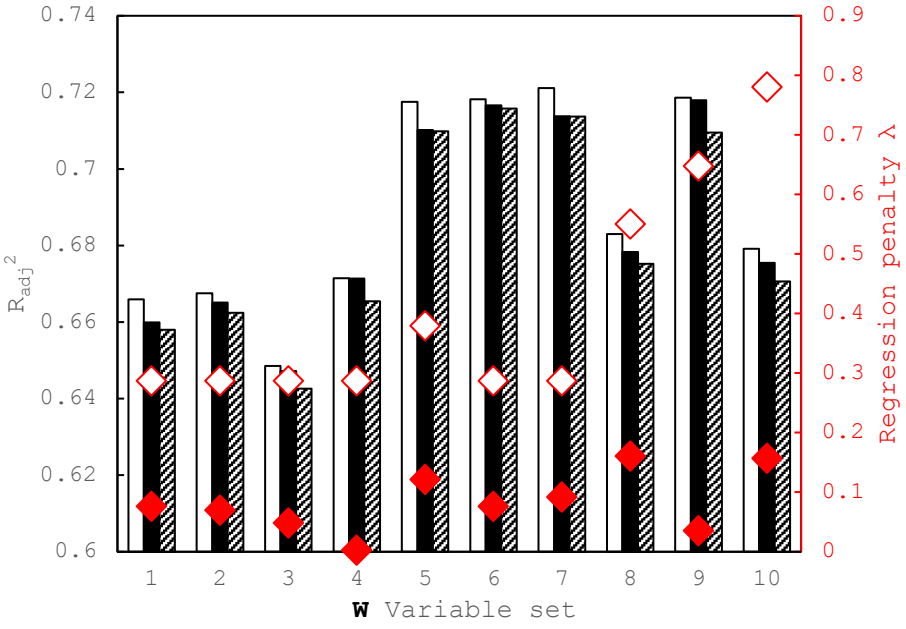


Figure 51: Adjusted R^2 for OLS (white bars), L1 regularisation (black bars) and L2 regularisation (dashed bars) and the penalisation magnitudes for L1 (filled diamonds) and L2 (empty diamonds) for W over the variable sets described in Table 22

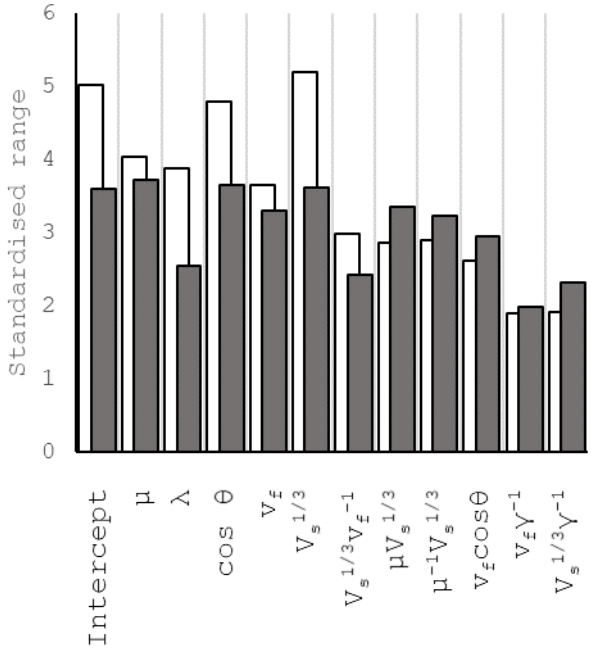


Figure 52: A depiction of the coefficient estimate variability in the regression procedure. The standardised range, maximum to minimum differences between determined coefficients divided by the standard deviations for each coefficient, are shown for H (white) and W (grey).

Additional to these variable sets tested, another series of functions were tested based on constructing dimensionally coherent functions from the linear regression of the synthesised variables shown in Figure 48. The summary of this process is shown in Table 23. The force terms in entries 3, 4, 7 and 8 were not found to be hugely correlated with any variables in the regression themselves. Equally, the calibration analysis found the force measurements and behaviours to be uncertain and subject to a large degree of error. It is useful to observe that, in support of those conclusions, the regression models tested involving force parameters do not add to the predictive utility when compared to the other models selected.

There was little consistency in the generated models' coefficient estimates for H and W in Table 21 and Table 22. This can be seen specifically in Figure 52. This shows the standardised range of coefficients produced throughout all the variable sets in Table 21 and Table 22. Large values show that the difference between the maximum and minimum

values are large compared to the standard deviations of the data set. Given that these values were generated for models with R_{adj}^2 values within 0.04 of one another, this clearly illustrates the non-uniqueness of the statistical models generated. For this reason, the explicit forms of each model are not shown, as they provide little physical insight.

The outputs of the L1 and L2 regularisation are found to be very different based on the parameter density of the data set, as discussed in section 2.4.

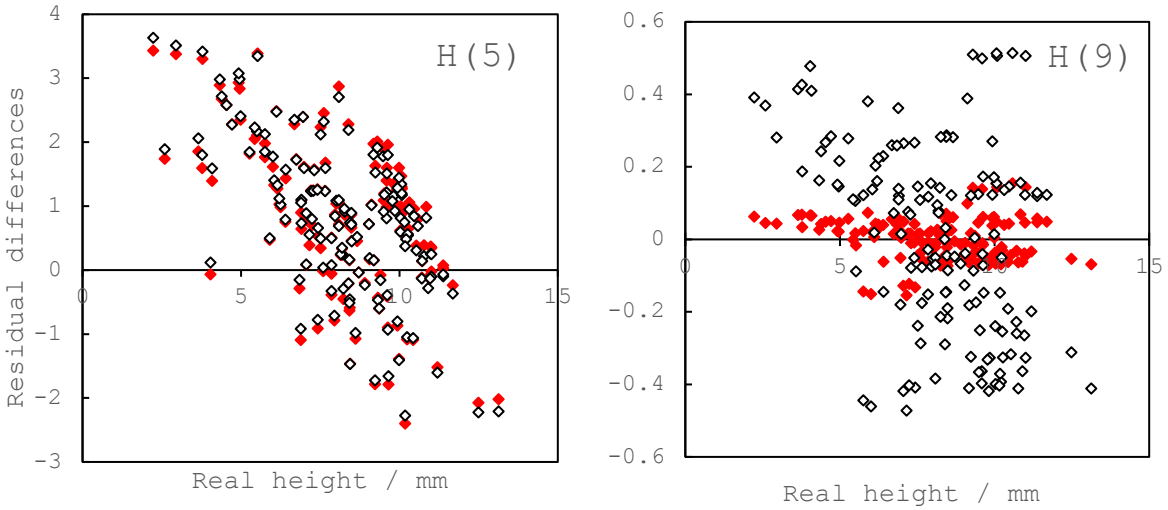


Figure 53: The differences between the OLS and L1 (red) and L2 (empty) residual values in the real/predicted output for (left) H(5) - a sparse data set and (right) H(9) – a dense data set. Note the differences in total scale.

H(5) contained 8 predictor variables, for which 4 had regression coefficients set to 0 by L1 regularisation. H(9), however, had no variables set to 0. The differences between OLS and L1 can be seen to be negligible for H(9) compared to L2, whereas in H(5) the output for L1 and L2 were almost identical. The differences were due to the contributions of the small coefficients selected by L2 for the parameters L1 shrunk to 0. However, the whole coefficient set for H(9) was very different by L1 than for L2. For instance, L1 selects a value of -121 for the variable $V_s^{1/3}\,\gamma^{-1}$. L2 selects a value of +82. The R_{adj}^2 of the L1 parameter space was only 0.01 larger than for L2 at 0.68 compared to 0.67. This highlights the number of statistical models that represent the behaviour adequately in the

parameter range investigated. Regularisation can be assumed to have made the coefficient estimates less susceptible to overfitting, as was designed, but a greater data set would have been needed to be generated to confirm this.

Figure 50 and Figure 51 show that, foremost, there is no one model that is substantially better than the others. For H, variable set 9 shows the highest R_{adj}^2 for OLS and lowest regression penalty that shows that it is the most descriptive variable set tested. The inclusion of the interaction terms $V_s^{1/3} v_f^{-1}$, $v_f\gamma^{-1}$ and $V_s^{1/3}\gamma^{-1}$ were intended to reflect the flow resistance due to displacement force, the contact line friction and specific surface tension forces respectively. The lack of a viscosity interaction term or a $cos\ \theta$ interaction term is unexpected, as the viscosity directly couples with flow speed in a number of known relations (Hagen-Poiseuille, Darcy, etc) and the contact angle is a more obvious material interaction quantity than the surface tension, which does appear. However, as previously discussed, L1 regularisation can have trouble selecting correlated inputs from one another. This is obvious from the correlation matrix from the regression output, 0.3 and 0.6 between $cos\ \theta$ and $v_f\gamma^{-1}$ and $V_s^{1/3}\gamma^{-1}$ respectively. This means that collinearity is high between these input variables. Given that the application of these models will be strictly interpolative, the exact representation of these effects was not investigated further, and this manifestation was accepted. However, the L2 regularised form of the variable sets was used to determine the regression coefficients, to provide a model with greater presumed noise cancellation.

Table 23: The regression statistics of a series of functions created from the dimensional analysis of the results of the initial linear regression shown in Figure 48. A constant of proportionality and dimensional correction is indicated as either α_i or β_i

#	Test function	R^2_{adj}	Intercept	Dimension of constant	Notes
1	$H = \alpha_1 \frac{v_f V_s cos\theta}{\gamma}$	0.0409	7.91	N s m^{-4}	Determined from linear regression output: no predictive power
2	$H = \alpha_{1b} \gamma^{1.715322} Cos\theta^{0.494824} v_f^{0.020269} V_s^{0.273247}$	0.581	1.03	N$^{-1.715}$ s$^{0.020}$ m$^{1.876}$	Determined from log-log plot of Entry 1. Dimensionality of linear regression not retained
3	$H = \alpha_2 \frac{F_m v_f V_s^{1/3} cos\theta}{\gamma}$	0.0415	7.91	s m^{-2}	Determined from dimensionality of α_1 in Entry 1: no predictive power
4	$H = \alpha_{2b} \frac{\gamma^{2.153353} (\cos\theta)^{0.593126} v_f^{0.038029} V_s^{0.281449}}{F_m^{0.06634}}$	0.654	0.835	m$^{2.272}$ s$^{0.038}$ N$^{-2.087}$	Determined from log-log plot of Entry 3. Dimensionality of α_2 not retained
5	$W = \beta_1 \frac{V_s cos\theta}{\mu\, v_f}$	0.324	13.2	N m^{-3}	Determined from linear regression output: no predictive power
6	$W = \beta_{1b} \frac{V_s^{0.294901} (cos\theta)^{0.114827}}{\mu^{0.09251}\, v_f^{0.07842}}$	0.750	1.28	N$^{0.093}$ m$^{0.007}$ s$^{0.015}$	Determined from log-log plot of Entry 5. Best observed correlation, and least biased distribution of residuals about expected value
7	$W = \beta_2 \frac{\sqrt[3]{V_s} F_m cos\theta}{\mu\, v_f}$	0.189	13.7	m^{-1}	Determined through β_1 dimensionality
8	$W = \beta_{2b} \frac{F_m^{0.039559} (\cos\theta)^{0.115924}\, V_s^{0.290774}}{v_f^{0.08816} \mu^{0.10048}}$	0.640	0.876	N$^{0.06}$ s$^{0.012}$ m$^{0.011}$	Determined from log-log plot of Entry 7. Dimensionality retained, but inferior to Entry 6

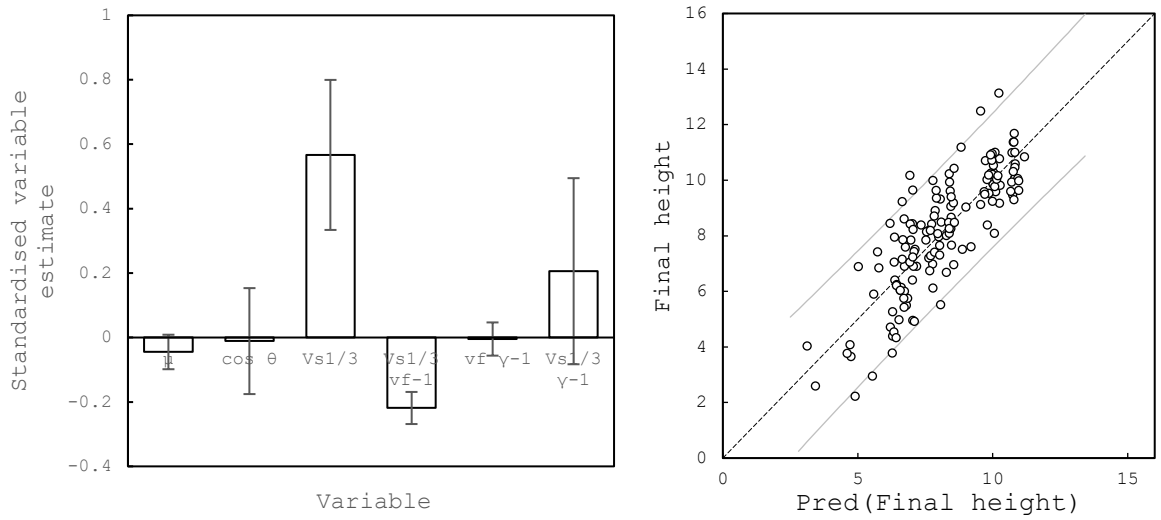


Figure 54: The standardised coefficients (left) with 95% confidence intervals and the model results superimposed with the true data points (right) for the L2 regularisation of variable set 9 for H.

The coefficients, Figure 54, generated by L2 regularisation for H variable set 9 are very different to the L1 regularisation versions (note that this graph shows standardised coefficients, which indicate the impact on the response variable as scaled by the sampling standard deviation of the particular predictor variable – indicating relative variable 'impact'). This is expected, as the value of λ_1 is very small. The value of λ_2 is similar across all the investigated variable sets. This, together with the reasonably low peak value of R_{adj}^2 (0.68) for OLS suggests that both there is a large error term, and that there is another systematic bias unaccounted for in the analysis. This is indicated also in the residual plot, Figure 55. Specifically, a loose positive gradient is seen in the residual plot. This is observed in all the regression equations in this work, and no set of variables included in regressions (not all tests are shown in this thesis) removed this bias. The smallest heights are recorded for the smallest injection volume tests: 0.025 and 0.05 cm^3. The volume is determined from the mass of the deposit and the slurry density and composition. The percentage of mass retained on the surface or around the needle hole out of plane with the cross section is highest in these low total added mass cases. Hence, this deviation will

lead to a disproportionately small height. The larger than expected height could be a result of inclusion of some slurry in the upper regions of the preform, left behind during the withdrawal of the needle, rather than flow from the injection centre; this would disproportionately extend the apparent measurement of H. Equally, it could be an effect of lower than average fibre density directly below the needle tip as a result of the degree of randomness in the fibre architecture, hence penetration by the particles would occur more than would be expected for other samples.

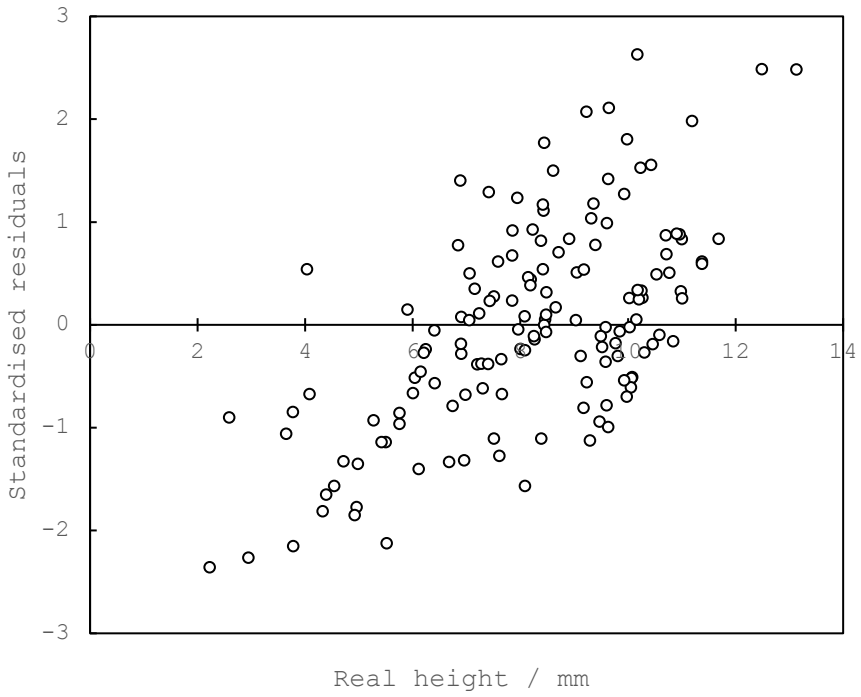


Figure 55: The standardised residual plot for the L2 regularisation of H variable set 9, data points representing the number of standard deviations the predicted height lie from the observed height.

Irrespective of the structure of the residuals, the majority of the data points are within the 95% confidence interval (right, Figure 54). Variable set 9 provided a superior OLS R_{adj}^2 than any of the entries 1-4 in Table 23, but entries 2 and 4 have a lower intercept value, compared to the value of 2.4 mm.

For W, the best variable set suggested from Figure 51 is set 8, in spite of the lower R_{adj}^2 than set 7. This choice is made on the basis of the reduced regression penalty. This

variable set notably lacks any surface tension or $cos\,\theta$ interaction term as in H(9), but does include a viscosity interaction term of $\mu_{eff}^{1}\ V_s^{1/3}$, which could represent the dependence of the viscous resistance on the total quantity of fluid already present. However, the best correlation by R_{adj}^2 is found for entry 6 in Table 23. Unlike H(9), which is an additive function of the regression variables, entry 6 is a product of the indicated variables raised to powers determined from a log-log plot. This function has the benefit of the lowest observed degree of structure in the residual plot, and good distribution in the predicted/real width, as shown in Figure 56.

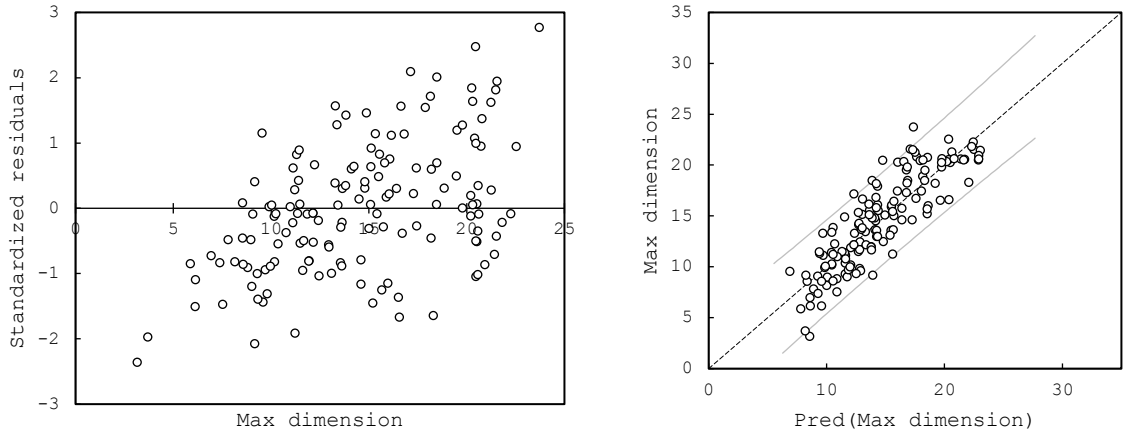


Figure 56: (left) The standardised residuals of entry 6 in Table 23 and (right) the superimposed model and real data points.

The index of the volume determined by all log-log plots in Table 23 are returned as reasonably close to 1/3, which is comforting with respect to the validity of the assumption that is made for the H and W variable sets. From this analysis, the selected best functions found for H and W are shown in Table 24.

Table 24: The final selected relations for H and W that displayed the highest statistical significance.

Function	R_{adj}^2	Intercept
$H = -1.02\mu_{eff} - 0.09\,cos\theta + 7.78\sqrt[3]{V_s} - 0.30\frac{\sqrt[3]{V_s}}{v_f} - 0.014\frac{v_f}{\gamma} + 82.4\frac{\sqrt[3]{V_s}}{\gamma}$	0.67	2.44
$W = 20.26\frac{V_s^{0.294901}(cos\theta)^{0.114827}}{\mu^{0.09251}\,v_f^{0.07842}}$	0.75	1.28

These relations are clearly not of the same form, nor are the dimensions obviously consistent. This forms an important caveat for this process. The relations produced by the regression procedure are reflections of whatever are the true, underlying analytical relationships between the input and output variables in this fluid and porous composite system. The relations reflect, to a specified degree of accuracy in the parameter range investigated, the trends that the analytical relation may reflect in this specific context. These relations are, by their nature, vastly complicated multidimensional sets of high order high degree differential equations that cannot be obtained analytically. On the production of these relations, the units and dimensions of the inputs are clearly not consistent with those of the output. This is not surprising and was never the goal of this analysis. The goal was to produce equations that, in this specific situation and under the range of input variables (which are far more general than found elsewhere in the literature) could be used to predict the behaviour of injection in this exact context and have more general relevance outside it. However, the fact that highly complicated underlying analytical relationships are mirrored by a simple relationship of few variables does not imply that the system of equations is, at its core, simple. Indeed, even concisely

defining the 'height' or 'width' used in this work in terms of the base differential equations would be non-trivial. For this reason, it can be expected that there are many variables that are left out of the regression equations, and that the form the variables are presented in are not the 'true' form. As a result, purposefully manipulating the equations to ensure they are dimensionally consistent is not useful; it assumes that the form of the equation determined through the regression procedure is physically meaningful and in particular obfuscates the fact that it is not a unique, or even optimal approximation for the behaviour of the underlying differential equations for this range of variables. As a result, dimensionalising the equations was viewed to be a redundancy, and to represent a fundamental misunderstanding of the significance and value that the relations hold.

The regression procedure has resulted in the adoption of two relations that best describe two of the output variables, H and W. The other output variables were not found to correlate meaningfully with any underlying physical variables. This is likely due to the fact that they are primarily compound variables of H or W and the fact that the system is geometrically complicated. The structure of the deposits is less like the ellipsoid a two parameter description would imply, but more like the alternating brick stack shown in Figure 46, with alternative high-extension deposit areas projecting along adjacent UD layers. However, in order to try to establish some predictive element for injection, the relations shall be used in their present form and the ramifications for the porosity structure discussed qualitatively later. The ability to produce selective concentration gradient composites relies on controlling two key areas of uncertainty:

1. The error inherent to the variables in the regression generated models (represented by R_{adj}^2)
2. The noise in the regression generated statistical model, unrelated to the parameters ($1-R_{adj}^2$)

The first of these may be influenced by setting the variables adequately. The second is a general uncertainty that requires allowance in the geometry of final products.

The error dependence can be seen to vary with each parameter. With respect to easy control of H, low μ_{eff}, $cos\ \theta$ and V_s reduce the error. Conversely, low γ increases the error. v_f, fluid velocity, is reduced when $v_f < \sqrt[4]{2.0\ \gamma^2 V_s^{2/3}}$. Also notable is that the value of H is negative for many values after extrapolation from the displayed ranges: small surface tensions and large viscosities. This is an artefact of the regression procedure being extended beyond the input range investigated, and therefore constitutes extrapolation, which is not an appropriate use of the model. This is clear when considering cases like $v_f = 0$, which from Figure 57 would indicate a height of around 9 mm. Obviously, for a stream with no velocity, no deposit would be generated. Hence, the relations should be viewed as valid only in the ranges indicated.

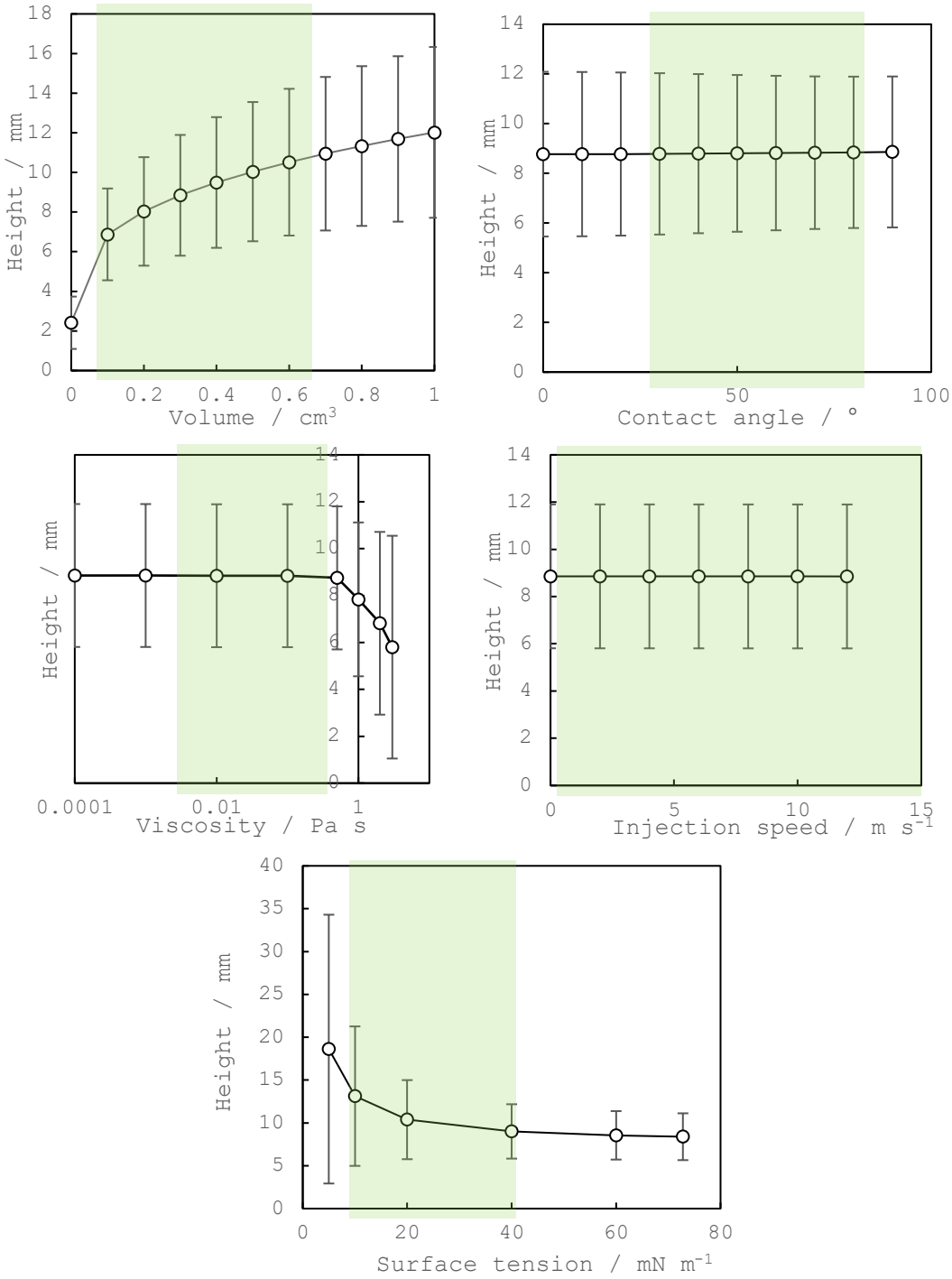


Figure 57: The dependence (both value and error) of H on each constituent variable. In each case, the default values set for the variables is μ_{eff} = 0.01 Pa s, θ = 80°, V_s = 0.3 cm^3, v_f = 4 m s^{-1} and γ = 45 mN m^{-1}. The green shows the interpolation range of the variables investigated.

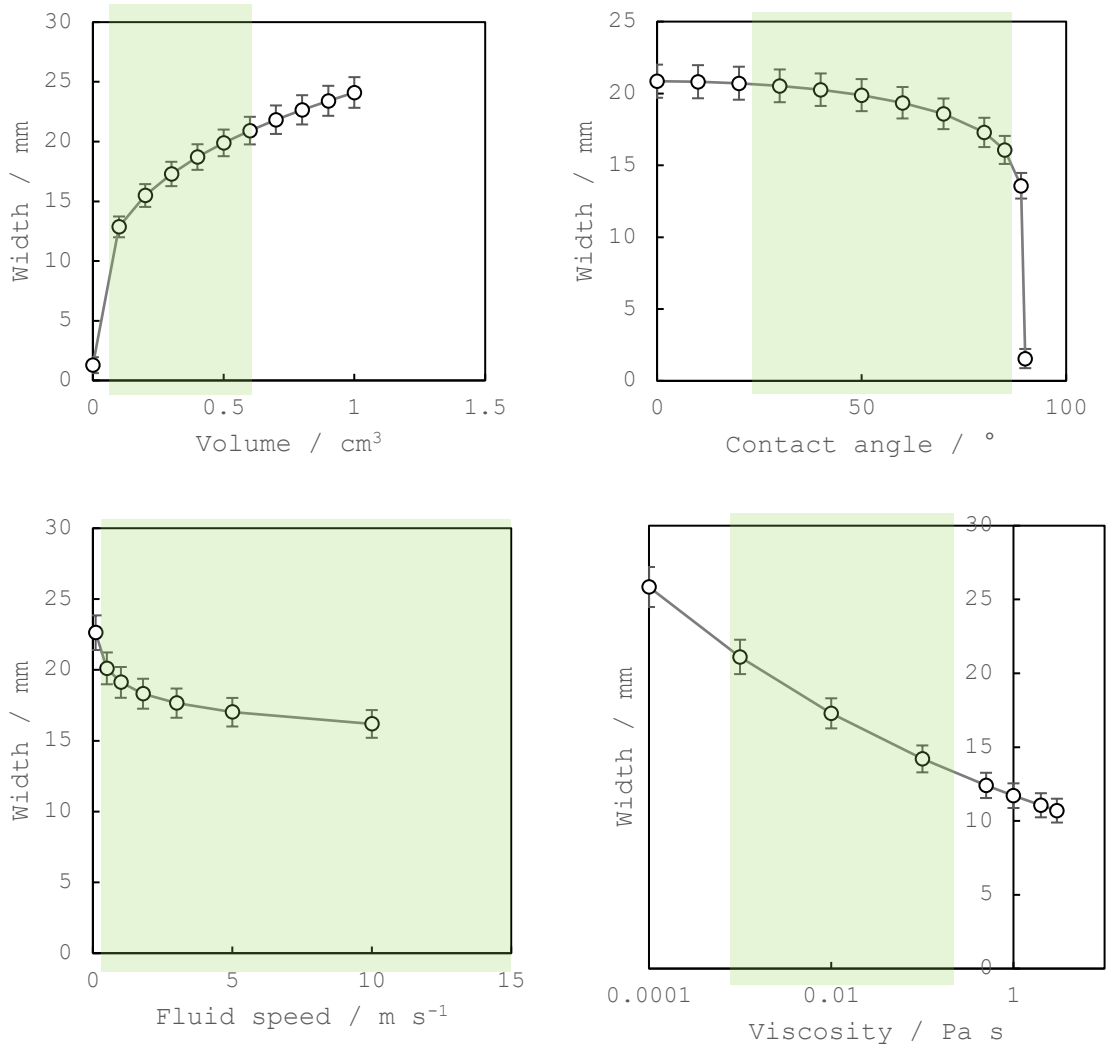


Figure 58: The dependence (both value and error) of W on each constituent variable. In each case, the default values set for the variables is μ_{eff} = 0.01 Pa s, θ=80°, V_s= 0.3 cm^3, v_f = 4 m s^{-1} and γ = 45 mN m^{-1}. The green shows the interpolation ranges of the variables investigated.

As in the case for H, the variation of each parameter affects both the value and error on W. In this case, all variables that increase the value of the function increase the error commensurately; V_s increasing exacerbates the error, while an increase of all other variables (valid only for θ between 0 and 90) reduces the error. The second area of uncertainty is the regression error. This is expressed for H and W by the grey confidence interval indicators in the right of Figure 54 and Figure 56 respectively. These confidence interval magnitudes (i.e. standard errors) can be plotted against final predicted dimension, Figure 59.

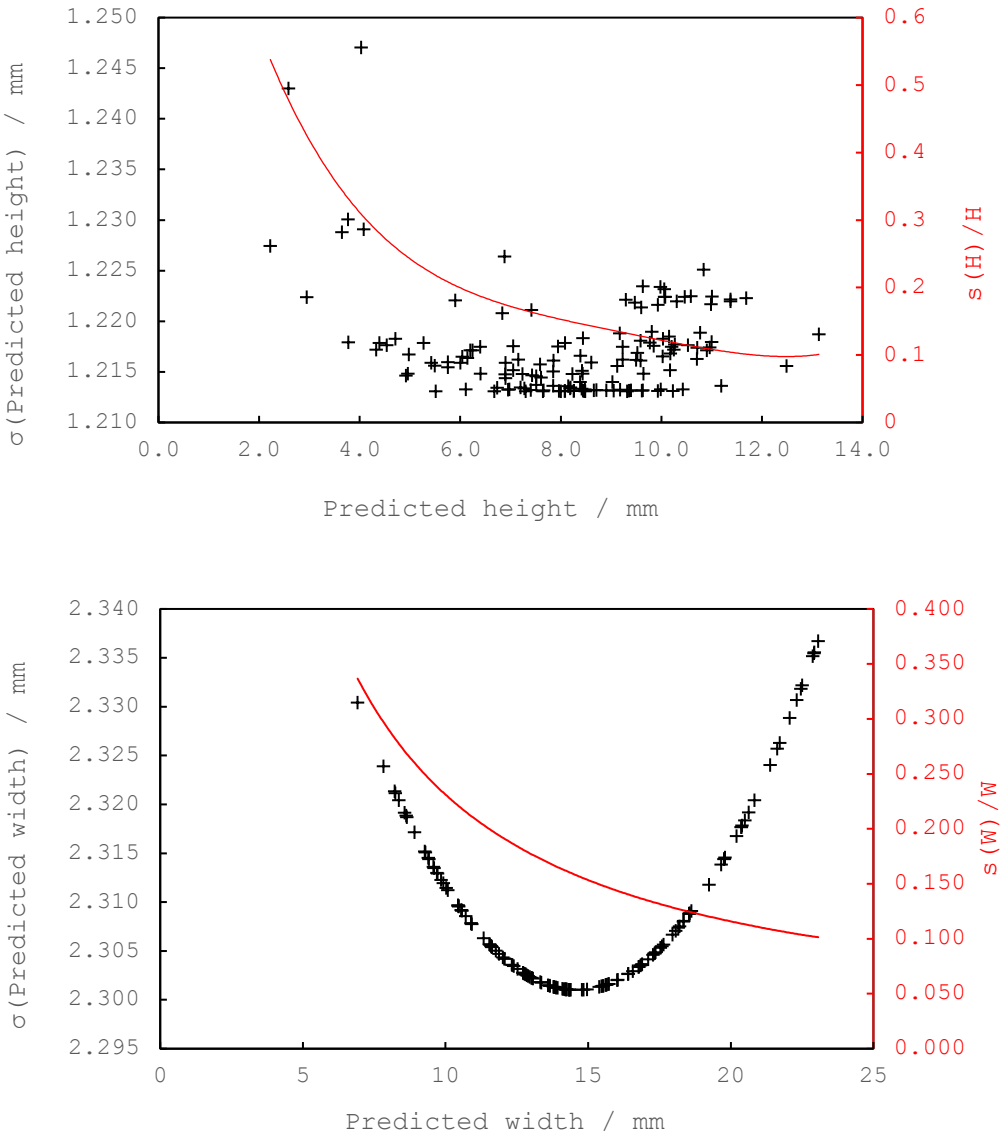


Figure 59: The standard error in the predicted dimension for H (top) and W (bottom) against predicted dimension. The black dots are the data points, and the red line is the value of error as a proportion of the total dimension.

Figure 59 shows the dimensions that have the lowest associated standard error sourced from the regression procedure. The values for W sit on a parabola due to the fact that the error function is, technically, a function of a single parameter. Inclusion of noise from more of the constituents would serve to increase the error, and therefore increase the height and spread of the curve as in the case for the error function of H, and should be therefore considered a lower bound for the error distribution of W. The red line indicates the ratio of the error to the overall dimension. It is asymmetric as the specific error is

larger when the absolute dimension is smaller, i.e. the error accounts for a greater percentage of the anticipated dimension. This has serious consequences for the production of selectively graded composites via injection. When trying to produce a graded structure, a specific concentration gradient needs to be engineered sequentially. This can be difficult to manage at the ratio of error to absolute size the statistical analysis has indicated. To illustrate this, an exemplary case will be used. To produce a two phase composite component, A and B being the constituent ceramic powders, with a maximum thickness of 10 mm (in the z direction- variable H) and a linear concentration gradient, injection obtained gradient profiles like those in Figure 60 would be needed.

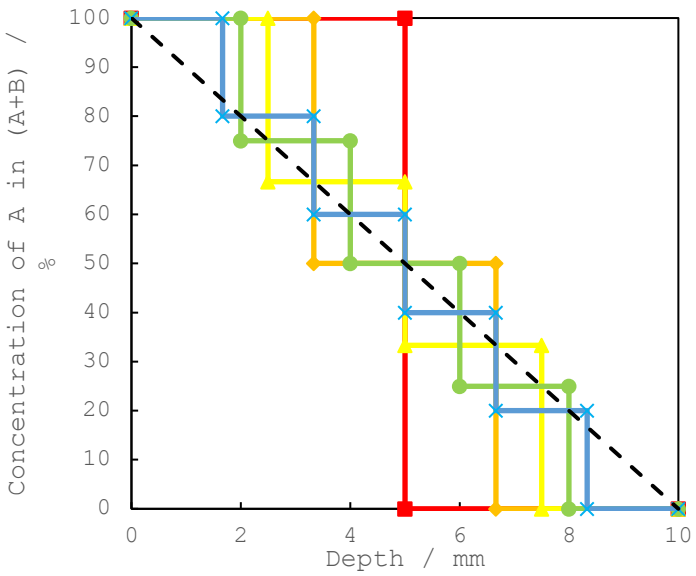


Figure 60: The concentration gradient provided by injection of phases of either pure A, pure B or a ratio matching the expected linear profile (---) over the thickness, as the number of injections increases: (■) 2 injections, (◆) three injections, (●) four injections, (▲) five injections, (×) 6 injections.

The concentration gradient is matched to a property gradient; the closer to a continuous gradient (the dotted black line), the better the expected properties of the overall component due to fewer discontinuities in material properties. Hence, for adequate performance, it would be expected in this example case to have a profile closer to that of the blue profile, which requires 6 injections of controlled height. The dashed line in Figure

60 shows a continuous concentration gradient for a composite of thickness D=10 mm. For two injections, a 100% A deposit would be centred at the 0.25D position and a 100% B deposit would be centred at the 0.75D position, each with H values of 5 mm. For three injections, a 50:50 mix deposit of A and B would be centred at the 0.5D location, with the 100% A and 100% B deposits shifting commensurately to the D/6 and the 5D/6 locations. As the number of injections increase, so do the number of compositions in order to match the continuous gradient change shown by the dashed line in Figure 60. Six injections would require six compositions (A:B): 100:0, 80:20, 60:40, 40:60, 20:80 and 0:100 centred at the (2n-1)/12 positions (i.e. 0.08̇3D, …). Hence, the height of these deposits would require that they be kept in the size range the concentration gradient suggests. For example: for six injections the 40% A deposit would need a height of 0.1ḋ mm centred at 5.8̇3 mm. This is the process for constructing the optimal injection configuration for the desired gradient. Using the error function in Figure 59 and comparing to the accuracy for the production of a deposit of the required height yields an error on the height shown in Figure 61.

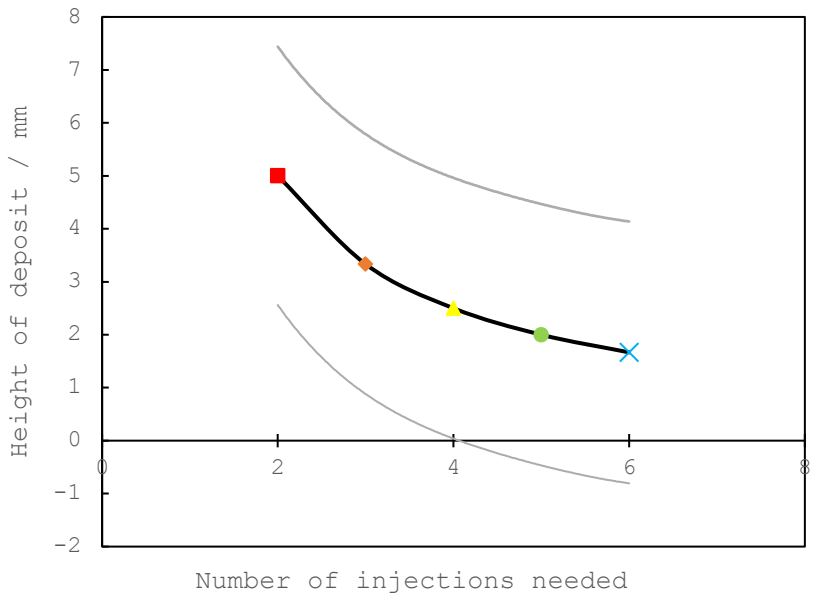


Figure 61: The deposit height vs number of injections required to produce the example component described in Figure 60.

Comparing to the reference case of a 10 mm thickness specimen of 6 injections (the blue cross and line in both Figure 60 and Figure 61), the required H value is 1.6̇ mm. The error function produces a 95% confidence interval of a thickness of -0.8 mm < H < 4.1 mm, far from the desired value of 1.6̇ mm. From Figure 61, it is clear that the process is uncontrolled for any number of injections for a component of this thickness. However, two injections provide the lowest amount of error, with 95% certainty representing a 4 mm total range on a desired H value of 5 mm (3 mm < H < 7 mm). This, however, would produce a single biphasic interface conforming to the red square gradient in Figure 60. However, the ± 2 mm uncertainty will mean that there is still uncertainty on the precise interface location, with potential for the centre region to remain porous.

The only means of producing a smooth gradient of the described nature is by increasing the thickness of the component overall. The percentage of the uncertainty in height over the absolute value as a function of total thickness for 5, 6 and 7 injection gradients is shown in Figure 62.

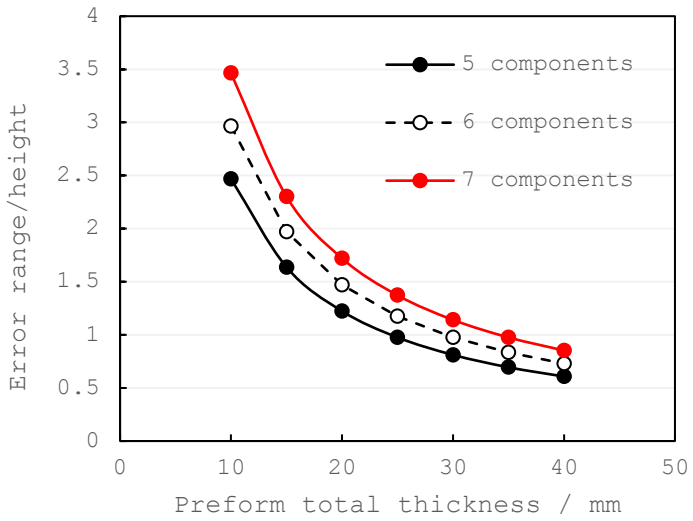


Figure 62: The effect of total thickness on the ratio of the overall error to the absolute height values.

It is clear from this that the error, as defined by the proportion that the 95% confidence interval is of the desired value itself, does not drop beyond 50% of the desired absolute value for any total thickness to produce the desired gradient, until above 40 mm. This thickness is substantially larger than most FGMs investigated in the UHTCMC literature, and far more than the scale of radii of curvature of rocket nozzles and control surfaces for aerospace applications; 'sharp' configurations can have radii of less than a millimetre [253]. This analysis can also be performed for W and yields similar conclusions at similar length scales. The error in the height will manifest as an over-injection, thereby skewing the distribution and submerging the locations for future prospective injections, or under-injection, which will introduce macroporosity in the component. In summary, the use of H and W equations already oversimplifies the kinematics of the spreading, but even this simplified analysis demonstrates the poor suitability of this method to producing high dimensionally tolerant FGMs at some total length scales. The increased requirements for high gradient definition at small component size leads to unfeasibly small deposit sizes, the error on which leads to incompatibility with the required gradient. This is illustrated graphically in Figure 63.

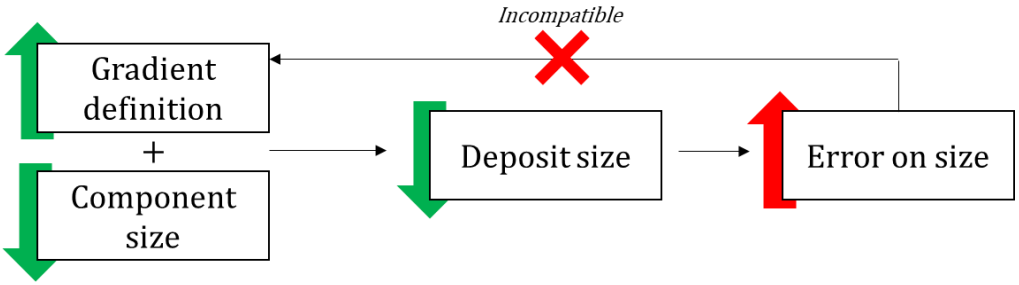


Figure 63: The relationship between the desired qualities of the FG composite and the output parameters of the regression

4.2.1.4.3 Microstructural analysis of injection study samples

Investigating some of the microstructures of the injection study samples can corroborate some of the suggested spreading mechanisms.

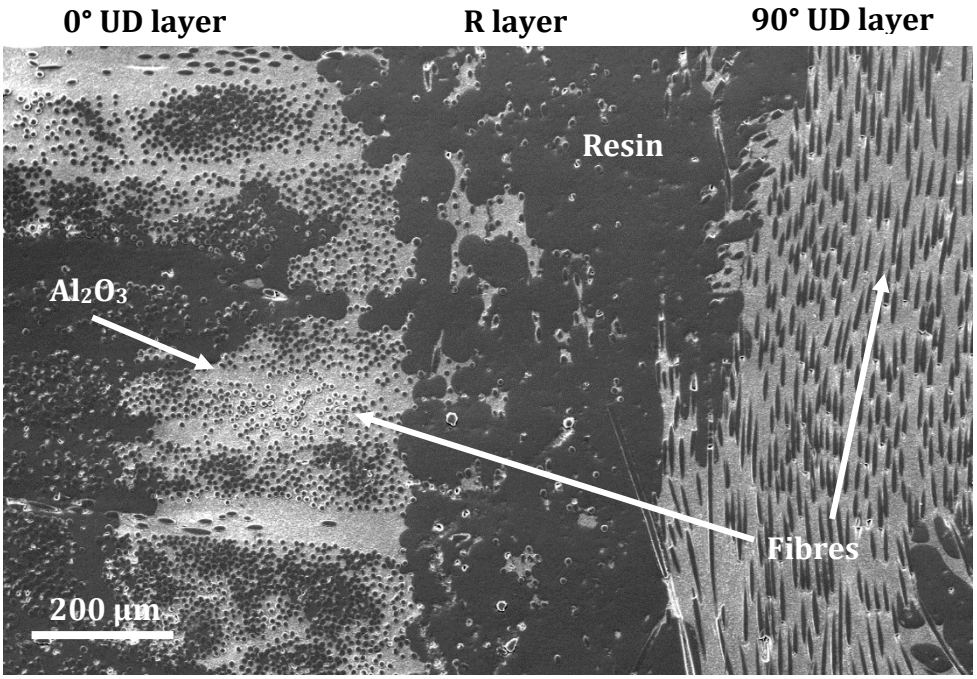


Figure 64: An image of the intersection between the 0°, random and adjacent 90° UD layer at the lower portion of sample produced with the most viscous and least wetting slurry, at a low injection speed with a 21G needle. Here, white is the deposit, the circular, or high aspect ratio, grey zones are fibres in the 0 and 90° layers respectively, and the wide structureless grey patches are resin (i.e. pore space)

Figure 64 shows the intersection between layer types for the injection of slurry Al_2O_3-20 (viscous and poorly wetting). It can be observed, as has been observed across the spectrum of the samples, that there is a poor uptake of slurry in the central random orientation layer. This is surprising, as the porosity and permeabilities are incredibly high, when compared to the unidirectional layers, in which a dense deposit may be seen.

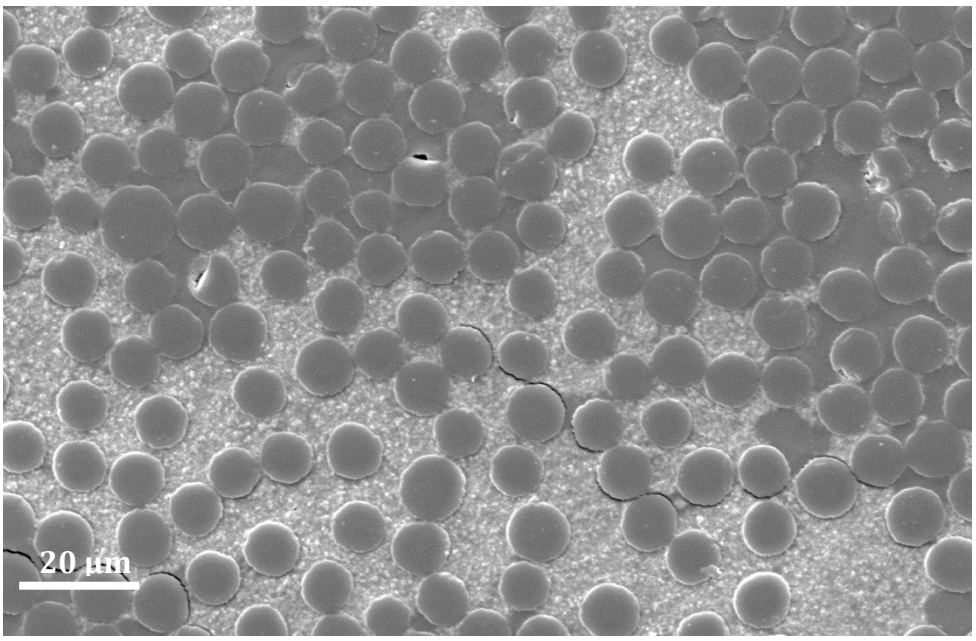


Figure 65: A higher magnification image on the 0° layer as seen in Figure 64 showing the details of the intratow porosity

From Figure 65 it can be seen that the slurry deposit intra-tow is reasonably dense. Shrinkage cracks can be seen from drying. Penetration into the tows is heterogeneous; significant areas remain unfilled. Qualitatively, the regions without significant powder density seem to be regions with higher fibre density. This belies the argument from capillary pressure that these should be the most easily infiltrated regions and adds the probable caveat that, in the case of particulate fluids, dense regions are preferentially filled so long as clogging of the channels by the entrained particles does not inhibit it. This may explain the poor densification of the random region seen in Figure 64; the fibre density is sufficiently low that, at this low flow rate and incredibly low capillary number (hence capillary pressure dominated), percolation through the unidirectional layer is far more favourable. An alternative, more prosaic, reason for the low observed powder fraction is that it was removed during the dry cutting of the preform.

Use of a higher injection speed (16x higher) resulted in capillary numbers from around 7 to 0.007 over the course of the injection. This is firmly within the viscosity-dominated regime and, hence, lower flow resistance through wider, less tortuous flow channels

would be expected to dominate. Figure 66 shows the microstructure for this case. The unidirectional layer can be seen to be less uniformly filled, and the inset shows evidence that UD tow filling was concentrated around the inter-tow pores through the UD layer. This is consistent with the change in capillary number. However, given that the fluid is still wetting and the calculated capillary number is unlikely to be as large in situ due to the presence of the flow impeding solid barriers, capillary suction can still be observed in the tows themselves where clogging did not preclude it.

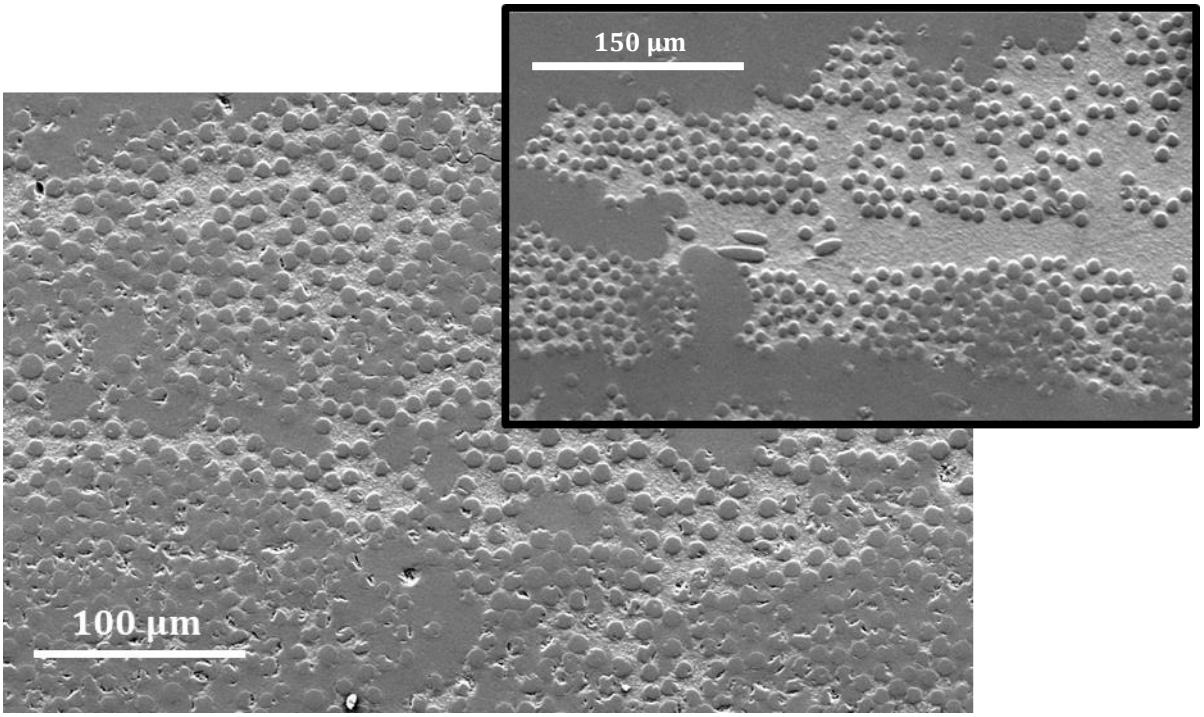


Figure 66: the injection of the same slurry as in Figure 65, but at a far higher injection speed (~16x) and therefore expected capillary number regime. It can be seen that the filling of the UD layer is far more inconsistent. Inset: a zoomed out view of a UD region.

Use of a more wetting, lower viscosity slurry (slurry 27, θ= 51° vs that of slurry 20, 79°) at this same high flow rate generated an infiltration microstructure more similar to the high viscosity slurry injected at lower speeds, seen in Figure 67b. This calculated range of capillary constants was, for comparison, around 20x smaller than for the higher viscosity slurry. The lowest estimated flow rates (an overestimate of the real flow) was in the capillary action dominated range, at around 0.0004. There was evidence from Figure 67a

that there is a large concentration of slurry within in the unidirectional layer. This reaffirms the contrast mainly between the high concentrations of the slurry in the UD vs R layers as being related to capillary uptake.

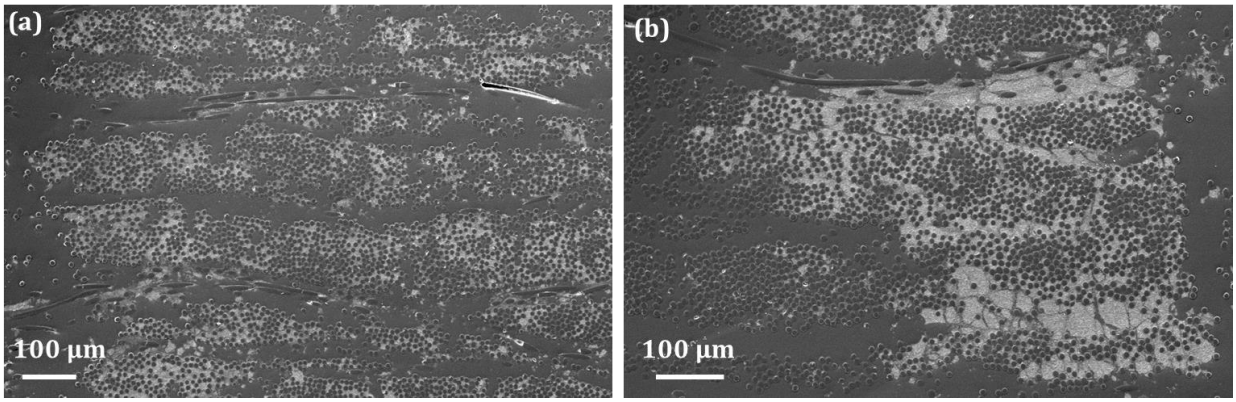


Figure 67: High-speed injection of a more wetting, lower viscosity slurry: (a) an extended view of the 0° layer, (b) the fringes of the impregnation, showing the slurry concentrated around the larger channels in the preform

This microstructural analysis of the tows is incredibly important as regards to selective impregnation. The capillary flow along the tows represents a fluid property controlled loss of input pressure spatial selectivity: the fastest speed and smallest volume was used in injection in Figure 67 and yet a large degree of flow occurred along the longest UD axis (10 mm) shown in Figure 68.

The flow in the unidirectional layer in the centre of the preform, closest to the injection tip, is extensive in many of the samples. Over 45% of the samples display a greater than 18 mm flow extent in this layer, with the preform diameter being 20 mm. Fewer than one third of the samples were of the maximum injection volume of 0.5 cm^3, and the next modal volume below this value was 0.2 cm^3, substantially smaller. The capillary suction of the white slurry was visible on the exterior of many of the preforms following the injection at this central UD layer. Interestingly, the width of the white area in this layer was a few millimetres in total, not dissimilar to the measured widths of the layers immediately above and below in the cross-section, as shown in Figure 68. This is indicative that

reasonably small channels of slurry were formed that were drawn by capillarity to the edge of the preform. This is potentially a key issue with the regression analysis. As the 20 mm limit of width was achieved by so many samples, it is possible that there was insufficient discrimination, from the perspective of the input variables. In essence, too many of the slurry and flow conditions may have provided a false result as they were artificially terminated at 20 mm of percolation though they may have percolated much further. This would obfuscate the true spreading potential of the slurries and also represent a higher error on the width.

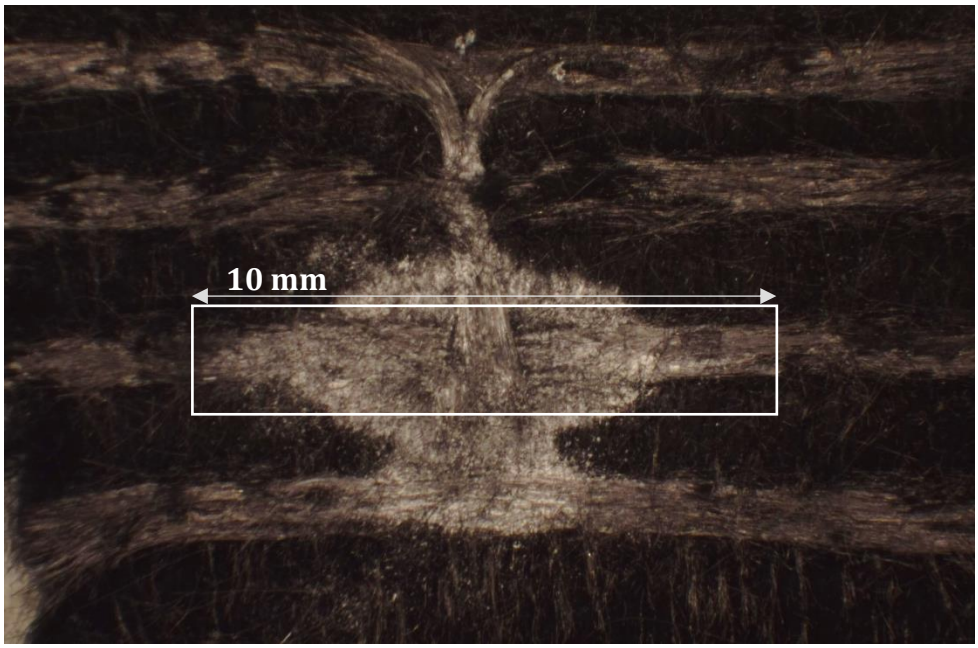


Figure 68: The cross section of the injection study sample shown in Figure 67. The box indicates the extent of the flow in the UD layer demonstrating the largest extent of slurry flow.

4.2.1.5 I_{cf} preform

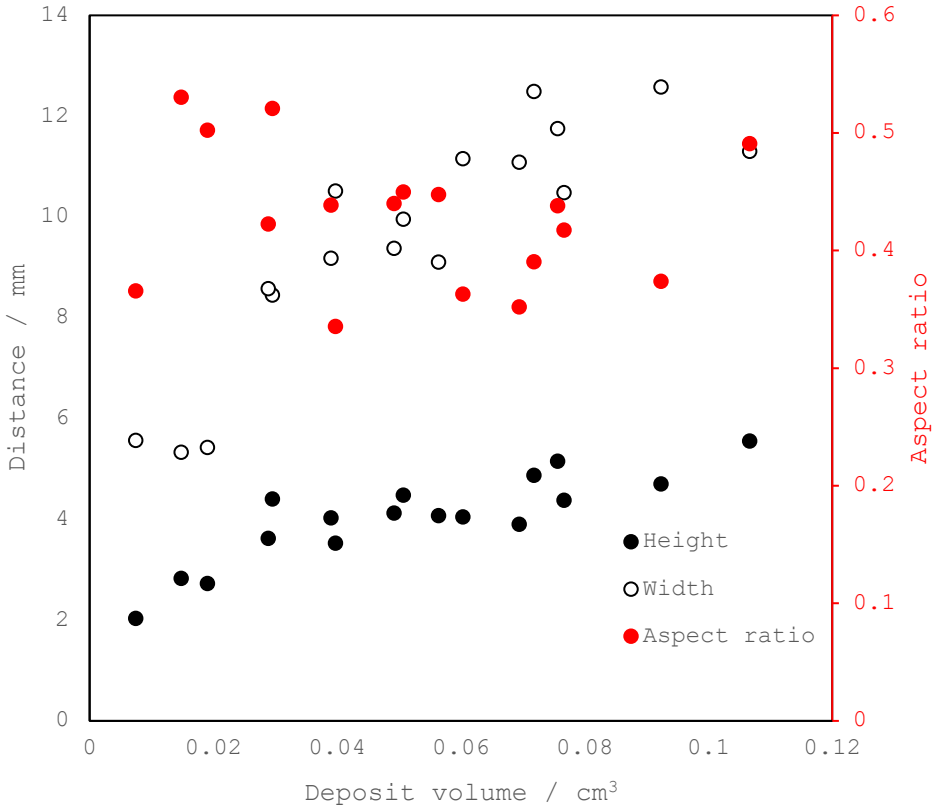


Figure 69: The height, width and aspect ratio of the injection of Al_2O_3-2 into I_{cf}.

For the felt preform (I_{cf}), fewer parameters were investigated and therefore analysis was easier. The only investigated independent variable was slurry volume. In this instance, both height and width of the deposits were consistently shaped, in 2D, as ellipses. The average aspect ratio was 0.43 ± 0.07, which is in the range of the ratio of the transverse and radial permeabilities of the preform: 0.37 ± 0.01. As the shape of the deposit is described well by the permeability ratio, it is thought that the microstructural effects of the preform were minimal, and that capillarity is not a dominant mechanism in the flow front progression. The relation between deposit volume and H and W match well with cubic laws, as shown in Table 25.

Table 25: The regression equations for the I_{cf} injection

Expression	R^2
$H = 10.59\sqrt[3]{V_s} + 0.218$	0.81
$W = 28.04\sqrt[3]{V_s} - 0.541$	0.84

The goodness of fit even at low values of H and W is high. This suggests that the selective impregnation of this material is controllable to within good margins of error. This is likely because while the flow channels were random and therefore not uniform, the porosity was sufficiently high and the tortuosity sufficiently low that flow channels were approximately uniform in each direction. The low values of the intercepts show that, as this was a one component model, the functions were good at describing the major and minor axes of the deposit for the whole range of volumes investigated.

4.2.1.6 STUD preform

The STUD preforms were injected at the same conditions as the I_{cf} preform, but the injection did not proceed in a controlled fashion. For the majority of the samples, there was fluid backflow from the injection hole, with slurry erupting from it onto the top surface. This is thought to be due to the occlusion of flow channels in the preform due to the fibre volume fraction.

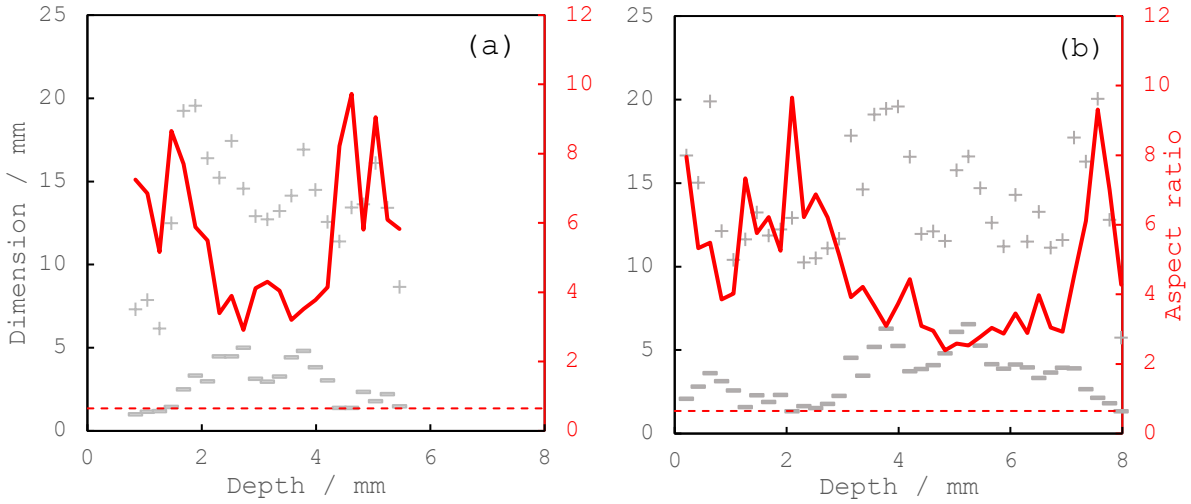


Figure 70: The spreading of slurry in the STUD preforms: (+) Major axis of slurry extent and (-) minor axis of slurry extent in plane as a function of depth. The dotted red line indicates the ratio of the major to minor axis permeability. (a) Injection of 0.1 cm^3 of Al_2O_3-2 and (b) injection of 0.2 cm^3 of Al_2O_3-2.

Unlike in the case of the I_{cf}, there was no clear adherence to the permeability ratio for the minor and major axes. However, these permeability values (k_v(90P)/K(0P)) are not a confidently produced material property, and it is considered that, as the preform was under greater pressure here than in the permeability test, that the permeability may be both reduced and that the ratio may be greater than 1, following the reasoning of Gebart [197]. Considering the major extents, many were at the 20 mm mark which coincided with the diameter of the preform. Hence, it is possible that the slurry flowed to the edge of the preform and then out around the sides into adjacent layers as the path of least resistance, so there is little flow front progression in the minor axis. This would clearly be an issue with the production of the preform itself. The method was chosen out of a number of possibilities, including a low concentration sizing agent adhering layers together, or simply compression between rigid plates with clips. However, no other method gave an adequate balance of 'injectability' and low interlayer porosity. Further testing at different degrees of STUD preform compression could determine whether this factor was responsible for the differences in flow seen. Apart from consideration of the permeability

values, another cause of the along-fibre flow could be the capillarity, which the permeability values do not account for. Greater capillary suction could occur down long channels formed by the fibre layers, where fibre layer nesting is largely present. Assuming channels of a diameter of four or five fibre widths, roughly 25 μm, and comparing to the capillary pressure estimates for certain characteristic pore widths in Figure 36, a result is a pressure of around 1 MPa – a large driving force.

The needle tip was located at 4 mm depth. The structure of the aspect ratio curves are not similar between (a) and (b) in Figure 70, with the exception that there is a region in the middle of the preform that is of aspect ratio closer to the value expected from the permeability. The maximum flow extent is lower and the minimum flow extent is larger in these central regions, located around the vicinity of the needle tip. As this is the location of the fluid exit from the needle into the preform, this will be the location of the fastest flowing slurry. Hence, it is possible in this high speed region, viscous forces may dominate due to the higher capillary number and hence a flow structure more similar to the true permeability ratio may be dominant. This may be a method of inferring an alternative permeability to than calculated in Section 4.1.2.4. Referring back to the general deposit morphologies in Figure 46, this would explain in some ways the differences between the alternating brick stack structure formed at low viscosity, low flow rate and high wettability, and the ellipsoid structure formed at high viscosities, high flow rates and poor wettability. The capillary number is increased in the latter case, from Equation 17, and therefore the adherence to the permeability regime would be expected. In this case, an oblate spheroid of aspect ratio around 2.3 would be the result for W/H.

4.2.2 Numerical simulations of impregnation

A number of tests were initially performed to fine-tune the parameters to produce a stable computation and to explore the extremes of flow behaviour producible by the geometry used. Figure 71 shows the general spade-shape produced by many of the simulations. Clearly, this is a deviation from the alternating brick stack structure produced in the real injection studies. This only occurred in simulations with high permeability ratios; lower ratios produced more ellipsoidal shapes. The results of tests 1-6 are shown in Figure 72, presented as the ratio of the extent of flow in the z axis to the extent in the x axis. The minimum flow resistance in the first UD layer the slurry flowed into was aligned with the z axis.

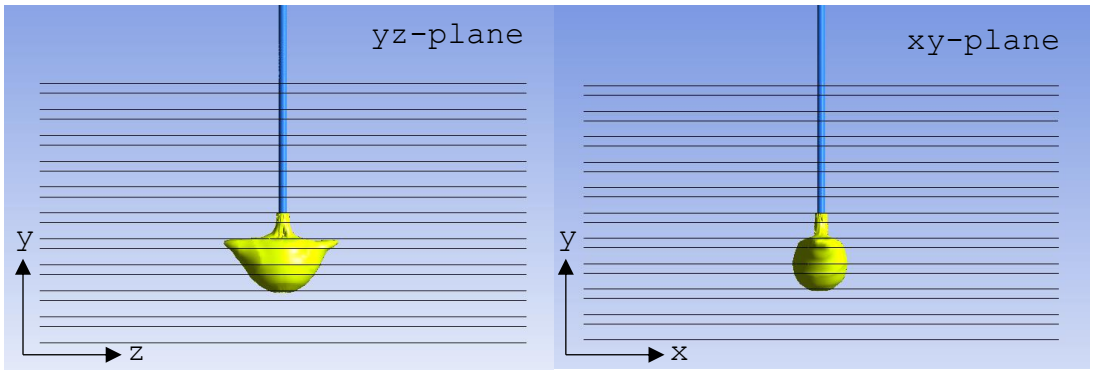


Figure 71: The deposit shape from test 3 in Table 13.

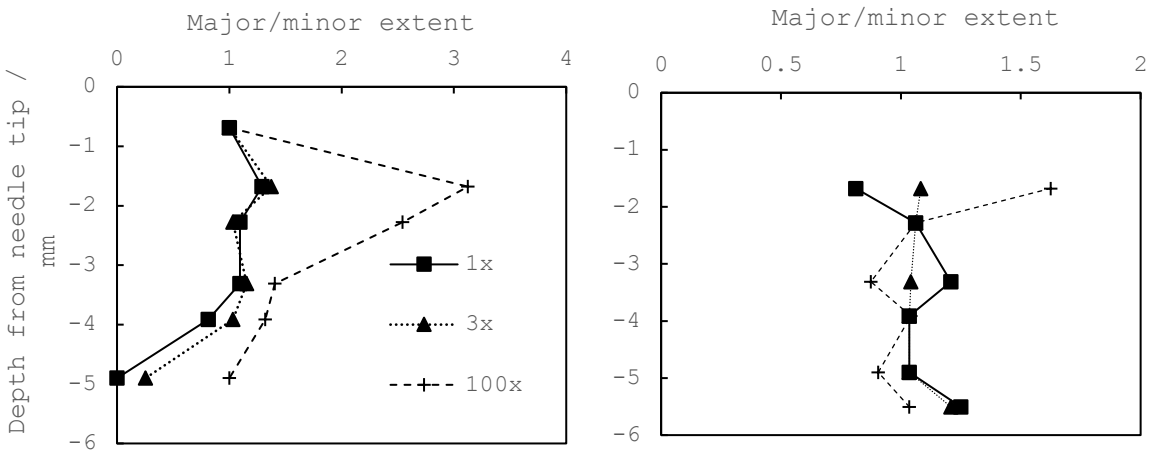


Figure 72: The ratio of the z to x extents of volume fraction>0.7 at 0.08 s for a 1:1, 3:1 and 100:1 viscous resistance in the UD-max:UD-min axes. Left: 0.001 kg s^{-1} flow rate and right: 0.0005 kg s^{-1}.

As the permeability of the different axes change (i.e. the ratio of $k_{UD\text{-}min}$ to $k_{UD\text{-}max}$), the flow becomes anisotropic. It is extended in the direction of lower resistance, and only obvious at high resistance multipliers, as in Figure 72. However, this is only prevalent for the first few millimetres of depth. As the flow enters the preform, it flows outwards along the first UD layer it enters. Fluid then mainly flows downwards and the lower aspects of the deposit become more cylindrical with respect to the y axis. At lower flow rate this is exacerbated further; the maximum extent axis is far lower in magnitude and the little anisotropy that exists in the upper layer drops off far faster at lower depths. This is suggestive that the fluid velocity is high enough that the flow percolates outwards in the first layer due to fluid resistance and streamline alteration, whereupon after this the momentum is downwards directed and does not percolate outwards. As the flow only has a *y* component there would only be perpendicular flow when there is a significant back pressure due to the flow resistance. This is clearly only the case at the level of pressure in the first layer.

Tests 7-9 involve the variation of the transverse flow resistance in the UD layers. The results of this are shown in Figure 73.

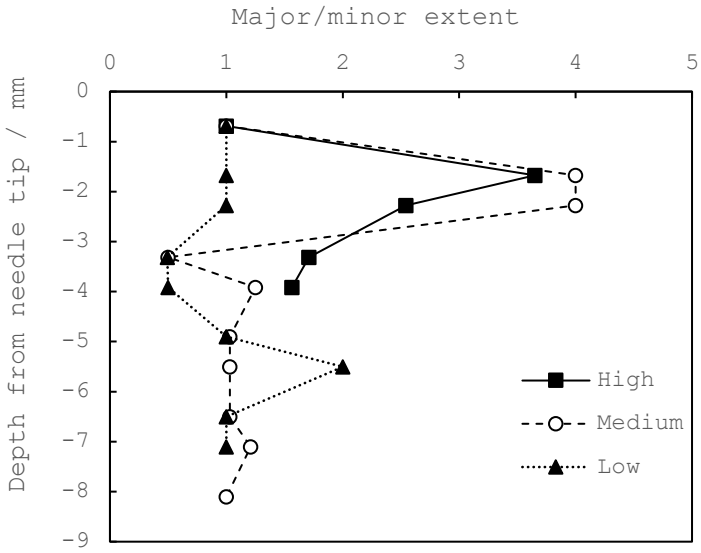


Figure 73: The ratio of the z to x extents of volume fraction>0.7 at 0.08 s for increasing transverse flow resistance in the UD layers, as in tests 7-9.

Where the transverse flow resistance is high (hence permeability is low), there is substantial outwards flow, and poor penetration through the preform. This shows the preferential conversion of motion from transverse to radial. At reduced resistance, the flow can be seen to pass through the preform without any radial flow whatsoever. While the ratio is high at -6 mm, this is due to low absolute value of flow extent, the deviation likely being caused by the mesh resolution (so the surface is artificially extended by the dimension of the element). This flow pattern supports the fact that the transverse flow in this is mainly influenced by only the first layer and the pressure in this layer and that as the fluid reaches the lower part of the preform, most momentum is directed downwards and there is little backpressure that warps the streamlines into the radial directions.

Tests 10-15 do not show any difference in the volume fraction profile, and therefore it can be concluded that the radial flow in the R layer does not create the more cylindrically symmetric lower part of the deposit profile. This supports the line of argument above. Increasing the mass flow rate, test 16, to show the effect on the flow lines, demonstrates the velocity component progression over time, displayed in Figure 74.

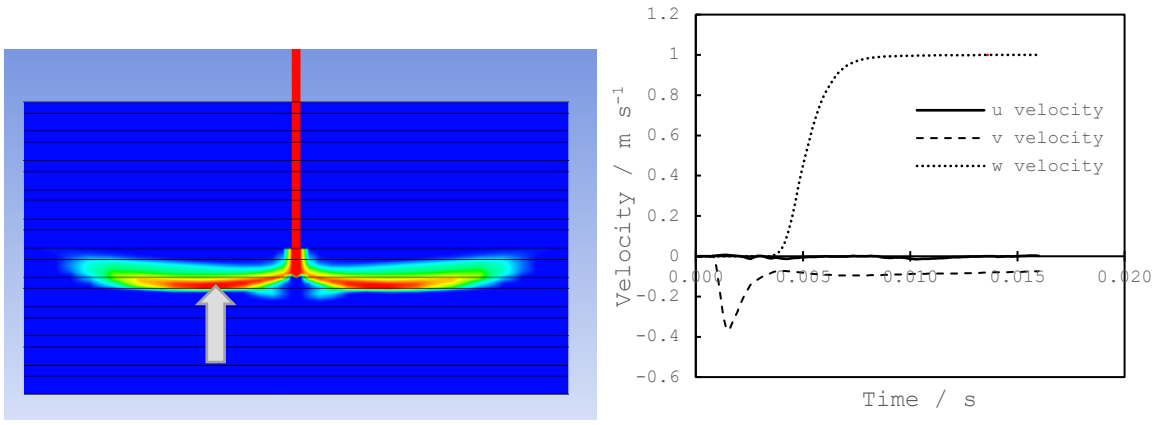


Figure 74: (right) The velocity distributions for test 16 (Table 13) at the location indicated by the arrow at 0.005 s in the simulation, (left) volume fraction plot.

The off-centre position from which the data is taken, in the upper UD in which the majority of the radial flow occurs, shows that initially there is a high y-direction component to the fluid velocity. Then, the z-direction velocity increases rapidly to a plateau, presumably as the streamline develops in the z-direction.

Tests 17-19 investigated the effect of using slurries of different properties; these did not produce any vast structural differences. A slight extension of the major axis is noted with the reduction in surface tension that slurry Al_2O_3-24 possesses, but no change is observed in the spreading patterns in any other layer. Figure 75 shows the minor scale of this change.

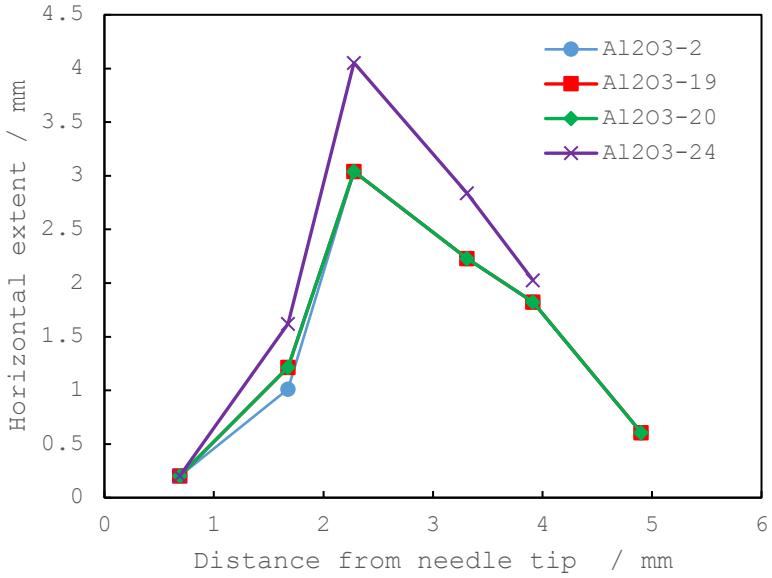


Figure 75: The z-axis extent of the slurry volume fraction (border at volume fraction > 0.7) as the slurry type changes.

Replacing the permeability variables for those determined experimentally in this work, a very different deposit profile was produced. The deposit was a cylindrically symmetric oblate spheroid, displayed in Figure 76.

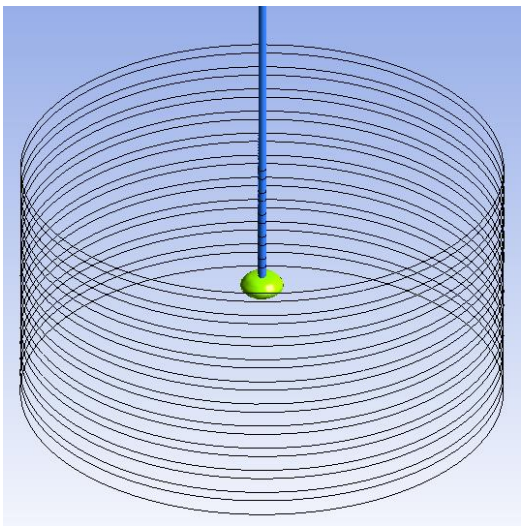


Figure 76: The deposit morphology from the injection into a preform whose permeability tensor components are those determined experimentally in this project.

This lack of preferential flow in the axis dimensions shows that, firstly, the lack of the inertial permeability terms did not allow real behaviour to be obtained. Inclusion of the permeability values from a Hazen-Dupuit fit of the data did not allow the calculation to be

performed at any investigated mesh density or time step duration; in all cases the problem was rapidly divergent. This can occur in highly anisotropic porous media (i.e. >1000x difference in permeability components) or where there are large pressure gradients in the flow direction [241]. However, better initial parameter guesses may have allowed the calculation to proceed [254].

The suitability of the experimentally derived permeability values were investigated with a separate modelling procedure. The preform permeability as a function of the number of layers of R and UD were determined analytically using Equation 25 in Figure 77a, and the permeability of model preforms using the empirically determined values of permeability in section 4.1.2.4 were simulated, see Figure 77b.

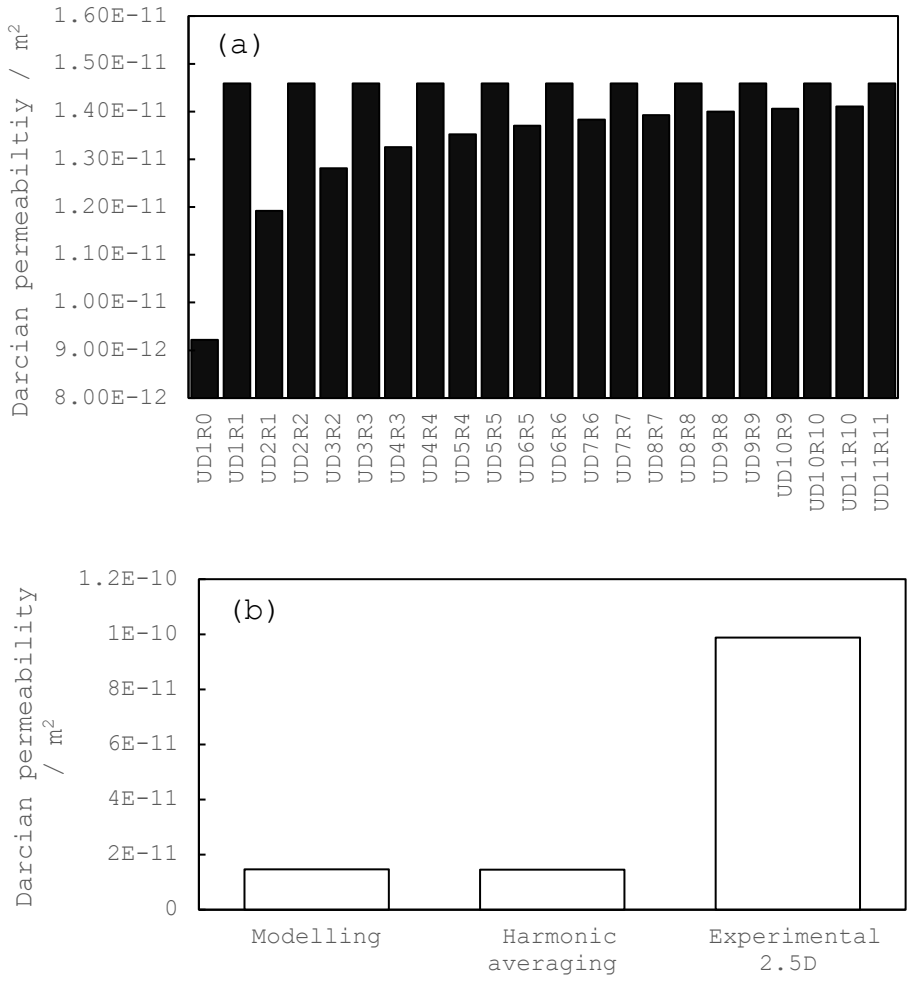


Figure 77: (a) the permeability of the preform as it builds up layer by layer, (b) the comparison of the model 2.5 preform permeability to the empirically measured value.

The preform permeability tends towards 1.47 x 10^{-11} m^2, based on the component UD and R layers. This value was obtained both through the numerical scheme and also through the harmonic averaging. By taking Equation 25, and substituting *N* for *2x+1* where *x* is the number of UD layers, and *L* for *x* l_{UD}*+ (x+1)* l_r to represent the case of unequal numbers of UD and R layers and taking the limit of the function as *x* tends to infinity, the result is Equation 27.

$$\lim_{x\to\infty}\left(\frac{xl_{UD}+(x+1)l_r}{(x+1)\frac{l_r}{K_r}+x\frac{l_{UD}}{K_{UD}}}\right)=\frac{(l_R+l_{UD})(K_rK_{UD})}{l_RK_{UD}+l_{UD}K_R} \tag{27}$$

On substituting the values of the layer widths and transverse components of the permeability into Equation 27, the correct value is obtained. In the case of equal numbers of UD and R layers, the proportion of each is constant for any absolute number of layers, hence the permeability is always 1.47 x 10^{-11} m^2. However, as the number of layers increases and there are unequal numbers of each layer type, the contribution of the 'extra' layer to the overall ratio of R to UD layer thickness tends to 0, hence the value of the permeability tends to the limiting value.

This suggests that the computational procedure is good and that no major errors were present in the mesh or problem discretisation. The transverse permeability values calculated are not close to the 2.5D transverse permeability determined experimentally; $K_{exp}/K_{Numerical}$ is about 7. This suggests that the model (with the STUD and I_{cf} derived values) was a mediocre representation of the preform in this flow direction, with flow less facile. However, this suggests that the ratios of the transverse permeabilities are not responsible for the unrealistic flow behaviour seen in Figure 76. Using a simple cross-sectional area-weighted average of the STUD and I_{cf} layers for the in-plane porosity of the 2.5D preform, as described by Ahmed et al. [246], yields a permeability estimate of 1.31 x

10^{-9} m^2. This is around 1.3x the in-plane permeability measured for the 2.5D preform, and is similar to the permeabilities determined for most of the in-plane layers. Given that the injection behaviour is certainly not that found in the real material, it suggests that the areas that the model does not account for, i.e. physical structure, tortuosity and capillary action, as opposed to the in-plane permeability differences (notwithstanding the corollary discussed at the end of section 4.2.1.6), are incredibly dominant in the real injection behaviour. Given that the injection behaviour in the STUD layers is high-aspect ratio, it suggests that only the capillarity could induce upflow to the degree seen in the injection studies (slurry flow upwards from the needle tip), or substantial flow turbulence (and this is not supported from the preform channel width analysis in the preform characterisation section, or included in the model). Hence, the capillarity must be a hugely dominant aspect of the impregnation, and has been seen to cause huge aspect ratio flows not only in the 2.5D material but also possibly the STUD preform.

The modelling work has given insight to the mechanisms of the injection into the 2.5D preform. However, no adaptation to the model, presented or not, could reproduce the alternating brick stack shape seen. For this reason, it is likely that the modelling approach itself cannot reproduce the behaviour with the present set of parameters. As discussed in previous sections, the approach of permeability assignation to free areas of space does not account for capillary effects. However, structuring the geometry to incorporate these effects would make the computation too expensive for both the available resources and for easy parametric sweeping. Other approaches, such as more bespoke modification of the underlying equations of motion to incorporate directional sink terms replicating the capillarity or attaching one dimensional elements to nodes of the mesh, may help in the development of a truer to life predictive tool, but would require that the modelling methodology was overhauled completely. It is possible that the refinements to the

procedure described in section 3.5 may modify the shape of the observed free surface to closer to that obtained experimentally. However, the velocity distributions in each layer do not show there being much of a drive for this and this is the basis of the sharpening schemes used in Fluent.

The issues with multiphase porous flow analysis were discussed in section 2.3. These issues centre on the difficulties in defining the structure of the porous medium well enough in the first instance. The definition of anisotropic permeability is, therefore, a workaround. Another workaround employed here is to treat the fluid as a single phase fluid instead of the particle-laden liquid that it is. The scale of the porosity in preforms is similar in scale to the particles used in ceramic slurries for composite manufacture, which unfortunately results in microscopic interactions between the two which will modify the porosity of the medium as a function of time over the injection. Attempting to represent this as a model is a challenge; these microscopic flow-influencing mechanisms cannot be resolved while still performing a transient, multiphase simulation to obtain a macroscopic free surface evolution due to the huge difference in scale and mesh resolution and simulation size this would require. The empirical effects of these clogging behaviours are discussed in the following section.

4.2.3 Tow suction and capillary interactions

4.2.3.1 Sample preparation

The spectrum of sample fibre fraction is shown in Figure 78.

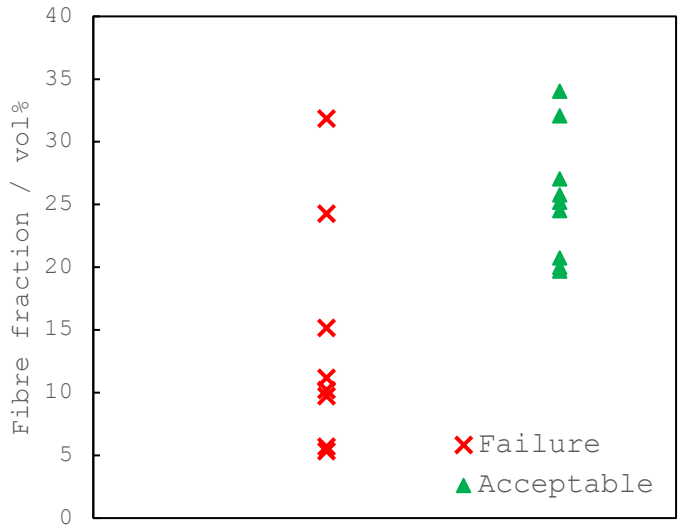


Figure 78: The fibre fractions of PTFE tubing samples produced. The green triangles represent the homogeneously packed samples, and the red crosses the heterogeneous samples displaying fibre clumping and large regions of porosity. The x-axis holds no information.

Samples produced were level and only slightly curved due to the tubing. It can clearly be seen that a large proportion of samples were not appropriate for analysis due to heterogeneous fibre distribution and the existence of obvious and large internal pores. The effect of this is to deny knowledge of the average flow cross section or the effective channel widths. Hence, a reliable and consistent fibre spacing cannot be assumed. For this reason, the samples were not included in the analysis.

Samples were not measured for capillary constant as a result of a separate investigation showing that the Washburn method was unsuccessful for reproducing the fibre contact angle. However, as the capillary constant, determined via a completely wetting liquid like hexane, would have stripped away the specific geometry differences to give a

representative geometrical description. This may have been a useful parameter to measure, however the movement of fibres during hexane wetting or subsequent drying cannot be ruled out.

4.2.3.2 Tow suction

An example of the mass vs time (and calculated flow speed vs time) is included in Figure 79. The Washburn equation produces a tendency to infinity for flow speed at low values of time, due to the exclusion of inertial effects relevant at the beginning of the suction. This is improved by alternate flow equations such as the Bosanquet equation of motion [255]. The durations, gradients and particularities of the inertial, transitional or frictional regimes were not found to be strongly related to fibre volume fraction, and hence are not referred to further. Stange et al. [256] describe the durations of these regimes as being based on the Ohnesorge number, *Oh*, the ratio of the viscous to inertial and surface tension forces, $\sqrt{\frac{\mu^2}{\rho\sigma R}}$. Low values of Oh yield long transitioning times between the inertial, frictional and gravitational regimes. As the viscosity, density and surface tensions of the fluid are constant between tests and only the pore sizes R are changing, it would be expected that the durations of these regimes should correlate with the volume fraction. The lack of correlation may speak to a more diverse channel width distribution than expected, hence provide evidence of clumping of fibres in the tubes. The mass gain of the tows, relative to the as-prepared mass, at 300 s when wet, and after drying, are shown in Figure 80 along with the measured visual extent of the slurry (highest point slurry can be seen through the translucent PTFE tube). From these two former measurements, the water content of the infiltrant liquid can be estimated, as is shown in Figure 81, by subtraction.

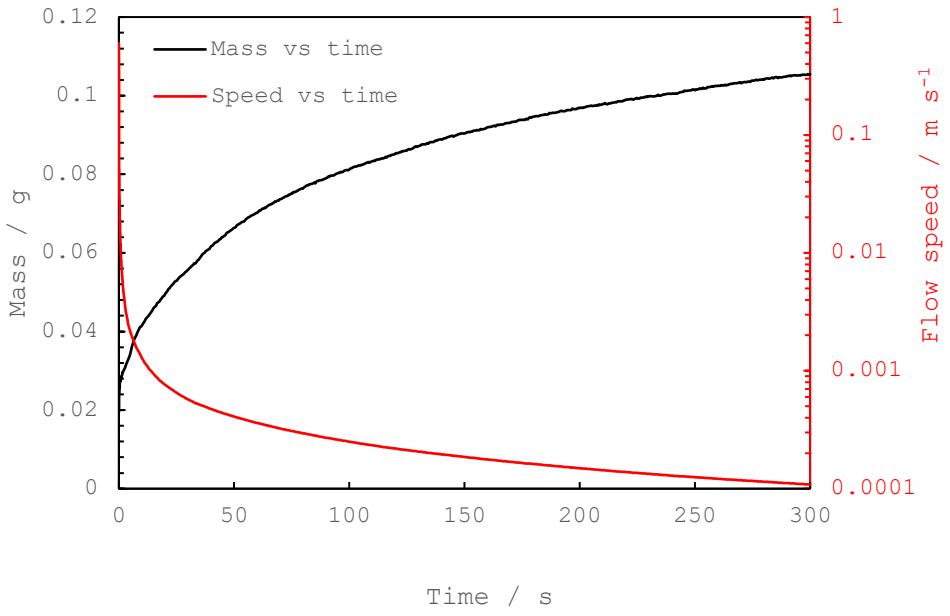


Figure 79: An example of the mass gain and calculated flow speed for the 10 vol% sample.

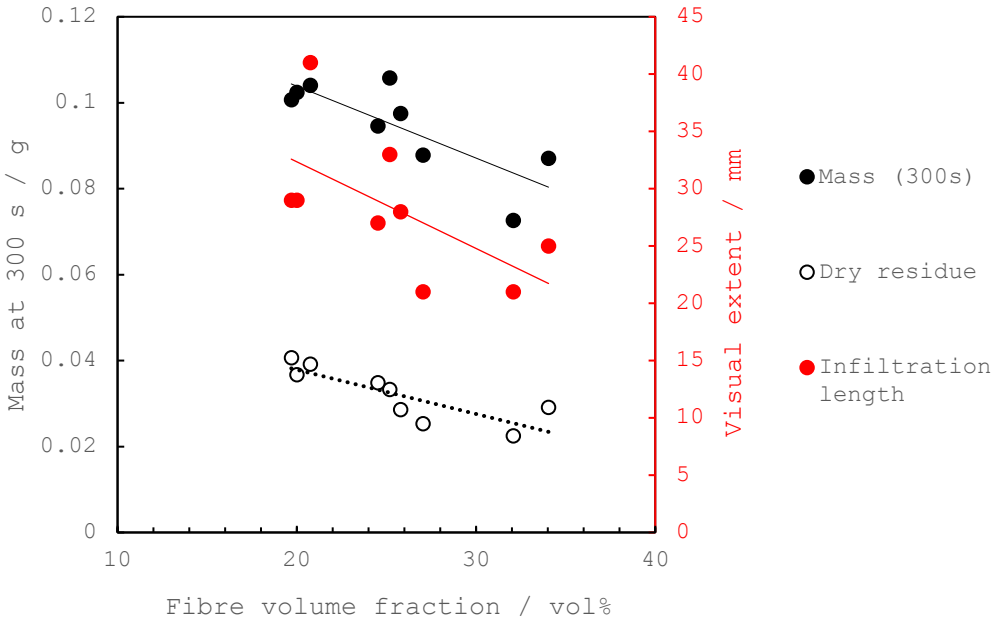


Figure 80: The mass gain relative to as-prepared while wet at 300 s duration and after drying, in addition to the visual extent of the penetration.

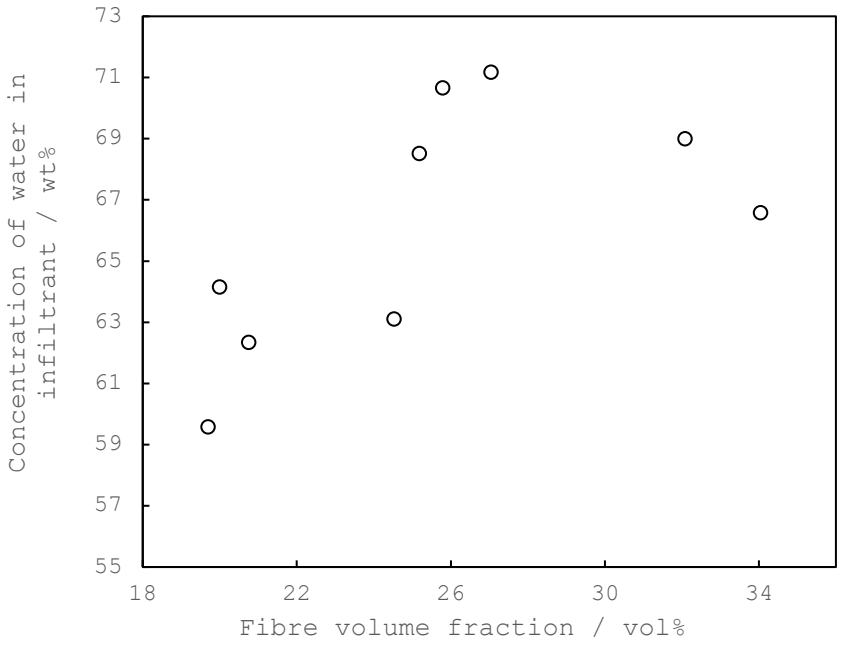


Figure 81: The concentration (wt%) of water in the infiltrant liquid for different fibre volume fractions.

The results show that an increase of fibre content above 20 vol% yields a reduction of penetration as calculated by both visual inspection and mass gain. Correspondingly, the percentage of water in the infiltrant liquid is shown to increase. This could be due to the fluid part of the slurry being able to be sucked through narrower channels where particle loaded liquid could not, the very definition of clogging as an effect. However, the correlations against these parameters are not strong. The large quantity of failed samples indicates that production of samples with a representative volume percentage is not easy, and the internal pore width distribution is uncertain. This distribution will dominate the sorption response. Mercury porosimetry could have been employed to determine the actual pore size distribution in the material.

Using the assumption of a square array of equally spaced fibres in the x and y direction (a wholly unrealistic situation, but useful for illustrative purposes), the nearest neighbour spacing in the tube as a function of fibre volume fraction can be shown to follow Equation 28. The derivation of this can be found in Appendix 2.

$$d = \frac{\sqrt{\pi} r_f (r_t - r_f)}{r_t \sqrt{V_f}} - 2r_f \tag{28}$$

Here, r_t is the tube radius, r_f is the fibre radius and V_f is the fibre volume fraction. This is illustrated graphically in Figure 82.

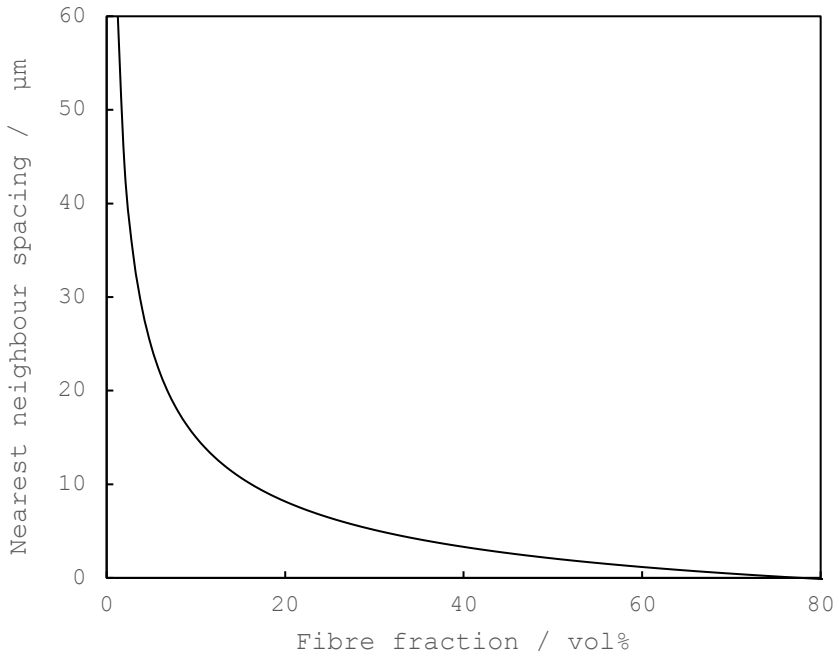


Figure 82: The dependence of nearest neighbour spacing on fibre volume fraction for an ideal square array of equal sized circles bounded by a circle.

This is presented in the general and highly idealised case because the determination of spacing in non-regularly packed circles of this nature is not trivial [257].

Comparison of the particle size in the slurry to these calculated spacing shows that the approximate order of magnitude expected in between fibres (which can only be smaller than that calculated in Equation 28) is consistent with the order of magnitude of some aggregates of the primary particle size in the slurry; the particle size distribution of the bodies in suspension was monomodal, centred around 1.29 µm (SE = 0.09 µm). Hence, if deposition is to occur on fibres or at fibre contact regions, it is conjectured that a clog

could build reasonably easily, thereby explaining the clogging behaviour possibly observed. Cross-sections of the 32 vol% fibre sample were investigated microscopically for the powder distribution as a function of height from the submerged tip of the tow.

4.2.3.3 Micrograph analysis

The volume fractions of the pore, fibre and deposits as a function of distance from the submerged tip are shown in Figure 83. It can be seen that the concentration of the deposit does indeed decrease as a function of distance. However, there is no sudden discontinuity; indeed, the data is incredibly unstable so anything but a general trend considering the standard errors presented would be unwarranted. Instead, there is a commensurate increase of fibre concentration as the distance increases.

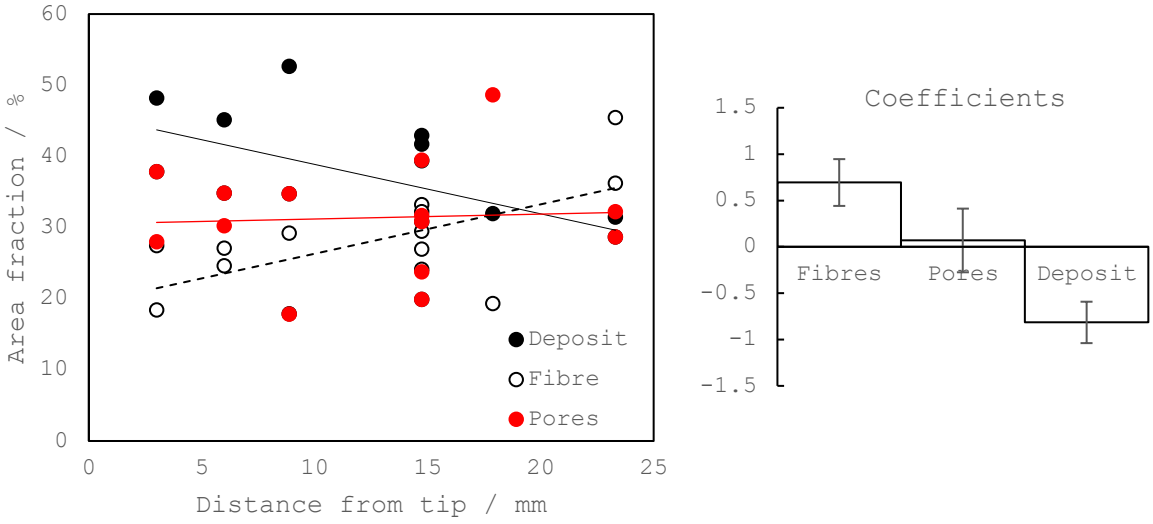


Figure 83: The change in deposit, pore and fibre volume fraction as the distance increases from the submerged end of the encapsulated tow.

This fact potentially accounts for the apparent randomness seen in the Washburn traces. One of the assumptions of the law is that the substrate remains unchanged over the process. Obviously, the fluid phase contains solid that, if dropping out of suspension and

adhering to the substrate, would constitute a change in this sense. Also, given that the method used to produce the tows should not result in a biased fibre distribution, it can be assumed that the fibre distribution changes over the course of the suction. That is, the ingress of the slurry may cause the fibres to move to the edges at the bottom of the region (the images were taken of the central regions of the fibre tow) or to ride up. The former is more likely, as no substantial increase in fibre height from the top of the encapsulated tow were seen. In this way, the slurry ingress may produce a converging set of pores up the tow, which would increase the effective contact angle in the manner found by Chassange [189] and make slurry impregnation more challenging. Equally, it would constrict pore widths in the upper regions exacerbating any clogging observed.

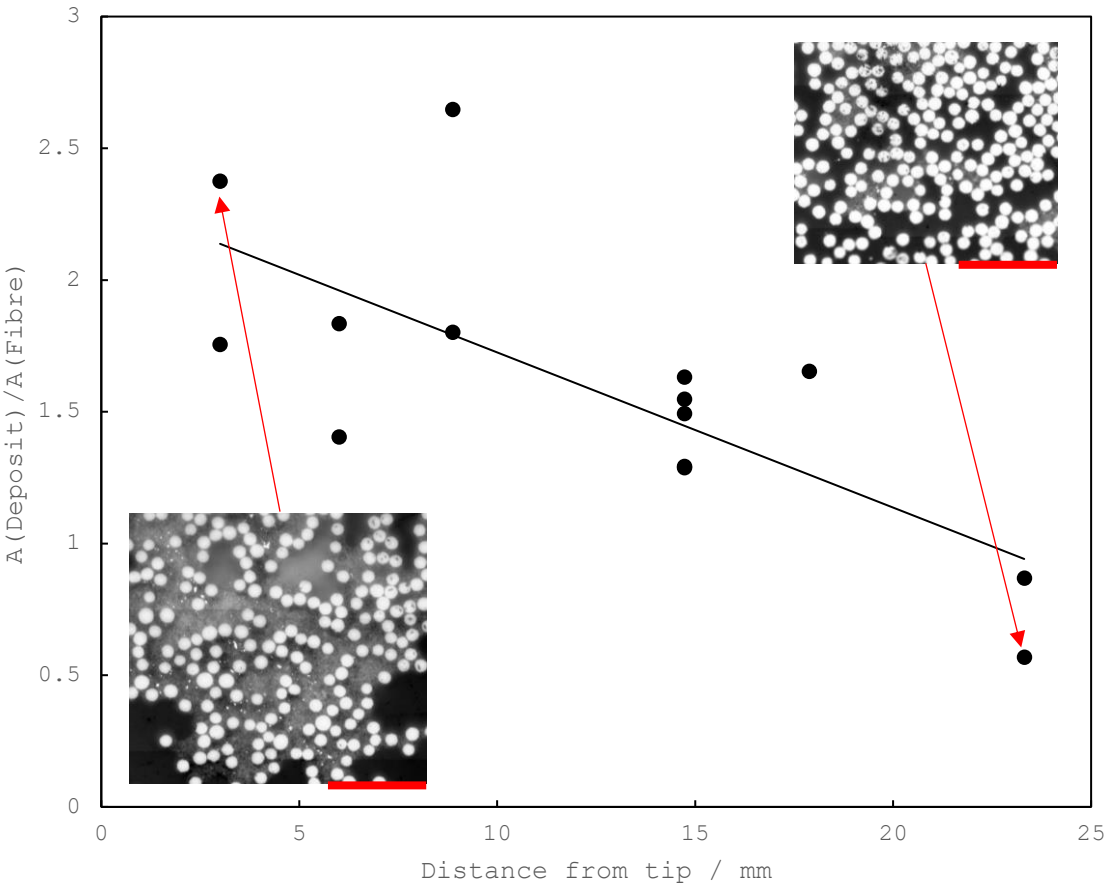


Figure 84: The ratio of deposit area to fibre area as the distance from the submerged tip increases. The inset micrographs show representative images of the tow. The black areas show pore space, the white circles represent fibres (the red scale bar represents 80 μm) and the grey represents Al_2O_3 powder.

Figure 84 shows the ratio of the thresholded deposit area to the fibre area, and includes as insets the images of the extremes of the data set. It is clear from the images that the concentration of the deposit is vastly reduced at higher penetration lengths and that the deposit that is present exists in regions of higher fibre fraction, which is consistent with a capillary suction mechanism. However, given that the absolute value of fibre fraction increases at higher penetration length, one would expect from the same argument that the deposit concentration should also increase in line with increased capillary pressure expected, as in Figure 36. As a result, and in line with the trends seen in Figure 80 and Figure 81, there is evidence that clogging is an active flow front retarding mechanism in the case of capillary suction in fibre tows.

The spreading in the UD layers can be seen to be related to the capillarity, contact angle and surface tension, in addition to viscosity. The dimension of the spreading in these layers then, exemplified by the W measures in the Injection Studies section, may be related to the sorption in the Lucas-Washburn equation, Equation 29. To test the closeness of fit of the W spreading to the Washburn equation, the measures used in the regression procedures were combined to produce:

$$\left(\frac{W}{2}\right)^2 = \frac{A\,\gamma\,cos\,\theta}{\mu}\frac{d}{\dot{d}} \tag{29}$$

where d is the depression length in the syringe and $\dot{d}$ is the depression rate, to give time. This equation is, then, in the same form as the Washburn equation when converted to volume in place of mass. A is a structure factor. Over the whole data set, W was then plotted against this function. This is shown in Figure 85.

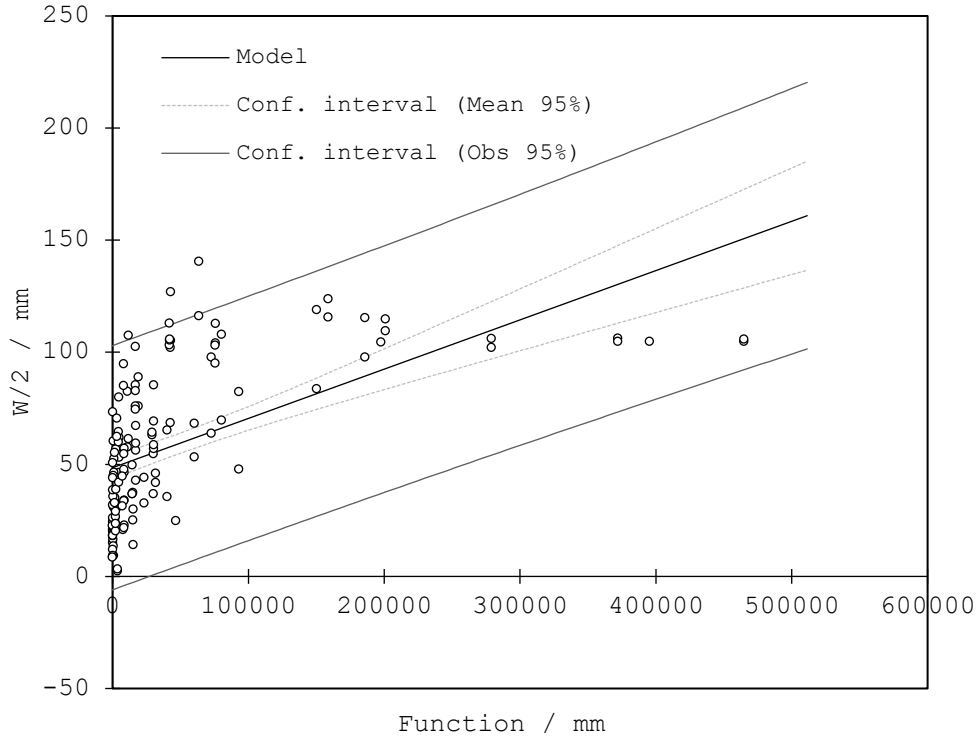


Figure 85: The results of the regression of W with the Washburn-sorption predicted values.

Clearly, there is little correlation between these values. This serves to show the influence of both the particulate nature of the fluid and the pressure driven nature of the flow. The flow is also multidimensional, hence does not obey Darcy's law. This is an important comment on the combined nature of the process.

The injection studies, tow suction and numerical simulations have all demonstrated the central part that the capillary action has to play in defining the flow front morphology. No solid and straight-forward relation has been seen to link the two, however. Equally, in considering the influence of the slurry properties, one must consider how the particle size distribution would affect the overall impregnation of the preform. The tow suction studies were a proxy to investigate the influence of changing particle size. As the particle size to gap size ratio, as represented by volume fraction of fibres, increased, the impregnation can be seen to have been inhibited. This shows that the influence of the capillary suction, for a slurry of nominally equal viscosity and wetting properties, was decreased at higher

particle size distributions. This is a factor that has not been accounted for in the injection studies. In fact, for the purposes of the analysis of injection deposits, the slurries were treated as single phase fluids whose flow extent was defined by the solid residue left behind. Negating some of the assumptions associated with this – for example that the liquid content of the slurry may be 'wicked away' from the solid particles and flow further than the residue as suggested in Figure 81, or that if this was to occur it would have a reduced viscosity due to the lower solids content – there are still issues. Slurries with particle sizes larger than the Al_2O_3 examples, such as the UHTC slurries described in Section 4.1.1.2, may suffer from greater clogging in the high fibre content locations, hence the flow progression would be completely different from that predicted. Indeed, given their higher viscosity, the main flow channels may be the R layers. In fact, previous work [17] has indicated that this is possibly the case for the case of UHTC/phenolic resin/acetone slurries. In any case, the injection studies are accurate for the given input ranges with the caveat that the expected level of tow clogging is similar to that found in this study. The tow suction has highlighted areas that need to be considered in order to extend the predictions, qualitatively, outside of the ranges of values studied. Particle size is not treated in the numerical simulations either. Both the fluid phase and the porous phase are treated as continua, lacking any sort of internal or real structure. While there is no consideration of capillarity here, the lack of real-world behaviour observed can be inferred to stem from the lack of inclusion of this in the model.

4.2.3.4 Microchannel suction studies

The microchannels did not display continuous penetration length behaviour. Figure 86 shows the penetration length for the different width channels. It can be clearly seen that

notable penetration only occurred in three cases: for two of the 6 and one of the 15 µm width channels. The intention of this study was to correlate the channel thickness with the impregnation extent, which are generally recognised in literature to be inversely correlated [258, 259] and to detect any differences due to the high solids concentration, i.e. the interplay between high clogging potential and high capillary pressure in narrow channels. However, the failure of the channels to induce flow, and in such a non-continuous fashion, does not suggest that this is due to the expected correlation as described. Instead, it was inferred that there was some issue with the surface quality of the channels due to the manufacturing method, which made the wider channels, those with a greater time under laser treatment, less wetting to the fluid. The degradation of the acrylic plastic may deposit non-wetting contaminants on these wider channels, inhibiting suction. The surface quality (i.e. roughness) was observed to be approximately equal for all channels, hence this explanation was dismissed as a potential cause of the reduced imbibition. This conclusion was not useful in itself, but this information is included as a follow-up point for further work. In particular, use of laser-etchable glass may produce a more suitable wetting substrate for these fluids for further work.

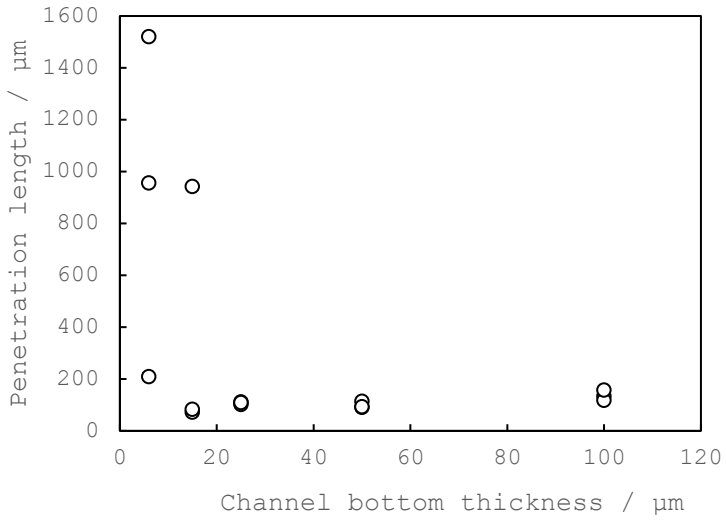


Figure 86: The penetration length of the microchannels shown in Figure 13 for full reservoirs of Al_2O_3-24.

4.3 Composite performance and analysis

Composite specimens were produced to observe the microstructural features and to gauge the performance of these ordered multi-ceramic materials.

4.3.1 Microstructural analysis

A large sample (30 x 20 x 18 mm^3) was produced and the interface location and structure investigated.

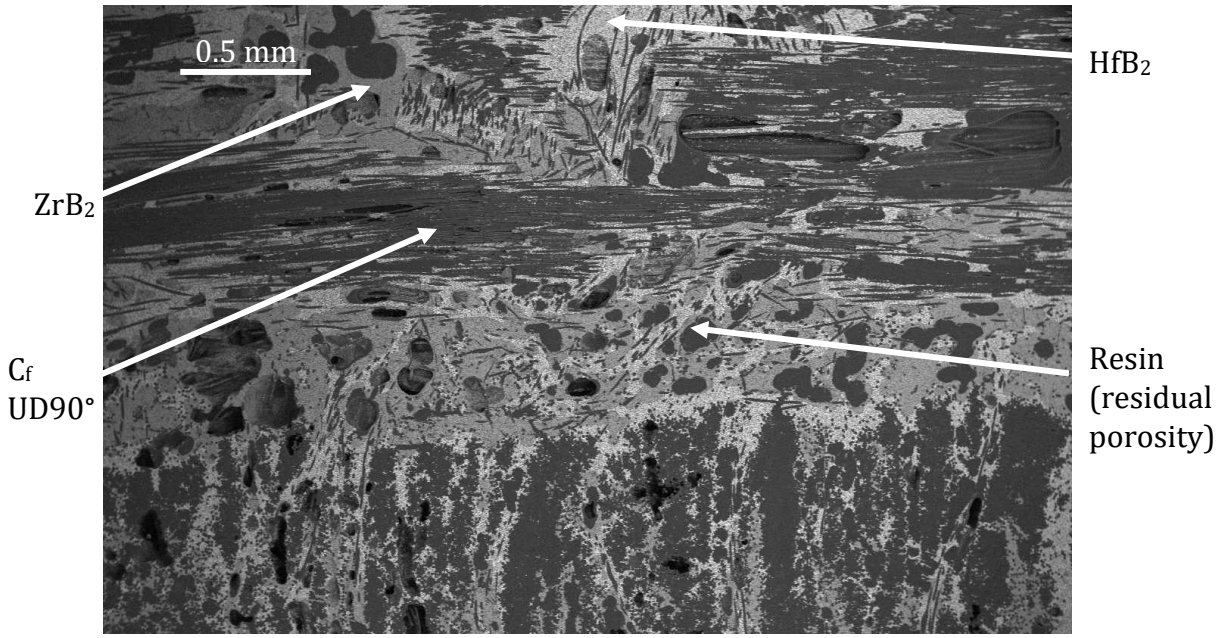


Figure 87: BSE image of a position along the interface at the 0 mm surface. Three contrasts can be seen; bright grey (HfB_2), medium grey (ZrB_2) and dark grey (carbon: fibres, resin or PyC).

The interface can be seen, as in Figure 87, to be neither flat nor linear. Specifically, inclusions of the darker contrast ceramic phase can be seen distributed across the whole 3-4 mm height of this micrograph. Equally, there are large bubbly features of carbon contrast. This is likely to be mounting resin that has filled in the porosity released during the curing and pyrolysis of the phenolic resin. There are also large bubbly unfilled pores that showed that they were closed during the mounting procedure. This shows that the

method includes substantial macroporosity from the inclusion of the condensation polymer, and potentially even the injection.

The concentration gradient was mapped at different locations from the top of the sample (ZrB_2 pure) to the bottom (HfB_2). Superimposing each of the graphs of concentration gradient in Figure 88 clearly shows the range of depths at which the interface exists across the whole sample. By presenting the 94 and 6% HfB_2 as the tips of error bars, this interface can be replotted in Figure 89 to show how the location of the interface varies across the component.

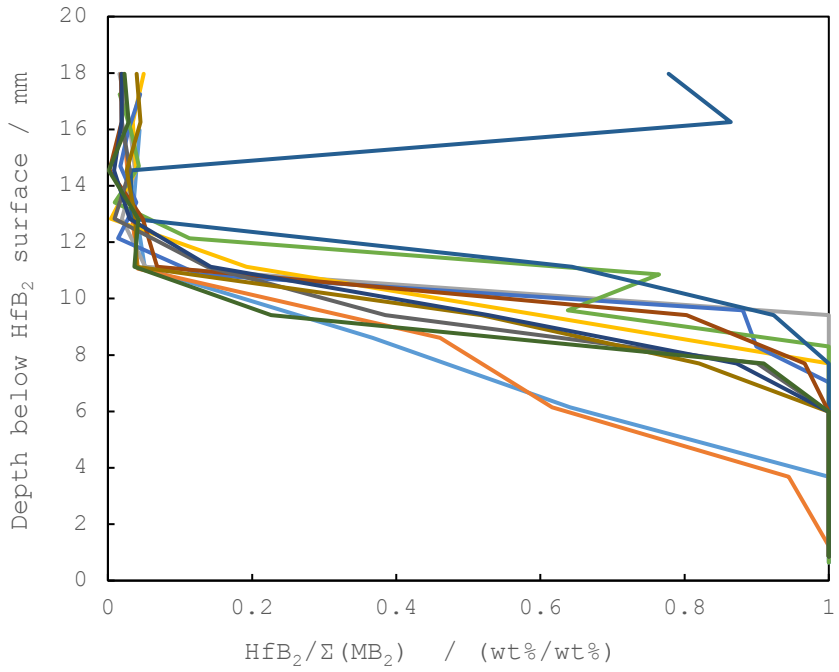


Figure 88: Concentration gradient for all the through-thickness scans at numerous depths and cross-section co-ordinates superimposed to show the variability of interface starting depth, thickness and gradient.

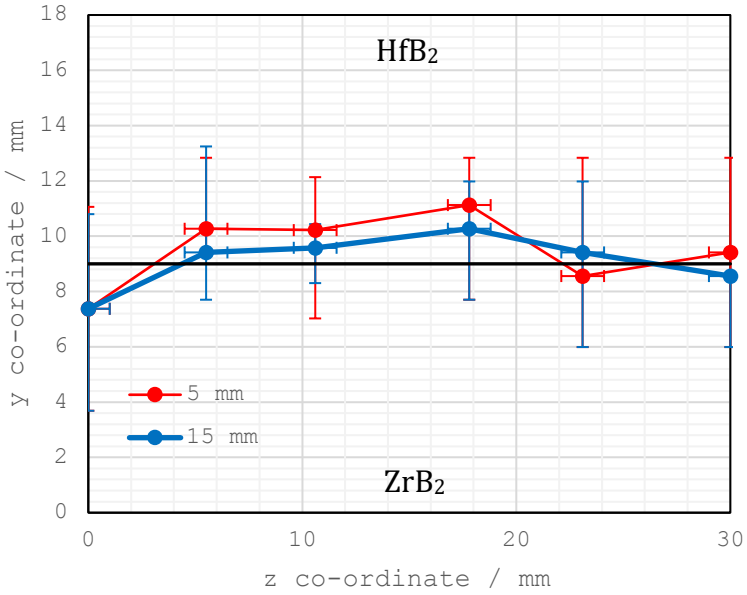


Figure 89: A schematic representation of the interface position for the sample investigated both at a 5 mm and 15 mm x co-ordinate position through the length of the sample. The central point represents the 50:50 concentration interface, and the upper and lower error bars represent the location of the 94% and 6% wt%(Hf)/[wt%(Hf)+wt%(Zr)] depths. The thick black line represents the nominal 50:50 level, the goal configuration.

The black line indicates the desired interface in the component. The interface locations and thicknesses are centred on this value, but there is significant irregularity. Particularly, there seems to be a bias towards HfB_2 in that the layer was thicker than that of the ZrB_2.

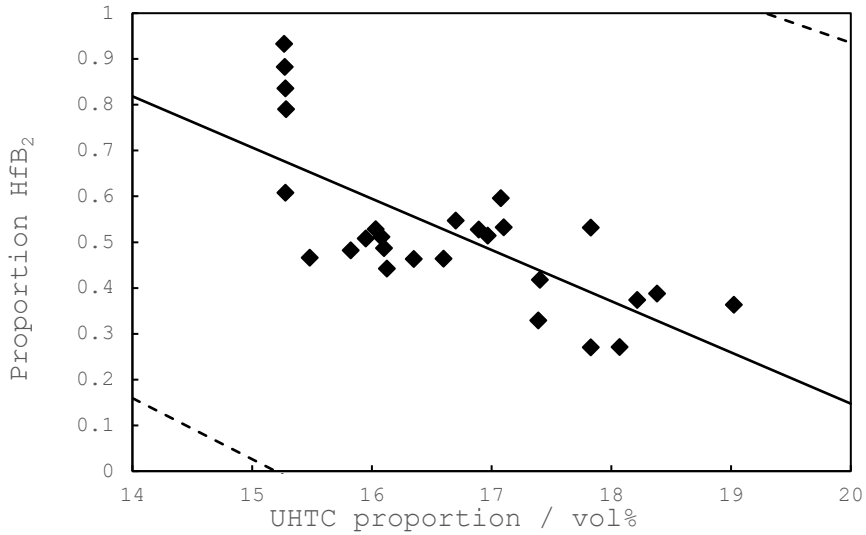


Figure 90: The proportion of HfB_2 as a function of overall UHTC content in the samples. The solid line indicates the line of best fit and the dashed lines indicate the confidence interval within one standard deviation of the regression.

Figure 90 shows the proportion of HfB_2 in the samples produced for mechanical testing as a function of total ceramic content. This figure shows that as the overall ceramic content of the samples increase, that the proportion of the HfB_2 in the sample decreases. Given that the materials are produced with the HfB_2 injected first into the lower half of the preform, it suggests that the higher volume fraction UHTC materials are better impregnated when the total content of HfB_2 is lower. Hence, the ceramic content increases most when little HfB_2 is in the intermediate product. As the second injection results in the attempted saturation of the preform, it suggests that this is more effective when the HfB_2 content is low. Hence, the first injection can be inferred to occlude a significant amount of space with a reasonably high closed porosity proportion as far as the second impregnation is concerned. This is likely due to the non-efficient packing of HfB_2 deposits in the first stage, trapping porosity both within and behind the PR region (as PR will become foamy and porous after curing). It can be supposed that the most densified samples will also be the least well-defined (in terms of the 50:50 intended interface).

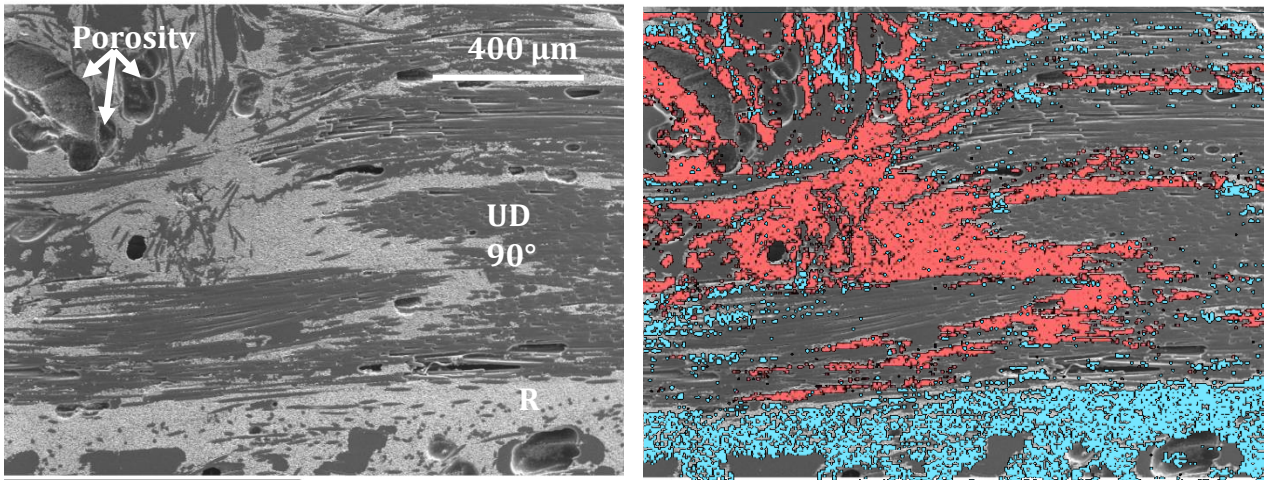


Figure 91: An example of an EDS dotmap at a transitional region at a depth of around 10 mm in the sample with (red) Zr and (blue) Hf indicated.

The interface region is not of high quality. In addition to the bubble features shown in Figure 87 and Figure 91, there are also concentration overlaps that are not necessarily

desirable and certainly not intentional. Equally, there are significant cracks between the different ceramic phases shown in Figure 92.

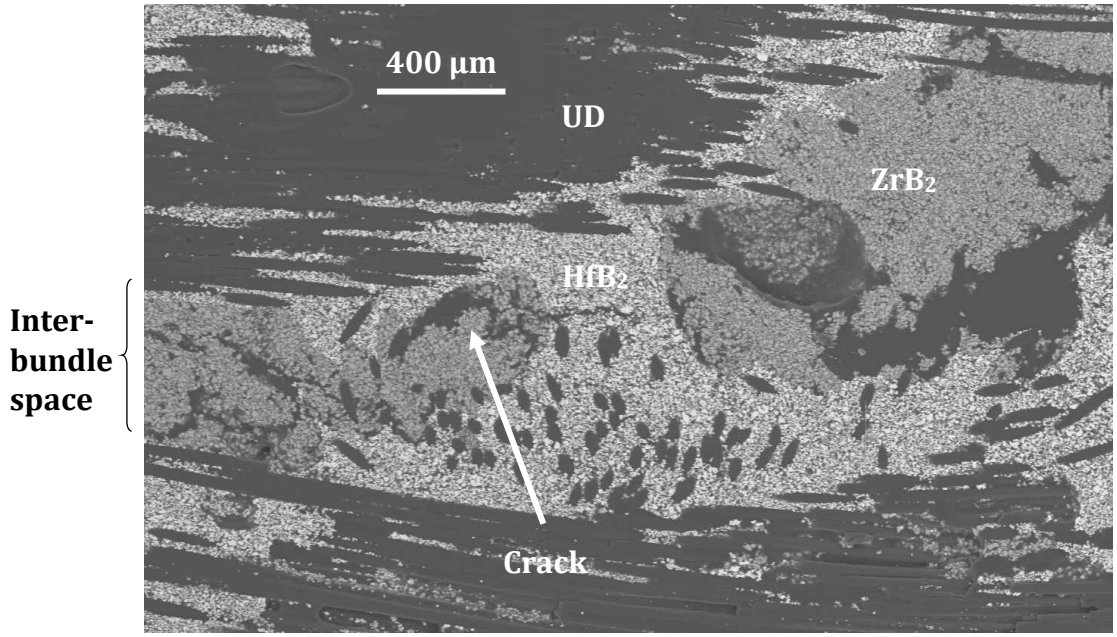


Figure 92: A BSE image of multiple phases and the presence of cracks in the C/UHTC matrix. Three contrasts can be seen: bright grey (HfB_2), medium grey (ZrB_2) and dark grey (carbon: fibres, resin or PyC).

The integration of powder in the UD layers can be seen, from Figure 87, to be less prevalent than those samples investigated during the injection studies. This is exemplary of previous comments discussing the capillary suction prospects of the viscous, higher particle size slurries used in the production of these samples. However, the interface can be seen to be a reasonably uniform 9 mm in thickness, with concentration overlap at the centre of the composite. There is no regularity or control in the quality or structure of this interface. This is clear from both Figure 88 and Figure 89 and the micrographs presented. However, the effect of this on the properties is not known. It is possible that the average performance of this approaches the desired properties. Whether this level of control is adequate will very much depend on the anticipated application and the tolerances associated with that.

The results of the injection studies show that, to produce a 9 mm height deposit with the models established in Table 24, as for the composite samples here, the height can be obtained between 8.8-9.2 mm at the 95% confidence level, the deviation only representing 5% of the total required height. This shows that these dual phase architectures can be comfortably obtained, and the drop in concentration at the periphery may even produce the desired property transition. However, it may also entrain a larger degree of structured porosity. Further testing of such samples would be needed to confirm this.

4.3.2 Performance testing

4.3.2.1 Flexural testing

The flexural strengths of composite bars were measured. The 3-pt bend flexural strength was obtained as 39 ± 8 MPa. While low, samples were not densified; the range of densities was from 1.9 to 2.2 g cm^{-3}, with densification from 33.8 to 43.7 vol% porosity. Samples demonstrated the step-wise failure mode expected of fibre-reinforced composites; in one case, a sample retained a load of 1000 N at 4 mm strain. Of the four samples tested to high deflection, one failed via a through-thickness crack and three failed through an additional delaminative mode. These are shown in Figure 93. There was no statistically significant difference in failure strength or load-deflection behaviour for these modes. This result indicates that the ceramic distribution does not necessarily dominate the fracture behaviour. It should be noted that interlaminar failure is the general failure mode exhibited in the past for this sort of 2.5D C_f/C ceramic powder modified composite. This conclusion is based on previous work not shown here.

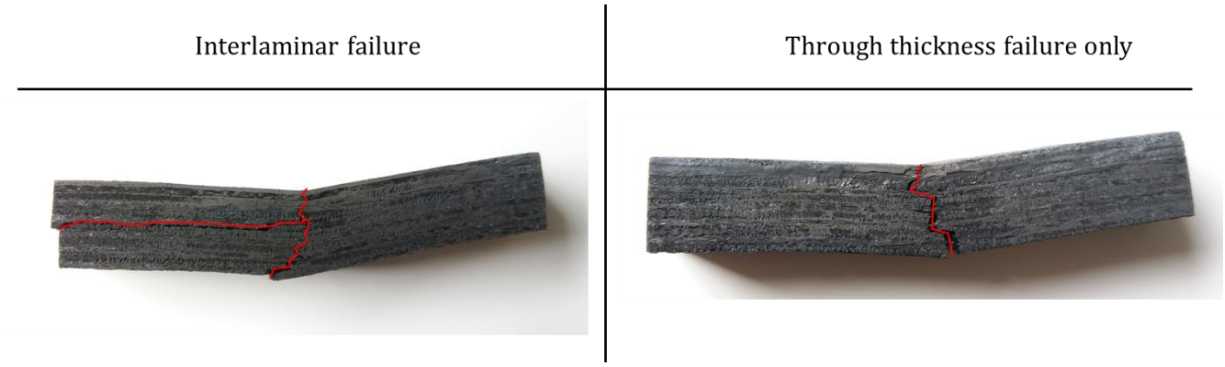


Figure 93: The failure modes observed at high deflection for the 50:50 C_f/C-HfB_2-ZrB_2. Bars were 105 mm long.

4.3.2.2 Thermal testing

The heat loss rate of the single phase and multiphase C_f/C-(Zr/Hf)B_2 samples were not meaningfully different from one another. From this it was assumed that there were no substantial portions of interphase porosity retarding heat transfer within the composite. However, due to the highly uncertain nature of the test, with significant sources of uncontrolled heat loss, gain and unquantified surface qualities, the confidence in this conclusion is low.

4.3.3 Context of FGMs by injection

The results of this study have shown that the use of injection to obtain small total thickness FGMs is unlikely to be possible, certainly with any useful degree of reproducibility, in this fibre substrate. However, there are a few considerations or steps that may ameliorate this issue.

The required property gradient may not be strictly defined. Application dependent, there being a roughly defined interface with a certain degree of random interpenetration may not compromise the desired properties of the final component. For materials in this study,

the final step of which would be to densify with pyrolytic carbon or ZrB_2 via CVI, the issues associated with entrained porosity would be minimised.

If a strict gradient is required, then the method still may be salvageable. For a large piece of material produced by this method, there is a probability that a certain gradient will be produced at some location. By increasing the size of the component beyond the shape and size needed, the likelihood of producing an area of the desired grading is increased. This area may then be determined through non-destructive testing, depending on the composition of the composite. Nano X-ray CT was attempted on samples of C_f/C-1.0ZrB_2-1.0HfB_2 produced in this study to elucidate the gradient structure, but sufficient phase distinction was not obtained at any power/voltage settings with the samples inspected. However, composition and equipment dependent, this method is viable, and its feasibility would be a function of machinability of the final component and cost-effectiveness for the final part when taking into account the machining cost and cost of the 'wasted' material.

A major issue in this study has been the heterogeneity of the preform. While 'good' predictions for the general shape and size of the deposit were possible, with 68 and 75% of the height and width variation explicable by the selected statistical models, the margin of error was still reasonably large when compared to many other processes. Some of this is likely due to uncertainty in some of the assumptions, such as the use of the initial slurry velocity as the regression statistic instead of somehow incorporating some more representative 'velocity distribution', or having a reasonably small number of total entries with a relatively small range of investigated slurry properties. It is also likely that the structural inhomogeneity of the preform contributed to the error. The elements include locations of the needling fibres through the UD layers, the exact tow alignments and locations of the intra-tow gaps in the UD layers, and the thicknesses of the R layers, which

are found to vary from 0.51 to 0.60 mm. Use of a more predictable and regular structure, such as full 3D woven or noobed* preforms may alleviate this uncertainty.

Other anisotropic impregnation strategies may also hold promise. A high affinity for this preform for capillary suction has been demonstrated, with suction along a whole single layer without substantial upwards or downwards flow. Suspensions with low viscosity and volatility and high wettability could be introduced coplanar with the UD layers from the exterior of the preform. Some device or shape as shown in Figure 94, may allow for single layer impregnation in this fashion. This, however, is simply conjecture.

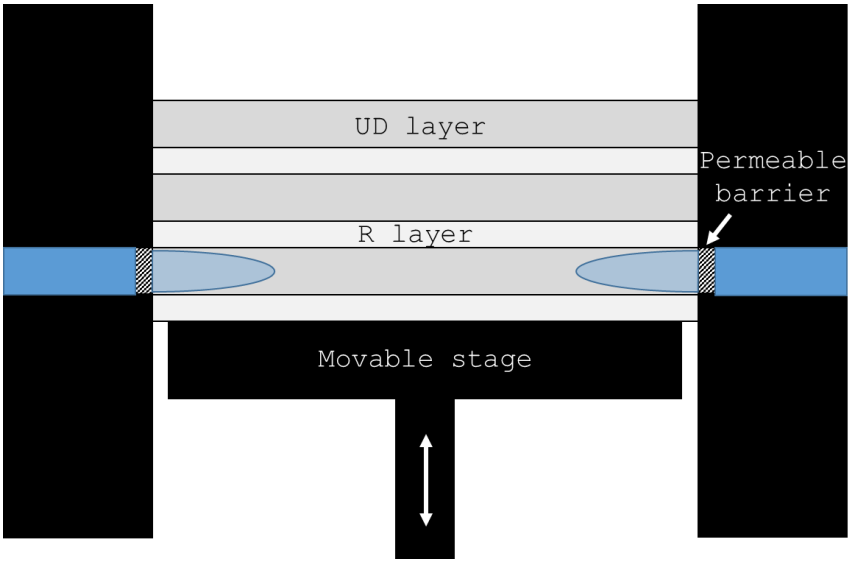


Figure 94: A potential capillary suction stage to allow for single-layer capillary impregnation.

Other theoretical impregnation methods yielding selectively anisotropic structures are possible. Photochemistry is an advancing research area. Melding photochemical methods for the excitation of gaseous precursors and combining with methods such as those found in X-ray radiotherapy could produce a 3D printing technique for creation of ceramic structures within reinforcements.

* Crimpless weft and warp 3D fibre architectures with through-thickness stitching to provide delamination resistance. The interior structure can be made more regular at a shorter length scale than the 2.5D preform used in this study.

5 CONCLUSIONS AND FUTURE WORK

This thesis sought to address the problem of producing functionally graded ceramic fibre composites via injection into a 2.5D substrate. To do this, the interaction between the fluid properties and the processing variables on the shape, extent and growth of injected deposits was investigated and the limits of potential control were established. The way that these deposits could be built up to tailor material gradients were explored. Particular attention was paid to the effect of capillarity and particulate-induced clogging on the flow front progression.

The growth and shapes of the deposits were found to be complex with respect to the input variables. Statistical models were produced via a multiple regression procedure relating the two principle spreading axes of the deposits as a function of both processing variables: flow speed, total injection volume, and material variables: viscosity, surface tension and contact angle. The adjusted coefficients of determination for deposit height and width were 0.68 and 0.75 respectively. The relations were, therefore, useful to some extent in explaining the variation in spreading behaviour. However, a large amount of variation remained unexplained. Further to this, the explicit form, dimensionality and mathematical behaviour at the limits of the variables were not indicative that the relations were phenomenological, or particularly indicative of a true physical relationship. This was evidenced further by the existence of a wide range of proposed regression relations that, incredibly different in variable configuration, performed similarly well. There were a number of potential limitations in the study that resulted in the high variation. Had there been two (or more) orthogonal wetting/viscosity slurry series instead of the one produced, there may have been a greater span of observed behaviours. In turn, this may have permitted functions that may have pertinently explained noise in the present data

set. A greater obtained range of flow rates may also have benefitted in this way, though this variable was limited by the frame speed of the equipment used for the injection studies. An area potentially responsible for the present degree of model variation is in the selection of the regression terms. An exhaustive combinatorial analysis with the variables used was not possible as there was an infinite subset of combined interaction parameters. The selected combinations for testing were chosen based on the correlation matrices from previous analysis, from the signs of the coefficients in the linear analysis and from physically coherent interaction mechanisms. However, the value of the relations as meaningful physical representations is low, so limiting the study to justifications on this basis in variable selection is indicative of a systemic bias. A more even-handed approach would have been a far more extensive relation testing scheme. Specifically, a systematic variable production matrix producing interaction terms of every variable with every other variable, with a testing regime exhaustively performing each permutation of original and interaction variables. This, however, would have been technically challenging to instigate, computationally intensive to the point of being beyond the available resources, and, at the limit of large numbers of proposed interaction variables, could have introduced an element of the overfitting that the regularisation methods were designed to alleviate. Equally, inclusion of highly collinear high order interaction parameters is unlikely to have provided superior fitting. Obtaining unique and fundamentally consistent solutions for these variables was not the goal of the analysis, however. It was to gauge the feasibility of injection as a means of producing FGMs and delineating the specificity with which such materials could be defined via this method. As such, the statistical relations should be handled in the spirit with which they were intended, incidental reflections of the underlying phenomena within the specified ranges of certainty.

The ability to produce FGMs via this method was probed both experimentally and mathematically. The mathematical analysis was clearly contingent on the validity of the statistical analysis. The results showed that there was an incredibly sensitive interplay between the deposit size reproducibility, the total thickness of the component and the desired gradient. The regression procedure, which can be considered a lower bound for the magnitude of the errors due to unquantified uncertainties, did not produce results that can confidently be claimed to produce 'well-defined' gradients at small total sample size. This was shown using an exemplary case. This is specifically not to say that FGMs are not obtainable through this method, but that there are limits on the definition and total size. Likewise, FGMs are only produced when a very specific material composition has been associated with an explicit component geometry with expected conditions known. It is possible that the limitations associated with this method are compatible with a huge range of required material gradients. In such a case, this injection method provides a handy tool with regards to material preparation. This analysis does not take into account, however, the more qualitative effects and the deviations from the geometric assumptions of the model. For instance, material inhomogeneities sourced from shrinkage cracks, improper tessellation of deposits that produce macroporosity and the capillary effect that can wick slurry into distant parts of the preform. These effects will all act to prevent a well-defined concentration gradient and, ultimately, a quality product. Use of CVI densification after injection may partially or wholly mitigate these flaws, however. Again, a more specific set of final material requirements is required to judge the feasibility of this method holistically.

The effects of particle size and clogging was analysed to address the 'single phase liquid' assumption in operation for the regression studies and numerical simulations. Via encapsulated tow slurry sorption, there was evidence to suggest that the narrower flow

channels were less conducive to slurry uptake than wider channels. This manifested as reduced mass gain, reduced suction distance, and increased water content in the absorbed fluid. Image analysis showed that solid residue decreased as a function of distance from the tip of the encapsulated tow. It is also likely that fibre movement was induced by slurry suction, which possibly impeded further slurry sorption further in. These features suggested that low particle-size/pore width ratios reduced absorption extent. However, there were significant uncertainties in the pore size distribution of the produced tows, and this would dominate the sorption behaviour. This value could be made more certain by production of far more samples and determination of the capillary constant, or by a representative sample of tows being analysed with mercury porosimetry, though time constraints prevented this. The general conclusion is that clogging, and therefore flow in the higher density layers was related to the particle size distribution. Primarily, as the flow in the UD layers was not unequivocally seen to be limited in the injection studies, it is advisable that the results of the injection study analysis only be used with materials with a similar particle size distribution relative to the pore widths and with similar stability. Secondarily, the sorption studies are applicable to wider slurry infiltration routes. Tow penetration is something many researchers do not consistently manage and, while for some applications this is desirable, this study has demonstrated clearly a set of criteria for good tow penetration. The injection studies show that high wetting low viscosity liquids with sufficiently low particle size distributions penetrate homogeneously and consistently throughout the dense unidirectional layers. The sorption studies indicate the importance in controlling the relative sizes of the pores and particles to permit extensive sorption. The modelling analysis has supported the central role that capillarity must play in the impregnation of dense fibrous substrates by granular liquids.

The original contribution of this work has been two-fold. No other researcher, to the author's knowledge, has explicitly considered the joint case of the wetting and viscosity properties of granular liquids and the anisotropic infiltration mechanics of fibre substrates. The contribution has been novel in this sense; if anything, reiterating and quantifying the impact of the wettability of slurries in the preforms and the particle size distributions of the ceramic starting materials is a novel and key contribution, even for those seeking to optimise isotropic infiltration methods. Secondly, the injection method for fibre composites, a recent entry to the literature, has been shown to have a degree of feasibility for the production of a functionally graded continuous fibre composite. Additionally, the core processing considerations for using injection as a potentially scaled up method have been elucidated.

There are a number of future directions that are important to explore. With regards to the practical application of injection to make functionally graded composites, the key requirement is specific optimisations for a desired end product. The range of test fluid properties could also be extended and the analysis repeated to allow for a wider potential set of starting materials to be viable. Such an extension would also identify areas where greater control can be exerted on deposit shape. The production of more model microstructures for clogging tests would allow a better understanding of the requirements for the particle sizes in slurries for good tow penetration and suction. There is still a vacancy for a multiphase simulation that accurately depicts the impregnation kinematics for slurries in the 2.5D substrate. Such a step would be necessary should this method be desired as a commercially relevant solution for FGMs based on this substrate via injection.

At its core, this work has set out a method for the production of FGMs via injection into a 2.5D fibre substrate and has explicitly identified the tolerances of the products of the

process. The feasibility of the method can only be fully realised when a final product's properties and geometry are also identified. Until such a point, it is worthwhile addition to the toolbox of the material designer.

LIST OF REFERENCES

1. D. M. Van Wie, D. G. Drewry, D. E. King and C. M. Hudson, *Journal of Materials Science*, 2004, **39**, 5915-5924.
2. L. V. Kravchuk, K. P. Buiskikh, I. A. Gusarova, A. M. Potapov and N. N. Feofentov, *Strength of Materials*, 2018, **50**, 565-574.
3. M. J. Zhang, F. G. Li, S. Y. Wang and C. Y. Liu, *Materials Science and Engineering: A*, 2011, **528**, 4030-4039.
4. D. Bianchi and F. Nasuti, *Journal of Propulsion and Power*, 2013, **29**, 547-558.
5. D. Bianchi and A. Neri, *Journal of Propulsion and Power*, 2018, **34**, 482-498.
6. S. Gulli and L. Maddalena, *Journal of Spacecraft and Rockets*, 2019, **56**, 780-788.
7. J. Binner, M. Porter, B. Baker, J. Zou, V. Venkatachalam, V. R. Diaz, A. D'Angio, P. Ramanujam, T. Zhang and T. S. R. C. Murthy, *International Materials Reviews*, 2019, DOI: 10.1080/09506608.2019.1652006, 1-56.
8. S. Tang and C. Hu, *Journal of Materials Science & Technology*, 2017, **33**, 117-130.
9. W. G. Fahrenholtz and G. E. Hilmas, *Scripta Materialia*, 2017, **129**, 94-99.
10. L. Li, Y. Wang, L. Cheng and L. Zhang, *Ceramics International*, 2011, **37**, 891-896.
11. J. Han, P. Hu, X. Zhang, S. Meng and W. Han, *Composites Science and Technology*, 2008, **68**, 799-806.
12. D. B. Marshall, B. N. Cox and A. G. Evans, *Acta Metallurgica*, 1985, **33**, 2013-2021.
13. B. Budiansky, J. W. Hutchinson and A. G. Evans, *Journal of the Mechanics and Physics of Solids*, 1986, **34**, 167-189.
14. D. Koch, K. Tushtev and G. Grathwohl, *Composites Science and Technology*, 2008, **68**, 1165-1172.
15. Y. Cheng, P. Hu, W. Zhang, C. Ma, J. Feng, Q. Fan, X. Zhang and S. Du, *Journal of the European Ceramic Society*, 2019, **39**, 2251-2256.
16. P. Hu, Y. Cheng, X. Guo, C. Ma, P. Hu, Q. Qu, H. Zhao and S. Du, *Journal of the American Ceramic Society*, 2019, **102**, 70-78.
17. B. Baker, V. Rubio, P. Ramanujam, J. Binner, A. Hussain, T. Ackerman, P. Brown and I. Dautremont, *Journal of the European Ceramic Society*, 2019, **39**, 3927-3937.
18. P. Hu, Y. Cheng, D. Zhang, L. Xun, M. Liu, C. Zhang, X. Zhang and S. Du, *Composites Part B: Engineering*, 2019, **174**, 107023.
19. D. D. Jayaseelan, Y. Xin, L. Vandeperre, P. Brown and W. E. Lee, *Composites Part B: Engineering*, 2015, **79**, 392-405.
20. J. Bear, in *Dover Civil and Mechanical Engineering*, Dover Publications, 1972, ch. 1.1.
21. R. Savino, M. D. S. Fumo, D. Paterna and M. Serpico, *Aerospace Science and Technology*, 2005, **9**, 151-160.
22. W. G. Fahrenholtz, E. J. Wuchina, W. E. Lee, Y. Zhou and G. Geiger, *Ultra-High Temperature Ceramics : Materials for Extreme Environment Applications*, John Wiley & Sons, Incorporated, Hoboken, UNITED STATES, 2014.
23. Netschz, *Poster series- Thermal Properties of Ceramics*, 2012.
24. A. L. Chamberlain, W. G. Fahrenholtz, G. E. Hilmas and D. T. Ellerby, *Journal of the American Ceramic Society*, 2004, **87**, 1170-1172.
25. K. Gürcan and E. Ayas, *Ceramics International*, 2017, **43**, 3547-3555.
26. M. M. Opeka, I. G. Talmy, E. J. Wuchina, J. A. Zaykoski and S. J. Causey, *Journal of the European Ceramic Society*, 1999, **19**, 2405-2414.
27. P. Schwarzkopf and R. Kieffer, Macmillan Company, New York, 1953, p. 5.
28. H. S. Hong and K. S. Lee, *Journal of Alloys and Compounds*, 2003, **360**, 198-204.
29. E. Wuchina and M. Opeika, in *Ultra-High Temperature Ceramics*, 2014, DOI: 10.1002/9781118700853.ch14, pp. 361-390.
30. W. G. Fahrenholtz, G. E. Hilmas, I. G. Talmy and J. A. Zaykoski, *Journal of the American Ceramic Society*, 2007, **90**, 1347-1364.

31. A. K. Kuriakose and J. L. Margrave, *Journal of the Electrochemical Society*, 1964, **111**, 827-831.
32. F. Stig and S. Hallstrom, *Advances in Materials Science and Engineering*, 2019, **2019**, 8439530.
33. A. Nisar, S. Ariharan and K. Balani, *Ceramics International*, 2017, **43**, 13483-13492.
34. Y. Zu, J. Sha, J. Li, Z. Zhang, S. Wang, Z. Lv and J. Dai, *Ceramics International*, 2017, **43**, 7454-7460.
35. J. J. Sha, J. Li, Z. Z. Lv, S. H. Wang, Z. F. Zhang, Y. F. Zu, S. Flauder and W. Krenkel, *Journal of the European Ceramic Society*, 2017, **37**, 549-558.
36. K. Gui, P. Hu, W. Hong, X. Zhang and S. Dong, *Journal of Alloys and Compounds*, 2017, **706**, 16-23.
37. D. Sciti, S. Guicciardi and L. Silvestroni, *Materials & Design*, 2014, **55**, 821-829.
38. F. Yang, X. Zhang, J. Han and S. Du, *Materials Letters*, 2008, **62**, 2925-2927.
39. R. Inoue, Y. Arai, Y. Kubota, K. Goto and Y. Kogo, *Ceramics International*, 2018, **44**, 15859-15867.
40. A. Vinci, L. Zoli, D. Sciti, C. Melandri and S. Guicciardi, *Materials & Design*, 2018, **145**, 97-107.
41. S. Failla, P. Galizia, L. Zoli, A. Vinci and D. Sciti, *Journal of Alloys and Compounds*, 2019, **777**, 612-618.
42. P. Hu, Y. Cheng, P. Wang, X. Guo, C. Ma, Q. Qu, X. Zhang and S. Du, *Ceramics International*, 2018, **44**, 14907-14912.
43. H. Hu, Q. Wang, Z. Chen, C. Zhang, Y. Zhang and J. Wang, *Ceramics International*, 2010, **36**, 1011-1016.
44. S. Tang, J. Deng, S. Wang and W. Liu, *Journal of the American Ceramic Society*, 2007, **90**, 3320-3322.
45. W. Zhang, C. Xie, M. Ge and X. Wei, in *MAX Phases and Ultra-High Temperature Ceramics for Extreme Environments*, 2013, DOI: 10.4018/978-1-4666-4066-5.ch013, pp. 413-434.
46. C. Yan, R. Liu, Y. Cao and C. Zhang, *Materials Science and Engineering: A*, 2014, **591**, 105-110.
47. F. Ahmad, N. Yuvaraj and P. K. Bajpai, *Polymer Composites*, 2020, **41**, 2518-2534.
48. A. Vinci, L. Zoli, D. Sciti, J. Watts, G. E. Hilmas and W. G. Fahrenholtz, *Journal of the European Ceramic Society*, 2019, **39**, 3594-3603.
49. D. L. Poerschke, M. D. Novak, N. Abdul-Jabbar, S. Krämer and C. G. Levi, *Journal of the European Ceramic Society*, 2016, **36**, 3697-3707.
50. C. Carney, D. King, M. De Stefano Fumo, C. Purpura, E. Trifoni, A. Martucci, B. Larson, T. Parthasarathy, M. Cinibulk and G. Marino, *Advances in Applied Ceramics*, 2018, **117**, s19-s25.
51. V. Rubio, J. Binner, S. Cousinet, G. Le Page, T. Ackerman, A. Hussain, P. Brown and I. Dautremont, *Journal of the European Ceramic Society*, 2019, **39**, 813-824.
52. L. Silvestroni, S. Mungiguerra, D. Sciti, G. D. Di Martino and R. Savino, *Corrosion Science*, 2019, **159**, 108125.
53. E. Eakins, D. D. Jayaseelan and W. E. Lee, *Metallurgical and Materials Transactions A*, 2011, **42**, 878-887.
54. X. Yao, H. Li, Y. Zhang, H. Wu and X. Qiang, *Ceramics International*, 2012, **38**, 2095-2100.
55. L. Silvestroni, C. Melandri, V. Venkatachalam, J. Binner and D. Sciti, *Materials & Design*, 2019, **183**, 108078.
56. A. Dorogoy, *SIMULATION*, 2018, **95**, 941-953.
57. F. Erdogan, *Composites Engineering*, 1995, **5**, 753-770.
58. P. Gu and R. J. Asaro, *International Journal of Solids and Structures*, 1997, **34**, 3085-3098.
59. D. Gayen, R. Tiwari and D. Chakraborty, *Composites Part B: Engineering*, 2019, **173**, 106982.
60. S. Hofmann, *Engineering Fracture Mechanics*, 2017, **182**, 506-520.
61. M. J. Presby, R. Mansour, K. Manigandan, G. N. Morscher, F. Abdi, C. Godines, A. Eftekharian and S. R. Choi, *Ceramics International*, 2019, **45**, 2635-2643.

62. M. Presby, M. Kannan, G. Morscher, C. Godines, A. Eftekharian, J. Ahmad, F. Abdi and S. R. Choi, *Journal of Engineering for Gas Turbines and Power*, 2019, DOI: 10.1115/1.4044490.
63. C. Li, Y. Niu, X. Zhong, T. Liu, X. Pan, M. Shi, X. Zheng and C. Ding, *Journal of the European Ceramic Society*, 2019, **39**, 4565-4574.
64. Y. Jiang, T. Liu, H. Ru, W. Wang, C. Zhang and X. Yue, *Ceramics International*, 2019, **45**, 6541-6551.
65. A. Paul, J. G. P. Binner, B. Vaidhyanathan, A. C. J. Heaton and P. M. Brown, *Advances in Applied Ceramics*, 2016, **115**, 158-165.
66. T. Liu, Y. Niu, X. Pan, M. Shi, X. Zheng, J. Yu and C. Ding, *Journal of the American Ceramic Society*, 2019, **102**, 4247-4258.
67. S. Sun, Z. Ma, Y. Liu, L. Liu, F. Wang and X. Luan, *Surface and Coatings Technology*, 2020, **381**, 125132.
68. Y. Dong, K. Ren, Y. Lu, Q. Wang, J. Liu and Y. Wang, *Journal of the European Ceramic Society*, 2019, **39**, 2574-2579.
69. R. Anton, V. Leisner, P. Watermeyer, M. Engstler and U. Schulz, *Acta Materialia*, 2020, **183**, 471-483.
70. Y. Arai and R. Inoue, *Journal of Advanced Ceramics*, 2019, **8**, 438-447.
71. A. Moro, Y. Kuroda and K. Kusaka, *Acta Astronautica*, 2002, **50**, 427-432.
72. M. Rahnavard, M. J. Ostad Ahmad Ghorabi and H. Rafiee, *Surface Engineering*, 2017, **33**, 444-450.
73. A. P. Garshin, V. I. Kulik, S. A. Matveev and A. S. Nilov, *Refractories and Industrial Ceramics*, 2017, **58**, 148-161.
74. N. Patra, N. Al Nasiri, D. D. Jayaseelan and W. E. Lee, *Journal of the European Ceramic Society*, 2018, **38**, 2297-2303.
75. Z. Xie, T. Zhou and Y. Gou, *Ceramics International*, 2015, **41**, 6226-6231.
76. M.-y. Zhang, K.-z. Li, X.-h. Shi and W.-l. Tan, *Materials & Design*, 2017, **122**, 322-329.
77. J. He, Y. Gao, Y. Wang, J. Fang and L. An, *Ceramics International*, 2017, **43**, 1602-1607.
78. L. Zhuang, Q.-G. Fu and T.-Y. Liu, *Corrosion Science*, 2016, **112**, 462-470.
79. G. Ziegler, I. Richter and D. Suttor, *Composites Part A: Applied Science and Manufacturing*, 1999, **30**, 411-417.
80. L. Zhang, S. Dong, H. Zhou, Y. Kan, F. Zhou and Z. Wang, *Ceramics International*, 2014, **40**, 11795-11801.
81. Y. Liu, Q. Fu, J. Zhang, L. Li and L. Zhuang, *Journal of the European Ceramic Society*, 2016, **36**, 3815-3821.
82. D. Wang, S. Dong, H. Zhou, Y. Kan, Z. Wang, G. Zhu, X. Chen and Y. Cao, *Ceramics International*, 2016, **42**, 10272-10278.
83. C. Xiaowu, F. Qian, G. Le, Z. Xiangyu, D. Shaoming, W. Jingxiao, Z. Qiang, K. Yanmei and N. Dewei, *Journal of the American Ceramic Society*, 2017, **100**, 4816-4826.
84. S. Berthon and G. Malé, *Composites Science and Technology*, 1997, **57**, 217-227.
85. I. Golecki, *Materials Science and Engineering: R: Reports*, 1997, **20**, 37-124.
86. V. Rubio, P. Ramanujam and J. Binner, *Advances in Applied Ceramics*, 2018, **117**, s56-s61.
87. Y. Miao, F. Zhang, Z. Yang, D. Jia and Y. Zhou, *Journal of the European Ceramic Society*, 2020, **40**, 1078-1085.
88. D. Wang, S. Dong, H. Zhou, X. Zhang, Y. Ding and G. Zhu, *Ceramics International*, 2016, **42**, 6720-6727.
89. Q. Li, S. Dong, Z. Wang, J. Hu, B. Wu, H. Zhou, P. He and J. Yang, *Ceramics International*, 2013, **39**, 877-881.
90. C. Sun, H. Li, Q. Fu and J. Zhang, *Corrosion Science*, 2014, **79**, 100-107.
91. D. D. Jayaseelan, R. G. de Sá, P. Brown and W. E. Lee, *Journal of the European Ceramic Society*, 2011, **31**, 361-368.
92. S. Tang, J. Deng, W. Liu and K. Yang, *Carbon*, 2006, **44**, 2877-2882.
93. L. Zoli and D. Sciti, *Materials & Design*, 2017, **113**, 207-213.
94. A. Paul, V. Rubio, J. G. P. Binner, B. Vaidhyanathan, A. C. J. Heaton and P. Brown, *International Journal of Applied Ceramic Technology*, 2017, **14**, 344-353.

95. A. Paul, S. Venugopal, J. G. P. Binner, B. Vaidhyanathan, A. C. J. Heaton and P. M. Brown, *Journal of the European Ceramic Society*, 2013, **33**, 423-432.
96. Q. Feng, Z. Wang, H. J. Zhou, P. He, L. Gao, Y. M. Kan, X. Y. Zhang, Y. S. Ding and S. Dong, *Ceramics International*, 2014, **40**, 1199-1204.
97. H. Zhou, D. Ni, P. He, J. Yang, J. Hu and S. Dong, *Ceramics International*, 2018, **44**, 4777-4782.
98. L.-p. Ran, F. Rao, K. Peng, H. Yin and M.-z. Yi, *Transactions of Nonferrous Metals Society of China*, 2019, **29**, 2141-2150.
99. I. M. Smallwood, *Handbook of Organic Solvent Properties*, 2012.
100. B. Wu, S. Dong, Z. Wang, Y. Kan, L. Zhang and F. Zhou, *Ceramics International*, 2013, **39**, 4729-4734.
101. C. Leslie, E. Boakye, K. Keller and M. Cinibulk, in *Processing and Properties of Advanced Ceramics and Composites V*, 2013, DOI: doi:10.1002/9781118744109.ch1.
102. P. Hu, D. Zhang, S. Dong, Q. Qu and X. Zhang, *Journal of the European Ceramic Society*, 2019, **39**, 798-805.
103. J. Y. Yang, J. H. Weaver, F. W. Zok and J. J. Mack, *Journal of the American Ceramic Society*, 2009, **92**, 1087-1092.
104. C. Leslie, E. Boakye, K. Keller and M. Cinibulk, *International Journal of Applied Ceramic Technology*, 2015, **12**, 235-244.
105. A. Scola, N. Eberling-Fux, S. Turenne and E. Ruiz, *Journal of the American Ceramic Society*, 2018, **102**, 3256-3268.
106. F. Uhlmann, C. Wilhelmi, S. Schmidt-Wimmer, S. Beyer, C. Badini and E. Padovano, *Journal of the European Ceramic Society*, 2017, **37**, 1955-1960.
107. A. Scola, M. Podgorski, N. Eberling-Fux, S. Turenne and E. Ruiz, *Journal of the American Ceramic Society*, 2019, **102**, 2337-2352.
108. S. Singh, J. Yin, F. Lun, D. P. Mondal, D. Kim and S.-H. Lee, *Journal of the European Ceramic Society*, 2020, DOI: https://doi.org/10.1016/j.jeurceramsoc.2020.01.009.
109. H. Hemmingsen, M. Niemeyer, M. R. Hansen, D. Bucher and N. B. Thomsen, *Diabetes Technology & Therapeutics*, 2011, **13**, 1207-1211.
110. A. Fry, *Pharmaceutical Technology*, 2014, **38**, http://www.pharmtech.com/injecting-highly-viscous-drugs.
111. a. S P Sutera and R. Skalak, *Annual Review of Fluid Mechanics*, 1993, **25**, 1-20.
112. R. F. Edlich, J. F. Smith, N. E. Mayer, B. L. Farris, D. E. Chang, R. F. Morgan and J. G. Thacker, *The Journal of Emergency Medicine*, 1987, **5**, 83-90.
113. S. Aldritch, Syringe Needle Gauge Chart, https://www.sigmaaldrich.com/chemistry/stockroom-reagents/learning-center/technical-library/needle-gauge-chart.html, (accessed 02/03/2020, 2020).
114. D. Stout and V. Vilivalam, *Pharmaceutical Technology*, 2009, **2009 supplement**, http://www.pharmtech.com/plastic-prefilled-syringes-better-fit-autoinjector-systems.
115. E. Krayukhina, A. Fukuhara and S. Uchiyama, *Journal of Pharmaceutical Sciences*, 2020, **109**, 515-523.
116. J. Gadsden, *Expert Review of Medical Devices*, 2018, **15**, 571-578.
117. J.-C. Veilleux and J. E. Shepherd, *Drug Delivery and Translational Research*, 2018, **8**, 1238-1253.
118. J. C. Veilleux and J. E. Shepherd, *Journal of Pressure Vessel Technology, Transactions of the ASME*, 2019, **141**.
119. J. Yu, H. Kwon, H.-s. Park, S. Hong and Y. Choi, *Biomedical Engineering Letters*, 2016, **6**, 250-255.
120. J. R. Wagner, E. M. Mount and H. F. Giles, in *Extrusion (Second Edition)*, eds. J. R. Wagner, E. M. Mount and H. F. Giles, William Andrew Publishing, Oxford, 2014, DOI: https://doi.org/10.1016/B978-1-4377-3481-2.00017-X, pp. 203-206.
121. M. De Bardi, R. Müller, C. Grünzweig, D. Mannes, M. Rigollet, F. Bamberg, T. A. Jung and K. Yang, *European Journal of Pharmaceutics and Biopharmaceutics*, 2018, **127**, 104-111.
122. L. Xing, Y. Li and T. Li, *PDA Journal of Pharmaceutical Science and Technology*, 2019, **73**, 260-275.

123. Q. Long, X. Y. Xu, B. Ariff, S. A. Thom, A. D. Hughes and A. V. Stanton, *Journal of Magnetic Resonance Imaging*, 2000, **11**, 299-311.
124. G. Segré and A. Silberberg, *Journal of Fluid Mechanics*, 2006, **14**, 136-157.
125. R. Claudio, A. Hadzic, H. Shih, J. D. Vloka, J. Castro, Z. Koscielniak-Nielsen, D. M. Thys and A. C. Santos, *Regional Anesthesia & Pain Medicine*, 2004, **29**, 201-205.
126. R. Moreno, *Journal of the European Ceramic Society*, 2020, **40**, 559-587.
127. A. Maestro and E. Guzmán, *Processes*, 2019, **7**, 942.
128. C. Bruel, S. Queffeulou, T. Darlow, N. Virgilio, J. R. Tavares and G. S. Patience, *The Canadian Journal of Chemical Engineering*, 2019, **97**, 832-842.
129. J.-P. Minier and J. Pozorski, in *Particles in Wall-Bounded Turbulent Flows: Deposition, Re-Suspension and Agglomeration*, Springer, Cham, Switzerland, 2016, pp. 209-261.
130. H. Ohshima, in *Electrical Phenomena at Interfaces and Biointerfaces*, 2012, DOI: 10.1002/9781118135440.ch3, ch. 3, pp. 27-34.
131. K. B. Oldham, *Journal of Electroanalytical Chemistry*, 2008, **613**, 131-138.
132. A. M. Smith, A. A. Lee and S. Perkin, *The Journal of Physical Chemistry Letters*, 2016, **7**, 2157-2163.
133. G. W. Lu and P. Gao, in *Handbook of Non-Invasive Drug Delivery Systems*, ed. V. S. Kulkarni, William Andrew Publishing, Boston, 2010, DOI: https://doi.org/10.1016/B978-0-8155-2025-2.10003-4, ch. 3.1.2.4, pp. 59-94.
134. C. A. Kraus and R. M. Fuoss, *Journal of the American Chemical Society*, 1933, **55**, 21-36.
135. R. M. Fuoss and C. A. Kraus, *Journal of the American Chemical Society*, 1933, **55**, 1019-1028.
136. P. C. Van Der Hoeven and J. Lyklema, *Advances in Colloid and Interface Science*, 1992, **42**, 205-277.
137. S. Leo, C. Tallon and G. V. Franks, *Journal of the American Ceramic Society*, 2014, **97**, 3807-3817.
138. S. Leo and C. Tallon, *Journal of the American Ceramic Society*, 2016, **99**, 3883-3892.
139. G. V. Franks, C. Tallon, A. R. Studart, M. L. Sesso and S. Leo, *Journal of the American Ceramic Society*, 2017, **100**, 458-490.
140. S. Tanurdjaja, C. Tallon, P. J. Scales and G. V. Franks, *Advanced Powder Technology*, 2011, **22**, 476-481.
141. C. Tallon, D. Chavara, A. Gillen, D. Riley, L. Edwards, S. Moricca and G. V. Franks, *Journal of the American Ceramic Society*, 2013, **96**, 2374-2381.
142. D. G. Goski, A. T. Paulson, R. A. Speers and W. F. Caley, *British Ceramic Transactions*, 1999, **98**, 192-195.
143. N. Brahma and J. B. Talbot, *Journal of Colloid and Interface Science*, 2014, **419**, 56-60.
144. G. Wang and P. S. Nicholson, *Journal of the American Ceramic Society*, 2001, **84**, 1977-1980.
145. B. P. Singh, S. K. Swain, S. K. Dash and S. Bhattacharjee, *Journal of Dispersion Science and Technology*, 2006, **27**, 251-258.
146. M. Trunec, P. Stastny, J. Kelar and M. Pazderka, *Ceramics International*, 2019, **45**, 9381-9385.
147. R. Chen, J. Qi, X. Guo, D. Ye, X. Wang, Q. Shi, D. Wu, Z. Liao and T. Lu, *Ceramics International*, 2019, **45**, 7916-7922.
148. B. W. Brian and J. C. Chen, *AIChE Journal*, 1987, **33**, 316-318.
149. S. Liu, J. Liu, G. Liu, Y. Liu and H. Zhong, *Applied Surface Science*, 2020, **505**, 144467.
150. P. R. Waghmare and S. K. Mitra, *Langmuir*, 2010, **26**, 17082-17089.
151. D. T. Wasan and A. D. Nikolov, *Nature*, 2003, **423**, 156-159.
152. S. Vafaei, T. Borca-Tasciuc, M. Z. Podowski, A. Purkayastha, G. Ramanath and P. M. Ajayan, *Nanotechnology*, 2006, **17**, 2523-2527.
153. K. Sefiane, J. Skilling and J. MacGillivray, *Advances in Colloid and Interface Science*, 2008, **138**, 101-120.
154. Y. Zhou, X. Wu, X. Zhong, S. Reagen, S. Zhang, W. Sun, H. Pu and J. Xiaojun Zhao, *Fuel*, 2020, **267**, 117251.
155. N. Yekeen, E. Padmanabhan, A. H. Syed, T. Sevoo and K. Kanesen, *Journal of Petroleum Science and Engineering*, 2020, **186**, 106779.

156. P. Rostami, M. Sharifi, B. Aminshahidy and J. Fahimpour, *Journal of Dispersion Science and Technology*, 2020, **41**, 402-413.
157. L. Ha Eun, C. Kyu Hwan, M. Xia, K. Dong Woo and P. Bum Jun, *Journal of Colloid and Interface Science*, 2020, **560**, 838-848.
158. X. Li, H. Zhong, J. Zhang, Y. Duan, H. Bai, J. Li and D. Jiang, *International Journal of Applied Ceramic Technology*, 2020, **17**, 239-247.
159. H. Xing, B. Zou, Q. Lai, C. Huang, Q. Chen, X. Fu and Z. Shi, *Powder Technology*, 2018, **338**, 153-161.
160. Y. Liang, X. Yuan, L. Wang, X. Zhou, X. Ren, Y. Huang, M. Zhang, J. Wu and W. Wen, *Journal of Colloid and Interface Science*, 2020, **564**, 381-391.
161. X. Cheng, F. Li, L. Luo, Z. Ding, L. Zeng, Y. Mao, X. Huang and H. Hao, *Powder Technology*, 2020, **363**, 593-601.
162. M. C. Blanco López, B. Rand and F. L. Riley, *Journal of the European Ceramic Society*, 2000, **20**, 1587-1594.
163. M. C. Blanco López, B. Rand and F. L. Riley, *Journal of the European Ceramic Society*, 2000, **20**, 1579-1586.
164. J.-H. Yang, S.-M. Shih, C.-I. Wu and C. Y.-D. Tai, *Powder Technology*, 2010, **202**, 101-110.
165. X. Ge, M. Wei, S. He and W.-E. Yuan, *Pharmaceutics*, 2019, **11**, 55.
166. M. A. Hamza, Z. M. Abou-Gamra, M. A. Ahmed and H. A. A. Medien, *Journal of Materials Science: Materials in Electronics*, 2020, **31**, 4650-4661.
167. L. Shi, Y. Lei, J. Huang, Y. Shi, K. Yi and H. Zhou, *Colloids and Surfaces A: Physicochemical and Engineering Aspects*, 2019, **583**, 123948.
168. Q. Zhao, X. Li, Z. Shao, C. Liu and R. Zevenhoven, *Ionics*, 2019, **25**, 5565-5573.
169. M. Vukovic, I. Dinic, M. G. Nikolic, B. A. Marinkovic, A. M. L. M. Costa, K. Radulovic, O. Milosevic and L. Mancic, *Bulletin of Materials Science*, 2019, **43**, 2.
170. W.-L. Zuo, A. Murtaza, C. Zhou, C. Kong, Y. Zhang, F. Tian, L. Wang and S. Yang, *Journal of Magnetism and Magnetic Materials*, 2020, **499**, 166250.
171. J. Shang, Z. Xiao, L. Yu, P. Aprea and S. Hao, *Nanotechnology*, 2020, **31**, 125603.
172. S. Yokoyama, J. Nozaki, K. Motomiya, N. Tsukahara and H. Takahashi, *Colloids and Surfaces A: Physicochemical and Engineering Aspects*, 2020, **591**, 124567.
173. D. A. Lever, M. H. Bradbury and S. J. Hemingway, *Journal of Hydrology*, 1985, **80**, 45-76.
174. H. Cai, Y. Jiang, J. Feng, Q. Chen, S. Zhang, L. Li and J. Feng, *Ceramics International*, 2020, **46**, 12489-12498.
175. X. Liang, Y. Li, J. Yang, Q. Wang, S. Sang and Z. He, *Ceramics International*, 2020, **46**, 16820-16826.
176. M. B. Allen, *Advances in Water Resources*, 1985, **8**, 162-187.
177. E. Baché, C. Dupleix-Couderc, E. Arquis and I. Berdoyes, *Applied Composite Materials*, 2018, **25**, 1287-1305.
178. H. Darcy, in *Les fontaines publiques de la ville de Dijon. Exposition et application des principes à suivre et des formules à employer dans les questions de distribution d'eau*, ed. V. Dalmont, Paris, 1856, pp. 559-603.
179. P. Bobeck, in *Henry P. G. Darcy and Other Pioneers in Hydraulics*, 2003, DOI: doi:10.1061/40683(2003)5, pp. 37-50.
180. S. Whitaker, *Transport in Porous Media*, 1986, **1**, 3-25.
181. E. M. Sozer, P. Simacek and S. G. Advani, in *Manufacturing Techniques for Polymer Matrix Composites (PMCs)*, eds. S. G. Advani and K.-T. Hsiao, Woodhead Publishing, 2012, DOI: https://doi.org/10.1533/9780857096258.3.243, pp. 245-309.
182. D. Ruth and H. Ma, *Transport in Porous Media*, 1992, **7**, 255-264.
183. M. Medraj, E. Baril, V. Loya and L.-P. Lefebvre, *Journal of Materials Science*, 2007, **42**, 4372-4383.
184. Z. Cheng, Z. Ning, Q. Wang, Y. Zeng, R. Qi, L. Huang and W. Zhang, *Journal of Petroleum Science and Engineering*, 2019, **172**, 391-400.
185. K. Williamson, P. Burda and B. Sousedík, *Mathematics and Computers in Simulation*, 2019, **166**, 266-282.

186. J. Nichele and D. A. Teixeira, *Journal of Petroleum Science and Engineering*, 2015, **134**, 76-78.
187. V. H. Nguyen, M. Lagardère, C. H. Park and S. Panier, *Journal of Materials Science*, 2014, **49**, 6449-6458.
188. E. W. Washburn, *Physical Review*, 1921, **17**, 273-283.
189. R. Chassagne, F. Dörfler, M. Guyenot and J. Harting, *Computers & Fluids*, 2019, **178**, 132-140.
190. F. A. L. Dullien, M. S. El-Sayed and V. K. Batra, *Journal of Colloid and Interface Science*, 1977, **60**, 497-506.
191. L. Galet, S. Patry and J. Dodds, *Journal of Colloid and Interface Science*, 2010, **346**, 470-475.
192. T. Ozgumus, M. Mobedi and U. Ozkol, *Engineering Applications of Computational Fluid Mechanics*, 2014, **8**, 308-318.
193. K. Yazdchi, S. Srivastava and S. Luding, *International Journal of Multiphase Flow*, 2011, **37**, 956-966.
194. W. Sobieski, *Mathematics and Computers in Simulation*, 2019, **166**, 1-20.
195. H. L. Liu and W. R. Hwang, *Composites Part A: Applied Science and Manufacturing*, 2012, **43**, 2030-2038.
196. N. Vernet and F. Trochu, *Journal of Composite Materials*, 2016, **50**, 1951-1969.
197. B. R. Gebart, *Journal of Composite Materials*, 1992, **26**, 1100-1133.
198. N. K. Naik, M. Sirisha and A. Inani, *Progress in Aerospace Sciences*, 2014, **65**, 22-40.
199. N. Kuentzer, P. Simacek, S. G. Advani and S. Walsh, *Composites Part A: Applied Science and Manufacturing*, 2006, **37**, 2057-2068.
200. C. Binetruy, J. Pabiot and B. Hilaire, *Polymer Composites*, 2000, **21**, 548-557.
201. J. Delannoy, S. Lafon, Y. Koga, É. Reyssat and D. Quéré, *Soft Matter*, 2019, **15**, 2757-2761.
202. M. T. Senoguz, F. D. Dungan, A. M. Sastry and J. T. Klamo, *Journal of Composite Materials*, 2001, **35**, 1285-1322.
203. M. Li, S. Wang, Y. Gu, Z. Zhang, Y. Li and K. Potter, *Composites Science and Technology*, 2010, **70**, 1628-1636.
204. K. V. Sharp and R. J. Adrian, *Microfluidics and Nanofluidics*, 2005, **1**, 376-380.
205. G. H. Goldsztein and J. C. Santamarina, *Applied Physics Letters*, 2004, **85**, 4535-4537.
206. B. Mustin and B. Stoeber, *Microfluidics and Nanofluidics*, 2010, **9**, 905-913.
207. M. Trofa, G. D'Avino, L. Sicignano, G. Tomaiuolo, F. Greco, P. L. Maffettone and S. Guido, *Chemical Engineering Journal*, 2019, **358**, 91-100.
208. K. Shahzad, G. D'Avino, F. Greco, S. Guido and P. L. Maffettone, *Chemical Engineering Journal*, 2016, **303**, 202-216.
209. K. Shahzad, W. V. Aeken, M. Mottaghi, V. K. Kamyab and S. Kuhn, *Microfluidics and Nanofluidics*, 2018, **22**, 104.
210. J. Hu, in *3-D Fibrous Assemblies*, ed. J. Hu, Woodhead Publishing, 2008, DOI: https://doi.org/10.1533/9781845694982.194, pp. 194-220.
211. B. Yang, S. Wang and Q. Tang, *Polymer Composites*, 2018, **39**, 4408-4415.
212. Z. Chen, S. Pan, Z. Zhou, T. Lei, B. Dong and P. Xu, *Materials*, 2019, **12**, 3594.
213. A. Nabovati, E. W. Llewellin and A. C. M. Sousa, *Composites Part A: Applied Science and Manufacturing*, 2009, **40**, 860-869.
214. A. Nabovati, E. W. Llewellin and A. C. M. Sousa, *Composites Part A: Applied Science and Manufacturing*, 2010, **41**, 453-463.
215. E. W. Llewellin, *Computers & Geosciences*, 2010, **36**, 115-122.
216. I. Cimrák, M. Gusenbauer and T. Schrefl, *Computers & Mathematics with Applications*, 2012, **64**, 278-288.
217. P. Yazgan-Birgi, H. A. Arafat and M. I. Hassan Ali, *Science of The Total Environment*, 2019, **691**, 1251-1261.
218. M. Louis and U. Huber, *Composites Science and Technology*, 2003, **63**, 2081-2088.
219. NIST, in *NIST/SEMATECH e-Handbook of Statistical Methods*, ed. 2nd, US Department of Commerce, 2012, ch. 4.1.4.1 Linear Regression.
220. P. Bickel and B. Li, *TEST*, 2006, **15**, 271-344.
221. M. J. Wainwright, *Annual Review of Statistics and Its Application*, 2014, **1**, 233-253.

222. B. Efron, T. Hastie, I. Johnstone and R. Tibshirani, *The Annals of Statistics*, 2004, **32**, 407-499.
223. T. Hastie, R. Tibshirani and J. Friedman, in *Springer Series in Statistics*, Springer, 2nd edn., 2009, ch. 3.4 Shrinkage methods, p. 61.
224. D. Vidaurre, C. Bielza and P. Larranaga, *International Statistical Review / Revue Internationale de Statistique*, 2013, **81**, 361-387.
225. P. Zhao and B. Yu, *Journal of Machine Learning Research*, 2006, **7**, 2541-2563.
226. A. Benfenati, P. Causin, M. G. Lupieri and G. Naldi, *Journal of Physics: Conference Series*, 2020, **1476**, 012007.
227. M. Haeri and M. Haeri, *Journal of open research software*, 2015, **3**, e1.
228. M. Schmid, Radial Distribution Function, https://imagejdocu.tudor.lu/macro/radial_distribution_function, (accessed 07 05 2020).
229. ASTM, *Journal*, 2013.
230. E. Vogel, *International Journal of Thermophysics*, 2010, **31**, 447-461.
231. H. Oun and A. Kennedy, *Journal of Porous Materials*, 2014, **21**, 1133-1141.
232. J. H. Friedman, T. Hastie and R. Tibshirani, *Journal of Statistical Software*, 2010, **33**, 22.
233. E. Vittinghoff, D. V. Glidden, S. C. Shiboski and C. E. McCulloch, in *Regression methods in biostatistics: Linear, Logistic, Survival, and Repeated Measures Models*, Springer-Verlag New York, New York, 2005, ch. Linear Regression, p. 75.
234. J. Freeman-Steffe, *Rheological Methods in Food Process Engineering*, Freeman Press, 1996.
235. ANSYS, Contents, https://www.afs.enea.it/project/neptunius/docs/fluent/html/ug/node1.htm, (accessed 06 05 2020).
236. V. R. Gopala and B. G. M. van Wachem, *Chemical Engineering Journal*, 2008, **141**, 204-221.
237. M. S. Saidi, M. Rismanian, M. Monjezi, M. Zendehbad and S. Fatehiboroujeni, *Atmospheric Environment*, 2014, **89**, 199-206.
238. C. W. Hirt and B. D. Nichols, *Journal of Computational Physics*, 1981, **39**, 201-225.
239. ANSYS, 16.3.2 Volume fraction equation, https://www.afs.enea.it/project/neptunius/docs/fluent/html/th/node299.htm, (accessed 30/06/2020, 2020).
240. ANSYS, 24.2.2 Choosing a Volume Fraction Formulation, https://www.afs.enea.it/project/neptunius/docs/fluent/html/ug/node722.htm, (accessed 30/06/2020, 2020).
241. ANSYS, 7.2.3 Porous Media Conditions, https://www.afs.enea.it/project/neptunius/docs/fluent/html/ug/node233.htm, (accessed 15 05 2020, 2020).
242. ANSYS, 4.4 Standard, RNG, and Realizable k- epsilon Models, https://www.afs.enea.it/project/neptunius/docs/fluent/html/th/node57.htm#13856, (accessed 22/06/2020, 2020).
243. ANSYS, 18.4.3 Pressure-velocity coupling, https://www.afs.enea.it/project/neptunius/docs/fluent/html/th/node373.htm, (accessed 02/07/2020, 2020).
244. B. Andersson, B. van Wachem, L. Håkansson, M. Mortensen, R. Sudiyo and R. Andersson, in *Computational Fluid Dynamics for Engineers*, Cambridge University Press, Cambridge, 2011, DOI: DOI: 10.1017/CBO9781139093590.004, p. 49.
245. ANSYS, 18.4.1 Discretization of the Momentum Equation, https://www.afs.enea.it/project/neptunius/docs/fluent/html/th/node371.htm, (accessed 22/06/2020, 2020).
246. T. Ahmed, in *Reservoir Engineering Handbook (Fifth Edition)*, ed. T. Ahmed, Gulf Professional Publishing, 2019, DOI: https://doi.org/10.1016/B978-0-12-813649-2.00004-9, pp. 167-281.
247. ASTM, *Journal*, 2018.
248. H. Schlichting and K. Gersten, in *Boundary Layer Theory*, Springer, 9 edn., 2017, ch. Pt III Ch 15, pp. 416-419.
249. M. Ding and A. Kantzas, *PETSOC-07-02-03*, 2007, **46**, 6.

250. V. P. Dimri, R. P. Srivastava and N. Vedanti, in *Handbook of Geophysical Exploration: Seismic Exploration*, eds. V. P. Dimri, R. P. Srivastava and N. Vedanti, Pergamon, 2012, vol. 41, pp. 89-118.
251. R. Mohais, C. Xu, P. A. Dowd and M. Hand, *Geophysical Research Letters*, 2012, **39**.
252. D. Takhanov, MSc, Imperial College London, 2011.
253. W. S. Hinman, C. T. Johansen and P. E. Rodi, *Aerospace Science and Technology*, 2017, **70**, 549-558.
254. J. Tu, G. H. Yeoh and C. Liu, in *Computational Fluid Dynamics*, eds. J. Tu, G. H. Yeoh and C. Liu, Butterworth-Heinemann, Burlington, 2008, DOI: https://doi.org/10.1016/B978-075068563-4.50008-2, pp. 224-276.
255. K. G. Kornev and A. V. Neimark, *Journal of Colloid and Interface Science*, 2001, **235**, 101-113.
256. M. Stange, M. E. Dreyer and H. J. Rath, *Physics of Fluids*, 2003, **15**, 2587-2601.
257. R. L. Graham, B. D. Lubachevsky, K. J. Nurmela and P. R. J. Östergård, *Discrete Mathematics*, 1998, **181**, 139-154.
258. F. Ouali, G. McHale, H. Javed, C. Trabi, N. Shirtcliffe and M. Newton, *Microfluidics and Nanofluidics*, 2013, **15**.
259. R. Urteaga, L. N. Acquaroli, R. R. Koropecki, A. Santos, M. a. Alba, J. Pallarès, L. s. F. Marsal and C. L. A. Berli, *Langmuir*, 2013, **29**, 2784-2789.

APPENDICES

Appendix 1

To model the injection speed ranges in the substrates, the speed of the injection fluid can be modelled as the speed of the surface of a spherical droplet, radius *r*, as it expands. As constant volumetric flow rates Q were used in this study, this implies that:

$$Q = \frac{\partial V_{dep}}{\partial t} = constant, c$$

As:

$$V(t) = Qt$$

It therefore follows that:

$$\frac{4}{3}\pi r(t)^3 = Qt$$

Hence the radius as a function of time is:

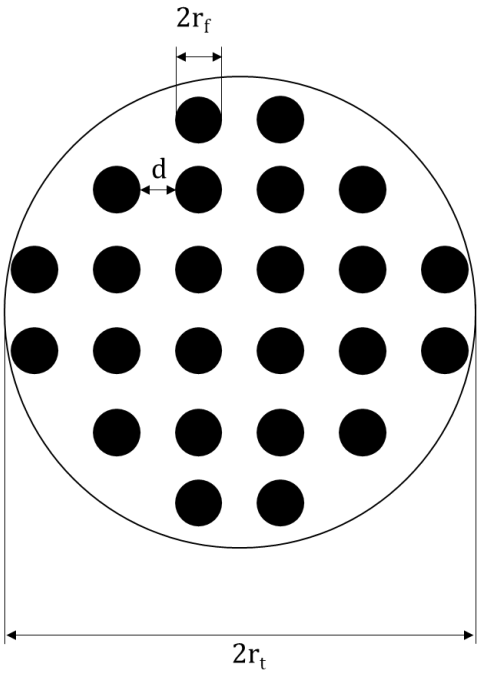
$$r(t) = \left(\frac{3Qt\pi}{4}\right)^{1/3}$$

The speed of a point on the surface can then be shown to be the derivative of radius, which is:

$$\frac{\partial r}{\partial t} = \left(\frac{Q\pi}{36t^2}\right)^{1/3}$$

Hence, the speed of the injection front can be estimated to scale with time$^{-2/3}$. By substituting in known volumetric flow rates and durations to obtain deposits of certain volume, the range of expected flow speeds can be calculated and, therefore, the range of capillary numbers expected over an injection can be determined.

Appendix 2



For a square array of fibres radius r_f with edge-to-edge closest distance d packed into a larger tube radius r_t, at a known volume fraction V_f, the volume fraction may be written as:

$$V_f = n\left(\frac{r_f}{r_t}\right)^2$$

The area A_t of the tube may be given by:

$$A_t = \pi r_t^2$$

The bounding square of this circle has an area of:

$$A_{t-sq} = 4r_t^2$$

The ratio of these areas is therefore:

$$\frac{A_{t-sq}}{A_t} = \frac{4}{\pi}$$

The number of fibres in a square if the fibres were extended out of the tube into the bounding square of the tube, n_{sq}, can be determined by scaling by the area of the tube to the area of the bounding square, which is:

$$n_{sq} = \frac{4n}{\pi}$$

The number of fibres along each side can therefore be given by:

$$\sqrt{n_{sq}} = \sqrt{\frac{4n}{\pi}}$$

As the edge length is $2r_t$ the edge length can also be expressed, through the sum of the fibres widths and spacings, as:

$$2r_t = 2r_f + (2r_f + d)\sqrt{\frac{4n}{\pi}}$$

Rearranging for the nearest neighbour spacing d yields:

$$d = \frac{2r_t - 2r_f}{\sqrt{\frac{4n}{\pi}}} - 2r_f$$

This, however, is not useful in terms of understanding the packing distance versus total capacity. Hence, replacing n with the previous identity for V_f gives, after some rearrangement, Equation 28 as required:

$$d = \frac{\sqrt{\pi} r_f (r_t - r_f)}{r_t \sqrt{V_f}} - 2r_f$$

This result can be verified by setting d to 0 to determine the maximum packing efficiency. Doing so yields, for the values of r_t and r_f used in this project (850 and 4.2 μm respectively), a value of 0.778. This is just below the 0.785 ($\pi/4$) value for a primitive array of circles in a unit cell. This slight variation is due to the bounding space being circular; the limiting value of volume fraction tends to $\pi/4$ as r_f/r_t tends to 0.